University of Brighton

Advanced Engineering Centre

Combustion, efficiency, and inlet dynamics in a Recuperated Split Cycle Expander

SIMON A HARVEY

A thesis submitted in partial fulfilment of the requirements of the University of Brighton for the degree of Engineering Doctorate (EngD)

In collaboration with Ricardo UK

June 2023

Abstract

The recuperated split cycle engine (RSCE) is a split cycle engine with quasi-isothermal compression and exhaust recuperation. This novel concept allows the decoupling of efficiency and peak combustion temperature. In this work a methodology for evaluating the efficiency limits brought on by emissions limitations of thermal engine is demonstrated, before focussing on modelling and experimental work on the expander/combustor of a RSCE.

When evaluating the RSCE expander in isolation of the other systems, thermal and brake efficiency metrics can be skewed by the free Rankine work of the simulated recuperator. Metrics are proposed in this work which discount this effect to enable evaluation of the efficiency of the expander. A 0D model of the single cylinder combustion research engine (SCCRE), representing the RSCE expander, is presented. With studies and analysis of responses to key variables effecting performance, engine setup, and expander design analysed and discussed.

Experimental results and analysis produced from the SCCRE test bed demonstrated 35.6% efficiency. However, this was limited by low combustion efficiencies of 60-70%. If combustion efficiency (CE) can be increased, 50.6% efficiency in the expander is demonstrated to achievable, before consideration of additional work reductions and heat recuperation from quasi-isothermal compression and exhaust recuperation in a full RSCE system.

High FSN (> 1) results combined with lowering CE at the higher pressures tested (>3.5MPa) demonstrated low combustion system optimisation at high inlet pressures and therefore high load conditions. With these factors in mind, the best $BSNO_x$ achieved from the parameter swings was 2.16g/kWh. With nitrogen dilution to 18% oxygen by volume, this drops to 0.58g/kWh. Emissions data from the expander cylinder suggested a lower plateauing of FSN and increasing NO_x response to diesel rail pressure than that of a conventional ICE.

Hypotheses of mixing methods and conditions affected by high pressure air injection at that could be occurring in the SCCRE and RSCE are proposed, due to the unique inlet dynamics in a RSCE expander at intake valve opening. Schlieren optical data from a high pressure flow rig, replicating the SCCRE cylinder head, is presented which starts to investigate these hypotheses. The initial results confirm that significant shockwaves are created in cylinder by the intake valve and high pressure upstream conditions. This is unique to split cycle engines, has not been reported in the literature, and, as hypothesised, is likely contributing to responses seen.

To fully capitalise on the potential of the RSCE, a combustion, fuel, and air injection system needs to be designed and developed from the ground up with the understanding of unique operation and conditions. A well designed RSCE could in theory provide an on demand premix style of combustion with high combustion efficiency and low emissions. A few potential methods and concepts to achieve this are proposed and discussed.

Contents

List of Publications

S.A. Harvey; K. Vogiatzaki; G. de Sercey; W. Redpath; R.E. Morgan, “Starting to Unpick the Unique Air–Fuel Mixing Dynamics in the Recuperated Split Cycle Engine”. Energies 2021, 14, 2148. https://doi.org/10.3390/en14082148

M. Jaya Vignesh; S. Harvey; A. Atkins; P. Atkins; G. De Sercey; M. Heikal, R. Morgan; K. Vogiatzaki, “Use of cryogenic fluids for zero toxic emission hybrid engines”, in Internal Combustion Engines and Powertrain Systems for Future Transport 2019: Proceedings of the International Conference on Internal Combustion Engines and Powertrain, (ICEPSFT 2019), 1st Edition., Taylor and Francis, 2020, pp. 117–130. https://doi.org/10.1201/9781003023982-10

R. Morgan; C. Lenartowicz; K. Vogiatzaki; S. Harvey; D. Kennaird; N. Owen; R. Pickett; A. Atkins, “The Ultra Low Emissions Potential of the Recuperated Split Cycle Combustion System,” in SAE Technical Paper Series, Sep. 2019, vol. 1, https://doi.org/10.4271/2019-24-0189

F. Khalid; R. Morgan; S.A. Harvey; F. Firmansyah; D. Mason; K. Vogiatzaki; M. Heikal, “Towards zero emission engines through the adoption of combustion lead engine design realised through a split cycle topology”, Sep. 2018, Paper presented at Thermo and fluid dynamic processes in direct injection engines (THIESEL) conference, Valencia, Spain

List of Tables

List of Figures

List of Acronyms

Abbreviation	Definition
AFR	Air fuel ratio
AHR	Apparent heat release
AHRR	Apparent heat release rate
AMRC	Advanced Manufacturing and Research Centre
ASI	After start of injection
ATDC	After top dead centre
BDC	Bottom dead centre
BEV	Battery electric vehicle
BMEP	Brake mean effective pressure
BSE	Brake specific emissions
BSFC	Brake specific fuel consumption
BTE	Brake thermal efficiency
CAD	Crank angle degrees
CE	Combustion efficiency

CH_4	Methane
CMA	Centred moving average
CMEP	Combustion mean effective pressure
CO	Carbon monoxide
CO_2	Carbon dioxide
CO_2e	Carbon dioxide equivalent
CTE	Combustion thermal efficiency
CW	Combustion work
DAC	Direct air capture
DCEE	Double compression expansion engine
DI	Direct injection
DOC	Duration of combustion
EAMEP	Expander adjusted mean effective pressure
EAW	Expander adjusted work
EC	European Commission
EFE	Expander fuel efficiency
EGR	Exhaust gas recirculation
ELMEP	Exhaust energy loss mean effective pressure
EPA	Environmental Protection Agency
ESE	Expander specific emissions
ESFC	Expander specific fuel consumption
ETE	Expander adjusted thermodynamic efficiency
EU	European Union
EVC	Exhaust valve closure
EVIVS	Exhaust valve inlet valve separation
EVO	Exhaust valve opening
EVP	Exhaust valve period
EW	Expander work

FMEP	Friction mean effective pressure
FSN	Filter smoke number
FuelMEP	Fuel energy mean effective pressure
GHG	Greenhouse gas
GIMEP	Gross indicated mean effective pressure
GRW	Gross Rankine work
GW	Gross work
GWP	Global warming potential
HC	Hydrocarbons
HCHO	Formaldehyde
HCPC	Homogenous charge progressive combustion
HDV	Heavy duty vehicle
HFC	Hydrogen fuel cell
HLMEP	Heat loss mean effective pressure
IAT	Intake air treatment
ICE	Internal combustion engine
IGN	Ignition
IMEP	Indicated mean effective pressure
INJ	Injection
IVC	Inlet valve closure
IVO	Inlet valve opening
IVP	Inlet valve period
LHV	Lower heating value
LN_2	Liquid nitrogen
LTC	Low temperature combustion
MEP	Mean effective pressure
MEXA	Motor Exhaust Analyser
MFB	Mass fraction burned

N_2O	Nitrous oxide
NH_3	Ammonia
NIMEP	Net indicated mean effective pressure
NO	Nitric oxide
NO_2	Nitrogen dioxide
NO_x	Nitrogen oxides
NRMM	Non-road mobile machinery
PAH	Polycycle aromatic hydrocarbons
PHE	Public Health England
PLCV	Passenger and light commercial vehicles
PM	Particulate matter
PMEP	Pumping work mean effective pressure
PN	Particle number
PPCI	Partially premixed compression ignition
PRR	Pressure rise rate
QMEP	Thermal energy mean effective pressure
RCW	Recompression work
RDE	Real driving emissions
REW	Rankine expansion work
ROHR	Rate of heat release
RSCE	Recuperated split cycle engine
SCCRE	Single cylinder combustion research engine
SCE	Split cycle engine
SI	Spark ignition
SOC	Start of combustion
SOI	Start of injection
TDC	Top dead centre
TE	Thermodynamic efficiency

TPS	Thermal propulsion system
TSWIN	Thermo swing wall insulation technology
WHO	World Health Organization
ZEV	Zero exhaust/tailpipe emission vehicle

Nomenclature

Symbol	Units	Definition
$\Delta_f H^{\ominus}$	J/mol	Standard enthalpy of formation
α	-	Cut-off ratio
λ	-	Lambda
η	-	Efficiency
η_C	-	Combustion efficiency
η_{CT}	-	Combustion thermal efficiency
η_{EF}	-	Expander adjusted fuel efficiency
η_{ET}	-	Expander adjusted thermal efficiency
η_{GE}	-	Gas exchange efficiency
η_M	-	Mechanical efficiency
η_V	-	Volumetric efficiency
η_{QR}	-	Quasi-recuperator efficiency
θ	°	Crank angle degrees
θ_{DOC}	°	Duration of combustion in crank angle degrees
θ_{DPRI}	°	Duration of pressure rise from intake valve opening
θ_{IGD}	°	Ignition delay in crank angle degrees
θ_{SOC}	°	Start of combustion crank angle
θ_{SOI}	°	Start of injection crank angle
σ	-	Recuperator effectiveness

τ	Nm	Torque
ϕ	-	Equivalence ratio
ω	rad/s	Angular velocity
A	m^2	Area
A_c, B_c, C_c, D_c	-	Constants
A_f	-	Pre-exponential factor
C	-	Isothermal index
c	J/kg·K	Specific heat capacity
c_{air}	J/kg·K	Specific heat capacity of air
c_{exh}	J/kg·K	Specific heat capacity of exhaust
c_p	J/kg·K	Specific heat capacity under constant pressure
c_v	J/kg·K	Specific heat capacity under constant volume
E_a	J	Activation energy
F	N	Force
h_θ	-	Computational steps per crank angle degree
K	-	Rate of reaction constant
k	-	Specific heat ratio
k_{hum}	-	Humidity correction factor
LHV_f	J/kg	Lower heating value of fuel
m_a	kg	Mass of air
$m_{b(i)}$	kg	Mass burned instant
$m_{b(total)}$	kg	Mass burned total
m_f	kg	Mass of fuel
$\dot{m}_a$	kg/s	Mass flow rate of air
$\dot{m}_e$	kg/s	Mass flow rate of emissions
$\dot{m}_{exh}$	kg/s	Mass flow rate of exhaust

$\dot{m}_f$	kg/s	Mass flow rate of fuel
MM	kg/mol	Molar mass
MM_e	kg/mol	Molar mass of emissions
MM_{exh}	kg/mol	Molar mass of exhaust
$\dot{mol}_{exh}$	mol/s	Molar exhaust flow rate
N	-	Temperature rise ratio
n	RPM	Revolutions per minute
p	Pa	Pressure
p_{CS}	Pa	Pressure of cold sink
p_C	Pa	Pressure from combustion
p_{HS}	Pa	Pressure of hot source
p_{Ia}	Pa	Pressure of intake air
p_{IVO}	Pa	Pressure at intake valve opening
p_{mc}	Pa	Maximum cylinder pressure
PRR_I	Pa/°	Pressure rise rate from intake valve opening
Q	J	Energy
Q_{AHR}	J	Energy of apparent heat release
Q_C	J	Heat energy from combustion
$Q_{components}$	J	Heat of components
Q_{exh}	J	Exhaust energy
Q_f	J	Fuel energy
Q_{ht}	J	Heat transfer energy
Q_{LH}	J	Energy from lower heating value of the fuel
Q_{RE}	J	Heat recuperation energy
Q_{REJC}	J	Heat rejection of compressor
Q_{REJE}	J	Heat rejection of expander

$Q_{reaction}$	J	Heat of reaction
Q_T	J	Thermal energy
$\dot{Q}$	W	Rate of energy
R	J/mol·K	Universal gas constant
S_f	-	Engine speed factor
s	m	Distance
s_s	m	Stroke length
T	K	Temperature
T_a	K	Ambient temperature
T_{CS}	K	Temperature of cold sink
T_{exh}	K	Exhaust temperature
T_{HS}	K	Temperature of hot source
T_{Ia}	K	Temperature of intake air
T_{ro}	K	Recuperator outlet temperature
V	m^3	Volume
V_{BDC}	m^3	Volume at bottom dead centre
V_d	m^3	Volume displaced
V_{IVC}	m^3	Volume at intake valve closure
V_{TDC}	m^3	Volume at top dead centre
v	-	Coefficient of each product or reactant in the balanced chemical reaction
$VF_{e\ dry}$	-	Dry volume fraction of emissions
W	J	Work
W_b	J	Brake work
W_C	J	Combustion work
W_{CE}	J	Combustion expansion work
W_{EA}	J	Expander adjusted work

W_G	J	Gross work
W_{GR}	J	Gross Rankine work
W_{RC}	J	Recompression work
W_{RE}	J	Rankine expansion work
$\dot{W}$	J/stroke	Rate of work
$\dot{W}_{CE}$	J/stroke	Combustion expansion work per stroke
$\dot{W}_{RC}$	J/stroke	Recompression work per stroke
$\dot{W}_{RE}$	J/stroke	Rankine expansion work per stroke

Acknowledgements

I'd like to thank the EPSRC, Ricardo, and University of Brighton for the grants and funding that provided me the opportunity to undertake this research. The academic and technical support from Professor Robert Morgan, Professor Konstantina Vogiatzaki, Professor Morgan Heikal, Christopher Lenartowicz, and Guillaume De Sercey. As well as family, friends, and my partner, all without which I am not sure I would have had the encouragement and perseverance to complete this work, even without a pandemic thrown in for good measure.

Declaration

I declare that the research contained in this thesis, unless otherwise formally indicated within the text, is the original work of the author. The thesis has not been previously submitted to this or any other university for a degree and does not incorporate any material already submitted for a degree.

Signed:

Simon Harvey

Dated: 07/10/2023

Chapter 1 Introduction

1.1 The Recuperated Split Cycle Engine

The recuperated split cycle engine (RSCE) has been touted as a potential alternative internal combustion engine (ICE) that could achieve both high efficiency and low toxic emissions. The potential benefit put forward by the RSCE, compared to other ICEs, is the ability to control and lower start of combustion temperature, implementation of a type of homogenous charge compression ignition (HCCI), and a novel thermodynamic cycle. With the thermodynamic cycle achieve higher efficiency through quasi-isothermal compression and heat recuperation.

The RSCE utilises a split cycle engine (SCE) architecture where the conventional four stroke cycle is split into two chambers/cylinders. One cylinder performs the induction and compression strokes and the other performing combustion/expansion and exhaust strokes. The RSCE innovation compared to other SCE concepts is the injection of coolant during the compression strokes, to achieve quasi-isothermal compression, and addition of a recuperator to recuperate otherwise wasted heat from the exhaust into the combustion cylinder intake air. A schematic diagram of an early RSCE concept known as the isoengine is shown in Figure 1.1. More detail on the RSCE, other ICE concepts, and novel technologies will be discussed in Chapter 2.

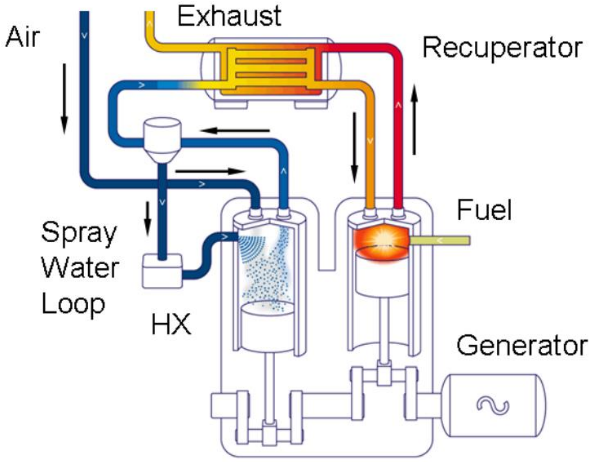

Figure 1.1 Schematic diagram of the isoengine [1].

Since 2015 the Advanced Engineering Centre at the University of Brighton have been running experiments on a single cylinder combustion research engine

(SCCRE) replicating the combustion/expansion cylinder of the RSCE. Initially Ricardo PLC were the industrial partner on the project until the intellectual property was spun out into a new company in 2017, Dolphin N2 Ltd, who then replaced Ricardo as the industrial partner.

Past theoretical research on the thermodynamics demonstrated the potential for 60% efficiency [2] and experimental research on the SCCRE demonstrated 50% efficiency [3]. However, the experimental research on the SCCRE had poor repeatability and a limited operating range. The "black box" approach had little consideration of the fundamentals affecting the combustion to achieve both high efficiency, low emissions, and general operation. In-cylinder conditions were also not considered.

1.2 The Research

1.2.1 Introduction

The validity of continuing combustion engine research has been called into question due to the climate crisis and the rise of new technology. However, there has been limited analysis of the theoretical limits of a nontoxic ICE, even in basic terms.

This research aims to better understand the theoretical and practical limitations of the current SCCRE, how the in-cylinder processes and general operation can be engineered, and therefore if a clean and high efficiency RSCE expander can be realised and potentially improved upon from the SCCRE.

The research will seek to answer the problem of ICE emissions and efficiency by taking an emissions' driven approach to combustion, to understand the upper efficiency limit considering emissions limitations, and undertake a detailed evaluation and discussion of one potential ICE candidate that has shown promise in previous initial research, i.e., the SCCRE at the University of Brighton representing the expansion cylinder of a RSCE. As the focus of the work is on emissions, the research will focus on the combustion/expansion cylinder but there will be discussion on the considerations and implications of the combustor responses on the wider RSCE system. The research will focus on improving emissions reductions in a reciprocating ICE and will not consider social or usage changes as part of the research. The research will not discuss the sustainability of manufacturing an engine, purely the in-use emissions which typically make up most of the emissions from an ICE. For the same reasons, the manufacturing of a sustainable fuel will not be analysed. Emissions directly from the combustion chamber will primarily be assessed and discussed, possible reductions with after treatment will not be discussed in detail but will be mentioned.

1.2.2 Research Question, Aim, & Objectives

Primary research question:

> Is the RSCE expander a combustion system that has the potential to realistically deliver both ultra-high efficiency and low emissions?

Through answering the primary research question, the research aims to explore the limits of what an ICE can theoretically achieve in terms of efficiency with the limitation of producing low or negligible toxic emissions. This will be achieved through research and theoretical work, as well as through a focused experimental programme that explores the phenomena affecting the mixing and combustion processes in the specific novel SCE under research at the University of Brighton, the RSCE.

An inductive reasoning approach was taken for the research through theoretical thinking from current knowns with experimentation, to prove or disprove the inductive reasoning. For example, the combustion system in the RSCE has atypical upstream fluid conditions compared to conventional engines due to the high upstream pressures of the combustor. Past research has demonstrated the RSCE produces rapid combustion and low NO_x emissions [3]. Therefore, changes in the fluid flow conditions are hypothesised to contribute to rapid combustion and low NOx emissions.

Through specific experimental studies the conditions inside the RSCE aim to be explored. With the aim of understanding the fundamental physics that govern the combustion system and the current performance of an unoptimised RSCE combustor. To build a better understanding of the responses for future development and engineering of new hardware, to fully capitalise on the phenomena taking place and improve the combustion system.

The primary research question and aim can be further split into 6 questions, with the objective to answer these questions through the research. The questions encompass two areas: a broad look at the efficiency limits of reciprocating ICEs brought on by toxic emissions limitations, and detailed evaluation of the RSCE expander. The refined questions and their respective areas are shown below.

Efficiency limits brought on by emissions limitations in an ICE:

1. Can an ICE achieve both high efficiency and ultra-low emission combustion?
2. Can conventional Otto or Diesel ICE cycles and combustion methods meet both ultra-low emissions and high efficiency targets?

Detailed evaluation of the RSCE expander:

3. What does the ideal RSCE expander thermodynamic cycle look like?
4. Does the RSCE expander respond to stimuli in line with conventional ICEs and combustion methods?
5. What are the potential fundamental physical processes governing induction, and therefore combustion, processes in the RSCE expander that are different to conventional ICEs?
6. Could the RSCE expander achieve ultra-high efficiency and low emission combustion?

Questions 3-6 are the main detailed focus of this work and will be covered in Chapter 4 through to Chapter 6. Chapter 3 will address questions 1-2.

Through answering the refined research questions, the research seeks to provide the below as a contribution to knowledge:

- A simple methodology for assessing the upper limit or efficiency for a low/zero emission combustion engine.
- Analysis of thermodynamic cycles to achieve the upper limit of a low/zero emission combustion engine.

- Requirements of a future ICE to achieve zero/low emissions.
- Performance and emissions of a RSCE combustor from a single cylinder research engine.
- Evaluation of the ideal RSCE expander cycle and it’s responses to main variables.
- Similarities between RSCE and conventional ICEs.
- The unique responses of the RSCE.
- Hypotheses for the enhanced atomisation observed in the RSCE.
- Optical images of the unique inlet conditions in the RSCE, exhibiting shockwaves.
- Recommendations, methods, and potential pathways to optimise the RSCE expander and combustion system.

Chapter 2 Literature Review

2.1 Introduction

A fundamental approach must be taken to understand the efficiency and emissions limits of what can be achieved with an ICE. Combustion phenomena, novel thermodynamic cycles, and ICE technologies need to be assessed to understand their limitations in achieving a high efficiency and low emissions system. A range of research topics and applicable ICE phenomena will therefore be presented and discussed in this chapter. With a particular focus on the ability of research topics to meet future sustainable needs.

2.1 Motivation & Background

2.1.1 Health & Sustainability

2.1.1.1 Introduction

Toxic emissions are hazardous to human health and greenhouse gases (GHG) are hazardous to global sustainability. These are the fundamental motivations for “cleaner” ICE, combustion systems and other propulsion systems now and in the future. However, there is a balance to be struck with other areas of society that could be impacted by rapid change or unforeseen consequences. The global population will not except a stagnation or declining trend in life expectancy and/or standard of life. The transition to a sustainable society should aim to not impact or add pressures to other areas of concern, for example funding for healthcare or global food pressures.

The Dieselgate scandal brought the issues of toxic emissions firmly into the public eye, pointing a spotlight on not just the issues of automotive manufacturers cheating emissions regulations but what the emissions regulations and accompanying tests are, and if they are applicable or just in the world today.

The World Health Organisation (WHO) and other researchers, such as Vohra et al, predict anthropogenic air pollution causes between 4.2 and 8.7 million premature global deaths every year [4], [5]. A Public Health England (PHE) review stated that human-made air pollution is the biggest environmental threat to health in the UK, with 28,000 to 36,000 deaths a year attributed to long term exposure to toxic emissions [6]. Five of the most damaging pollutants are outlined as fine particulate matter ($PM_{2.5}$), ammonia, nitrogen oxides (NO_x), sulphur dioxide, and non-methane volatile organic compounds [6]. Particulate matter (PM) is responsible for most air pollution deaths [5]. With coarse PM with a diameter of 10μm (PM_{10}) or less able to penetrate the lungs and fine PM with a diameter of 2.5μm ($PM_{2.5}$) or less able to pass through the lung barrier into the blood stream [6].

Since the decline of coal in the world at the end of the 20th century, transport has become a significant anthropogenic source of toxic PM and NO_x emissions. With the majority of PM in the atmosphere of urban areas, such as London, attributed to combustion of diesel for transportation [7]. In 2013 the European Environmental Agency (EEA) attributed 40% of NO_x emissions to road transport and 40% of $PM_{2.5}$ to transport [8]. Emissions legislation is starting to have an effect on in reducing PM and NO_x emissions. In 2020 99% of Londoners still lived in areas which exceed the WHO guidance for $PM_{2.5}$ exposure [9]. More recent data from the EEA on emissions from transport in 2019, shown in Figure 2.1, reports transport to account for 21% of CO, 55% of NO_x, 13% of PM_{10}, and 20% of $PM_{2.5}$ emissions, with road transport exhaust emissions reportedly accounting for significant amounts of these emissions.

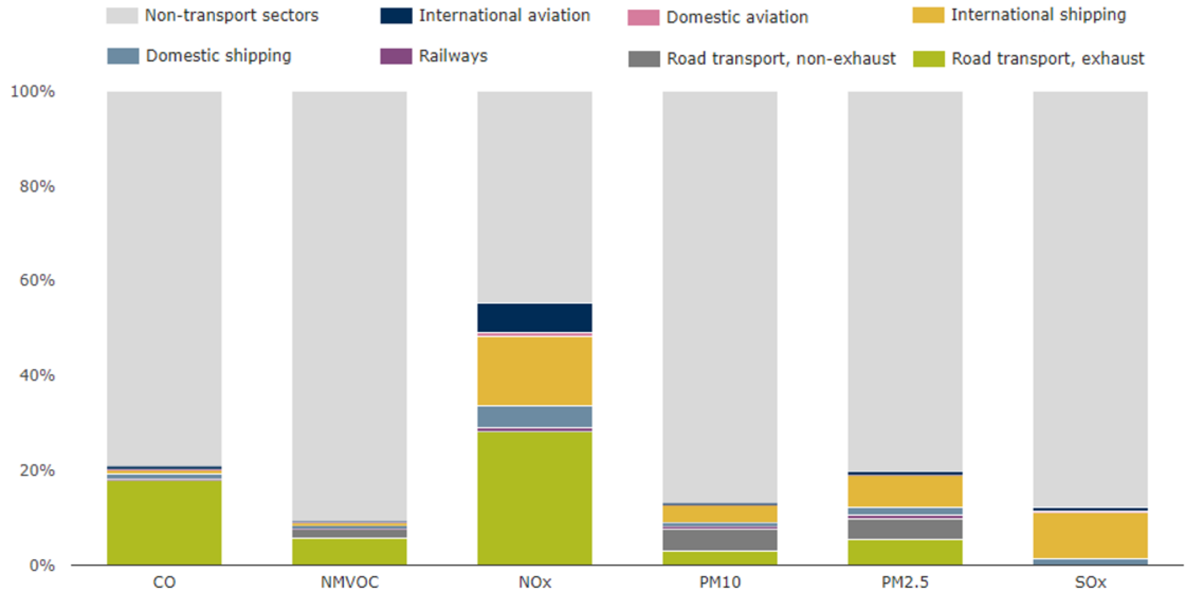

Figure 2.1 Contribution of the transport sector to total emissions of the main air pollutants [10].

The effect of these toxic emissions impact built up areas the most, where road transport is highly prevalent, as well as areas where vehicles accelerate from a standstill, such as road junctions. Policy makers have therefore sought to remove the highest polluters from built up areas. Leading to the implementation of higher minimum standards. One example being the Ultra-Low Emissions Zone in London, creating a financial disincentive to driving legacy emissions standard vehicles in these areas, which is starting to have an effect [9]. With many cities and towns throughout the world regularly exceeding the WHO daily and annual mean air quality guidelines, the implementation of similar low emissions zones is increasing, and will likely need to increase further to ensure areas in cities and towns meet air pollution limits to protect the health of the local population.

Maritime transport currently has much looser emissions legislation than that of the automotive sector. The CO_2 per kg cargo transported of the marine shipping industry is typically lower than that of road transport, due to the size and efficiency of modern ships [11]. However, NO_x and other emissions, such as SO_2 are usually higher. Though these emissions can have a lower effect on health, due to emission deposition usually not being located near built up populous areas. As shipping emissions have a low effect on public health compared to road transport, shipping will not be further expanded upon in this piece of work. However, the technologies that are discussed in this work can be applied to the maritime transport industry.

With the emergence of new propulsion technology and emissions concerns, the validity of continuing ICE research has rightly been called into question, due to these pressing issues of climate change and toxic emissions. However, there has been little questioning or steps back from where the modern ubiquitous Otto and Diesel cycle ICEs of today are in terms of technology, and what is theoretically achievable with an ICE in terms of emissions and sustainability when delimited from conventional approaches.

Changes in vehicle propulsion will be complemented by advances in other areas of mobility, such as smart cities, inter-vehicle connectivity and accessibility solutions. These technology solutions aim to both reduce the demand and energy consumed by the remaining transportation services. Delivering the right vehicle for the right journey instead of a ubiquitous vehicle for all duty cycles and a suboptimal duty cycle. These methods and others will help reduce emissions in g/km, such as aerodynamics, weight, and logistics, but will not be approached in this work.

2.1.1.2 Emissions Regulations

Regulations are the major driving force in the automotive sector to bring about change and investment in propulsion systems and their associated emissions. European Commission (EC) and United States Environmental Protection Agency (EPA) emissions regulations are the dominant emissions standards in the world, having been adopted in various countries outside of the European Union (EU) and the United States. In this section, only the EC emissions regulations affecting vehicle in use will be assessed and discussed in detail.

In major European cities, passenger and light commercial vehicles (PLCV) make up the vast majority of toxic emissions, with a prediction of 42% (Budapest) and 92% (London) of all cars needing to shift to zero tailpipe/exhaust emission vehicles (ZEV) to attain emission at or below European average guidelines [12].

Past regulations have led to a general public understanding and blame on the ICE for CO_2 emissions. Implying the ICE creates carbon emissions rather than the fuel, as is the case with most vehicle emissions regulations by the EU and EPA, such as past road tax on CO_2 emissions in the UK. Comparing metrics such as g/km of CO_2 are really metrics of efficiency of the overall vehicle, analogous to fuel consumption, rather than CO_2 emissions due to the combustor. While regulation of efficiency and toxic emissions through taxation is warranted, the comparison of CO_2 emissions has shifted the focus to the vehicle manufacturers and away from fuel companies up until recently.

Fuel efficiency for the consumer and regulations govern industry producing lower CO_2 output from conventionally fuelled ICEs. However, insufficient regulation and/or forward thinking led to increase uptake in the EU and UK, such as the “dash for diesel”, of diesel vehicles at the end of the 20th century. This enabled the UK and other countries to deliver vehicles with low CO_2 emissions per km to meet the 1997 Kyoto Protocol to reduce CO_2 emissions. However, this had the effect of increasing NO_x and PM, due to poor regulation and rapid uptake of diesel vehicles. Which had higher combustion temperatures and limited aftertreatment systems at the time. This has partially led to a relatively rapid reduction in non CO_2 emissions over the last two decades. Future legislation must ensure that these types of unintended consequences are learned from and not repeated.

Sustainable fuels are gaining wider publicity, understanding, and are increasing in research focus, but analysis of fundamentals to address whether it is theoretically possible to achieve high efficiency and low emissions with a sustainable fuel are still necessitated. If the carbon is from a sustainable fuel the focus of the combustor must be on the toxic emissions produced, followed by efficiency to reduce energy consumption, and cost.

The past, current, and proposed EC tailpipe emissions regulations for PLCVs under 1,305kg are shown in Table 2.1. While the specific emissions limits did not change in the separate regulations with for Euro 6 (Euro 6b, 6c, etc), the method under which the type approval were tested changed. Worldwide harmonised test procedure and the Real Driving Emissions (RDE) tests were introduced partially in response to “cycle beating” exposed in the Dieselgate scandal and criticism of emissions laboratory tests not being representative of real on road emissions [13]. RDE tests were introduced in 2015 to test emissions of vehicles on the road with realistic conditions. The RDE testing is of note, as this required vehicles to be tested on the road with portable emissions measurement systems from 2016 in the EU. The RDE tests have had an impact in combatting the difference between test cycle emissions and real-world emissions, resulting in an improvement in the Euro 6 and Euro VI emissions on the road. However, there continue to be issues with Euro VI trucks not meeting regulations once they are on the road [14]. Conformity factors are playing a role and will need to be tackled in the future with tighter regulation.

Table 2.1 European emissions standards for PLCVs under 1,305kg.

Type Approval	First Registration Date	Fuel	CO (g/km)	HC + NOx (g/km)	NOx (mg/km)	HC (g/km)	PM (mg/km)	NMHC (mg/km)	NH_3 (g/km)
Euro 1	01/1993	Diesel	2.72	0.97	-	-	140	-	-
		Petrol					-		
Euro 2	01/1997	Diesel	1.0	0.7			80		
		Petrol	2.2	0.50			-		
Euro 3	01/2001	Diesel	0.66	0.56	500		50		
		Petrol	2.3	-	150	0.2	-		
Euro 4	01/2006	Diesel	0.5	0.30	250	-	25		
		Petrol	1.0	-	80	0.1	-		
Euro 5a	01/2011	Diesel	0.5	0.23	180	-	5		
		Petrol	1.0	-	60	0.1		68	
Euro 5b	01/2013	Diesel	0.5	0.23	180	-	4.5	-	
		Petrol	1.0	-	60	0.1		68	
Euro 6 Current	09/2015	Diesel	0.5	0.17	80	-	4.5	-	
		Petrol	1.0	-	60	0.1		68	

Euro 7 Proposed	07/2025	All	0.5		60	0.1	4.5	68	0.2

There were significant reductions of carbon monoxide (CO) levels of ~50% each type approval from Euro 1 to Euro 4, before a stagnation until the proposal for Euro 7. Specific NO_x regulations only came into effect in 2001 in the Euro 3 emissions standard for PLCVs. Since then, NO_x regulations have become more stringent with the current Euro 6d regulation representing a minimum 84% and 60% reduction in NO_x production for diesel (500 mg/km to 80 mg/km) and petrol (150 mg/km to 60 mg/km) respectively.

The Euro 7 proposal harmonises emissions limits across fuels to the lowest level for the specific emission from the past diesel and petrol type approvals. The measurement of hydrocarbons (HC) and NO_x is removed and instead utilises the approach that has been used for petrol vehicles since Euro 3, in which HC and NO_x limits are separately measured. This results in a 25% reduction in NO_x emissions for diesel fuelled vehicles and a 50% reduction in CO for petrol vehicles. Notably past emission limits are otherwise unchanged. However, there is the introduction of new limits on ammonia (NH_3) due to the prevalence of urea based selective catalytic reductions in modern ICE vehicles to reduce NO_x emissions. Euro 7 has proposed the introduction of measurement of brake and tyre wear. With a proposed limit of 7mg/km from 2025, before a further reduction to 3mg/km by 2035 for brake abrasion emissions. At the time of writing there is no indication on the limits for microplastics emitted from tyre wear. Details on the procedure under which the emissions from brake and tyre wear will be measured have not yet been published.

Research has shown that freight transport may only make up to 20% of the distance travelled but account for 50% of the total energy consumption of road transport in Europe [15]. Heavy duty vehicles (HDV), such as trucks and buses, account for 2% of the vehicles on the road but are responsible for 28% of CO_2 emissions from road transport in the EU [16]. They are estimated to make up 20 to 36% of transport NO_x emissions in Europe’s biggest cities [12].

The emissions standards for HDVs follow a similar pattern to that of PLCV’s, but they are based on a mass per energy (g/kWh) basis rather than mass per distance (g/km). Below in Table 2.2 is the EC Euro emission type approvals for heavy duty trucks at the tailpipe.

Table 2.2 European emission standards for heavy duty trucks. All limits are g/kWh unless stated otherwise.

Type Approval	Year	Test Cycle	CO	HC	NO_x	PM	NH_3	CH_4	HCHO	N_2O
Euro I	1992, <85 kW	ECE R49	4.5	1.1	8.0	0.612	-	-	-	-
	1992, >85 kW					0.36				
Euro II	1995		4.0		7.0	0.25				
	1997					0.15				
Euro III	2000	ESC & ELR	2.1	0.66	5.0	0.10				
Euro IV	2005		1.5	0.46	3.5	0.02				
Euro V	2008				2.0					
Euro VI Current	2012	WHSC		0.13	0.4	0.01	10 ppm/kWh			
		WHTC	4.0	0.16	0.46					
Euro VII Proposal	2027	WHTC cold	3.5	0.2	0.35	0.012	65 mg/kWh	0.5	0.03	0.16
		WHTC hot	0.2	0.05	0.09	0.008		0.35		0.1

There has consistently been a prominent reduction in at least one of CO, HC, NO_x, and PM in each new Euro emissions standards for heavy duty trucks. With a 58% reduction in PM from Euro I to II, 47% reduction in CO from II to III, 80% reduction in PM from III to IV, 43% reduction in NO_x from IV to V, 80% reduction in NO_x from V to VI, and 87% reduction in CO from VI to VII. Notably in the proposal for Euro VII, there are also reductions of 61% for HC, 77% for NO_x, and 20% for PM, compared to Euro VI limits. Euro VI brought in new limits on NH_3, and Euro VII has proposed new limits for methane (CH_4), formaldehyde (HCHO), and nitrous oxide (N_2O) at the tailpipe. As well as proposing emissions legislation for brake and tyre wear, in line with PLCVs Euro 7. At the time of writing there are no specifics on the limits and testing.

Europe has the some of the most stringent tailpipe emissions regulations (Stage V) for non-road mobile machinery (NRMM) in the world. Legislation is more diverse and specific due the broad categories and uses of vehicles which the NRMM emissions legislation covers. With different limits for emissions for nonroad, waterways, rail, and engine power. Legislation on NRMM will not be discussed in detail due to the lower emissions legislation requirements than that of on road HDVs. Historically the regulations have been looser or lag behind than that of road transport. However, the recent 2020 Stage V regulations for NRMM engines of 56 to 560kW net power are similar that of Euro VI for HDVs. Suggesting they could coalesce in the future.

As well as Euro type approval, CO_2 average fleet emissions regulations play a role in regulating both PLCVs and HDVs tailpipe emissions. For PLCV manufacturers, fleet average CO_2 emissions can be drastically impacted by implementing a new battery electric vehicle (BEV) or hydrogen fuelled models into their fleet with zero tailpipe CO_2 emissions. However, this presents a greater challenge for HDVs. The total amount of CO_2 from the road heavy duty transport sector has stagnated and is predicted to increase in the EU, as shown in Figure 2.2.

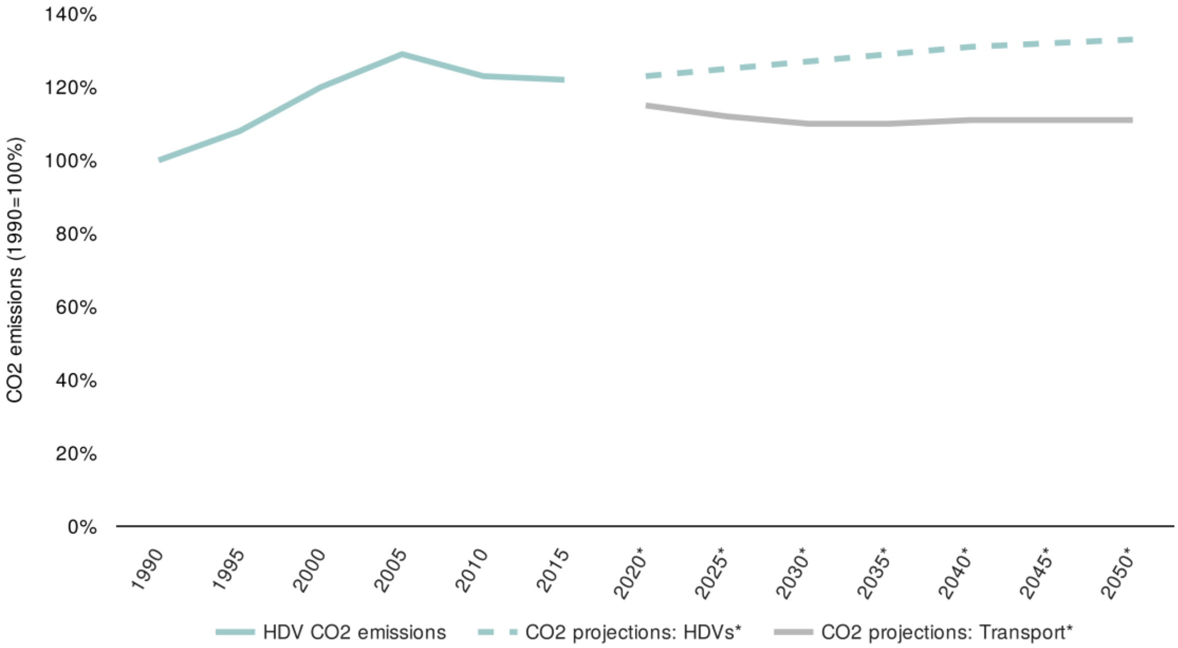

Figure 2.2 Reported and projected CO2 emissions from HDV for the EU-28 from the European Environment Agency in 2018 [17].

While CO_2 emissions per vehicle have been falling, the increase in number of HDV fleet sizes in EU is increasing [17]. Leading to an increase in overall HDV CO_2 emissions as well as an increasing percentage of transport CO_2 emissions being contributed by HDVs in the EU.

In 2019 the EC implemented its first regulation of average HDVs CO_2 emissions to curb the increasing emissions from the road freight sector [18]. The 2019 emission standard set targets for reducing the average emissions from new lorries for the next decade. The regulation legislated vehicle manufactures to reduce CO_2 average emissions 15% by 2025 and 30% by 2030, compared to levels in 2019. With heavy penalties for manufactures missing the CO_2 targets.

In January 2023 the EC proposed new stronger CO_2 regulations applicable to a broader range of HDVs to continue reducing CO_2 emissions from the sector and reduce dependency on imported fuels. New requirements of reducing CO_2 emissions 45% by 2030, 65% by 2035, and 90% by 2040 compared to 2019 levels were proposed [19]. A 90% reduction from 2040 is approximately equivalent to < 5g CO_2/tonne-km, effectively making carbon based fuels unviable form 2040 onwards.

2.1.1.3 Looking Ahead

Beyond the next set of regulations, a more effective looking method for the future would have to examine what would be classed and defined as zero emissions. First what health and sustainability means in this context must be further defined. It can be thought of as either an issue of what is acceptable to breathe for health or what the natural background nonanthropogenic air quality would be, which can vary depending upon the natural local environment without anthropogenic interference.

WHO guidelines for NO_2 exposure are to not exceed mean exposure of 400µg/m^3 (0.21ppm) over 1 hour and 150µg/m^3 (0.08ppm) over 24 hours, with no repeats of exposure within 8 hours [20]. This suggests that emissions control beyond the current Euro VI and VII limits could still be expected for heavy duty road transport in Europe (about 60ppm at the tailpipe) in areas of high sensitivity, such as towns and cities, in the future if this is used as a measure. Future legislation will likely increasingly include a wider range of compounds.

For sustainability, another wider view is that sustainability is the capacity for the biosphere and human civilisation to coexist. The Brundtland report defined sustainable development as development which “meets the needs of the present without compromising the ability of future generations to meet their own mean” [21].

Regarded more specifically within engineering, sustainability is generally defined as products, processes, and services which do not result in products that cannot be reused, recycled, or repurposed during manufacture, use, and end of life. This conceptual framework and methodology of analysis is commonly referred to as cradle to grave analysis, life cycle assessment, or life cycle analysis. In these analyses, the environmental or biosphere impact is assessed at each stage of the product's life.

To date the focus of legislators has been on vehicle tailpipe emissions but in the future consideration of the full lifecycle impact of the manufacture, use and disposal of transportation vehicles, infrastructure and services will be necessary to assess and achieve net zero targets and beyond, to ensure there are not unintended consequences of emissions production in the lifecycle of the vehicle. This has been raised in the calls for the Euro 7 and VII legislation proposals, leading to the inclusion of emissions from brake and tyre wear, as well as the longevity of vehicle useable life. However, the proposal suggests this will not be addressed by Euro standards, instead it will be addressed by reviews of the End-of-Life Vehicle Directive and part of the European Green Deal and the Circular Economy Action Plan in 2023 [22].

Human civilisation and the biosphere will always require energy to exist. However, ideally sustainability should incorporate low energy consumption, so that less energy production is required upstream of any process. This impacts the sustainability upstream of the process and influences cost, which can inhibit uptake in the concerning product or technology and increase the adoption timeframe of the efficient and/or clean technology.

This piece of work will focus on toxic emissions and sustainability of a heat engine during use, i.e., in use propulsion emissions. Embedded and end of life emissions will not be discussed in detail, as they are not main the subject focus of this work. However, it should be noted and assessed in future specific works due to their impact on full life cycle emissions.

2.1.2 The Right Tool for the Job

2.1.2.1 Introduction

Power technology has been dominated by electrochemical batteries on the micro-scale (10s W), ICEs on the medium-scale (kW-MW), and gas turbines at the large scales (10-100s MW) for over seventy years. With transportation and mobility dominated by the fossil fuelled ICE over the past century.

The climate emergency has promoted a rapid and dramatic shift to alternative propulsion technologies powered by renewable ‘green’ energy vectors. This pressing need to transition the world’s primary energy source away from fossil fuels requires a huge technological shift. Advances in technology over the last several decades have started to challenge this status quo, with electrochemical batteries transitioning into kW capacities for transportation and low MW for stationary energy storage. With conventional ICEs being largely displaced by electrochemical batteries in personal transportation and gas turbines by renewable technologies in power generation. However, in high energy mobile and remote applications, such as shipping, road freight, and distributed back up power, the fundamental low energy density of electrochemical battery technology means this is currently an unviable solution to decarbonise these areas.

The ICE is destined to be less ubiquitously used than it currently is due to competing technologies emerging and developing. However, there are circumstances where the ICE will be hard to outcompete, and continued advances will therefore be needed for an ICE to produce lower toxic and GHG emissions in these areas. It is recognised that there is “no silver bullet” technology that can replace all of the applications of the ICE, a portfolio of technologies will be required across the transport sector [23].

It is expected that in duty cycles with low energy requirements, such as the average car journey, or high stop-start drive cycles, such as vehicles in city centres, ZEV will be needed to meet current and future emissions guidelines and improve public health. Current BEV technology has shown that it is able to meet this requirement.

Other heavy duty or high energy drive cycles are currently hard for other propulsion technologies to compete with the ICE, such as intercity, international, and intercontinental travel. Requiring an ICE propulsion system for at least the near future unless an unpredictable breakthrough in technology is made.

The major drivers for differing propulsion technologies for each suitable application are efficiency, energy density, drive cycle, local energy infrastructure, and cost. For a vehicle the energy for the propulsion system must also be easily storable, transportable, and rechargeable. A fuel with a low volumetric and/or gravimetric energy density may not be an issue for local power generation but for a transporter, such as haulage or shipping, the fuel tank must not inhibit the payload capacity or cause undue energy consumption through its mass, shape, and/or size. This is the barrier which has prevented the use of the electrochemical batteries in the past. With electrochemical batteries only in the last decade able to power low energy vehicle drive cycle applications, such as PLCVs. However, this currently remains an issue for high energy drive cycles, such as international haulage and shipping, which limits the application of this solution.

Each propulsion system has individual benefits that suit specific applications and drive cycles. New technologies that have called into question the logic of the past century, of using ICEs for every application, will be discussed briefly in detail here. A short overview of the major new competing and emerging propulsion technologies and their applications will be outlined below. This is to state where the ICE will still play a role as it becomes less ubiquitous in the near and distant future.

2.1.2.2 Battery Electric Vehicles

Electrochemical battery electric vehicles (BEV) are a ZEV. However, it can be argued that BEVs export emissions from where they are used to where the vehicle or energy was created. If the electricity grid is assumed to be 100% renewable, then the energy use emissions are eliminated. Excluding this issue, they can still make a difference to local air emissions and public health by removing emissions from built up areas to areas where the effect on health is most impactful. However, there remain in use emissions from tyre and brake wear. These PM emissions can be higher in the case of BEVs compared to ICE vehicles, due to BEVs having more mass than an equivalent ICE vehicle. The EC is aware of these non-exhaust emissions, considering these emissions to be constitute 50% of PM_{10} and produce other chemicals that are dangerous to public health [24], hence the introduction into their in the latest Euro emissions regulations. While tyre wear with increased vehicle mass is unavoidable, BEV and hybrid vehicles can reduce brake wear, in comparison to purely ICE vehicles, if they utilise a regenerative braking system. Utilising the electric motor instead of traditional brakes to recapture otherwise wasted energy and reduce the amount of brake dust particles that would otherwise be emitted.

Considering road transport, the majority of personal transport vehicles in Europe are expected to use an electric drivetrain by 2050, and 80% of the driven kilometres are forecast to be under electric propulsion [15]. However, the same study forecasts that the remaining 20% of driven kilometres will require an alternative propulsion technology due to the high energy requirement of the journey.

The use of a purely electrochemical battery solution for these high energy applications is primarily impractical due to the store's mass, which compromises the payload capacity of the vehicle and the electrochemical battery. These applications represent only 20% of the driven kilometres but consume 40-50% of the total energy used by the road transport sector. Closer analysis of this research reveals these vehicles are primarily moving freight and people between cities. Others have suggested solutions to this issue by means of electrification of roads using overhead or under road pantograph [25]. Although this option negates the need for a breakthrough in electrochemical battery technology, there remains the challenge of delivering the infrastructure required to generate, store, and distribute the electricity. Considering remote applications, such as intercontinental shipping, this option is clearly unfeasible as the energy must be carried and transported in some form within the vehicle.

The emissions produced from the mining, manufacture and end of life processes are also significant factors with BEVs. With electric cars typically requiring more mining, expensive materials, manufacturing, end of life processing, and energy to produce, due to the electrochemical battery. There is a known concern regarding the supply, ethics and sustainability of mining lithium, nickel, cobalt, manganese, and other expensive mined elements [26]–[29].

The mining industry is an example of a difficult application to utilise BEVs, as they are typically in remote locations with no electricity grid and utilise high energy drive cycles. Recycling alone will not be able to meet the material demands needed to electrify PLCVs and other sectors in the short term to meet demand for BEV [26]. Therefore, continued advancement of other technologies will be needed to reduce and eliminate emissions in these hard to electrify areas.

While electrochemical battery technology will undoubtedly continue to advance, there is an upper limit to the energy density of electrochemical batteries. Aluminium-air, lithium-air and zinc-air are examples of electrochemical batteries with the highest theoretical energy densities, comparable to that of gasoline. Like combustion fuelled ICEs, atmospheric oxygen is utilised in each electrochemical reaction to produce electricity. They have high energy densities comparable to that of gasoline as they do not carry oxygen in the electrochemical battery. However, currently issues exist as they are non-rechargeable, and have issues with by-product removal, recycling, and anode cost, making them currently unviable.

There has been increased interest in solid state electrochemical batteries due to potential higher energy density, increased longevity, increased charging rate, and reduced thermal runaway issues, compared to lithium ion. However, solid state batteries have still not become manufacturable at scale and will still be difficult to penetrate high energy drive cycle applications. Therefore, there has been continued research interest in reducing anode and cathode sizes of lithium-ion until these issues have been overcome.

Increasing gravimetric and volumetric energy density as well as falling costs of electrochemical batteries has led to uptake into the kWh zone over the last decade, making electrochemical batteries viable for personal vehicles, as well as light duty and heavy duty vehicles with low energy duty cycles. Electrochemical battery propulsion will dominate the PLCV sector in the near future, where short low energy consumption journeys are prevalent [15]. However, long distance, large payload, high energy applications and remotely operated machines, such as inter-city transport, haulage, off-highway, marine, and portable power generation, are much harder areas to electrify due to the high energy duty cycles. Until an unpredictable breakthrough is made in energy density of sustainable electrochemical batteries, or other energy storage vectors, high energy chemical fuels will still be needed in the short and near future that can reduce emissions in these hard to electrify sectors.

2.1.2.3 Fuel Cells

Fuel cells have been the subject of increasing research interest over the last several decades and have been proposed as a solution to clean propulsion technology. However, challenges remain over the cost effectiveness of the fuel cell, storage tank, and cost of delivering the required infrastructure [30].

Green hydrogen and methanol have been outlined as the major potential sustainable fuels for utilisation in a fuel cell, with hydrogen gaining particular interest. Solid oxide and proton exchange membrane (PEM) electrolysers have made the most progress over the last decade. With examples of both technologies now in pilot and commercialisation stages.

Using hydrogen or methanol and an air as an oxidiser, fuel cells can achieve higher energy densities and power than that of electrochemical batteries but still slightly below that of current fossil fuelled ICEs. Storing fuel in tanks enables economics of scale at large capacities and provides rapid refilling, like current fossil fuels, in contrast to batteries. However, there are concerns. The implementation of a completely new fuel distribution and delivery infrastructure would be required, and this has a high capital barrier. Fuel cells can be composed of expensive materials, such as platinum. Membrane manufacture is currently relatively immature and expensive. Fuel cell specific power and energy is still less than an ICE.

Emissions are at very low levels, with less than 1ppm NO_x, 4ppm of CO, and less than 1ppm of reactive organic gases reported without aftertreatment. This is due to the low temperatures that the fuel cells operate at. Efficiency is reported to be as high as 70% at low load conditions (10% power) [31], with a range of 30-70% over the full load range [23]. In comparison current modern conventional ICEs have a efficiency range of 30-50% but are most efficient at higher load conditions [23]. Figure 2.3 displays a comparison of hydrogen fuelled ICE and fuel cell efficiencies over the load range.

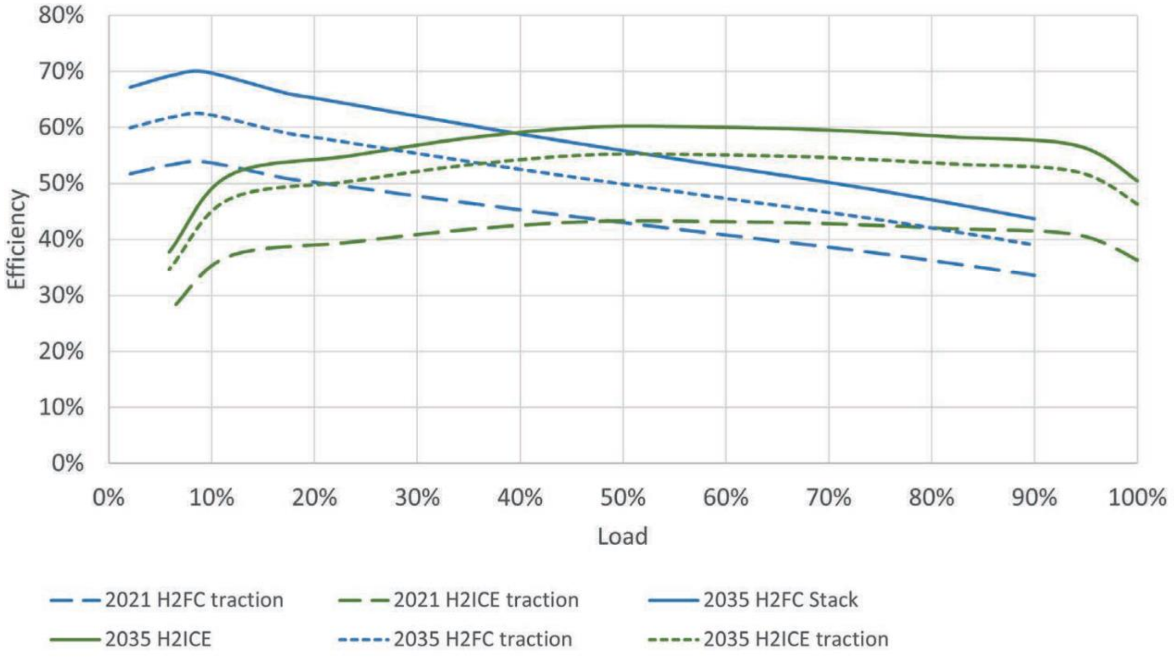

Figure 2.3 Comparison of hydrogen fuelled ICEs and fuel cell efficiencies [32]

Hydrogen fuel cells and hydrogen ICEs could be thought of as complimentary technologies, due to their commonality of fuel and suitability to different applications. With fuel cells most suitable to light to medium load applications, such as passenger and light commercial vehicles, and hydrogen ICEs suited to medium to heavy duty applications, such as international haulage, agriculture, and NRMM.

2.1.2.4 Internal Combustion Engines

The thermodynamic cycles used in conventional ICEs (Diesel and Otto cycles) have not changed for over a century. ICE’s have improved dramatically in terms of efficiency and emissions over this time, but this can mostly be attributed to reducing losses, improved air–fuel mixing, and combustion technologies, rather than a change or step improvement in the thermodynamic cycle itself.

Atkinson and Miller like cycles have been adopted in some recent vehicles, such as those by Toyota, as well as small gains through novel valve timings, high pressure injection systems, lean homogeneous compression ignition, and energy recuperation in modern engines. However, the basic Otto cycle is approaching the fundamental limits of the cycle and new novel cycles have shown interest and need. For example, through the UK Automotive Council’s Thermal Propulsion System roadmap and the US SuperTruck programmes [33], [34].

There remains an efficiency emissions coupling problem in conventional thermodynamic cycles. Increasing combustion temperature increases efficiency but also increases production of NO_x. Emissions are not directly addressed in-cylinder in conventional ICEs unless a cool lean strategy is adopted, such as low temperature combustion (LTC). LTC can be “forced” on a conventional ICE in a limited section of the engine operating map but the control over the end of compression temperature, and therefore the start of combustion, in these engines makes such strategies difficult to implement effectively. Therefore, alternative thermodynamic cycles and engine architectures are required that can deliver a step improvement in efficiency and emissions effectively and reliably.

The combustion engine, where the chemical energy is converted first to heat via a fast-chemical reaction and then via a thermal power cycle to work, is attractive due to the inherent low cost and high-power density of the power conversion device. However, to remain a viable solution two fundamental issues must be overcome: addressing toxic emissions, such as NO_x and carbonaceous PM that are a by-product of the combustion process and increasing thermal efficiency.

Reciprocating heat engines produce the greatest amounts of emissions during use, owing to the use of fossil fuels. However, the emissions from production and recycling of reciprocating engines are relatively low. With the large use of aluminium and steel in the primary engine systems making them highly recyclable and easy to manufacture, relative to electrochemical batteries and fuel cells.

CO_2 emissions are intrinsically linked to the fuels’ carbon source, meaning the CO_2 emission may not be a future issue if a sustainable fuel is utilised. An ICE can use a wide variety of fuel feedstock, making it suitable for reducing or eliminating by-products and waste from other processes in a circular economy.

All applications that continue to use a combustion engine still have the potential to be net zero carbon if they can utilise a combustor that utilised a carbon neutral fuel. Such as synthetic hydrogen, bio or ‘e-fuels’; made from biological and waste sources or CO_2 captured from the atmosphere and renewable energy. However, there remains an issue around other emissions produced during combustion in an ICE apart from CO_2. For an ICE to be truly zero emissions it must produce NO_x, PM, HC, CO, and other trace toxic emissions at levels below the WHO limits at the point of use.

It should be noted that carbon neutral fuels are still in early-stage development and are currently expensive in terms of resource and energy use. Any future sustainable chemical energy carriers will inevitably have a high initial cost than current fuels from fossil derived sources for a certain period. With carbon based renewables having a present cost of approximately 3.5 times that of fossil fuels [35]. Therefore, to mitigate this cost premium and shorten the adoption timeframe, efficiency will remain a key issue to move to cleaner propulsion systems and be a viable replacement for fossil fuels without a significant economic impact on society or barrier for adoption.

2.1.2.5 Comparison of Propulsion Technologies

Energy dense chemical energy carriers will still play a significant role in the transition to and final zero carbon economy. However, the retention of a chemically fuel propulsion system has challenges; the fuel must be sustainable, and the propulsion system must be clean.

Figure 2.4 displays the energy and volumetric densities of a range of chemical fuels and energy carriers. However, this does not include the energy conversion efficiencies of the process which must be considered when deciding on whether the energy vector is suitable for the required application. Figure 2.4 demonstrates some of the intrinsic issues of current and future energy technologies. Such as hydrogen having a low volumetric density unless stored at extremely high pressure (>30 MPa) or a low enough temperature to be stored as a liquid. Lithium-ion batteries have a better volumetric energy density than atmospheric natural gas and hydrogen but has the lowest gravimetric energy density of the compared energy carriers.

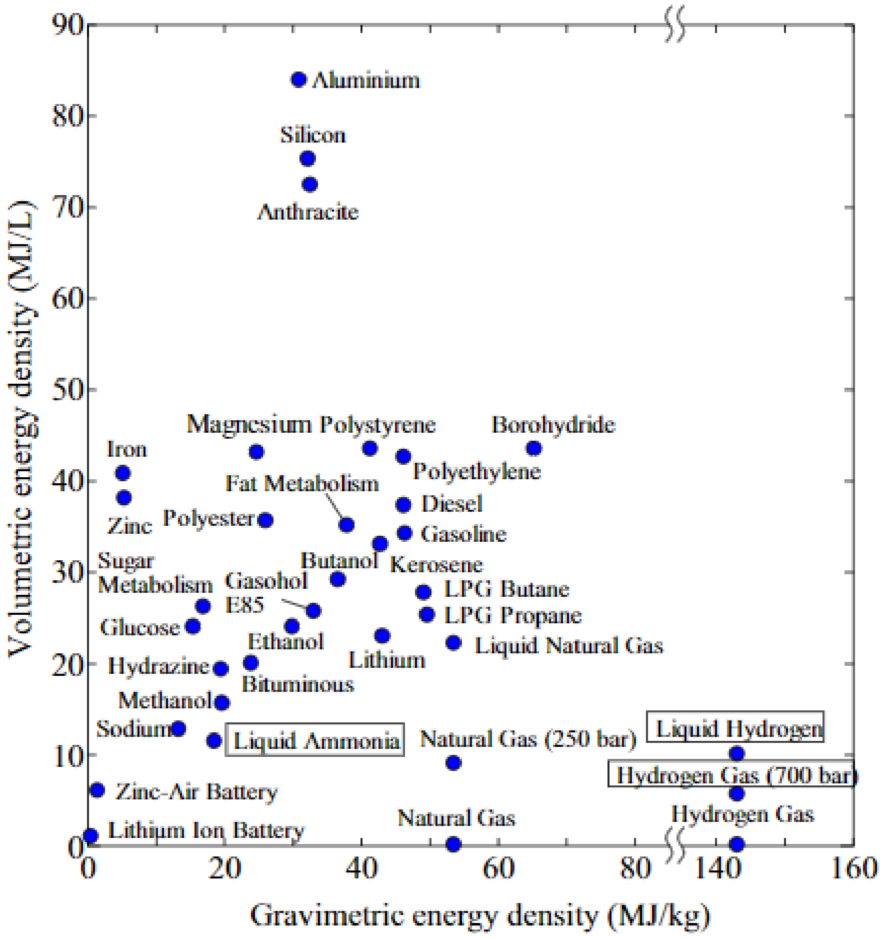

Figure 2.4 Gravimetric & volumetric energy density of combustible materials & electrochemical batteries. Higher heat value for fuels are used as metals are included [36].

Even after considering favourable conversion efficiencies for a lithium-ion battery (high conversion efficiency of 98%) and low efficiencies for a modern ICE (low conversion efficiency of 30%), lithium-ion batteries cannot compete with most gaseous and liquid energy carriers for high and dense energy applications.

Figure 2.5 displays a Ragone plot comparing the energy and power densities of fuel cells, ICE, capacitors, and three electrochemical battery chemistries. This highlights how gravimetric energy or specific energy can be thought of as the range of the vehicle and specific power can be thought of as the acceleration. The acceleration is an important factor for heavy duty high mass applications.

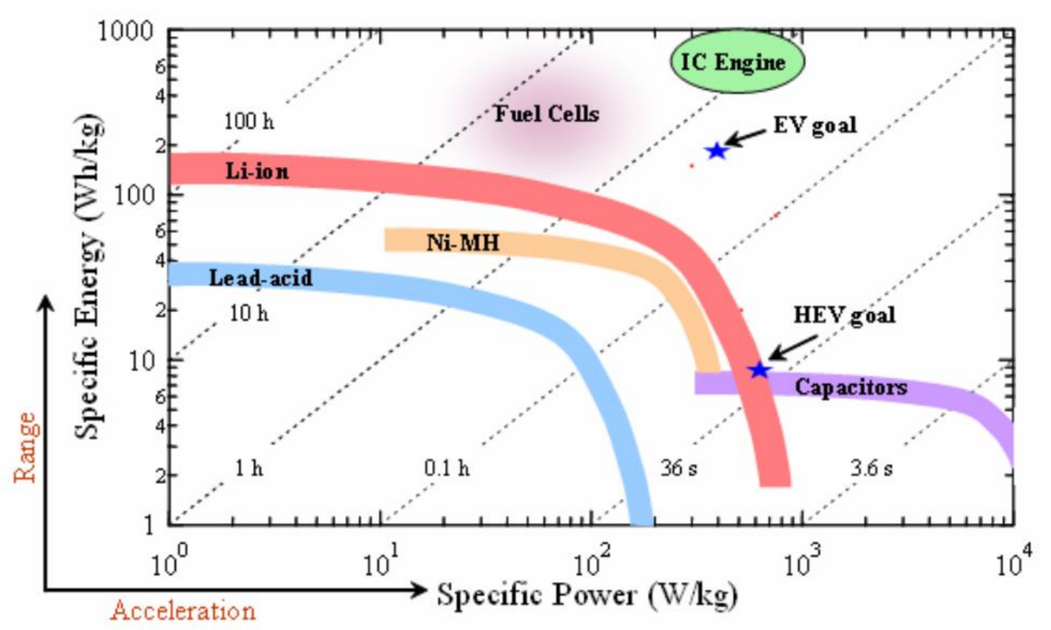

Figure 2.5 Ragone plot of different energy storage options [31]

The graph in Figure 2.6, from a report by the Transport Energy Network (supported by the UK Advanced Propulsion Centre, LowCVP, and the University of Brighton) [23], displays the total lifetime (500 Mm) CO_2 equivalent (CO_2e) emissions for an urban 7.5 tonne truck across with a range of powertrain technologies and energy sources. With the exception of a BEV on renewable electricity, in use CO_2e account for >50% the total vehicle emissions of the vehicle and fuel types considered.

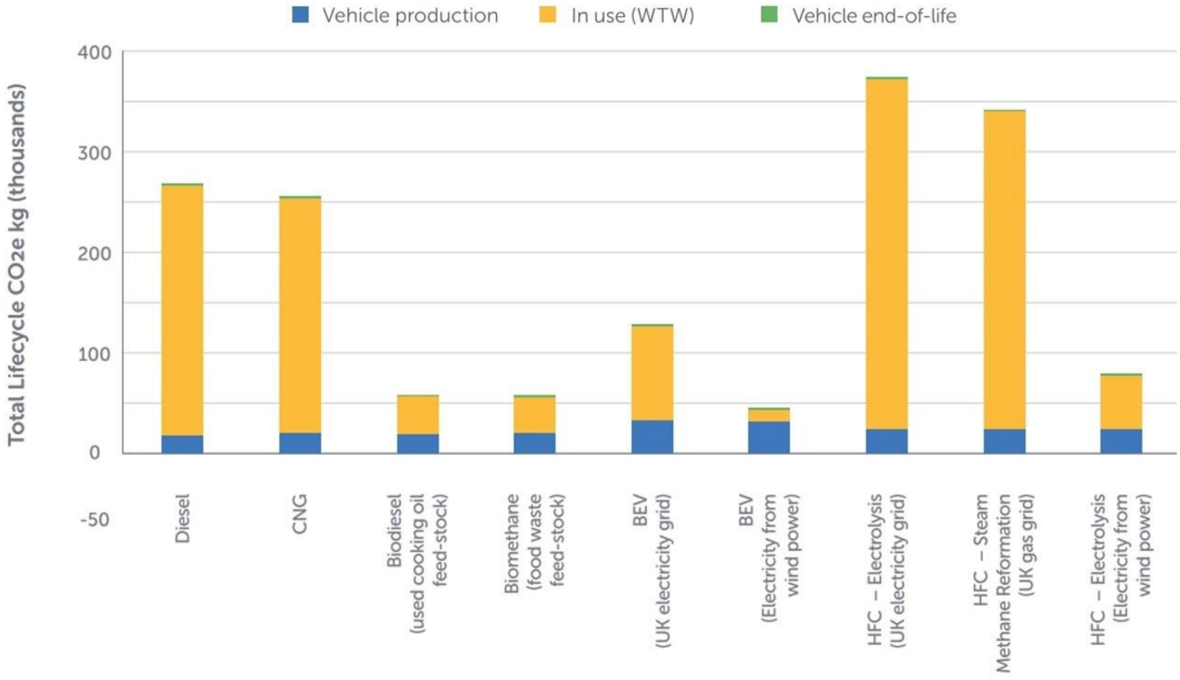

Figure 2.6 Vehicle lifecycle CO_2e emissions for an urban 7.5 tonne truck across different powertrain technologies and low carbon fuels over a life of 500Mm [23]

The graph indicates that HFCs utilising the 2020 UK electricity grid display the largest total lifecycle CO_2e, ~370 Mg CO_2e, due to the round trip efficiency of electrolysis and fuel cells, as well as the carbon intensity of the UK electricity grid. However, there is a dramatic decrease in total lifetime CO_2e for HFCs when the hydrogen is produced from renewable energy, ~75 Mg CO_2e. Steam reformation of H_2 is the predominant source of H_2 currently, however this displays the second highest amount of total lifetime CO_2e. BEV utilising current UK electricity grid equates to roughly half the total lifetime CO_2e of the Diesel and CNG powered trucks. However, the ICEs powered by waste feedstock, such as used cooking oil and biomethane from food waste are half of the current BEV, close to that of a BEV utilising renewable electricity. The low CO_2e and importance for circular economy make these waste fuels attractive as a fuel.

The capital and operational expenditure of the truck is another key consideration for use and adoption. Figure 2.7 displays an estimate of vehicle capital and operations cost amortised over the life of the vehicle in 2020. The costs are wholesale without tax, subsidy, or cost of infrastructure. The error bars display the maximum and minimum potential cost, this is predominantly dictated by the cost of the fuel for the propulsion system. The lowest potential costs is a Diesel engine running on a diesel fuel and a BEV with a small electrochemical battery. Followed by a SCE operating on green hydrogen, with a Diesel engine not far behind. Diesel fossil fuel and green ammonia fuel systems have the lowest variability in cost.

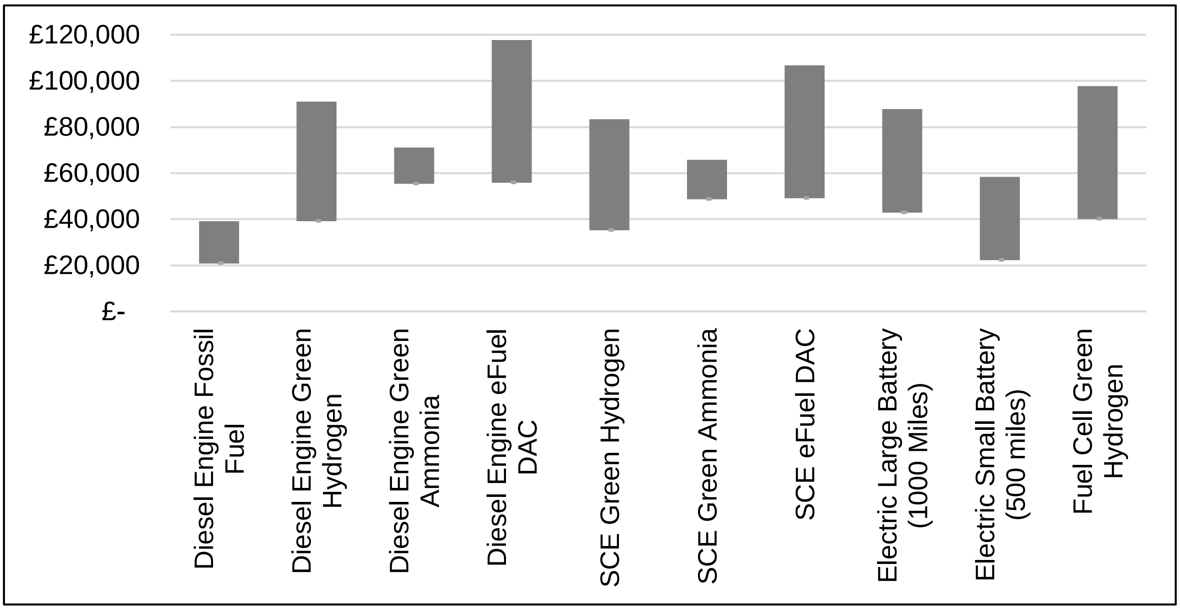

Figure 2.7 Estimated 2020 cost per year for a UK class 8 truck without tax or subsidy.

The 2040 estimated cost per year for competing technologies and fuels starts to become more competitive, as shown in Figure 2.8. There is still a large amount of uncertainty of cost for all the alternative fuels and technologies. This is predominantly dictated by the uncertainty in renewable electricity costs in the UK in 2040. The estimates of costing used for the comparisons in Figure 2.7 and Figure 2.8 can be found in Appendix 1.

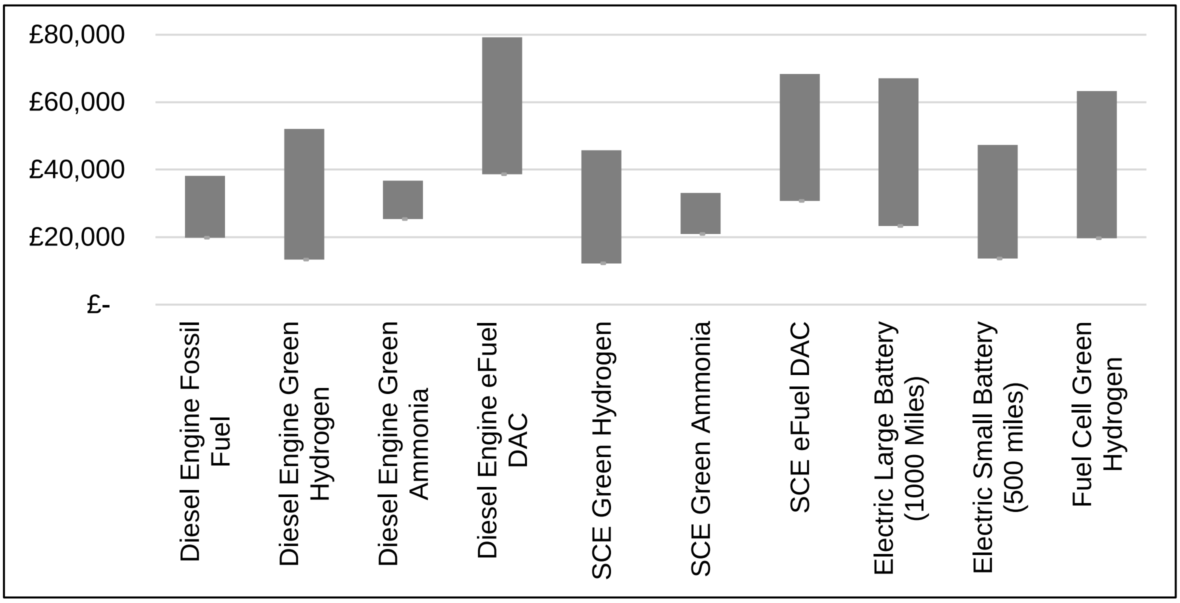

Figure 2.8 Estimated 2040 cost per year for a UK class 8 truck without tax or subsidy.

A SCE represents a cost saving per year and uncertainty reduction vs a Diesel engine over all three fuels, even with a higher capital expenditure, due to the efficiency gains and higher potential maximum efficiency in 2040. A Diesel engine utilising a direct air capture (DAC) efuel has a high chance of not being competitive in 2040. However, the cost saving of a SCE can dramatically increase DAC efuel competitiveness with a large electrochemical battery. Ammonia provides the least uncertainty due to the very small difference in cost for green ammonia in 2020 and 2040. This makes it a potentially less risky avenue for a TPS than DAC efuel or green hydrogen. Both green hydrogen and ammonia are carbon free fuels with great potential. The uncertainty with green hydrogen is the cost. If there is low-cost green hydrogen available in 2040, a Diesel engine retrofitted with a hydrogen fuel and combustion system could remain cost competitive route to decarbonise the heavy duty sector. Green hydrogen utilising a SCE has the lowest potential cost overall using current estimates. There remains a large uncertainty across all of the potential propulsion systems.

Metrics that are important to transportation are cost per kg and CO_2e per kg to move items over the course of the life of the vehicle. A deeper analysis is required to understand vehicle cargo weights, vehicle weight, refuelling, and down time of each vehicle technology for the vehicle application to understand which provides the best CO_2e saving at an acceptable cost. As well as other factors to consider, such as emissions other than CO_2.

Figure 2.9 displays a potential energy consumption view for transport put forward by Siemens. The figure does not suggest that all aviation, marine and road/heavy trucks will be powered solely by biofuel and e-fuels, instead illustrating that there will be a place for sustainable biofuels and e-fuels. Either through on demand grid power or through batteries, electricity will dominate the transport sector in the future. However, in areas that require and can afford the added cost of converting renewable electricity to a green fuel can provide clean energy vectors in these areas. Siemen’s report highlights green hydrocarbon feedstocks, such as methanol, will also be required for areas such as the pharmaceutical and medical industries.

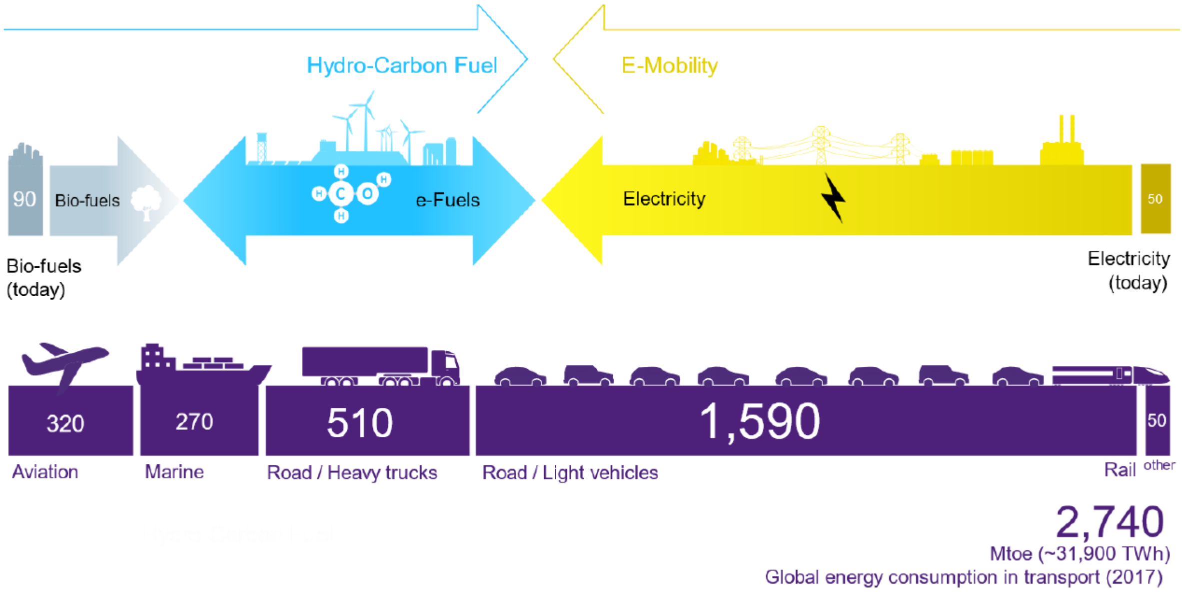

Figure 2.9 Siemens low-CO2 emission future fuel options for global transport in millions of tons [37]

2.1.3 Problems and Challenges

2.1.3.1 Toxic Emissions

As previously discussed, the impact of exhaust emissions on air quality, especially in cities, remains the largest concern and motivation. Any future propulsion system operating in an urban area must deliver near zero emissions in the real world no matter what the driving conditions are. The current range of legislated emissions are expected to widen to consider the size of the particles and other airborne emissions where there are health concerns, such as PM and other fine particles [38]. How zero emissions are defined is open to debate, and arguably should consider impacts in manufacturing, recycling, energy production, as well as in use emissions. This wider debate is beyond the scope of this work; with a focus only on emissions at the point of use and considering the Euro VII standard as the minimum target for a near future TPS.

2.1.3.2 Carbon Dioxide

In recent years, tailpipe toxic emissions have received the most attention. However, with countries committing to net zero targets for 2030-2050, CO_2 will remain a primary legislative driver. Current legislation is focused on the ‘tank to tailpipe’ emissions. In the future, life cycle carbon emissions, including the production and recycling of the vehicle as well as contributions from the energy the vehicle consumes in use, will need to be added to the current policy framework. The ‘net zero’ target will necessitate a transition to sustainable fuel from, for example, a renewable bio or synthetic source. Reviewing all the potential future fuel sources is beyond the scope of this piece of work, but a few of the current main alternative sustainable fuels will be discussed in Sections 2.2 and 2.3. However, it is important to underline that regardless of the source, the alternative sustainable fuel will most likely have a higher cost initially than current fossil fuels. It is therefore assumed that a significant rise in thermal efficiency will be required to best utilise precious sustainable energy in the future minimising operating cost and consumption of precious renewable resources.

2.1.3.3 Cost

The fossil fuelled ICE has delivered over a century of affordable transport. Any future solution must also deliver an affordable solution to society if the world is to maintain its current way of life. When considering cost, the whole value chain must be considered, including new infrastructure for energy production and distribution as well as the vehicle itself. As such, the avoidance of high-cost materials and as far as possible maintaining the general architecture of current engines is desirable.

2.1.3.4 Energy System

To date, the coupling of the transport and power energy supply systems has been weak. Some link between oil and gas prices has historically fed through to electricity prices, but with the electrification of much of the road transport system, this coupling will be inevitably strong in the future. Future transport propulsion technologies must consider the impact on the wider energy system, to avoid unnecessary costs and emissions being transferred from one sector to another, and ensure the minimum societal cost and emissions are achieved.

2.1.3.5 Discussion

The four challenges that must be overcome to transition fossil fuelled ICE vehicles to a clean, sustainable, and affordable propulsion solution are outlined. There remains a question over whether these challenges can be all overcome by an ICE. If they are achievable, the end solution should not be viewed as an ICE under the more traditional definition, but as a ‘thermal propulsion system’ in recognition of the fundamental changes that will be required to meet these challenges and separate it from the fossil fuelled ICEs of the past. This will include changes at the fundamental thermodynamic cycle level and reaction chemistries between the oxidant and the fuel. Within the scope of this thesis, the heat release process will remain within an enclosed expanding volume from which work is extracted via a crank, but all other aspects of the system can, and probably will, require changes.

2.2 Combustion

2.2.1 Introduction

This section will give an overview of the fundamentals of combustion phenomena affecting ICEs and what combustion technology could be used and aid the goal of ultra-low emissions. Chemistry will first be addressed before consideration of a flame and the effects the mixture preparation and combustion conditions have on the primary toxic emissions of NO_x and PM.

2.2.2 Chemistry

Combustion is a chemical process in which an exothermic oxidation reaction occurs. Typically, the reaction rate is relatively fast, although the reaction rate is heavily dependent on the fuel and oxidiser. Combustion is typically a relatively high energy exothermic chemical reaction; the high amount of energy release generally leads to high temperature and reaction rates. However, the reaction rates are lower than those of explosions.

Chemical mechanisms underpin the combustion process. Dictating the products, emissions, and conversion of chemical energy into heat, which an ICE converts into useful work. It is worth underlining the basic equations that are useful for quantifying energies and adiabatic flame temperatures at this point.

Stoichiometry describes “the relative proportions in which elements form compounds or in which substances react” [39, p. 505]. For a combustion reaction, this is the condition at which a fuel and oxidant are in proportion to produce products that conserve the elements or mass at the end of the reaction. Hydrocarbon reactants dominate combustion in the natural world and are the basis of current conventional fossil fuels. The ideal complete stoichiometric reaction for an acyclic saturated hydrocarbon (alkane) is shown in Equation (1).

$$C_nH_{2n+2} + \left(\frac{3n+1}{2}\right)O_2 \rightarrow nCO_2 + (n+1)H_2O \tag{1}$$

The ratio of reactants must also be considered. The mixture typically utilises air and operates over a range of air fuel ratios (AFR). At localised and macro levels the AFR will differ and cause differing amounts of heat release and chemical reactions to occur at different locations throughout the mixture. Equation (2) displays the formula for AFR. Equation (3) displays the formula for lambda (λ) and equivalence ratio (ϕ).

$$AFR = \frac{m_a}{m_f} \tag{2}$$

$$\lambda = \frac{1}{\phi} = \frac{AFR_{Actual}}{AFR_{Stoichiometric}} \tag{3}$$

As air is not completely oxygen, the concentration of oxygen in the air or working fluid must be considered. The introduction of other reactants with the fuel other than oxygen leads to a variety of products being produced during and post reaction which are unwanted or unhelpful. In Equation (4) below, only the main two components of air are considered, i.e., nitrogen and oxygen, as these generally constitute over 99% of the composition of air.

$$O_2\ \%\ mass = \frac{O_2\%\ vol. O_2\ mass}{(1 - O_2\%\ vol). N_2\ mass + O_2\%\ vol. O_2\ mass} \tag{4}$$

Relatively inert reactants, such as nitrogen, can reduce reaction rates and temperatures, acting as diluents. Dilution of the oxygen content of air can be achieved with various non-oxidisers other than nitrogen in air, with exhaust gas particularly of note for ICEs as a diluent. This reduces the amount of oxygen available to generate heat while simultaneously increasing the amount of other elements that are available to absorb heat, leading to lower adiabatic flame temperatures. Nitrogen dilution is of particular interest in this piece of work, the reason for which will be highlighted in Section 2.7.7 and further expanded upon in Section 5.10. The formula for the standard enthalpy of formation with no heat loss is shown in Equation (5).

$$\begin{aligned} Standard\ Enthalpy\ of\ Formation &= \Delta_f H^{\ominus} \\ &= \sum v \Delta_f H^{\ominus}(products) \\ &- \sum v \Delta_f H^{\ominus}(reactants) \end{aligned} \tag{5}$$

Combined with the initial temperature, heat capacity, and amounts of the products, the adiabatic flame temperature can be calculated, assuming that all the exothermic energy from combustion is contained within the products post combustion. Each product has a differing heat capacity that depends upon temperature. Using the overall heat capacities of the products, shown in Equation (6), the overall heat capacity for the products can be calculated.

$$Heat\ of\ Reaction = Q_{reaction} = c_p(T_f - T_i) \tag{6}$$

$$Heat\ of\ Components = Q_{components} = \sum Q_p \tag{7}$$

$$Q_{reaction} + Q_{components} = 0 \tag{8}$$

This assumes all products are homogenously mixed and heat is distributed evenly. As previously mentioned, in real combustion reactions there are many reaction pathways that will occur in the local area, which are dependent on the reactants, heat release, initial temperature, pressure, and products.

2.2.2.1 Chemical Kinetic Mechanisms

Real fuels are typically a complex mixture of many different compounds and structural analogues. It is generally agreed that the behaviour of the complex fuels can be well matched and reproduced through simpler surrogate fuels for modelling. Highly refined fuels, such as efuels, can be less complex and purer, enabling better matching and simpler modelling depending on the composition, but are still likely to be made up of several compounds. Detailed chemical mechanisms of surrogate fuels enable 0D to 3D models to be applied and well matched against real data. Providing insight to the combustion process and rapid combustion development.

There are many detailed chemical kinetic mechanisms that are available to model the combustion of fuels and reaction pathways, depending on the fuel that is of interest and the level of detail, complexity, computational power, and time available. Several chemical kinetic mechanism relevant to combustion will be discussed in detail in this section.

2.2.2.1.1 Natural Gas Surrogate

The GRI-Mech is a chemical mechanism developed by Berkeley for natural gas combustion, specifically optimised for methane and air [40]. However, reactions for other alkanes are also present, such as ethane and propane. The method of systematic and computational optimisation of the model is laid out by Frenklach et al [41]. In brief, with each new variation of the model, the systematic optimisation relies on literature of reliable experimentation, a computational model to solve the reaction mechanism kinetics and transport equations, and a final tuning optimisation to create a reliable and accurate model.

GRI-Mech 3.0 is composed of 53 species and 352 reactions, with associated rate and thermal data. Two comparison of ignition delay for several methane air compositions using the GRI-Mech 1.2 and 3.0 mechanisms against experimental data are shown in Figure 2.10, provided by the team at Berkeley [42], using data from shock tube ignition data by Seery & Bowman [43]. For the GRI-Mech 3.0, methane ignition delay data is well matched against experimental data by Seery et al. There is a broader range of comparisons made against various other experimental data points, such as by Cheng et al [44] in which the GRI-Mech 3.0 demonstrated good ignition matching for hydrogen and methane.

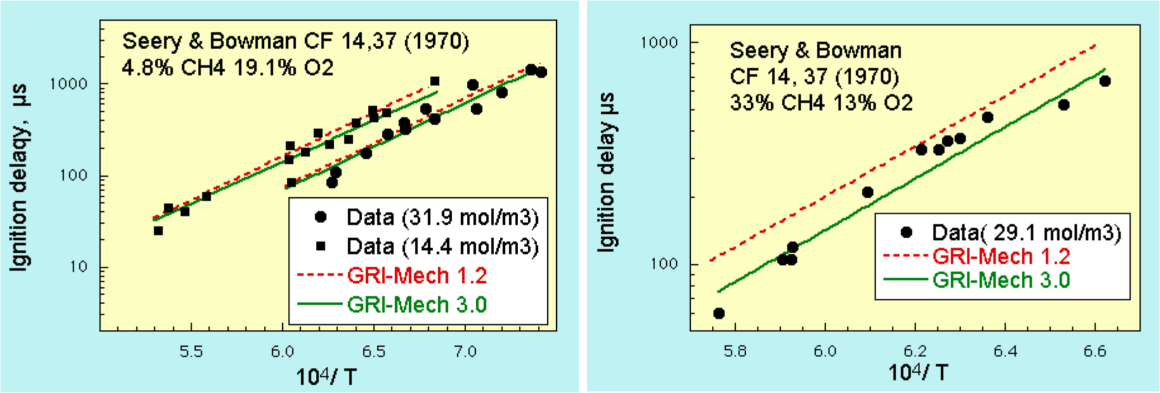

Figure 2.10 Comparison of ignition delay for three different mixtures of methane and oxygen by the team at Berkeley [42]*. In which they compared the GRI-Mech 1.2 and 3.0 mechanism results against real experimental data by Seery & Bowman* [43].

2.2.2.1.2 Gasoline Surrogate

Mehl et al developed a detailed chemical kinetics model for relevant component mixtures of gasoline [45]. The pure component fuels the scheme is optimised for are n-heptane, iso-octane, toluene, and 1-hexene. The full chemical kinetic scheme for all component fuels includes approximately 1550 species and 8000 reactions [45].

As a primary reference fuel for gasoline, iso-octane is of most interest as a simple single surrogate fuel and therefore will be discussed here in detail. A graph of ignition delay calculated by the scheme versus experimental data for pressures of 15, 34, and 45 atm is displayed in Figure 2.11. The ignition delay matches the trends of increasing ignition delay with decreasing pressure and is best matched against the 15 atm experimental data. However, the mechanism overpredicts the ignition delay against experimental data for the highest pressure case of 45 atm from approximately 1100K/T to 1300K/T. Although the temperature may not be highly accurate in this window, the model is otherwise well matched against the data.

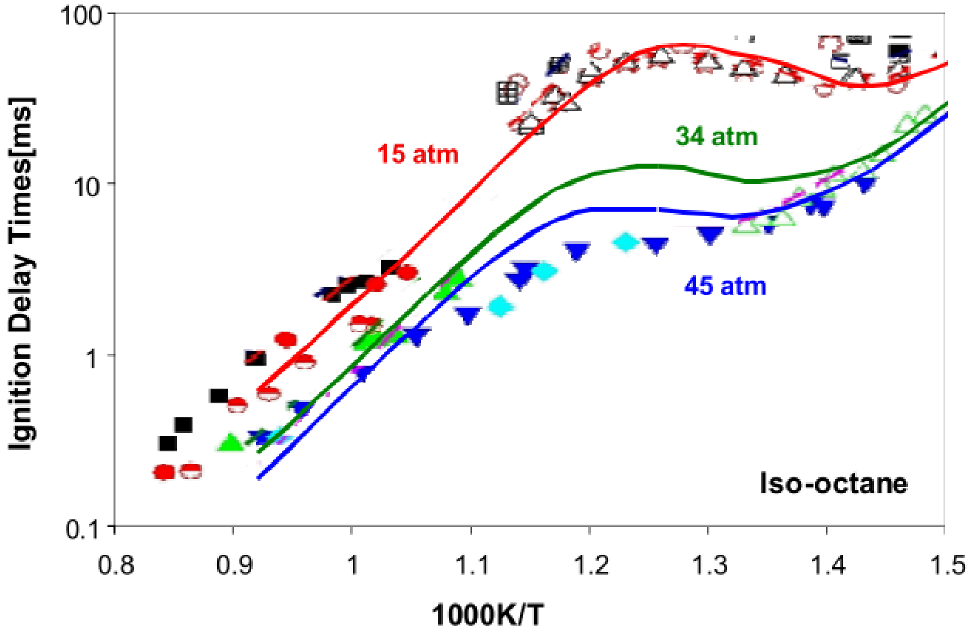

Figure 2.11 Experimental and calculated ignition delay of iso-octane over a range of conditions, with experimental data displayed as symbols and the chemical mechanism response displayed in solid lines for pressures of 15, 34, and 45 atm [45].

2.2.2.1.3 Jet Fuel Surrogate

JetSurF is a detailed chemical kinetics model for the combustion of a jet fuel surrogate. Developed through a multi university research collaboration, led by Stanford, and funded by the United States Air Force Office of Scientific Research [46]. The model is centred on development of high temperature chemistry for n-dodecane and n-butyl-cyclohexane, but also includes all n-alkanes up to n-dodecane, and mono-alkylated cyclohexanes, including n-propylcyclohexane, ethylcyclohexane, methylcyclohexane, and cyclohexane. The development effort aims to achieve consistent kinetic parameter assignment and predictions for a wide range of hydrocarbons. JetSurF 1.0 contains 194 species and 1459 reactions. JetSurF 2.0 contains 348 species and 2163 reactions.

Figure 2.12 display two graphs comparing the decane ignition response of the JetSurF 1.0 model against two conditions and sets of data. While having very different levels of equivalence ratio and pressure, both sets of data display that the JetSurF 1.0 model slightly overpredicts the length of ignition delay but fairly accurately predicts the trend in response to changes in temperature.

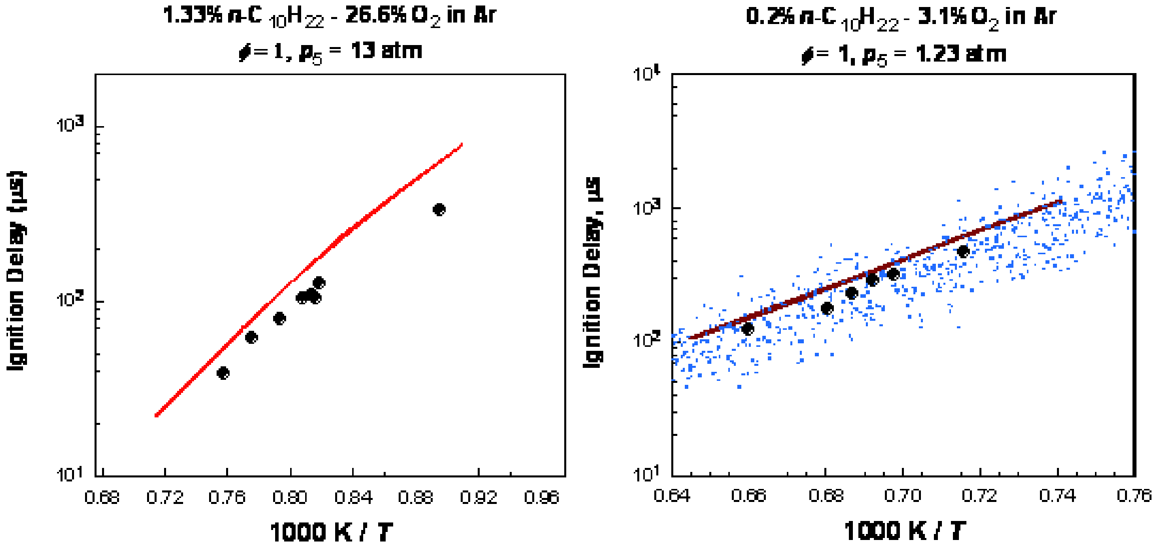

Figure 2.12 Comparison of ignition delay of decane from JetSurF 1.0 model (solid red line) and two sets of experimental data [47]*. The left graph is compared with data from Zhukov et al* [48] *(black symbols) and the right graph is compared with data from Horning et al* [49] *(black symbols) and includes uncertainty in JetSurF 1.0 predictions using Monte Carlo simulation (small blue symbols).*

2.2.2.1.4 Diesel Surrogate

Westbrook et al developed a detailed chemical kinetic reaction model for combustion of n-alkane hydrocarbons from n-octane to n-hexadecane [50]. Low temperature and high temperature reaction pathways are included for all of the alkanes in the model. The single mechanism can then be edited down for any of the alkanes included in the model for increased modelling efficiency.

Dodecane is of most interest as a surrogate for diesel fuel. Therefore the reported chemical mechanism results compared to experimental data by Westbrook et al [50] are shown in Figure 2.13 and Figure 2.14. There is high level of agreement between fuel conversion and temperature and residence time. There is good agreement of mole fraction of methane and propene.

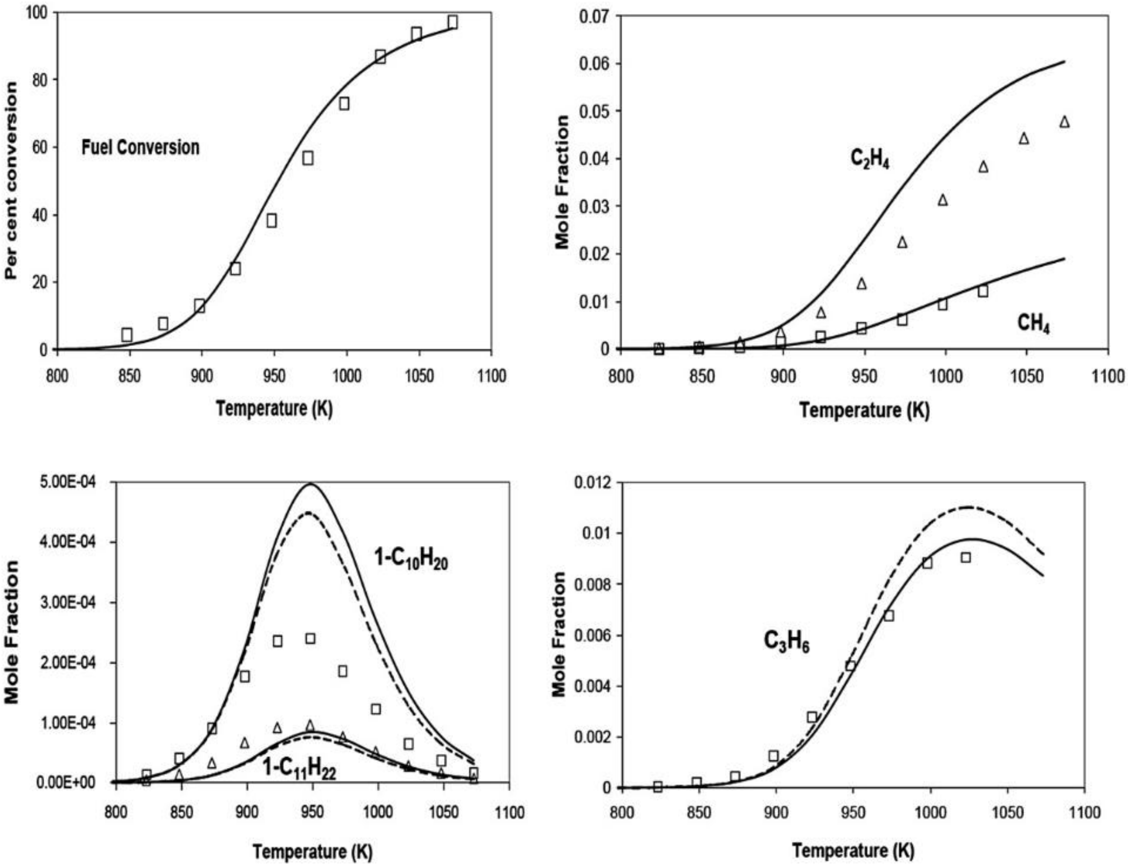

Figure 2.13 Conversion of fuel and species produced in n-dodecane pyrolysis (2% n-dodecane, 98% He) at 1s residence time for a range of temperatures. Experimental values are shown as symbols, lines show computed results, dashed curves include retroene reactions of 1-alkenes [50].

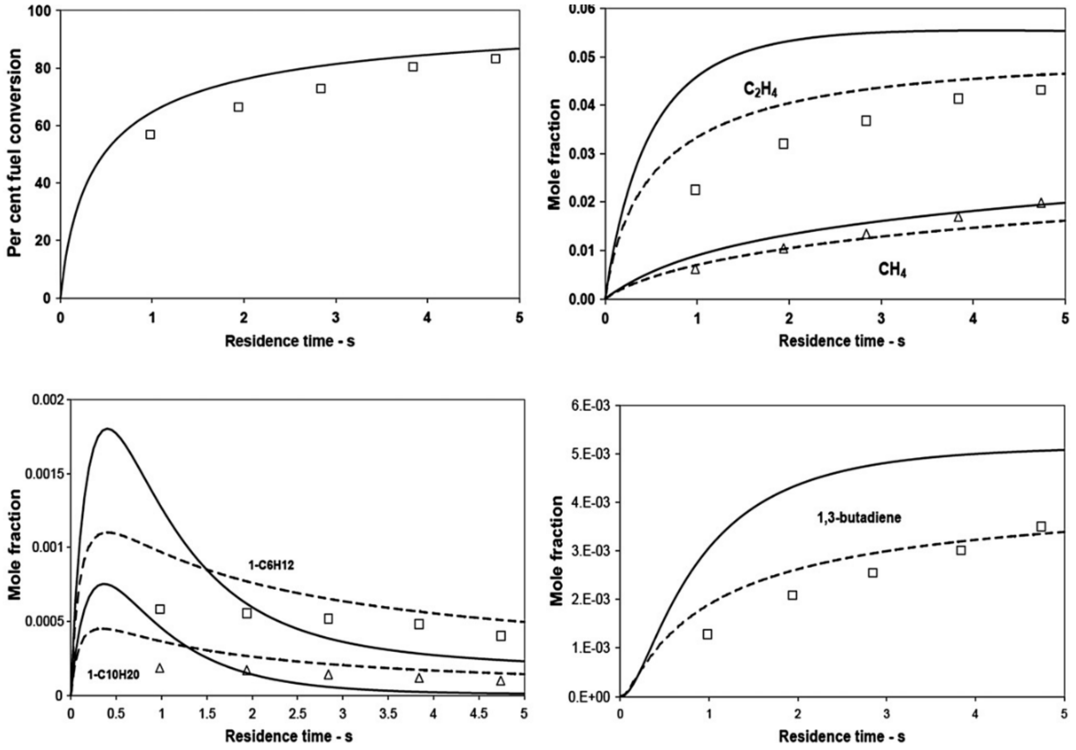

Figure 2.14 Fuel conversion and species histories in n-dodecane pyrolysis (2% n-dodecane, 98% He). Temperature is 973 K, symbols are experimental points, lines are computed results. Dashed curves include retroene 1-alkene decompositions, solid curves do not include them [50].

2.2.2.1.5 Discussion

While there are many chemical kinetic models aimed at combustion or a range of alkanes for surrogates for conventional fuels, there are limitations in pressures and temperatures in which the mechanisms have been validated against. In particular validated pressures higher than 1.5MPa are limited, with almost no chemical mechanisms validated above 5.0MPa. As many modern ICEs exceed 4.0MPa before combustion and may have peak cylinder pressures approaching or exceeding 15MPa with combustion, there is a need for more detailed chemical kinetic models validated against real data for these higher pressure conditions.

2.2.1 By-products/Emissions

Emissions are unwanted by-products from the chemical combustion process. Forming due to the complex chemical reaction pathways and varying nonideal circumstances within a real combustion process. Factors which influence emissions are intrinsically linked to that of the engine and combustion system design. With greater engineering and technology, the variabilities and by-products can and have been reduced. How and why these emissions products from must be understood to reduce emissions. Selected emissions and factors effecting the formation of these emissions will be discussed in this section.

2.2.1.1 Nitrous Oxides

Nitrous oxides (NO_x) are a group of seven gases based on various molecular arrangements of nitrogen and oxygen [51]. NO_x generally refers to the most common forms, which are nitric oxide (NO), nitrous oxide (N_2O), and nitrogen dioxide (NO_2).

N_2O is a significant GHG, with a global warming potential (GWP) estimate of 264 CO_2e over a 20 year period, 265 CO_2e over a 100 year period, and a lifetime of 121±10 years [52]. GWP is used as a comparison for the radiative forcing by greenhouse gases in the atmosphere, using CO_2 as mass-based equivalency, i.e., 1kg of CO_2 is equal to 1 GWP at any point in time. Due to molecules reacting and breaking down in the atmosphere, the GWP varies for molecules throughout their lifetimes. CO_2e and GWP are interchangeable, as CO_2e is calculated from GWP figures.

In the past it was believed that N_2O was directly produced by combustion systems. However, research demonstrated this not to be the case, and that N_2O was formed by post reactions of other NO_x molecules [53]. NO and NO_2 are the dominant NO_x products directly produced in combustion exhaust gas, with NO_2 the most prevalent form in the atmosphere from anthropogenic sources, and NO the most prevalent form produced by combustion [51]. In this piece of work NO_x will predominantly refer to NO and NO_2, which are significant air pollutants and hazardous gases produced from ICEs, contributing to smog, acid rain, and tropospheric ozone [51], [52], [54].

NO_x emissions are an unwanted by-product of combustion. In an ideal combustion reaction NO_x would not form. However, as combustion in an ICE typically utilises a fuel with a variety of components, and air as a working fluid, NO_x is formed through endothermic reactions of oxygen and nitrogen, and other intermediary compounds [54].

There are three main sources of NO_x from combustion: fuel NO_x, thermal NO_x, and prompt NO_x [51]. Thermal NO_x is formed from the reaction of nitrogen and oxygen at elevated temperatures and is the main source of ICE NO_x. Fuel NO_x is formed from the oxidation of ionised nitrogen located within the fuel and is a smaller component of exhaust in light oils and gases fuelled combustion. Prompt NO_x is formed from nitrogen reacting with fuel in oxygen depleted zones predominantly in the flame front with free radicals of CH, creating hydrogen cyanide (HCN) and NO before HCN goes through several intermediate compounds to create NO [54]. Prompt NO_x accounts for the smallest contribution to combustion NO_x, as shown in Figure 2.15. It can be seen in Figure 2.15 that the gradient of thermal NO_x formation increases as combustion temperature increases. It is generally agreed that thermal NO_x production significantly increases above temperatures of approximately 1550K [51] to 2200K [54].

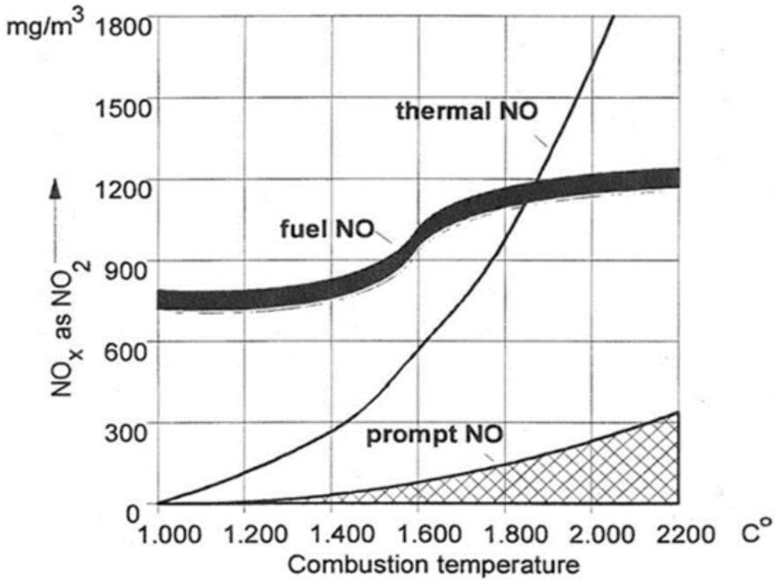

Figure 2.15 The relationship between the three main NOx formation types against combustion temperature [54].

NO_x production from ICE has generally increased as ICE efficiency has increased and with the wider uptake of Diesel ICEs with less stringent NO_x regulations, as previously discussed in Section 2.1.1.2. This is mostly due to the link between efficiency and temperature difference, i.e., with a higher temperature difference to that of ambient air there is a higher efficiency of a heat engine. This was achieved in Diesel engines and other combustion systems by utilising high compression ratios (CR) and therefore higher combustion temperatures.

Reducing local and bulk temperatures of the combustion event are key methods to reduce the formation of thermal NO_x emissions from an ICE. Fuel NO_x can be reduced through refined fuel with lower nitrogenous compounds, and prompt NO_x can be reduced by increased mixing reducing oxygen depleted areas in the flame front and local areas.

2.2.1.2 Particulate Matter & Soot

Particulate matter (PM) is a broad term for small particle pollution, consisting of an impure mixture of solid and/or liquid particles typically from incomplete combustion, dust, and other emissions. As previously mentioned in Section 2.1.1.1, PM is typically split into two groups based on particle diameter. Course PM of 10μm or less (PM_{10}) and fine PM of 2.5μm or less ($PM_{2.5}$).

The WHO, PHE, and other health bodies agree that PM, particularly $PM_{2.5}$, can have a significant on human health, affecting respiratory and cardiovascular morbidity, and lead to mortality from cardiovascular and respiratory diseases and from lung cancer [6], [38]. The WHO estimates that current levels of exposure to $PM_{2.5}$ reduces the life expectancy of the average European population by about 8.6 months [38].

Soot is generally agreed to be carbonaceous particles formed during pyrolysis of hydrocarbon fuel and typically includes various unsaturated hydrocarbons, particularly acetylene and its analogues and polycyclic aromatic hydrocarbons (PAH) due to their relative stability [55], [56]. PAH in particular has been shown to have serious adverse health effects, contributing to cancer, reduced lung function, obstructive lung disease, and cardiovascular disease [57]. The effects on health are the most concerning aspect of soot emissions, but the formation of soot is also an issue of wasted energy, loss of efficiency, increase in maintenance and wear, and operating cost.

Air fuel ratio, local and bulk mixing, temperature, and pressure impact the formation of soot. Soot should in theory only occur when the hydrocarbon and oxidiser are below equivalence ratios of greater than 1 [55]. However, the localised area conditions play a much larger role in formation than bulk conditions. Production of PM and soot varies depending on the combustion material, which may include a fuel and other impurities or additives.

Carbonaceous particle formation is complex and will not be discussed here in detail. In brief there are several methods of particle inception and formation such as nucleation, surface growth, chemical reaction, collisions, and condensation, as well as combinations of these processes [58]. Figure 2.16 displays an illustration of the complex chemical reactions and physical processes involved in soot formation.

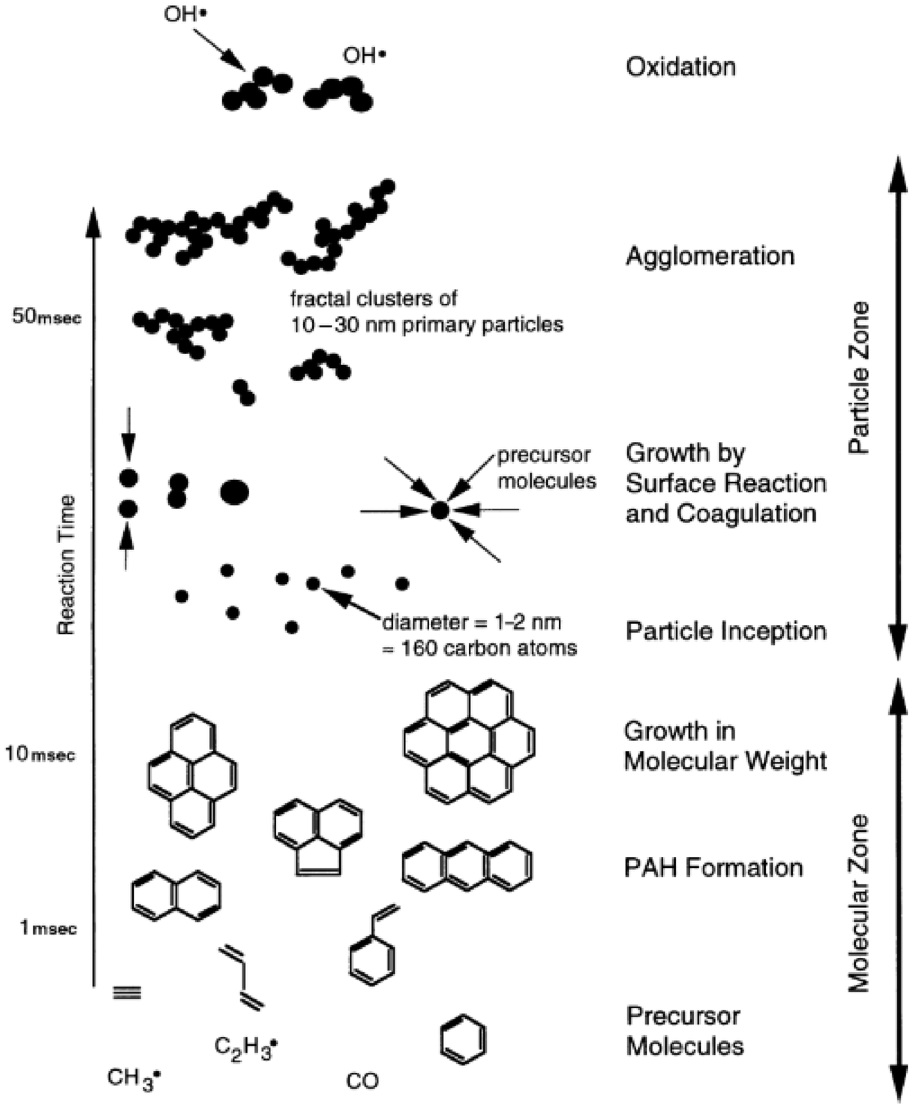

Figure 2.16 Kinetically limited chemical reactions and physical processes involved in soot formation [58].

Figure 2.17 Illustrates the effect local equivalency ratio and temperature can have on NO_X and soot exhaust products from an engine. The areas for three types of combustion, i.e., Diesel compression ignition (CI), spark ignition (SI) and LTC, are highlighted. These ICE combustion strategies and others will be discussed in Section 2.4.

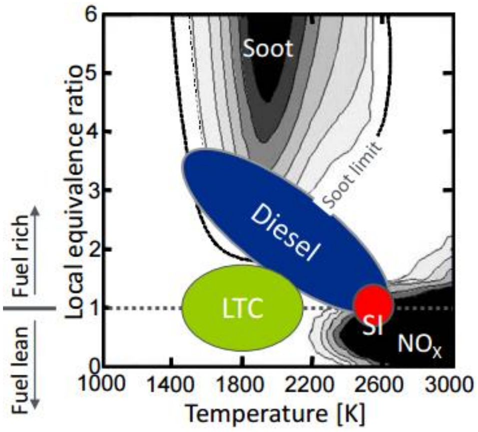

Figure 2.17 Temperature vs Equivalence Ratio Emissions Zones [59]

2.2.2 Discussion

Literature suggests with the right reactants and initial conditions it is possible for combustion to generate ultra-low levels of soot and NO_x emissions in the region of 1550 to 2500K. However, combustion methods, limitations, and controls will be required to maintain combustion in an optimum condition which produces ultra-low emissions throughout the whole mixture. A premixed method of combustion will be needed in future ICEs, in which the reactants are homogenous, and the initial temperature is tightly controlled, to eliminate and minimise NO_x and soot production. At the same time, the initial temperature must be high enough for the reaction to occur, be complete, and not produce other emissions such as carbon monoxide.

2.3 Alternative Fuels

2.3.1 Introduction

As the chemical fuel is the energy feedstock to an engine, the question of sustainability starts with the fuel. The chemical fuel is integral to the products or emissions produced from a combustion engine. Whether the carbon dioxide emitted post combustion is dependant on the source of the carbon deposition to the fuel.

It takes millions of years for a fossil fuel to form from the decomposition of carbon-based deposits. This contrasts with the extraction of fossil fuels which in the modern world can take days or hours from extraction to combustion. Therefore, fossil fuels are inherently unsustainable due to this imbalance of extraction and deposition rates. A sustainable alternative green fuel must be created or captured at the rate of use as a minimum, if not higher to rectify past unsustainable emissions of CO_2.

In this piece of work only “green” alternative fuels will be discussed in which the net CO_2 or CO_2e emissions can be neutral or negative. After considering whether the source of carbon is sustainable, the other combustion products produced from the combustion reaction and the properties of the fuel must be considered. After consideration as to whether the fuel can be sustainably sourced, this piece of work will not go further into detail of the production processes that could be utilised. The combustion of the fuel is the focus of this piece of work.

2.3.1 Green Synthetic eFuels & Biofuels

Longer chain hydrocarbons and alkanes remain attractive as a source of fuel due to their lower autoignition temperature, high energy density, and widespread use of associated fuels and technologies. As they are most closely related and comparable to the fossil fuels used today, this makes them adoptable to ICEs and other fossil fuel consumers and can utilise pre-existing distribution networks. For this reason, synthetic electrofuels (efuels), in which a chemical fuel is produced synthetically using renewable electricity, and synthetic biofuels are attractive. Figure 2.18 displays an overview of routes and processes to carbon based sustainable fuels.

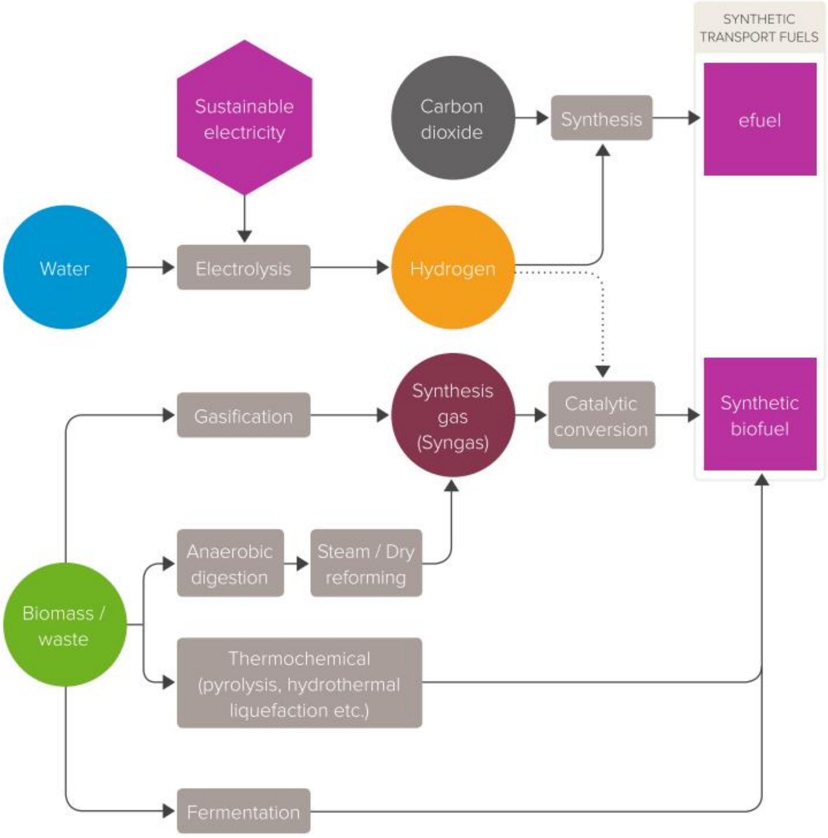

Figure 2.18 Routes to carbon based sustainable synthetic fuels [60].

Synthesis of fuels can eliminate impurities that are usually costly to remove in fossil fuels. Synthetic production would desire to be as efficient as possible in only creating the fuel required to bring down cost. Synthetic fuels would therefore tend towards producing a neat high grade of fuel as a cost benefit. In comparison fossil fuels would be cheaper if left unprocessed as dirty crude. These fuels have the potential to produce lower PM and other emissions due to less contaminants, such as sulphur, vanadium, iron, zinc, cycloalkanes, aromatics, among others, being present. The stability and lifetime of fuel could in theory be higher as there is less oxidation or likelihood of separation and breakdown of components due to the neat fuel [61].

However, there are currently issues with cost and energy for processing into longer chain hydrocarbons that would need to be overcome. Direct air capture is attractive due to carbon sequestration but is expensive, likely not being competitive with fossil fuels till beyond 2050 [60]. For this reason, there is an argument for utilising shorter chain hydrocarbons that could require less processing and energy in certain cases.

Synthetic biofuels could compete with cropland and push up food prices. Alternative farming methods for the biofuels, such as algae sea farming, could avoid this issue. While PM production may be lower with these fuels, there remains health issues utilising current ICE technology producing NO_x.

2.3.1 Green Methane

The simplest alkane, methane is an attractive sustainable fuel as it can be extracted or produced from a variety of waste sources, such as from landfill, agriculture, and sewage. It can also be manufacturable synthetically from methods such as the Sabatier reaction. The ideal combustion reaction for methane is shown below in Equation (9).

$$2\,CH_4 + 3\,O_2 \rightarrow 2\,CO_2 + 4\,H_2O + energy \tag{9}$$

Methane has an average lifetime of 12.4 ±3 years but can impact other components in the atmosphere, such as water, which contribute to global warming [52]. Therefore, methane has an estimated GWP of 56 [62] to 96 [63] over 20 years, 21 [62] to 34 [52] over 100 years, and 6.5 [62] to 7.6 [64] over 500 years. This is part of the reason methane and other fossil fuel gases are regulated to be captured or flared instead of emitted in some countries for safety and reduction of GWP.

If green methane is used that is produced from an unavoidable and circular sources, such as sewage and food waste, a combustion system could play a role reducing the waste and the overall GHG emissions in a circular economy. For example, methane produced from sewage and food waste cannot be endlessly captured to reduce overall GHG, it will need to be stored, released or utilised. In this situation, an ICE using green methane has the potential to be a greenhouse gas sink, by shortening the lifetime of methane in the atmosphere. Therefore, having the potential to reduce the overall GHG effect.

In the ideal reaction, shown in Equation (9), 1kg methane combusts to produce 2.74kg of CO_2. Therefore, if methane that would otherwise be released to the atmosphere is combusted, the overall GWP saving is the GWP of methane minus 2.74. In Figure 2.19 the global warming potentials from the latest IPCC report are used minus the 2.74kg of CO_2 that is produce from the combustion of 1kg of methane [52]. Embedded CO_2e emissions are used based on an average truck, with an estimate for the equivalent BEV to have 15% more embedded CO_2e than the ICE vehicle. Using assumed averages for a commercial truck of a lifetime of 12 years, annual mileage of 65,000 miles (104,000km), embedded CO2 of 30,000kg, 8 mpg (35 L/100km) and 11.5kg of CO2 kg/gallon (2.53kg/L). A conventional ICE would produce 1.15 million GWP, whereas using the lower values of GWP over 500 years would produce a negative GWP of 1.3 million over the 12 year lifespan of the truck.

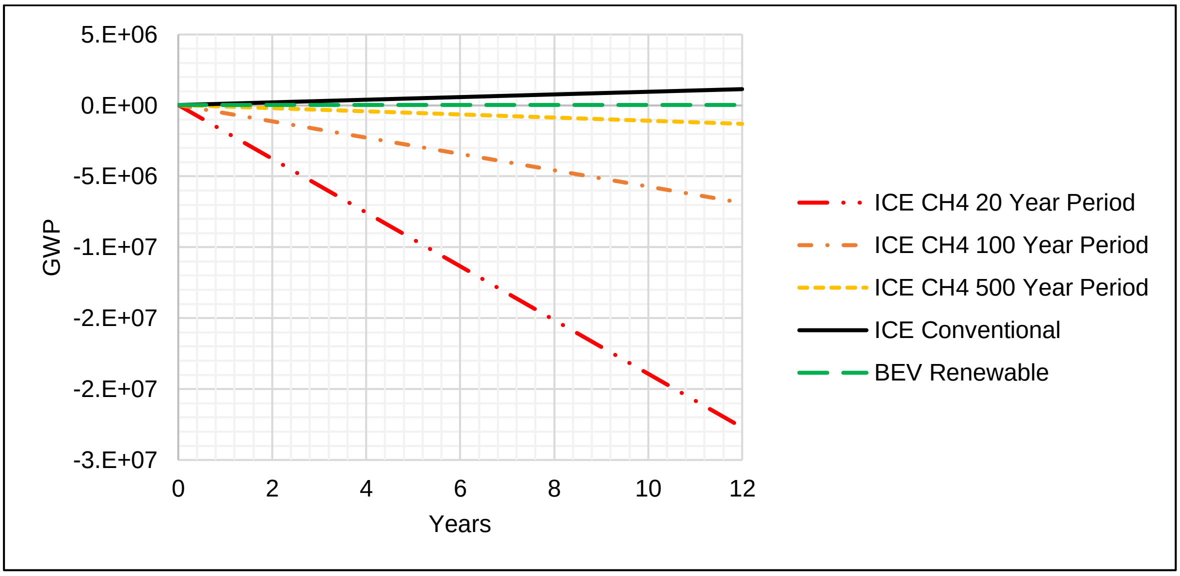

Figure 2.19 Truck GWP comparison of renewable BEV, conventional ICE and recovered green methane conventional ICE.

However, for this to be a true representation of what occurs during the waste methane cycle, the other emissions apart from CO_2 that are produced from ICEs must be addressed and accounted for. Methane and compressed natural gas (CNG), a mixture of predominantly methane (~95%) and other components, combustion has been shown to produce low levels of particulate matter, due to the lower length carbon chains, carbon density and gaseous state of methane making conditions more ideal for premix combustion with air [65]–[67]. However, there are issues the size of the PM particles produced more like to be in fine $PM_{2.5}$ particles [66].

The high autoignition temperature (>800K at 1bar) of methane makes compression ignition unsuitable when trying to avoid the formation of NO_x. Necessitating an ignition method, such as a spark, higher reactivity ignition fuel, or other source to avoid this issue. The high adiabatic flame and combustion temperature can cause high amounts of NO_x to form if the initial temperature, and therefore end temperature, is too high.

Research has shown the autoignition temperature of methane to be significantly affected by pressure, with the potential to spontaneously combustion far outside the flammability limits [68]. These effects must be considered in ICE applications and combustion systems but may have the potential to aid lowering the autoignition temperature of the fuel and reduce NO_x formation.

2.3.2 Green Hydrogen

Hydrogen has received increased research and wider public attention as an alternative fuel due to the ideal combustion reaction producing no CO_2 as a product, as shown in the ideal hydrogen reaction in Equation (10). For hydrogen to be green, the production method would need to utilise renewable electricity and water for electrolysis. The supply of water as a feedstock for green hydrogen can be thought of as almost infinite, due to the abundance of water on Earth, and is renewable and sustainable due to water being a product of the reaction. Another benefit of hydrogen is it’s use as a precursor to create other more complex fuels and molecules, as shown in Figure 2.18. For this reason, it has the potential to be cheaper than other competing green synthetic fuels. The cost of green hydrogen will be heavily associated with the cost of renewable electricity used in the electrochemical reaction used to separate the oxygen and hydrogen from water. However, hydrogen has the potential to be cost competitive with current fossil fuels if production is scaled up over the next 20 to 30 years [69], [70].

$$2\, H_2 + O_2 \rightarrow 2\, H_2O + energy \qquad (10)$$

The round-trip efficiency of green hydrogen production is currently 18-46% [71], therefore cost will need to decline from current levels before it becomes competitive and/or efficiencies would need to increase. Ideally generated renewable electricity would be kept as electricity to avoid the conversion efficiency penalty, rather than conversion to a green fuel. However, there is a tipping point where the capital cost of increasing electrochemical battery size will not be as cheap as taking the efficiency penalty to store the energy as a green hydrogen fuel, this is especially true at large scale (>0.5GW) but will come down with green hydrogen cost and increasing efficiency. Hydrogen is a better long term (>6 month) high-capacity energy store than an electrochemical battery, due to battery degradation and maintenance. For these reasons, co-deployment of renewable electricity generation, electrochemical batteries, and hydrogen storage have been proposed to minimise cost and maximise the amount of energy stored for large scale storage.

The main issues with utilising hydrogen as a vehicle fuel is its low volumetric energy density, high autoignition temperature and high adiabatic flame temperature. As shown in Figure 2.4, volumetric energy density of hydrogen can be overcome by raising it above ambient pressures or lowering the temperature cryogenically until it is a liquid. However, storing hydrogen at elevated pressures or as a liquid presents challenges and incurs an efficiency penalty. As energy is needed to compress the hydrogen and necessitates construction of a storage vessel that can withstand the pressure and/or retain low temperature.

Emissions from hydrogen fuelled ICEs shows great promise for toxic emissions reductions. As noted, the issues of carbon or PM from the fuel are mitigated with hydrogen with no carbon in the fuel and little to no contaminants present. NO_x emissions are lower than comparable fossil fuelled ICEs on the road today, with levels of 150-220ppm of NO_x reported at stoichiometric conditions [30]. However, with moderate dilution and rich or lean ratios this has been shown to be mitigated down to 10-120ppm when using a spark ignition or dual fuelled (reactivity controlled) ignition [30].

Wide flammability and low ignition energy allows hydrogen to be operated with significant dilution, this is a benefit for reducing NO_x but represents an issue for predictable and reliable combustion [30], [72]. The low flammability presents a challenge and hazard which must be mitigated, but this can be overcome through well engineered fuel delivery systems, storage, and combustion system specific to hydrogen ICEs.

2.3.3 Green Ammonia

Ammonia is attractive as a fuel as there is already an international shipping transportation infrastructure available due to the use of ammonia in agriculture as a fertiliser. Therefore, the infrastructure for transporting, storing, and distributing are readily available and attractive as a quickly adoptable energy vector, especially for the decarbonisation of the shipping industry [73].

Currently ammonia is predominantly produced using a fossil fuel-based process and, if made green, will be dependent on the cost of green hydrogen production. This will cause green ammonia to generally be higher in cost than green hydrogen, due to the additional processing of green hydrogen required. However, the higher volumetric energy density than hydrogen makes it attractive as an energy vector in its own right or as an alternative hydrogen storage vector. Liquid ammonia has a higher energy density than liquid hydrogen. Unlike hydrogen, ammonia can be stored as a liquid at near ambient temperatures and pressures.

Currently there is an abundance of ammonia research for gas turbines [36], [74] but less so for ICEs, though this area is growing [75]–[77]. Results from the gas turbine research is still useful for informing the emissions and combustion characteristics of the fuel. As can be seen in the ideal combustion reaction for ammonia below (Equation (11)), the only products of combusting ammonia are nitrogen and water.

$$4\,NH_3 + 3O_2 \rightarrow 2\,N_2 + 6\,H_2O + energy \tag{11}$$

The non-production of CO_2 and higher energy density than hydrogen are the key reasons why ammonia is being considered as a fuel [36], [73]. However, as with all combustion reactions, there is variability in the species that are produced. A study on a dual fuelled compression ignition engine with diesel and ammonia showed a factor of 7 increase in NO emissions with 20% fuel energy from Diesel, NO_2 was not reported [76]. Ammonia has a low flame temperature [36] which in theory should allow it to reduce thermal NO_x, which is formed purely due to heat in comparison to other fuels that burn in an ICE. Chemically produced NO_x is an issue at lean conditions due to the reaction pathways of ammonia. However rich conditions act as a NO_x reduction in the same method as urea based selective catalytic reduction in modern vehicles [77]. As ammonia is toxic, regulators have started to increase regulation on emissions of ammonia from vehicles, with the Euro 6 introducing a limit on the amount of ammonia that can be emitted.

The low combustion temperature and low laminar burning velocity (a fifth of methane) could lead to the flame being extinguished easily, leading to non-combustion or low conversion of fuel to its products [36]. This also creates issues with ignition delay [77]. Compression ignition ammonia is presented with issues due to the high autoignition temperature and NO_x emissions that a high initial temperature entails [78]. However, this can enable high compression ratios to be achieved. Ammonia could be co-injected or doped with a lower reactivity fuel such as diesel [76], [79]. Alternatively, ammonia can be decomposed to nitrogen and hydrogen gas utilising a catalyst [80]. With the potential to reap the high energy density benefits of ammonia and combustion benefits of pure hydrogen.

2.3.4 Discussion

All the fuels discussed in this section show promise as future alternative fuels. However, it is clear each have issues that still need to be overcome to before they are widespread and adopted as fuels. Green methane demonstrates the earliest promise as an early adoption fuel as it can be added into existing liquid natural gas fuelled vehicles and other areas, while also potentially removing methane as a harmful GHG emission from industries such as agriculture. Hydrogen will require extensive research and advances in use, storage and manufacturing efficiency but shows promise as a fuel due to its high flammability, high gravimetric energy, and ability to utilise excess energy created by intermittent renewable infrastructure, such as wind.

While the research in this paper will not perform testing on alternative fuels, the path forwarded to these fuels is important to highlight, as ICE technology must transition to these fuels. Future ICE and combustion technology that is proven on diesel or methane will be translatable to green synthetic eFuels, biofuels and green hydrogen. While combustion systems will need further research for green hydrogen and ammonia, ICE thermodynamic cycles and engine architectures will still be relevant for these future fuels to achieve high efficiency and zero carbon emissions.

2.4 ICE Combustion Methods & Systems

2.4.1 Introduction

Mixing in the RSCE is of great interest not only due to seemingly low emissions produced but also due to the unique conditions at which the air and fuel are combined. As inlet air conditions in the RSCE can be manipulated and can operate well above supercritical air temperatures (>133K), how the injected air and fuel mix and combust is of importance to understand and optimise the combustion system and engine.

Firmansyah et al demonstrated that when the air enters the cylinder, it is moving at Mach speeds, due to the differential pressure behind the valve and the combustion cylinder, and the small amount of valve lift that the air passes through [81]. A velocity contour map from this piece of work is shown in Figure 2.20. This jet of air could impinge against the injected fuel spray causing suspected rapid atomisation. This is suspected as one potential method due to the high pressure rise rate (PRR) during combustion.

Acoustic phenomena may be having effect on the mixing of the air and fuel due to the shock waves that are developed in the engine from the jets of air. The effect the expansion and phase change of the air has on the temperature may also initially prevent combustion taking place, giving time for the mixture to fully mix and atomise before combustion.

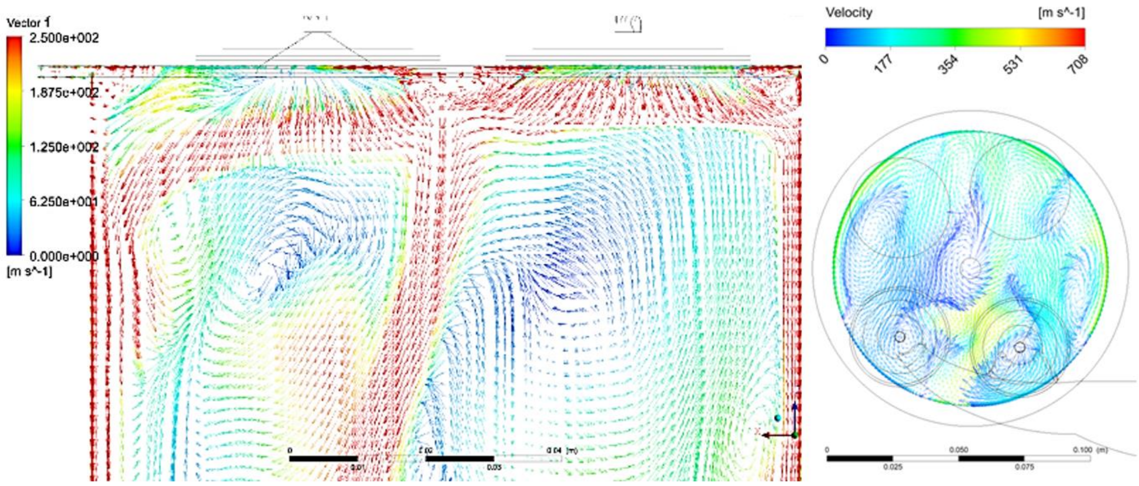

Figure 2.20 Simulation of velocity contour map of air motion in RSCE [81].

2.4.2 The Dec Model

The Dec Model is a conceptual model of a diesel plume with no swirl, wall or other phenomena [82]. The model is based on laser-sheet imaging of an optical single cylinder engine utilising a high pressure diesel injector, piston crown window, and side windows. The conceptual model can be seen in Figure 2.21. It conceptually demonstrates the different combustion products that are formed due to heterogeneous chemical and thermal regions in which the combustion is taking place. The model conceptualises the fuel spray, diffusion flame, and emissions generated in each mixture region throughout the spray and flame front from a single hole high pressure injector.

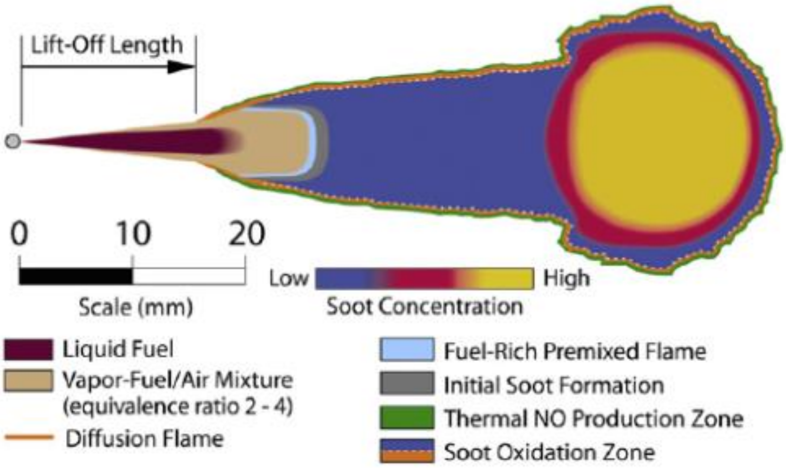

Figure 2.21 Dec Model for a diesel plume [82].

2.4.1 Low Temperature Combustion

Low temperature combustion (LTC) and specifically homogenous charge compression ignition (HCCI) have been the subject of much research over the past decade for reducing NO_x and soot emissions in ICE's. As mentioned previously, the Arrhenius equation shows that the only two variables that can be manipulated to reduce NO_x formation are temperature and the pre-exponential factor, with the pre-exponential factor predominantly governed by concentration of reactants. There has been research into ICE's utilising intake air treatment (IAT) systems to reduce the concentration of nitrogen in the working fluid and more widespread is the use of exhaust gas recirculation (EGR) systems in nearly all modern ICE's to reduce the formation of NO_x [83], [84]. IAT and EGR systems are not as effective as temperature at reducing NO_x formation due to their reduction in the overall thermal efficiency of the ICE. This is because they usually either incur comparatively high pumping losses or reduce the heat capacity ratio of the working fluid.

As temperature is the main variable contributing to NO_x formation in an ICE, LTC is an attractive solution to eliminating NO_x. The hope is this in turn reduces the need for expensive after treatment systems, such as catalytic converters and urea-based systems. Reducing peak combustion temperature potentially incurs an efficiency and power reduction, as the difference in pressure before and after combustion has a direct impact on the efficiency and power output of the ICE. Therefore, the objective for LTC is to reduce peak temperatures while maintaining or raising average temperatures during combustion up to or below the temperature threshold for NO_x formation (approximately $< 2{,}200K$).

2.4.1.1 HCCI

HCCI brings together the two advantages from the conventional Otto and Diesel cycles. The homogenous charge from Otto cycle and compression ignition from the Diesel cycle. The homogenous charge ensures there is no localised stratified air fuel mixtures to form soot during the combustion event. The compression ignition of the homogenous charge means there are many ignition kernels due to the spontaneous combustion of the mixture under compression, leading to low peak temperatures but a higher average temperature. Due to these low peak temperatures, there is potentially a small efficiency gain achievable as there is less heat lost to the cylinder walls, as long as the average temperature is maintained or increased in comparison to conventional combustion.

Although HCCI has been proven to be achievable in the lab its transition to real world scenarios with changing conditions has so far not been viable in terms of emissions and efficiency benefits versus cost. This is mainly due to the uncontrollability of the compression ignition combustion event, as well as rapid combustion resulting in high PRR which must be addressed, otherwise expensive solutions such as the use of exotic materials will have to be utilised to ensure the longevity of the engine for consumer use. Noise or ringing is a secondary problem that may be unpopular with consumers but has the potential to be addressed.

Methods have and are being researched and developed that maintain the benefits of HCCI but with the ability to control the onset of combustion. These “spinoffs” of HCCI are viable in real world conditions. Mazda’s spark assisted compression ignition Skyactive X engines is one such concept that has been shown to work in real world conditions.

2.4.1.2 RCCI

Another development of HCCI is reactivity controlled compression ignition (RCCI). RCCI maintains the benefits of HCCI with the added advantage of the ability to control the start of the combustion event. By having a low reactivity homogenous charge before increasing the air fuel mixture to high reactivity, ignition can be controlled during compression. The main research that has been carried out on RCCI has been into utilising two or more fuels with varying reactivity’s, although there has also been research into using single fuels with the air fuel ratio or steam reforming as a means of reactivity control [85].

Although RCCI has the potential to drastically reduce NO_x and soot emissions in comparison to conventional ICE's, it still has some of the drawbacks of HCCI. Unburned hydrocarbons and CO emissions are still a persistent problem in research to date, and would require exhaust after-treatment to meet current and future emissions regulations [86]–[91]. The majority of research has been using conventional engine architectures with only a few using modified piston head topologies [86], [88]. This is potentially a contributor as to why there is a greater amount of unburned HC, and CO being produced in some of the RCCI ICE's that are being researched. Varying the pilot direct injection (DI) spray angles and injection pressure has been shown to have a direct effect on the amount of HC produced, with "top down" combustion seemingly the best method to initialise the chain reaction combustion event between the two fuels being utilised [87].

New research in RCCI seems to have recently slowed and made little progress in implementation. Several studies at the University of Valencia have investigated the capability of RCCI meeting EURO VI limits for medium duty diesel engines. The first study slightly modified the original Volvo engine to include port fuel injection to allow for RCCI, but it could only comply with EURO VI limits up to 25-35% load at low-speed conditions. There was a small efficiency gain of up to 2% in comparison to the conventional Diesel combustion but utilised a relatively high amount of EGR, up to 32%, to meet the NO_x and soot limits at the higher 35% load, which may not be achievable in on the road [91]. A second study modified the piston head, reducing the CR from the stock value of 17.5 to 15.3, to allow for higher amounts of premixed main fuel. This heralded a much higher load of 75% or 1.4MPa IMEP while complying with EURO VI limits. There was a general efficiency gain of 3% and a maximum of 7% across the low speed and load range. However, above 0.5MPa IMEP the engine did not comply with soot limits and 1.4 MPa IMEP is on the low end of maximum operating pressure compared to modern ICEs [86].

The other problem is therefore highlighted with RCCI, which is that the CR is still predominantly governed by the auto ignition temperature of the air fuel mixture. Without using exotic and/or expensive fuels the maximum CR has not been pushed much further than 17 in studies, with a reduction in CR in comparison to conventional combustion to reduce knock [92]. This therefore limits the maximum efficiency possible utilising conventional thermodynamic cycles. As with pure HCCI research, RCCI has been shown to be sensitive to inlet temperatures, meaning tight control is still needed to reap the rewards. So far the benefits of RCCI have only been shown while working in low speed conditions (<2,000RPM) [93]. Although medium to high loads have been proven possible with EGR its ability to meet current and future emissions is not credible across the whole load range.

Utilising two or more fuels is not seen as an attractive, simple, or practical solution for consumers. Research is showing that RCCI has the potential to be a technology that could be the future of low-speed high load ICE applications such as ships and range extenders, as well as being a technology utilised in situations such as engine idle, but research will need to take a more drastic approach by designing new engine architectures and topologies to maximise the potential of RCCI combustion technology. For RCCI technology to continue to improve efficiency in the future it will need to be combined with new thermodynamic cycles and ICE concepts. Recent research and papers into RCCI have started to decline, showing a new form of combustion is still needed that produces LTC but without the pitfalls of HCCI and RCCI. High level of control of the start of the ignition and combustion event(s) is needed. Combined with a fast and efficient form of fuel and working fluid mixing to minimise emissions and maximise efficiency.

2.4.1 The Extended Dec Model

Musculus et al proposed an extension to the Dec model for LTC at low load for heavy-duty, diluted (10-15% oxygen), and partially premixed compression ignition (PPCI) diesel combustion [94]. The Dec model and extended conceptual model after start of injection (ASI) they proposed is shown in Figure 2.22. Compared to the previous Dec model, the extended Dec model displays a much larger amount of the fuel spray experiences first stage of ignition. Due to the differences in temperature and reactant composition, second stage ignition occurs 6 crank angle degrees (CAD) later in the extended model vs the Dec model. This allows for larger dispersion of the fuel spray, increasing the mixing, and reduces the zones of rich fuel areas. This allows for more of the fuel to reach stoichiometric conditions before second stage combustion, therefore reducing the amount of soot and soot precursors that form.

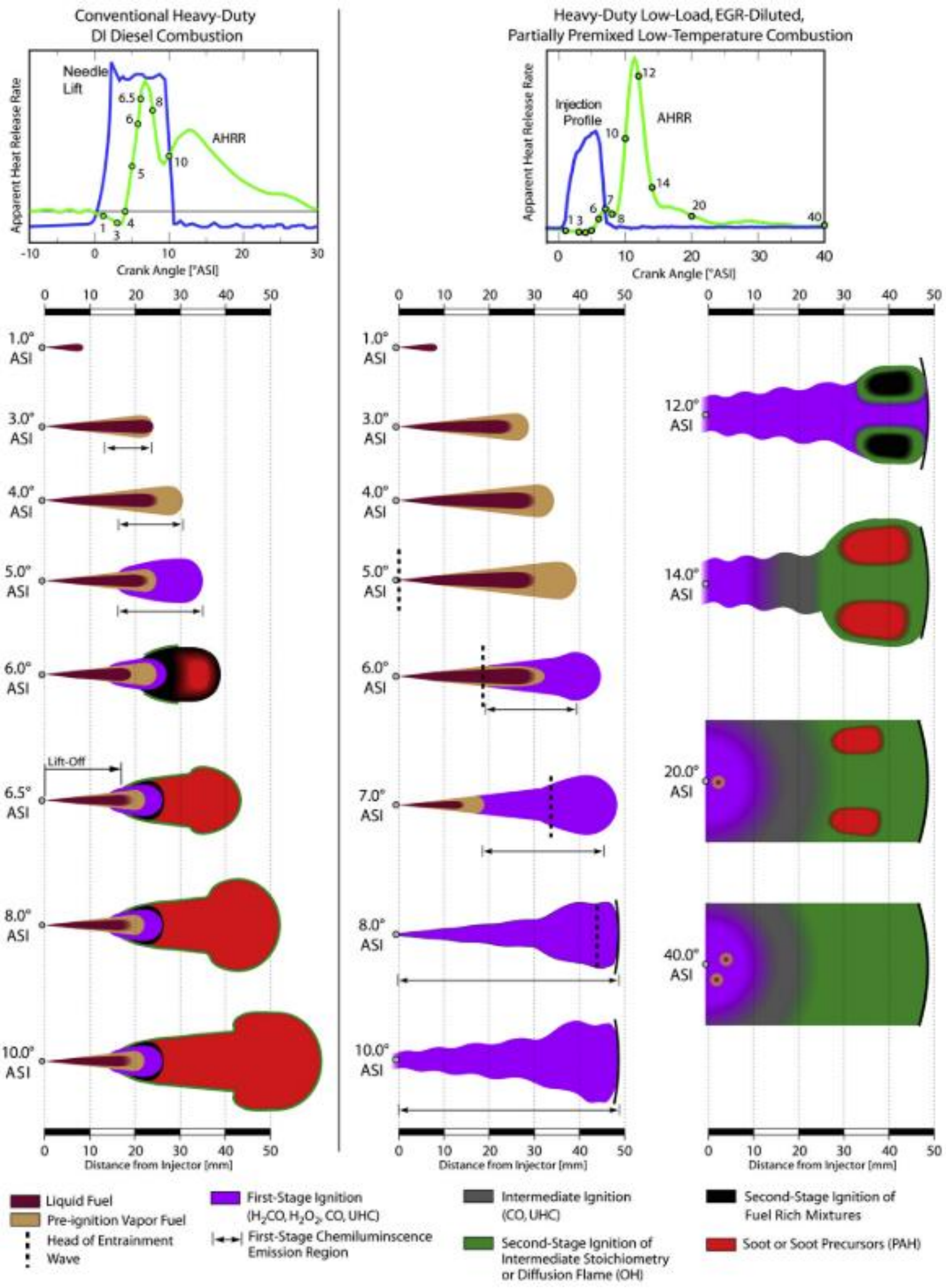

Figure 2.22 The extended DEC model: conceptual model for conventional heavy-duty diesel combustion (left column) and extension to low-load, single-injection, EGR-diluted. PPCI low-temperature heavy-duty DI diesel combustion (middle and right columns) [94].

2.4.2 Discussion

Conventional ICE combustion methods do not hold promise as a primary method of emission reduction for ICEs, due to diffusion combustion in both SI and CI engines. They are therefore unattractive as a path to lower emissions. LTC, extended DEC, and other methods will be needed for a future ICE combustion method and system. Premixed autoignition combustion methods will need to be used to achieve the ultra-low emissions. Achieving control of ignition for a low temperature and homogenous mixture combustion method over a wide operating range remains a key challenge that has still yet to be fully overcome.

2.5 Air-Fuel Mixing & Atomisation

2.5.1 Introduction

This section will look at air-fuel mixing and atomisation that are typically not seen in conventional ICEs but are of interest due to the alternative ICE cycle and combustion methods. Many of the air-fuel mixing and combustion methods are novel to ICEs but are found in other combustion technologies, such as jet engines and rockets.

2.5.2 Impinging Jet Atomisation

Impinging jet atomisation or air blast atomisation has typically been researched for rocket propulsion systems with no research within the automotive research or commercial sector. Hence experiments have predominantly been looking at the impingement of nitrogen jets and liquid oxygen jets over supercritical conditions [95].

Figure 2.23 depicts the differing atomisation profiles with increasing chamber pressures. There has been no work looking at impinging jets of air or nitrogen with liquid fuels such as gasoline or diesel.

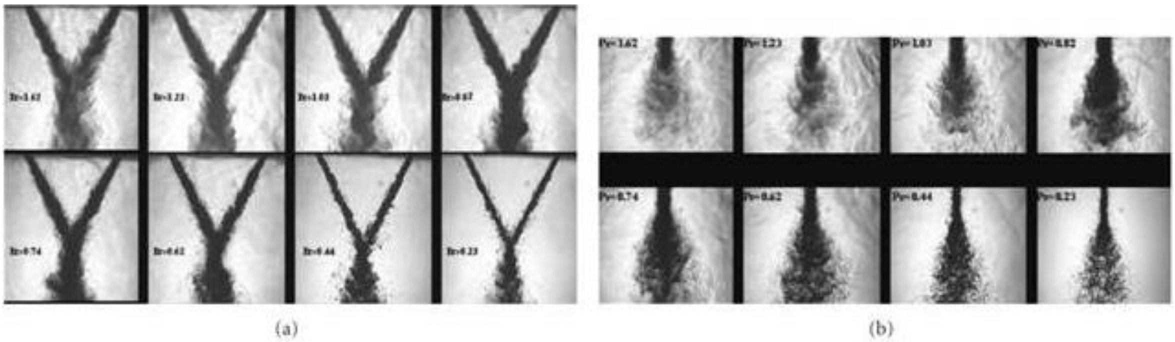

Figure 2.23 Instant images of sun-, near- and supercritical impinging jets for liquid N_2 *into gaseous* N_2 *(room temperature) injection by Chehroudi. The images in (a) are taken at 90-deg to the corresponding images in (b)* [95].

2.5.3 Supersonic Crossflow Atomisation

Research in the field of supersonic crossflow atomisation is primarily related to aerospace applications, such as gas turbines and relatively recently scramjets. Experiments in this area have shown that the velocity, momentum and shockwaves generated influence the atomisation of the fuel jet, with shockwaves increasing the separation effects from the main jet [96]–[100]. Figure 2.24 below shows a generalised description of the flow field produced from an injection into a supersonic crossflow.

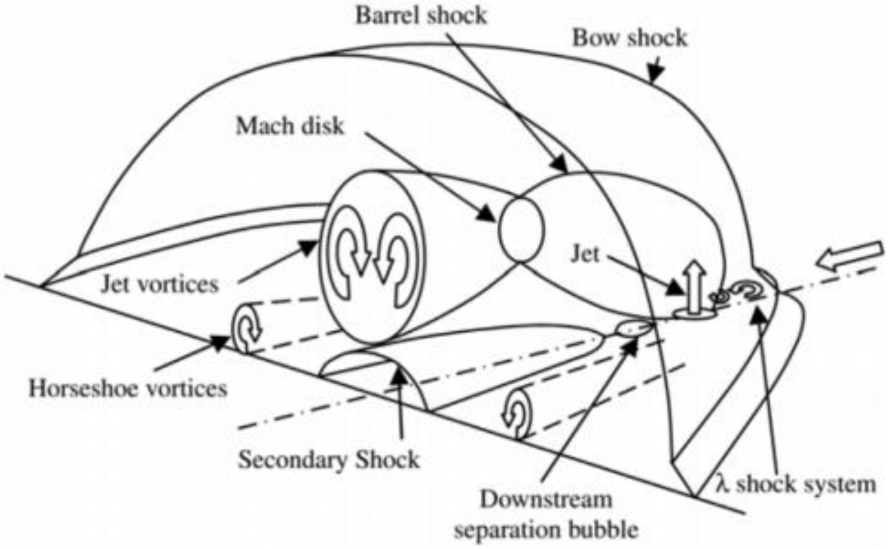

Figure 2.24 Schematic diagrams of a transverse jet in supersonic crossflow showing some of the dominant flow features [99].

The difference between this field of research and that of the impinging/crossflow of jets in the RSCE is that the crossflow is not uniform and is expanding. Therefore the temperature and density are both decreasing from the point of injection which have effect both on mixing and combustion phenomena.

2.5.1 Injection into Supercritical Conditions

Research involving ICEs and supercritical conditions has predominantly centred on injecting fuel, typically diesel, at high pressure into air at supercritical conditions, which replicated the conditions during DI in Diesel engines. Work in this area has shown that even if the air is at supercritical conditions this does not necessarily mean that diffusive mixing occurs [101], [102]. At RSCE operating conditions classical mixing should occur but this is not the case when analysing the pressure rise rate inside the engine.

Figure 2.25 displays a diagram of conditions displaying evaporation, transitional, and diffusive mixing test points by Manin et al [101], overlaid with an approximate are of RSCE operating conditions. This simple analysis is not a full accurate representation of the mixing occurring in the RSCE, as the air is travelling and expanding at high velocity in comparison to conventional Diesel engine air motion and combustion as well as entering a chamber at almost ambient conditions.

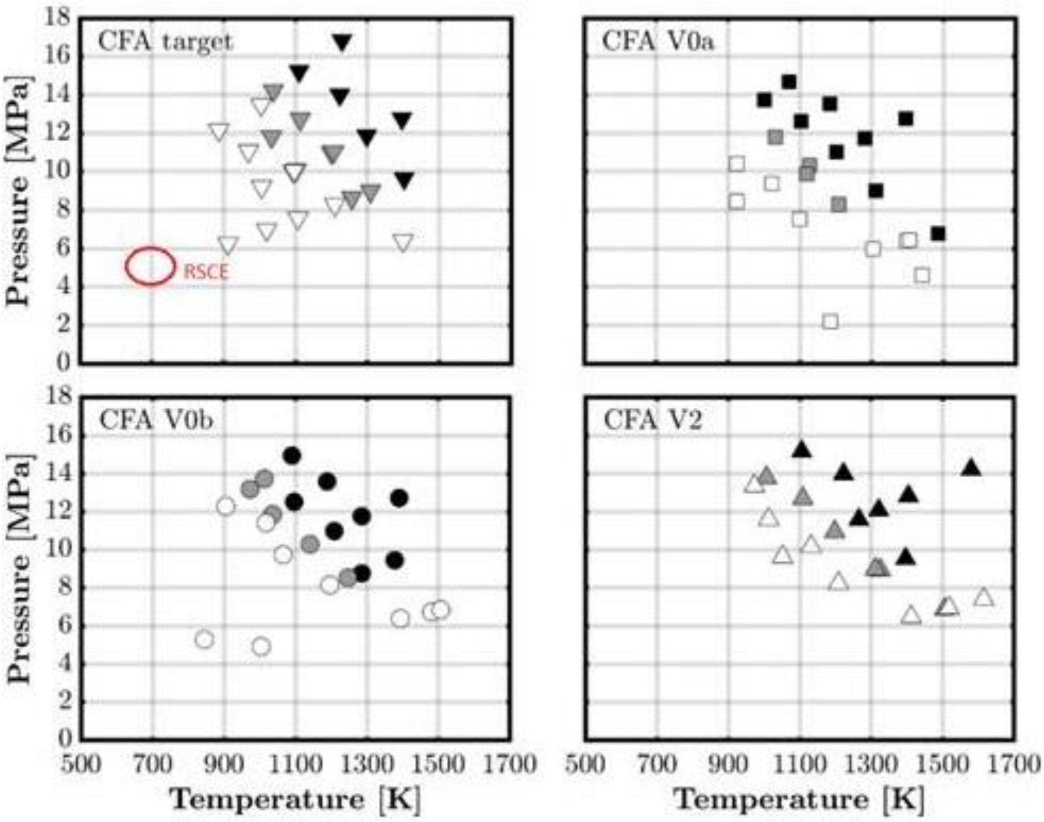

Figure 2.25 Pressure-temperature diagrams showing the tests points for four multi-component fuels. The white symbols represent test conditions where only classical evaporation is observed; the grey markers represent conditions showing transitional mixing; black symbols represent test conditions where the fuel exhibits diffusive mixing. CFA target is close to conventional Diesel. Diagram modified by author from Manin et al [101]

2.5.2 Boiling and Pseudo-Boiling

Due to the pressure and temperature conditions, it is possible for boiling and pseudo-boiling effects to be present in an ICE. Conventional boiling phenomena of water is well documented with the three main regimes highlighted in Figure 2.26. Film boiling is a regime which demonstrates the Leidenfrost effect. In this regime when a droplet is in contact with a hot enough surface a vapour cloud is quickly created. This vapour cloud is a layer between the hot surface and the droplet which inhibits the heating of the rest of the droplet, as the vapour cloud has poor thermal conductivity. This is of interest in terms of spray injection, as this could help or hinder heat transfer between the fluid and fuel, depending on the regime, as well as preventing wetting of in cylinder components, i.e., piston, cylinder walls, valves, etc.

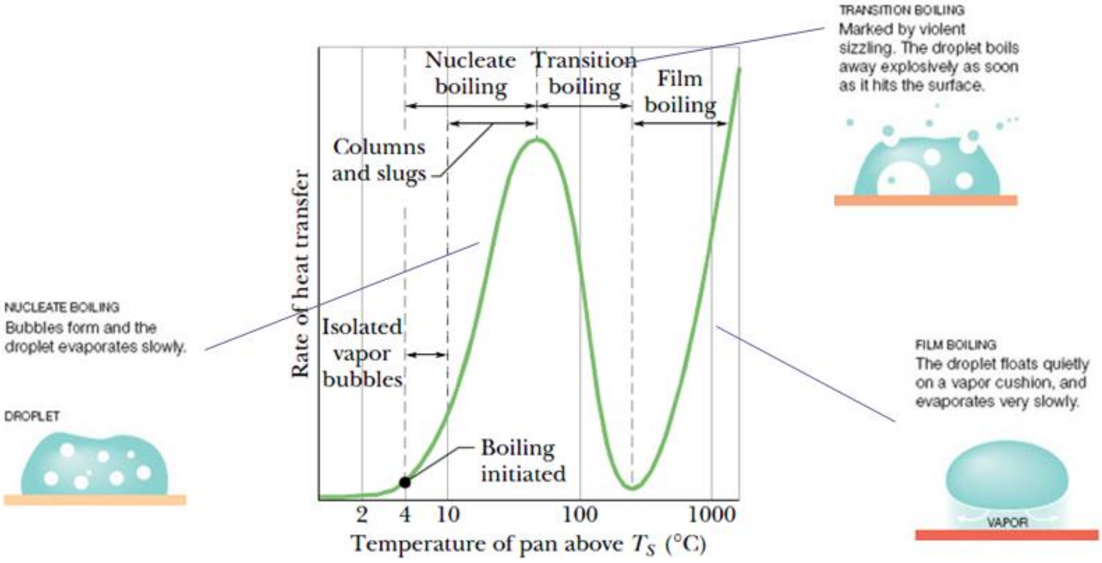

Figure 2.26 Heat Transfer for Water at 1 atm [103]

Recent research has shown that the supercritical regime can be separated into two distinct regions, with liquid-like and gas like-properties, separated by the Widom line as shown in Figure 2.27 [104], [105]. Supercritical pseudo-boiling has recently been demonstrated to exist [106].

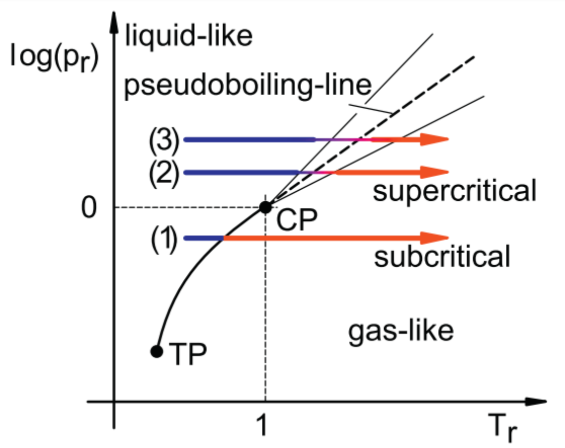

Figure 2.27 Structure of the supercritical state space and comparison of subcritical (1) and supercritical isobaric processes (2) and (3) [106].

2.5.3 Discussion

Alternative mixing methods that than that of current ICEs will be required to produce premixed combustion on demand. A few possible atomisation strategies and effects are explored that could be present and/or optimised.

The ideal situation would be to produce homogenous charge premixed combustion at the same time as direct injection. There are potential phenomena that could be harnessed that show promise to produce premixed combustion on demand in novel engines. Notably, SCEs show promise as they are able to utilise high pressure air as an alternative or in addition to fuel injection dominated breakup. The ability to combine the mixing energy available from the high pressure of both air and fuel has the potential to increase the difference in relative velocities to induce catastrophic fuel droplet breakup. As well as inducing high velocity bulk airflow motion in the cylinder such as swirl, which can aid combustion efficiency and emissions reductions. This will be explored in more detail in Section 2.7

2.6 Reduction of Heat Losses in Conventional ICEs

2.6.1 Introduction

This section reviews the ongoing scientific advances in the reduction of losses in conventional Diesel and Otto ICEs and explore the limitation of this approach. Typically, modern engines in PLCV’s and HGV’s can achieve anywhere from 14% to 45% efficiency from fuel to wheel depending on the drive cycle and technology utilised [107], [108]. The largest loss of approximately 30-40% of energy is from the efficiency of the thermodynamic cycle. Stone generalised and broke down the other losses into six main areas with approximate values shown in Table 2.3.

Table 2.3 Conventional ICE Losses [109]

Area	**Loss**
Mechanical	3%
Blowby	1%
Cycle to cycle variations	2%
Gas exchange	2%
Heat transfer	7%
Finite combustion	3%
Total	18%

The importance of recovering waste heat is highlighted when analysing Stone's losses, with the largest single loss of 7% from heat transfer. The difficulty with addressing these other losses is that it is almost impossible to address one loss without impacting another in a conventional ICE. For example, if cylinder insulation was increased to reduce the heat lost to the cylinder walls the compression work would increase, exhaust temperature would increase, and volumetric efficiency may decrease, giving potentially no net gain in heat transfer loss. Although turbochargers do recoup a portion of lost heat in modern engines, they are still limited in their ability to harness exhaust heat. For heat loss to be addressed meaningfully a more fundamental approach to harnessing wasted heat through engine design and architecture must be taken, rather than "retro fitting" to a conventional ICE cycle.

In comparison to the heat transfer loss the thermodynamic loss is far greater but added together they account for almost half of the energy lost at ~47%. For a new heat engine to have a step increase in efficiency, in comparison to today's modern conventional four stroke ICEs, it must make significant gains in terms of fundamental thermodynamic efficiency and wasted heat recuperation to achieve "Ultra-high efficiencies" of greater than 60%.

To investigate areas of improvement, Robert Morgan created a Sankey diagram to help identify useful potential pathways to higher efficiency from a conventional ICE, shown in Figure 2.28. Underlining the difference between low grade heat rejection and high grade exhaust heat rejection.

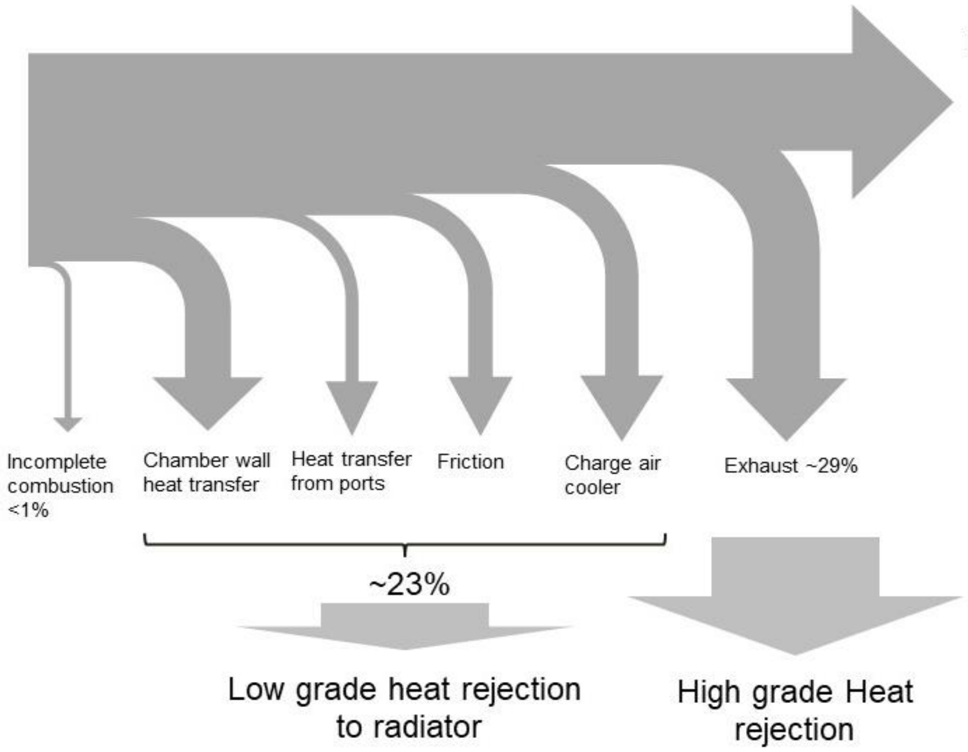

Figure 2.28 Sankey diagram for a typical internal combustion engine. Credit to Robert Morgan.

Four broad approaches are apparent from the Sankey diagram:

- Reduction of in-chamber heat transfer losses
- Recovery of waste heat from the exhaust and cooling system
- Reduction of friction
- New thermodynamic cycles that achieve one or more of (a) heat loss reduction (b) heat recovery (c) improved work recovery

Within the current work, reduction in friction will not be considered. Each of the other opportunities will be considered in this section.

A reduction in heat losses from the combustion chamber could be achieved by reducing the temperature difference between the chamber wall and working fluid, by reducing the working fluid temperature and/or increasing the combustion chamber wall temperature by adding a thermal barrier to the chamber wall. Several approaches have been proposed and are discussed.

2.6.2 Low Temperature Combustion

While the major function of LTC, HCCI and RCCI combustion technologies is to reduce emissions there is also a potential efficiency gain from heat transfer. As peak combustion and working fluid temperature is reduced, the heat loss to the combustion chamber walls, cylinder head, and piston are also reduced. This has been observed to produce an efficiency gain of approximately 1-5% while also reducing emissions in certain operating conditions in research to date [91], [93].

Lean homogenous combustion occurs at a lower flame temperature than conventional stoichiometric combustion, as discussed and shown in Section 2.2.1 and Figure 2.17, respectively. As such, NO_x emissions are very low. Several approaches have been reported for achieving various degrees of lean combustion from complete homogenous lean burn HCCI [110] and develops including low temperature combustion [94] and RCCI [89]. The majority of recent research that has been on the RCCI variant, which utilises two fuels of differing reactivity to improve the control of ignition process, indicated efficiency gains of 2-7% have been reported in low to medium speed and loads [86], [91], [93]. The main issue in achieving high cycle efficiencies is the control of knock, resulting in sub-optimal compression ratios or high levels of dilution using EGR (increasing pumping work). Without using exotic fuels, the CR is limited to 17:1 and often lower to control knock [92]. This therefore limits the maximum efficiency possible utilising conventional thermodynamic cycles. In reality, large quantities of EGR are required to control knock in HCCI and RCCI applied to conventional ICEs, which further reduces the maximum efficiency through higher pumping losses.

2.6.3 Thermal Barriers – Combustion Chamber Insulation

Several methods of combustion wall insulation with thermal barriers to reduce heat loss to the combustion chamber surfaces have been proposed over the years, such as a thin ceramic layer [111]–[113]. Considerable research was undertaken in the 1980's with the aim of creating an "adiabatic engine" which required no coolant. The concept ultimately failed as the increased combustion chamber wall temperatures adversely effected the engine breathing, trading reduced heat losses with increased pumping work and reduced volumetric efficiency [114]. Indicated efficiency gains of up to 7% were reported, but with an increase in NO_x emissions and brake efficiency largely unchanged from the baseline.

Toyota research have proposed a novel solution to the problem with combustion chamber insulation via Thermo-Swing Wall Insulation Technology (TSWIN) [115], [116]. The insulating layer is porous with a low conductivity and thermal inertia. The layer therefore rapidly cools during induction, reducing adverse heating of the charge air (and associated increases in pumping losses and volumetric efficiency) but heats rapidly during combustion, delivering the required reduction in heat losses with a lower penalty on the induction stroke in conventional ICEs. The material proposed is a porous anodized aluminium reinforced with a silica layer to achieve the desired qualities. Under cold start NO_x and fuel consumption were also shown to reduce by approximately 10% and 5% respectively [115], [116]. Limited benefits of 2% have been reported under steady state conditions.

2.6.4 Waste Heat Recovery

Approximately 47% or more of the fuel energy is typically lost as heat from the engine. Methods of converting waste heat to usable power have been proposed as an attractive method to increase the overall efficiency of conventional engines. Three common methods proposed are thermoelectric generators, turbocompounding and organic Rankine cycle (ORC) systems. The merits of a thermoelectric generator are that it has no moving parts and a high reliability but current technology has low conversion efficiency, mainly due to the material properties required [117]. A prediction of the reduction in fuel consumption of a thermoelectric generator is 0.18% [118] when including the effects of exhaust back pressure and limits of current technology. Therefore, it is not currently considered economically feasible to add on such a system but as the technology continues to develop this could change.

Turbocompounding is seen as a promising technology for reducing fuel consumption in the future with low volume and weight attributes of the technology, combined with the ability to optimise and integrate the device with the prime mover [119]. A significant advantage, in comparison to other waste heat recovery methods, is the relatively low cost. However, the main drawbacks associated with turbocompunding are high exhaust back pressure, low energy conversion at low load conditions, and a need to be able to optimise the system over a wide load range. Theoretically up to two thirds of the exhaust energy could be recovered but practically this has limitations in terms of the turbine and extra exhaust back pressure [119]. As the technology evolves inevitably there will be conventional ICE technologies that will start to incorporate such systems.

The addition of an ORC systems to recover exhaust and coolant heat offers an enticing add on systems for heavy goods vehicles. The systems rely on high grade heat usually by adding a heat exchanger to the exhaust or engine cooling system, which has been shown to increase brake thermal efficiency up to 1.8% [120]. These post combustion heat recovery systems are however limited in comparison to recovering the heat pre combustion as shown by Morgan et al [121]. As previously demonstrated, ORCs applied to ICEs are limited by the CR of the ICE and the heat addition. The amount of heat that can be recovered is determined by the recuperating efficiency of the heat exchanger and the energy conversion efficiency. The conversion efficiency of ORC systems is generally poor as the system must remain within sensible heating.

2.6.5 Discussion

The literature suggests a reduction in heat losses in conventional ICEs could increase brake efficiency by a maximum of ~2% for conventional ICEs with individual technologies. There is the potentially further improvement with several technologies applied. However, the consequences and trade-offs would have to be considered. The presented methods of reduction and post heat recovery on conventional ICEs will not provide a path to step increase in efficiency alone to reach ultra-high efficiencies of >60% in conventional ICEs. This suggests a novel or alternative thermodynamic cycle is needed to provide a step increase in efficiency to tackle the largest single loss of fuel energy.

2.7 Alternative ICE Concepts & Cycles

2.7.1 Introduction

With the limits of current ICE thermodynamic cycles being reached and incremental advances becoming more costly, new approaches to achieving more efficient thermodynamic cycles are being researched and developed. Many new concepts have centred on “over-expansion”, with the idea of extracting more energy from the expansion of the working fluid, as well as potentially providing more control over the working fluid before combustion.

An engine concept that has been re-energised in the past couple of decades is the split cycle engine (SCE) [122]. In a SCE, the conventional four stroke cycle is split into two separate chambers. One chamber performs the intake and compression strokes, and the other performs the combustion/expansion and exhaust strokes. The inherent benefits of the SCE concept are that the CR and expansion ratio (ER) can both be independently optimised, as they are no longer occur in the same chamber. With both chambers separated into effectively hot and cold cylinders, each cylinder can be optimised for its intended use and thermal losses have the potential to be reduced. The SCE concept in theory enables some of the issues with conventional engine insulation to be overcome due to this temperature decoupling.

SCE are not a new concept. The Brayton cycle was originally developed on a reciprocating piston engine, with George Brayton patenting his “Ready Motor” in 1872 [123], [124]. Making the Ready Motor one of the first ICEs for motive power and the first recorded SCE. Harry Ricardo patented his so called “Dolphin” engine in 1906. It was a SCE used both in a passengers car and for local fishing boats, and anecdotally produced less smoke than other equivalent engines of the time [125]. This section will review and discuss alternative ICEs and thermodynamic cycles, with a focus on SCE and the RSCE.

2.7.2 Scuderi Engine

The Scuderi engine is a basic concept of the SCE but is claimed to benefit from the advances in engine design, in particular the valve gear in the period between the realisations of the engine [126], [127]. The fast-actuated valve train allows for pneumatic hybridisation with idea of the engine acting as an air pump when rolling down hills or under engine braking to store kinetic energy as compressed air for redeployment into the engine when required. The main disadvantage to this kind of system is the extra mass and volume required to store the compressed air, as well as the complicated plumbing work of the cylinder head, but the potential efficiency benefits are claimed to have the potential to outweigh this. A diagram of the Scuderi SCE is shown in Figure 2.29.

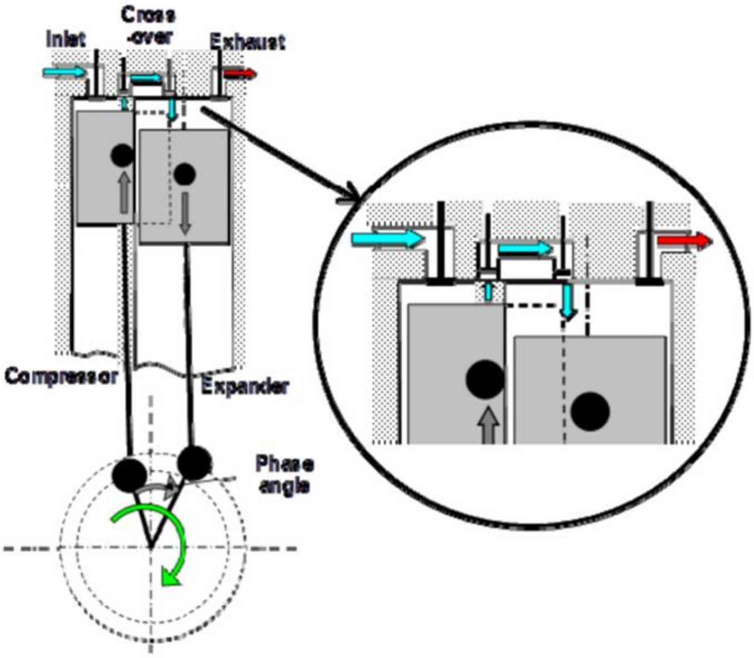

Figure 2.29 Diagram of Scuderi engine [126]

Toxic emissions are also claimed to be reduced but exact figures are not given and as the engine still operates SI, the emissions benefits are inherently limited with no control over start of combustion temperature or other changes in chemistry. The simulated efficiency benefits are given as approximately 3-5% with a general increase in torque across the operating range of 2,000 - 6,000 RPM [127].

2.7.3 Z engine

The Z engine is a SCE that uses a novel approach to fuel air mixing with self-proclaimed HCCI and RCCI style combustion using a single diesel fuel [128]. The exhaust valve of the engine is opened very late and closes very early in comparison to typical engine valve timings [129]. By having the exhaust valve open (EVO) late as much work as possible is extracted from the working fluid during the expansion stroke. The exhaust valve closes (EVC) early as a method of EGR. This is a common feature of a SCE.

Overall, the engine cycle runs at lambda 1.6-1.7 with 96-98% of this fuel injected into the exhaust gas before the intake valve opens (IVO) [128]. This ensures a homogenous mixture of fuel and exhaust gas before air is introduced. Although when the air is injected into the combustion cylinder the air and fuel are at high pressure and temperature, the mixture does not auto-ignite as the air fuel mixture is too lean. The combustion event is therefore controlled by a pilot injection of 2-4% of the fuel which brings the overall air fuel mixture up or beyond a critical lambda level, where the reactivity is high enough to start combustion [128]. By having no valve overlap in theory this also reduces the potential for emissions such as UHC.

A unique valve design is incorporated into the Z engine. The intake valves are designed to encourage high swirl ratios, 20-40 compared to 1-10 in a conventional diesel engine, before combustion [128], [130]. This ensures a homogenous mixture of air, exhaust gas and fuel, preventing localised stratification that could result in premature auto ignition. This also reduces soot formation, as there is very little or no stratification of fuel during combustion. These high swirl ratios could potentially increase combustion event length to slow down or control the high PRR. The reported emissions would comply with EURO VI without exhaust after treatment, produce comparatively low maximum peak temperatures of 800- 1200K, and a claimed thermal efficiency 44.8% part load, 49.4% best point. There was no increase in overall efficiency compared to modern conventional heavy duty truck engines during operation, but a large decrease in toxic emissions under the same conditions [129].

The reported emissions and fuel consumption are; NO_x 0.02g/kWh, BSFC part load 192g/kWh, best point 174 g/kWh (49.4% brake efficiency) and 188 g/kWh at full load (44.8% brake efficiency) [128]. Combustion temperatures; top dead centre (TDC) part load temperature 800K, TDC full load temperature 700K, maximum temperature at full load 1,900K.

2.7.4 Five Stroke Engine

The five stroke ICE concept utilises two conventional four stroke high pressure cylinders and another larger low-pressure expansion cylinder [131], [132]. The two four stroke cylinder cycles are offset by 360 degrees and feed the low-pressure expansion cylinder with exhaust gas every 360 degrees. The extra expansion stroke gives the concept its name and is how the engine achieves increased overall efficiency due to the increased or over expansion of the exhaust gas, compared to the Otto cycle. The limitation of the five stroke ICE concept is that the working fluid cannot be compressed further, presenting the same limitations as the Otto cycle, and is similar in concept to the Atkinson and Miller cycles.

A five stroke concept was developed and tested as a turbocharged port injected spark ignited engine, for use as a range extender or series hybrid [131]. Boost pressure delivered by the turbocharger is controlled through separation of the exhaust gas delivery. The aim of the smart wastegate is stated to reduce and control exhaust back pressure from the turbocharger, allowing the turbine to operate at its most efficient point. An illustration of the five stroke concept is shown in Figure 2.30. The experiment produced an efficiency of 36.1% and comparison with the 0D and 1D simulation suggested a combustion efficiency of 99% at an engine speed of 4000 RPM and brake power of 32.8kW [131].

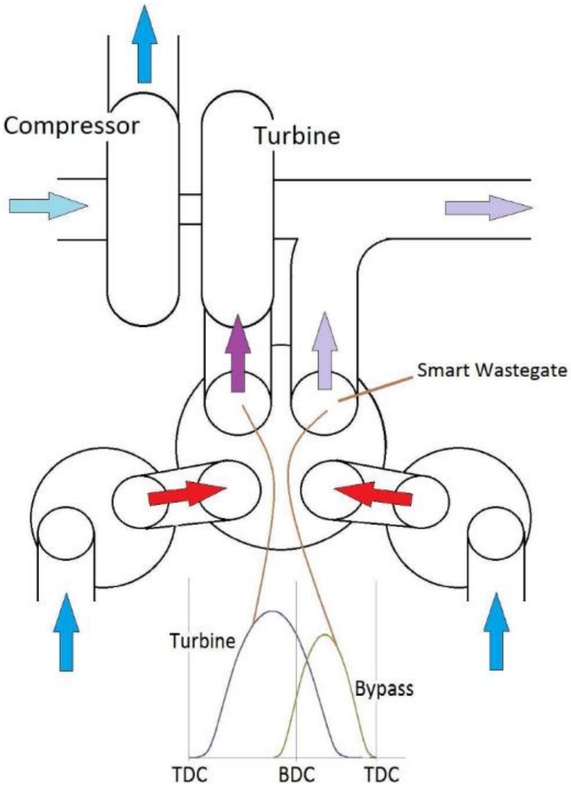

Figure 2.30 Illustration of the architecture of the five stroke engine showing the location of the valves, smart wastegate, and the low pressure exhaust valve lifts [131].

A simulation study comparing the heavily downsized Miller and five stroke engine cycles showed that at low loads the Miller cycle exhibited higher fuel conversion efficiency than that of the five-stroke cycle [132]. With a brake efficiency of 36.1% in the best case Miller cycle and 31.5% in the five stroke cycle at 1000 RPM and 58Nm. Conversely at high load conditions the five stroke cycle exhibited higher fuel conversion efficiency than that of the Miller Cycle. With a brake efficiency of 26.1% in the Miller cycle and 38.3% at 2600 RPM and 165Nm.

Apart from an efficiency gain, there is not necessarily any benefit in terms of other emissions such as NO_x and soot. This is due to no advancement in combustion technology to control peak combustion temperatures or improved air fuel mixing from conventional port or DI gasoline or Diesel ICEs.

2.7.5 Double Compression Expansion Engine

The double compression expansion engine (DCEE) concept can be thought of as an amalgamation of the split cycle and five stroke engine concepts. The DCEE concept comprises of two cylinders; a large low-pressure cylinder inducts and performs the first compression of the working fluid before it is transferred to a smaller high pressure cylinder [133]–[137]. The high pressure cylinder then passes the high pressure exhaust gas back into the low pressure cylinder to perform the second expansion. An illustration of this cycle and system layout is shown in Figure 2.31.

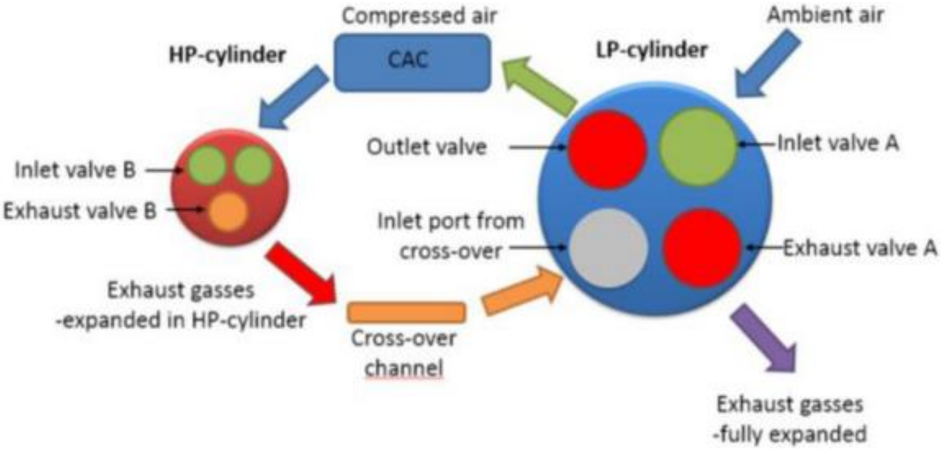

Figure 2.31 System layout of the DCEE concept [134].

With a smaller volume high pressure cylinder there is a small efficiency gain as less heat is transferred and lost to the walls due to the smaller surface area. The largest efficiency gain is obtained from the “over-expansion” of the exhaust. There is an increase in pumping losses of up to 3 time that of conventional CI ICEs due to the inherent design of the DCEE concept [134]. This could potentially be due to the throttling of the compressed exhaust and air as they are transferred between the two cylinders via traditional poppet valves. Initial simulations predicted brake efficiencies of up to 56% could be achieved. However, this was revised to 53.7% once heat transfer and friction losses were updated and the subsystems were optimised [135]. NO_x emissions were measured at 0.3g/kWh [135].

2.7.6 Homogenous Charge Progressive Combustion Engine

The homogenous charge progressive combustion engine (HCPC) is a SCE concept which utilises the compressed air and port fuel injection to gradually admit a homogenous charge of air and fuel into the combustion chamber [138]–[142]. An illustration of the concept is shown in Figure 2.32. By forming a homogenous charge before progressively adding fuel into the chamber, it is proposed that the concept can provide on demand HCCI.

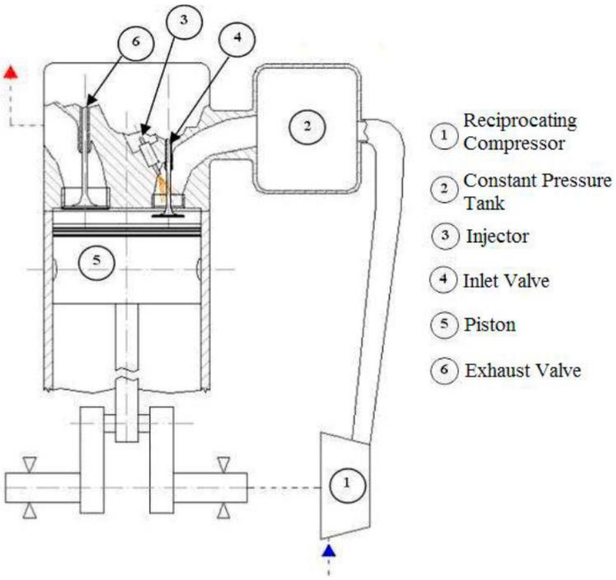

Figure 2.32 The HCPC concept [138].

A unique transfer duct containing the injector is proposed to achieve the homogenous charge [139]–[142]. The transfer valve is located between the compression cylinder and the transfer duct which controls the timing of the combustion event. Figure 2.33 displays the proposed arrangement of the transfer duct and injector.

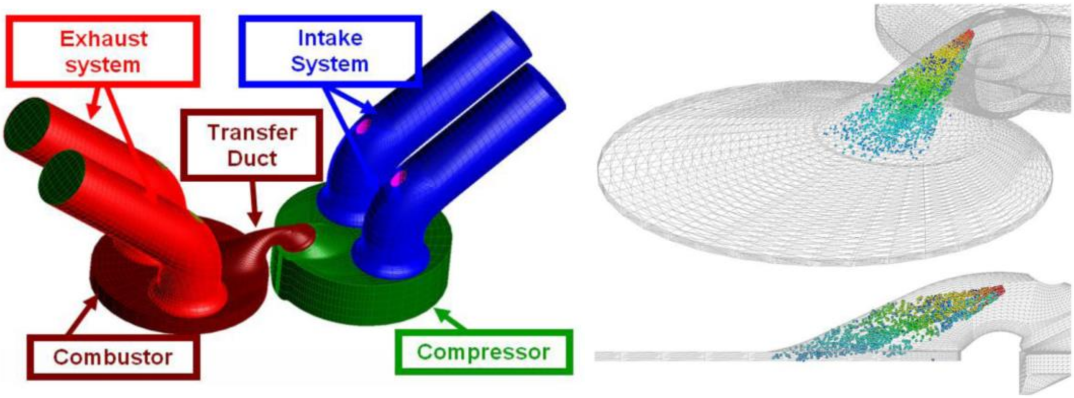

Figure 2.33 HCPC engine computational domain and injector position [142].

Research demonstrated that with engine wall insulation it was possible to increase indicated thermal efficiency from 46% up to 56% with little to no impact on HC and soot production [139]. However, as expected, NO_x emissions increased due to higher temperatures. It was suggested the effect of NOx emissions can be compensated by EGR at low to medium load conditions and by water injection into the compressor at high load to further increase thermal efficiency [139].

In one study, experimental validation against an Iveco Cursor 9 engine was undertaken before a range of CFD simulations were undertaken comparing the emissions response of the two engines over a range of conditions [142]. Figure 2.34, Figure 2.35, and Figure 2.36 display comparisons of the local equivalency ratio and temperature for each of the computational cells in the CFD simulation at 10, 20, and 30 CAD ATDC for Cursor 9 and HCPC CFD simulations at full load.

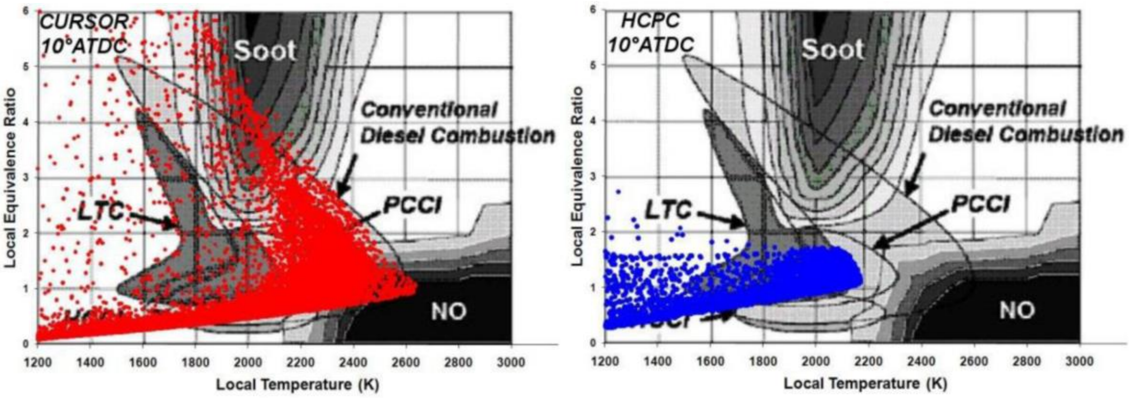

Figure 2.34 Comparison of local equivalency versus temperature for 10 CAD ATDC of the cells within the combustor computational domain [142].

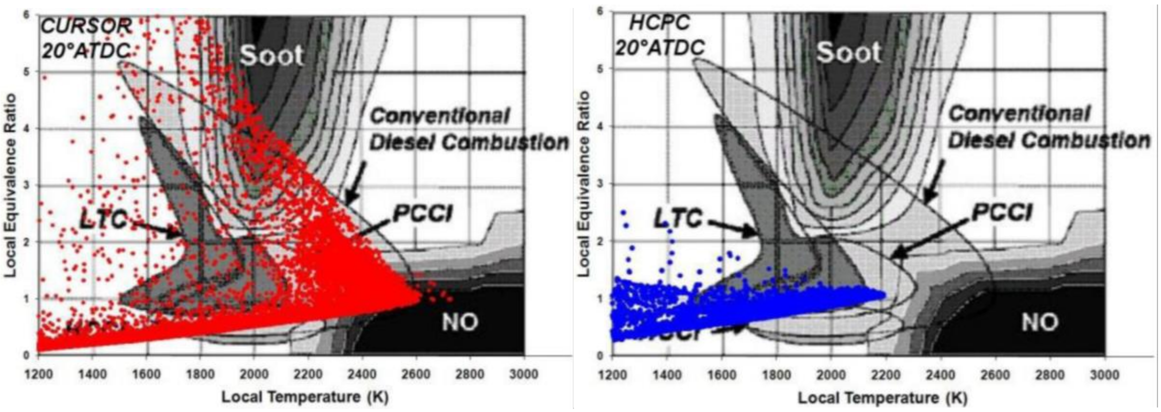

Figure 2.35 Comparison of local equivalency versus temperature for 20 CAD ATDC of the cells within the combustor computational domain [142].

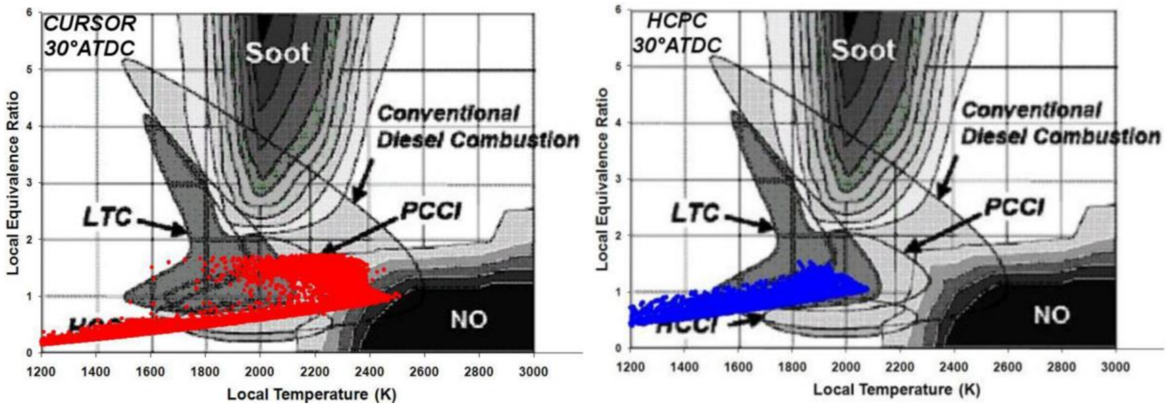

Figure 2.36 Comparison of local equivalency versus temperature for 30 CAD ATDC of the cells within the combustor computational domain [142].

The Cursor 9 results display a conventional response of a wide range of temperatures and local equivalence ratios in each cell across the combustor. The results from the HCPC simulation show a much narrower range of temperatures and local equivalency ratios in each point and broadly stick within the LTC zone. There is an expected drop in temperature in for both the Cursor 9 and HCPC simulations but the narrower operating window for the HCPC engine remains.

2.7.7 The Isoengine & Recuperated Split Cycle Engine

The recuperated split cycle engine (RSCE) incorporates two novel processes into a SCE, quasi-isothermal compression, and heat recuperation. The first RSCE concept was the so called “isoengine” project by Coney et al [1], [143]–[147].

2.7.7.1 Isoengine

The isoengine concentrated on the specific design of a large scale (MW) SCE concept for electric power generation, due development by National Power and later Innogy plc, in 1995. The concept was predicted to achieve up to 60% electrical efficiency operating at 600 rpm and 7MW of electric power in the final design [143]. The novel engine relies on three features: isothermal compression of combustion air to high pressure, (achieved with water injection during compression reducing compression work), extensive air pre-heating (integrating exhausted waste heat back into the cycle), and isobaric combustion (extracting energy from the fuel at high average temperatures without increasing peak temperature).

Although the average combustion temperature of the isoengine is expected to be high, the peak temperatures are lower than that of a diesel engine, due to the isobaric combustion and higher water content of the working fluid [143]. Therefore, it is expected that the NO_x emissions from the isoengine would be lower than a comparative diesel engine. However, testing and development of the combustion system is stated as needed to quantify and optimise the emissions response [143].

The isoengine project initially focussed research on achieving quasi-isothermal compression through water injection in the compressor [144]. The initial proof of concept was performed by converting one cylinder of a marine diesel engine [143]. With the aim of reducing compression work and lowering the charge air pressure out of the compressor, while maintaining air mass flow. Quasi-isothermal compression is achieved in the proof of concept through water injection through multiple satellite spray nozzles pointing towards the centre of the chamber. High pressure ratios of up to 30 are stated as achievable with a single stage and the associated reduction in work from wate injection. A diagram of the isoengine compressor proof of concept test rig and the varied rig test parameters are shown in Figure 2.37.

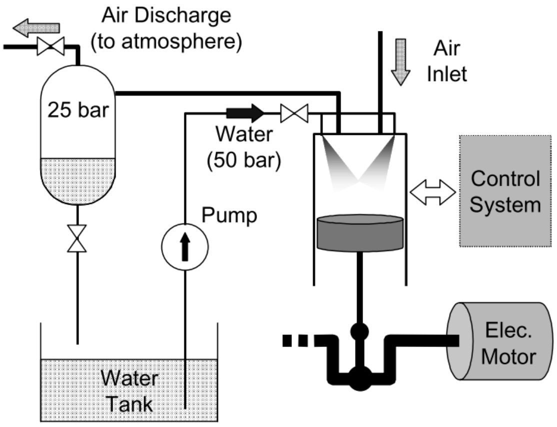

Rig Test Parameters

- Rig running speed (50 - 200 rpm)
- Atomizer type and set up
- Timing of main water addition
- Mass of water added
- Cylinder clearance volume
- Intake and discharge valve timings

Figure 2.37 Isoengine compressor proof of concept – Rig test schematic diagram and test programme [144].

The proof of concept demonstrated that achieving a large heat transfer through large water droplet surface area (small droplet size), high injected water mass, high spray penetration, and homogenous distribution were key to reducing compressor work. In the best proof of concept experimental result, a work saving of 28% was achieved, relative to the reference adiabatic case [144]. Reliable operation of the proof of concept was achieve with pressure ratios of up to 25 and the tests demonstrated that transient air temperatures can be maintained below 100°C compared to the adiabatic temperature of ~500°C. Further research suggested ideal work savings of up to 41% could be achieved with a pressure ratio of 30 and isothermal compression [146].

Research on the isoengine then focused on the complete isoengine [1], [146]. A heat exchanger is added to recuperate exhaust heat into the compressed air from the compression cylinder. This acts similarly to regenerative or inverted Brayton cycle concepts, increasing the potential thermal efficiency of the engine cycle [148]. This is enabled through the low temperatures out of the compression cylinder, which cannot be achieved without quasi-isothermal compression in the compression cylinder. The schematic diagram for the prototype isoengine is shown in Figure 2.38.

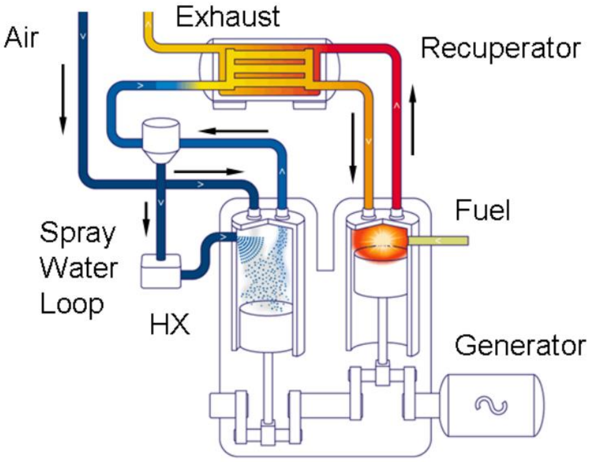

Figure 2.38 Schematic diagram of the isoengine [1].

A 3MW prototype engine was built at Ricardo in Shoreham-by-Sea, UK. The 3MW prototype was the first engine to incorporate all the unique features of the isoengine concept, with the aim of producing a 7MW commercial demonstrator engine after the 3MW engineering demonstrator. The target efficiency of the 3MW engineering demonstrator was 50%, with the aim of achieving 60% for the 7MW commercial demonstrator [1]. This is primarily governed by the maximum cylinder pressure of 100 bar.

An example of the pressure traces and valves lift timings for the engineering demonstrator is shown in Figure 2.39. A high amount of exhaust gas recompression was utilised to provide heat for ignition of the fuel. With the exhaust valve starting to close at 90 BTDC and fully closing at ~30 BTDC. This recompression of the exhaust is undesirable and would have negatively affected the efficiency of the isoengine.

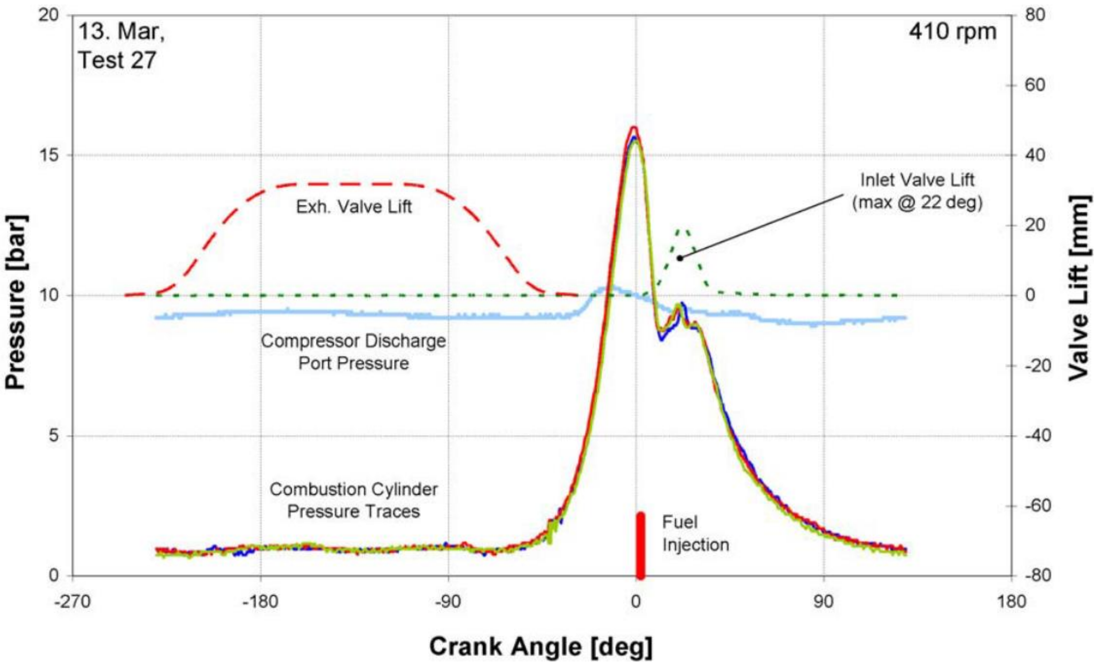

Figure 2.39 Pressure traces and valve timings for the 3MW engineering demonstrator naturally aspirated [1].

Fuelled and motored cylinder pressure traces for the engineering demonstrator are shown in Figure 2.40, demonstrating the isobaric combustion achieved. Notably the intake valves are open for the majority of the combustion event. Combustion was found to deteriorate significantly as fuelling was increased, with some tests of the tests shown in Figure 2.40 resulting in smoke levels above a Bosch Number of 1.0. Calculations of fuel spray break-up length indicated that the nozzle design was unsuitable for the cylinder pressures and temperatures at certain conditions, leading to impingement onto the piston crown, this was also supported by carbon deposits on the piston crown [1].

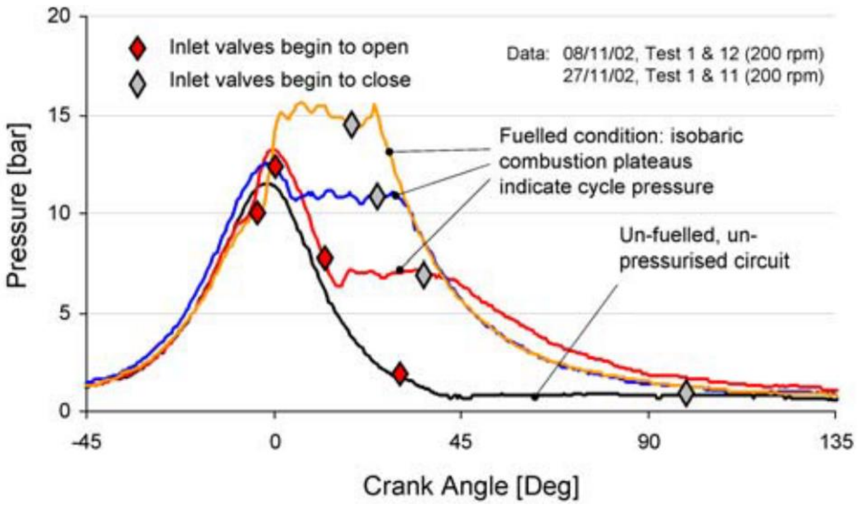

Figure 2.40 Pressure traces of isobaric combustion for the 3MW engineering demonstrator [1].

Further analysis of the data was presented from the 3MW model and added into a model to extrapolate the potential efficiency [147]. The results of this work suggested that an efficiency 57.3% is achievable with an increase in cylinder pressure from 100 to 150 bar for the commercial demonstrator. With further improvements suggested that could bring the efficiency up to 60%, shown in Figure 2.41. Combustion is noted as needing improvements in the work. However, no numbers or figures on combustion efficiency are provided to quantify the improvement that could be made and are not noted in the potential efficiency improvements graph. The issues with high soot in a natural gas engine indicate combustion development was needed to improve mixing, emissions, and increase fuel consumption. No hypotheses are presented as to why this may be.

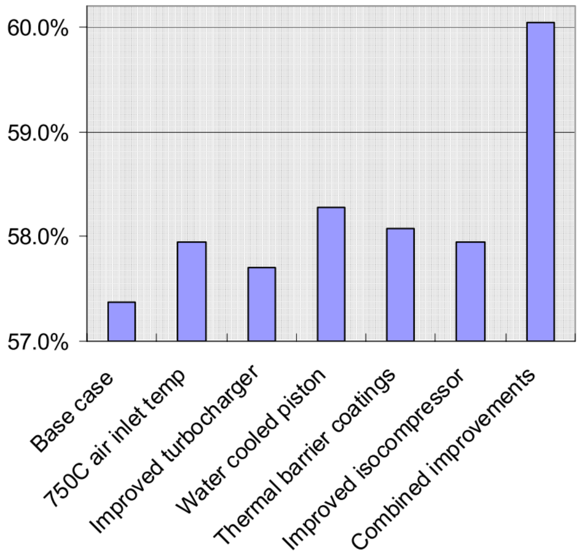

Figure 2.41 Potential efficiency improvements for the isoengine [147].

2.7.7.2 Recuperated Split Cycle Engine

As the isoengine project encountered issues and eventually came to a halt, Ricardo continued research on the concept with a new focus on medium duty engines with the University of Brighton. The conceptual schematic for the RSCE is identical to the isoengine concept shown in Figure 2.38.

The RSCE concept provides the ability to control the intake air and working fluid temperature entering the cylinder so that the combustion reaction can be optimised to produce LTC. Versions of RSCE have also been touted utilising coolants in the compressor other than water, such a liquid nitrogen. The other coolants could be used that serve other purposes as well as a coolant in the compression cylinder, such as liquid nitrogen, or a liquid fuel. These would enable dilution and/or fuel atomisation and heating. Versions of the RSCE have been attributed names by Ricardo and Dolphin N2, with ThermoPower being the water injection version of the RSCE, and CryoPower being the liquid nitrogen fuelled version [149]. The CryoPower version brings with it challenges in terms of operating liquid nitrogen in ICE chamber conditions, the specifics of which will not be delved into in detail in this review, but it is worth noting that research and experimentation considering the effect on liquid nitrogen fuel atomisation and the thermo-physical properties are being investigated [150], [151]. This section will review and discuss thermodynamic and the initial experimental research on the RSCE.

Several studies on the RSCE thermodynamic cycle were produced by Dong et al [2], [121], [152]. The temperature entropy (T-S) diagrams shown in Figure 2.42 demonstrate that the improvement in efficiency is gained from the additional heat captured from the quasi-isothermal compression and precombustion heat recuperation of the RSCE, i.e., the area between points 1, 2', and 3.

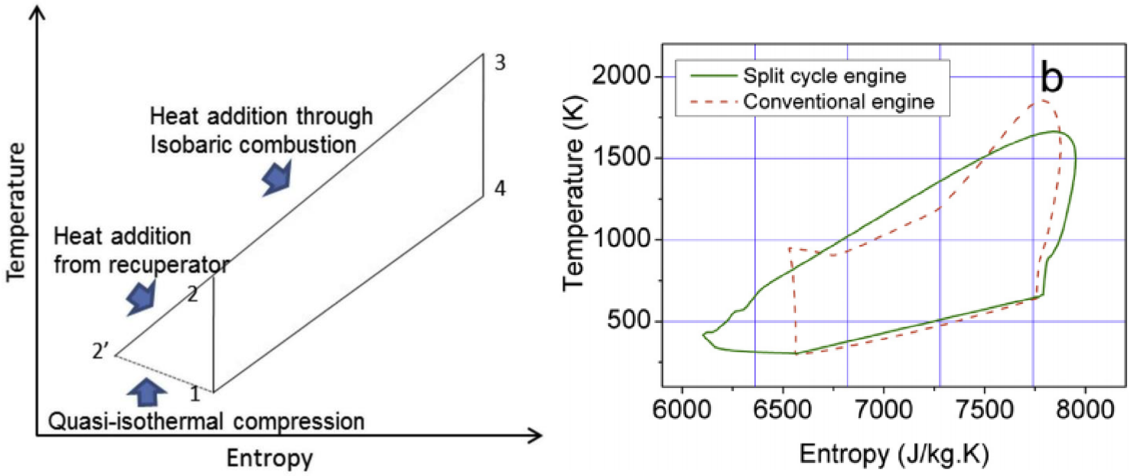

Figure 2.42 Theoretical temperature entropy (T-S) diagram of the RSCE (left), and T-S diagram comparison of SCE and a diesel engine (right) [2].

Dong et al [2] present an equation for calculating the thermodynamic efficiency of a RSCE, shown in Equation (12). Dong et al state upon inspection that the ideal thermal efficiency is determined be four parameters: the ratio of CR/ER, isothermal index C (where C = 0 is isothermal), temperature rise ratio N (which represents the energy released by the fuel), and the recuperator effectiveness σ. Dong et al present several sensitivity studies on these variables.

$$
\begin{aligned}
\eta &= \frac{(Q_{LH}+Q_{RE})-(Q_{REJC}+Q_{REJE})}{Q_{LH}} \\
&= \frac{ER^{(k-1)}-1}{ER^{(k-1)}-\sigma} + \frac{Cp\cdot T_1}{Q_{LH}\cdot\left(ER^{(k-1)}-\sigma\right)}\cdot\begin{bmatrix} 2\cdot\sigma\cdot CR^{(k-1)\cdot C}-\sigma\cdot ER^{(k-1)}\cdot CR^{(k-1)\cdot C} \\ -CR^{(k-1)\cdot C}+ER^{(k-1)}-\sigma \end{bmatrix} - \frac{Cv\cdot T_1\cdot(C-1)}{C\cdot Q_{LH}}\left(CR^{(k-1)\cdot C}-1\right)
\end{aligned} \tag{12}
$$

The sensitivity study by Dong et al [2], shown in Figure 2.43, demonstrated the ability for the RSCE to produce a higher efficiency (~90% peak thermal efficiency) than the Otto cycle. In the studies presented in Figure 2.43, the CR/ER ratio is assumed to be 1, and the recuperator effectiveness is assumed to be 80% for the CR swing. The RSCE thermodynamic efficiency peaks at a CR of ~3, much lower than that of the Otto cycle.

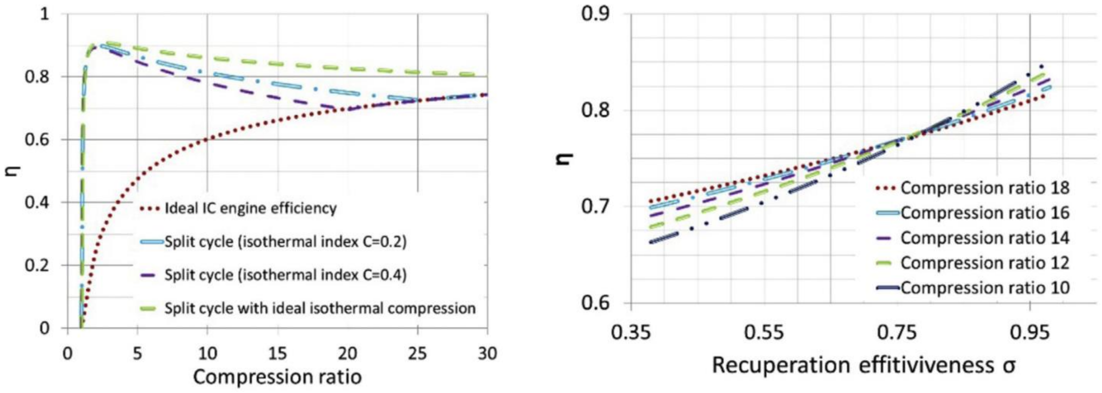

Figure 2.43 Diagram of thermodynamic efficiency of RSCE against compression ratio (left) and recuperation effectiveness (right) [2].

The study against recuperator effectiveness demonstrated the potential cause of higher RSCE cycle at lower CRs with an assumed recuperator effectiveness of 80%. With a range of CR presented, a lower CR delivered higher thermal efficiency above ~77% recuperator effectiveness, whereas a higher CR delivered higher thermal efficiency at below ~77% recuperator effectiveness. This is likely due to a lower ER in the expander increasing the temperature of the exhaust and therefore increasing recuperator efficiency. Due to this, lower CR or ER produced overall higher system efficiencies with recuperator effectiveness of ~77% or higher, as shown in Figure 2.43. Decreasing ER has the additional benefit of increasing specific power in SCE, as chamber volume at IVC dictates the air mass and therefore energy that is added to the system.

Although not discussed by Dong er al, if the CR/ER ratio is increased to greater than 1 or the amount of fuel is increased, it is likely that the crossover point of whether higher or lower CR produces greater efficiency will lower. This is due to the recuperator becoming more efficient with a higher exhaust temperature. The crossover in efficiency is due to whether the expander or the recuperator are most efficient at harnessing the exhaust energy, either through expansion of the gas in the expander or by heat transfer in the recuperator. This would require further analysis and modelling to determine the trade-off between the two conditions for a range of conditions.

Several isothermal indexes are shown in CR sensitivity study in Figure 2.43. Figure 2.43 highlights the diminishing returns of the RSCE at higher CR, with an isothermal index of 0.4 not providing any benefit in thermal efficiency over the Otto cycle due to there not being enough heat available to recuperate [2]. The figure demonstrates the benefit of reducing compression work and increasing recuperator efficiency with more ideal quasi-isothermal compression. Interestingly at the peak efficiency of ~3 CR shown in Figure 2.43, the three isothermal efficiencies converge at this condition, suggesting the recuperator effectiveness is more important than isothermal compression with lower a CR for this condition.

Dong et al presented another sensitivity study of two temperature rising ratios, which represents the and manner of heat addition from the energy from the fuel, shown in Figure 2.44. The response shows that for a given CR and recuperator effectiveness thermodynamic efficiency increases with N. The differences between a value of 4 and 6.5 for N demonstrates that for a higher value the efficiency is more forgiving in response with a lower gradient in efficiency against CR. However, there is a higher gradient in response to recuperator efficiency with recuperator effectiveness.

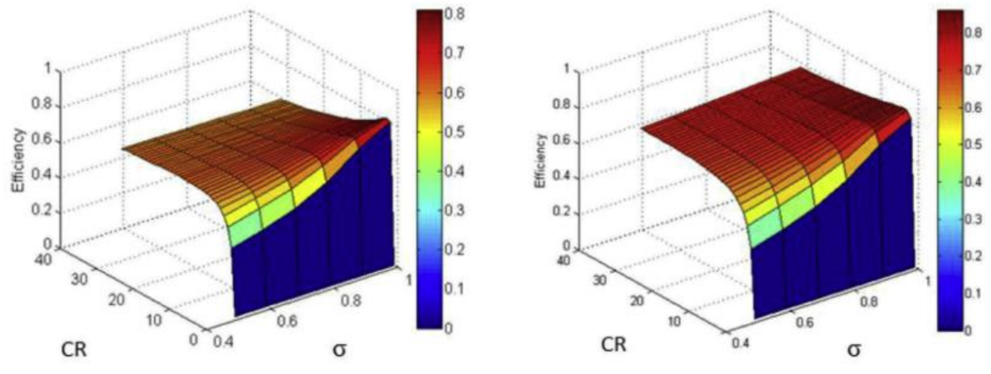

a. N=4

b. N=6.5

Figure 2.44 3D thermal efficiency maps of the RSCE for two temperature rising ratio (N) conditions [2].

Unfortunately, Dong et al did not present a sensitivity study of independent CR and ER in their work in the same manner as Figure 2.44. However, it can be theorised from the expression and sensitivity studies presented, that a higher CR would increase pressure and therefore energy available to add to the system. Therefore, a suitably high CR and low ER would yield the highest thermal efficiency in a RSCE, as long as the quasi-isothermal compression and recuperator effectiveness are able to recuperate heat and results in a high recuperator efficiency due to a large difference in temperature and other losses are unaffected.

Dong et al [2] present a graph which suggests that increasing ER independently of CR, with a CR of 23, increases efficiency. Dong et al suggest that this is the result of reduction in heat transfer with higher ER. However, this is for a given fuel injection rate of 53mg/cycle. It is unclear if the amount air mass is constant or changes with the variation in ER in the results shown in Figure 2.45. It is unclear what recuperator effectiveness was used for this sensitivity study and if the recuperator conditions achieved convergence for each condition, as the recuperator efficiency and temperature transfer is dependent on the heat exchange from the previous cycle. The increase in efficiency could be the result of leaning out of the fuel with an increasing air mass and more “free” Rankine work from the gas but this cannot be said with any certainty either way. Graph (a) in Figure 2.45 shows that the heat loss occurs during the heat addition from the fuel. However, there is a higher peak temperature for the lower ER conditions the cause of which is not clear.

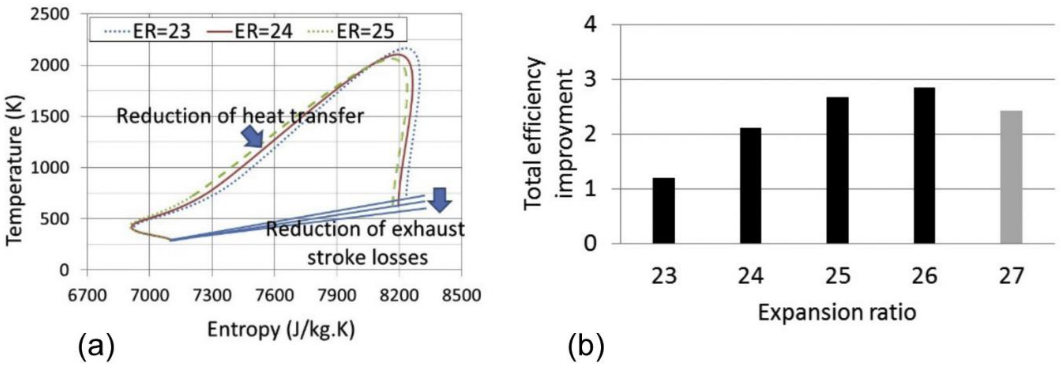

Figure 2.45 Effects of ER on T-S diagram (a) and thermodynamic efficiency improvement (b) for a RSCE [2].

Initial experimental results from a single cylinder test rig representing the expander cylinder of the RSCE were presented by Morgan et al [3]. The results presented in this work demonstrated stable and rapid combustion over a limited range of test conditions at 800 and 1200 RPM. The high speed test data for test points 15 and 18 at 1,200 RPM are shown in Figure 2.46. In comparison to the pressure traces of the isoengine in Figure 2.39 and Figure 2.40, the intake valves fully close around TDC and fuel is added approximately as the intake valves begin to close. There is a higher intake pressure utilised of ~28 bar, increasing to a peak pressure of 50 bar, compared to an increase of 10 to 15 in Figure 2.39. Isobaric combustion is not utilised, instead there is a relatively high pressure rise rate, in comparison to that of the isoengine and comparable diesel engines [3].

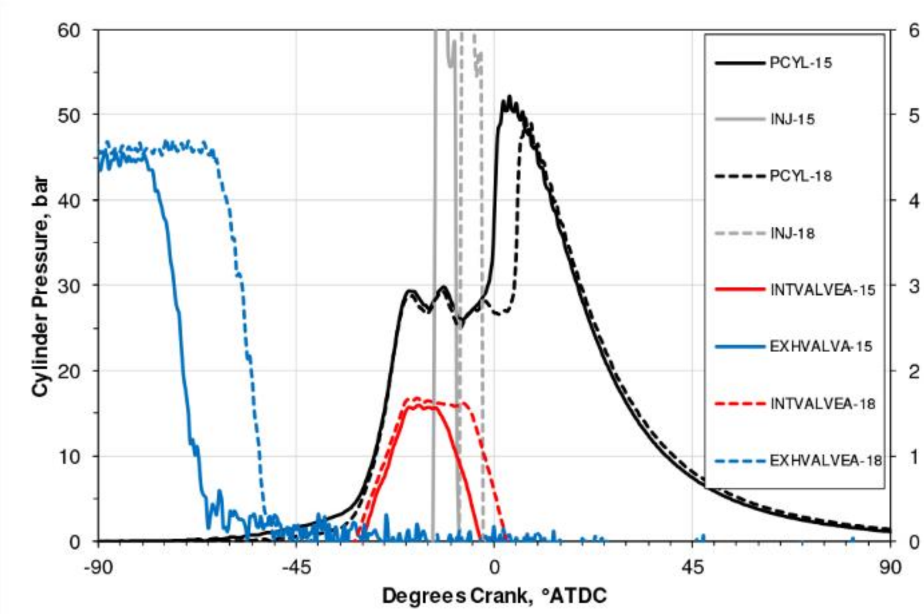

Figure 2.46 High speed cylinder data for two test points (15 & 18) at 1200 RPM from a single cylinder test rig representing the expander cylinder of a RSCE [3].

Morgan et al state that conventional heat release analysis are invalid as the fuel is injected while the intake valves are open and it is likely initial fuel reactions begin while the intake valves are open, therefore close volume assumption could not be made [3]. Instead, Morgan et al utilised an approach of matching measure pressure data to a 1D simulation model created by LMS AMEsim package and Ricardo WAVE. The results of the normalised rate of heat release (ROHR) data from the two test points (15 & 18) are presented in Figure 2.47. Morgan et al do not provide units to the ROHR but claim it is more comparable to that of gasoline than diesel combustion [3]. No evaluation of combustion efficiency is provided to quantify how good and well mixed the combustion process is, with or without using the simulation model.

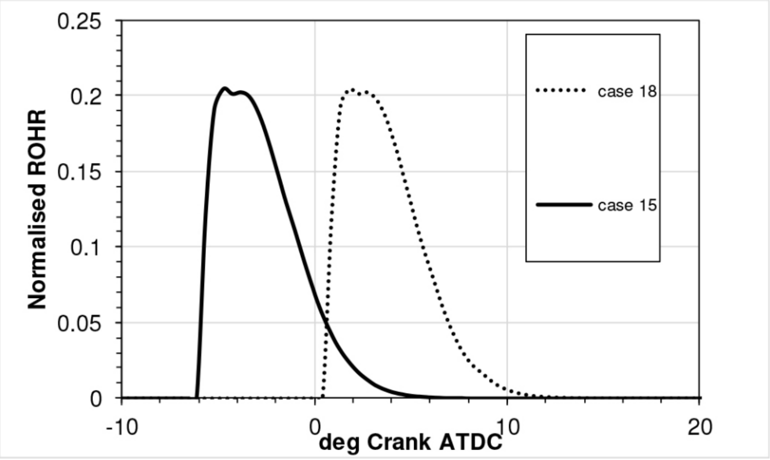

Figure 2.47 Rate of heat release (ROHR) results for test points 15 & 18 at 1200 RPM from a single cylinder test rig representing the expander cylinder of a RSCE [3].

AMEsim cycle simulation study of combustion period and comparison to representative conventional diesel engine thermodynamic efficiency by Morgan et al [3] is presented in Figure 2.48. This shows a ~10% increase in brake efficiency over a comparative diesel cycle and the reduction in combustion period demonstrating the benefit of rapid combustion in the RSCE and diesel engine.

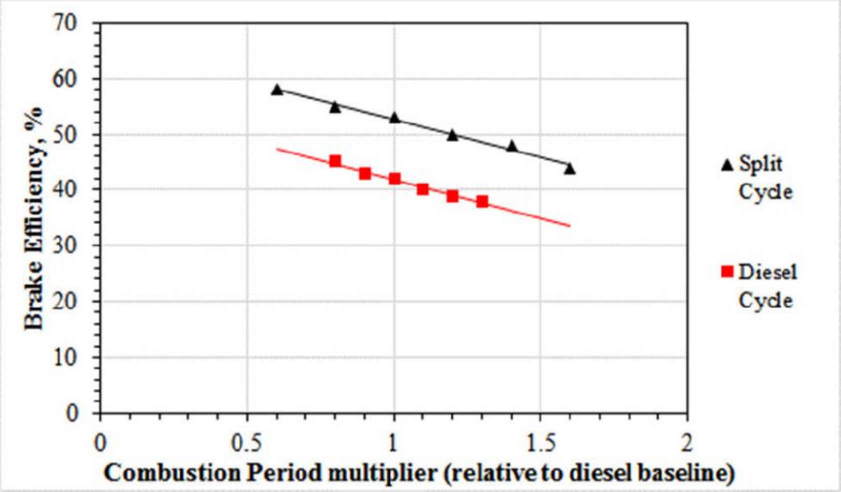

Figure 2.48 Trade off of brake efficiency against combustion period [3].

The data in Figure 2.48 is then used to support the efficiency walk shown in Figure 2.49. However, there is some optimism shown for the RSCE of ~60%, whereas Figure 2.48 shows an efficiency of 58%. There is also a reduction in the improved Diesel cycle, with Figure 2.49 demonstrating an efficiency of 45% BTE whereas Figure 2.48 displayed an efficiency of 47%.

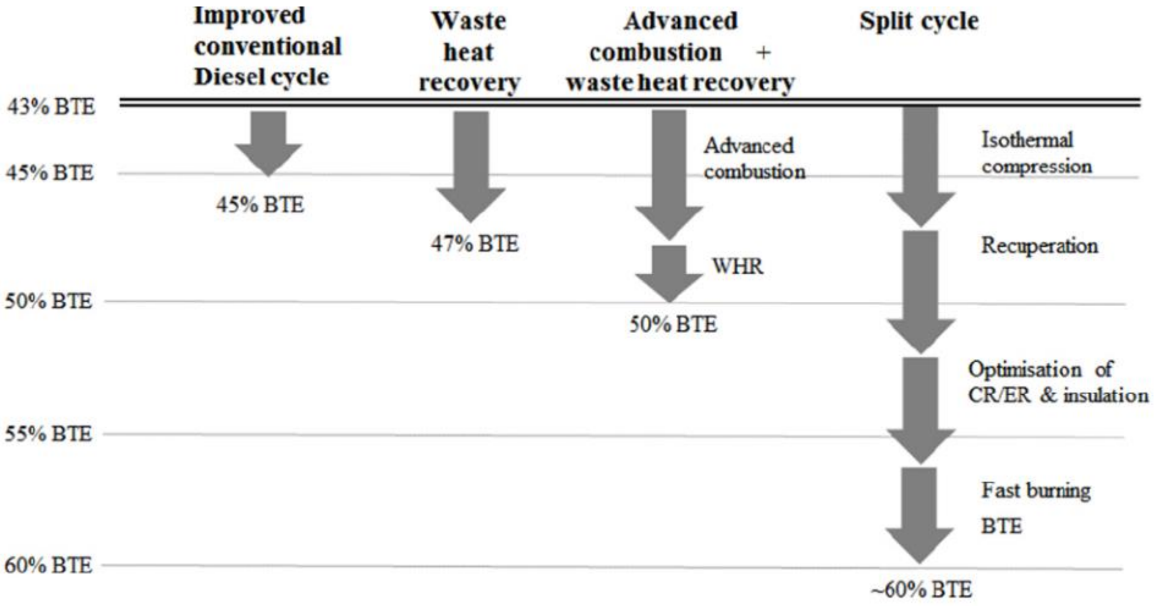

Figure 2.49 Efficiency walk in terms of Brake Thermal Efficiency (BTE) at the best operating point for conventional and advanced diesel combustion with waste heat recovery and predictions for a RSCE [3].

Limited emissions data was gathered in the initial experimental research [3], with the main goal originally to produce and replicate the high efficiencies shown by the past research on the isoengine project and produce stable combustion. A black box approach was initially taken during experimentation leading to questions over the mixing and combustion phenomena that takes place within the engine. Therefore, investigations into the causes and phenomena taking place to produce low emissions require further investigation.

2.7.8 Discussion

Alternative and novel thermodynamic cycles show promise to provide a step increase in efficiency. However, only a few novel cycles demonstrate promise in tackling the inherent issues of toxic emissions productions in conventional ICEs at source, i.e., through engineered and controlled combustion conditions favourable to low emissions. Many concepts attempt to increase efficiency through increased or over expansion. However, only the RSCE attempts to reduce compression work. Due to this, the RSCE is also the only concept which could control start and therefore peak combustion temperatures to control emissions formation at source.

An overview of the concepts discussed in this section is shown in Table 2.4. This comparison demonstrated that there are not enough novel engine concepts being researched that will be able to meet future emissions regulations and achieve ultra-high efficiency of greater than 60%. This highlights the need for innovation in this area to create new novel engine concepts that fundamentally address emissions first as well as providing a step improvement in efficiency. The ICE cycle and combustion technology needs to be designed with emissions and combustion designed in mind from the outset, rather than developing systems that may have a step increase in efficiency, but which inherently do not reduce emissions at source. This will be further discussed in Chapter 3.

Table 2.4 Comparison of ICE Concepts.

ICE Cycle/ Concept	Control of peak combustion temperature	Premix style charge & combustion proposed	Waste Heat Recovery	Efficiency achieved to date	Efficiency potential
Otto	No	Possible	None	45% [153]	-
Diesel	No	No	None	52% [154]	-
Scuderi	No	No	None		-
Z Engine	No	Yes	None	49.4% [128]	-
5 Stroke	No	No	Post	36.1% [131]	-
DCEE	No	No	Post	47% (indicated) [135]	56% [135]
HCPC	Yes	Yes	None	-	49% (indicated)
RSCE	Yes	Yes	Pre	53% [3]	60% [3]

2.8 Summary of the Literature

Through the course of this literature review the fundamental limitations of current and future ICE concepts highlight the requirements of a nontoxic emissions engine which are described below:

- Utilises renewable or synthetic chemical fuel.

This may be a biofuel from waste products, such as human effluent, biofuels from renewable and ethically sources, or green synthetic fuels from carbon capture or water and renewable energy sources. New ICE concepts must be able to run on one of these fuels and ideally would be fuel agnostic to enable it to not compete with premium buyers of renewable fuels, such as the aviation sector.

- Zero or near zero toxic emissions

This stipulates that the combustion process must utilise a premix style of combustion and control peak combustion temperature, requiring control over intake air temperature entering the combustion cylinder.

- Ultra-high efficiency of 60% or greater

For reduced energy consumption, economic impact, and high and quick commercial adoption and viability. This will require greater efficiencies than that of the Otto cycle and therefore a different thermodynamic cycle. In addition, likely utilising a form of reducing or recuperating exhaust heat as well as low friction and heat losses.

- Utilise cheap, abundant, recyclable, and sustainable engine design/architecture that does not utilise exotic materials.

For high recyclability and low cost, the material choice must consider the life cycle impact of the engine during and at the end of the products lifecycle and be highly recyclable with low recycling complexity and cost.

The RSCE concept is currently one of the best proposed ICE concepts for addressing the point outlined. Currently the RSCE is the only ICE concept discussed which is potentially fuel agnostic, provides control over the start of combustion, and therefore peak combustion temperatures, reduces compression work through quasi-isothermal compression, reduces frictional losses through reduced compression temperature, can potentially reduce heat losses through individual optimisation of the two compression and expansion chambers, and insulation of the expansion chamber surfaces. However, there remain gaps in the literature on the theoretical limits and capability of what an emissions limited ICE could potentially achieve in terms of efficiency and combustion efficiency of the RSCE and phenomena potentially contributing to mixing and combustion in the RSCE.

Chapter 3 Efficiency Limits brought on by Emissions Limitations

In theory, how efficient could an ICE be while meeting sustainable limitations on emissions during use?

3.1 Introduction

This chapter will present fundamental theoretical analysis concerning whether the operational emissions of an ICE can be sustainable, followed by efficiency limitations within the set boundary of low to zero toxic emissions ICE. First analysing if a combustion chemical reaction can be sustainable followed by efficiency limitations within the limitations of clean toxic emissions. The focus of this work is on avoidable toxic emissions that are a result of the ICE, with a focus on NO_x. Carbon dioxide is not considered a toxic emission in this context as it is unavoidable from the exhaust of an ICE if utilising a carbon-based fuel. Instead, the approach of reducing carbon dioxide is tackled through increasing efficiency, which will be covered in the last section of this chapter.

3.2 Methods to Reduce Toxic Emissions

Several paths and methods are available to reduce in use emissions from ICEs. These can be thought of as three groups, chemical, thermodynamic, and physical, though there is invariably interconnection between these broad groups. These can further be split into the main variables that effect chemical reactions, their products, and therefore unwanted emissions.

- Initial temperature
- Initial pressure
- Working fluid composition
- Oxygen concentration
- Fuel composition
- Reaction area, interface, and mixing (atomisation & motion)

What can be controlled, what has the greatest effect, and what should be controlled to reduce and eliminate the unwanted emissions products will be discussed in more detail in the following sections.

3.2.1 Fuels, Reactants, Products & Energy

What is classified as an emission is still widely debated by academics, society, and industry. As previously discussed in Section 2.1.1, there is agreement between health bodies on toxic emissions that are hazardous to health, such as carbon monoxide, particulate matter, and nitrous oxides. However, carbon dioxide is not considered a toxic emission and whether it is considered an emission is dependent on the life cycle of the carbon fuel product it is released from. Carbon produced from fossil fuels is considered an emission as during the lifecycle of fossil fuels, fossil fuels are extracted extremely quickly in comparison to their formation. The formation of fossil fuels is an extremely slow process of carbon lifeform decomposition into fossil fuels over millions of year's deep underground. Whereas it is generally agreed that biofuels from biomass such as wood, biogas, and bioethanol, can be sustainable due to biofuel production and sequestration generally being of similar speed. However, there are societal concerns with biofuels, due to the possibility of competing land space with other resources, such as food. The lifecycles of carbon fuels must be diligently evaluated to assess the carbon lifecycle. Alternative fuels are discussed in detail in Section 2.3. In this chapter the carbon in an organic molecule will be assumed to be from a sustainable source.

3.2.2 Temperature

Temperature plays a key role in the reaction rate of this plethora of reactions, such as the oxidation of the nitrogen in the air to produce NO_x, as other parameters typically remain constant or have very little variation affecting the reaction rate. The rate of the reaction is described by the Arrhenius equation (Equation (13)) where K is the rate of the reaction, T is the temperature, R is the universal gas constant, E_a is the activation energy specific to the fuel utilised and A_f is the pre-exponential factor. A_f can be modified through dilution such as with by exhaust gas recirculation (EGR) and the AFR. Temperature has a much larger scope for modification and reduction.

$$K = A_f . e^{-\frac{E_a}{R.T}}, \tag{13}$$

To reduce the formation of NO_x in an engine, the temperature must be kept low enough to sufficiently slow the nitrogen oxidation reaction. A stated previously, if the peak temperatures are kept below 2,200K, NO_x formation rates are low enough to meet current regulation, this is illustrated in Figure 2.17. It should be noted that a lower threshold of 1,550K may be required to meet future emissions standards. Common hydrocarbon fuels will oxidise rapidly at temperatures above 1,000K, therefore there is a temperature window where the desirable oxidation reaction of the fuel can progress rapidly whereas the undesirable oxidation of nitrogen will not. This is illustrated in Figure 3.3, where the typical operating regions of current diesel and gasoline cycle engines and the target region of operation for a zero-emission engine are shown.

Unfortunately, the temperatures generated by the reaction mechanisms encountered in conventional diesel and gasoline fuelled engines are high enough to produce significant NO_x emissions. The other significant variable that affects the formation of emissions is the concentration of the fuel in the air, expressed as the equivalence ratio. Under normal engine operating conditions at a local equivalence ratio of 1, NO_x formation rates are high at typical combustion temperatures. In addition, there are local regions in a Diesel engine around the fuel dense spray where the fuel can form soot emissions through a pyrolysis reaction. However, there are temperature and fuel concentration conditions where little to no NO_x nor soot emissions will form. The challenge is to design a reaction regime that preferentially operates in these regions.

3.2.3 Fuel Mixing & Atomisation

Soot is generally formed from unreacted carbon atoms, which has two main causes: poor mixing of air and fuel before and during reaction and rich air to fuel ratios. The majority of modern Diesel vehicles operate at lean AFR to ensure there are plenty of oxygen atoms to each carbon atom, ensuring low levels of soot. This does however have a small effect on the production of NO_x as there are also more oxygen atoms available to react with nitrogen, but this is negligible in comparison to the effect of temperature. For the engine of the future to create zero or near zero levels of soot the reaction cannot be rich and must be at maximum Stoichiometric. Leaner mixtures will continue to be used but as air fuel mixing technology improves, the closer engines will run at Stoichiometric to maximise specific power.

3.3 Perfectly Stirred Reactor Model

A fundamental question is then raised. What fuel, if any, is most suitable and able to produce no toxic emissions such as soot and NO_x? As soot is attributed to air mixing technologies as mentioned previously, a study understanding the NO_x potential of fuels in an ideal environment needs to be understood. Khalid et al conducted a piece of work investigating this for autoignition for N-dodecane, iso-octane, and methane utilising a 0D FORTE CHEMKIN combustion model and several reduced chemical kinetic schemes [155].

In the work a perfectly stirred reactor (PSR) model was used to assess the NOx emissions potential for a range of fuels. This imagines that the air and fuel is perfectly mixed in a constant volume of ~1L. This is a useful step for understanding the capability of an optimised combustion system achieving low emissions before considering other aspects, such as topology, air flow, ignition points, flames, etc.

A new PSR model was created, run, and analysed by the author utilising the full mechanism, rather than reduced mechanism utilised by Faizan et al. For n-decane JetSurF 2.0 scheme was utilised [40], [46] and the full scheme developed by Luo et al [156] was utilised for n-dodecane, compared to the reduced skeletal mechanism comprising of 105 species and 420 reactions that was used in Faizan et al's work. N-dodecane and n-decane to 0.6 equivalence ratio are included in comparison to the previous work by Faizan et al. Both results from the new model and Khalid et al's results are shown in Figure 3.1, with additions by the author in grey (full scheme N-dodecane) and orange (N-decane). The use of full schemes has led to less variability in the end temperature for the new set of results compared to the results from Khalid et al.

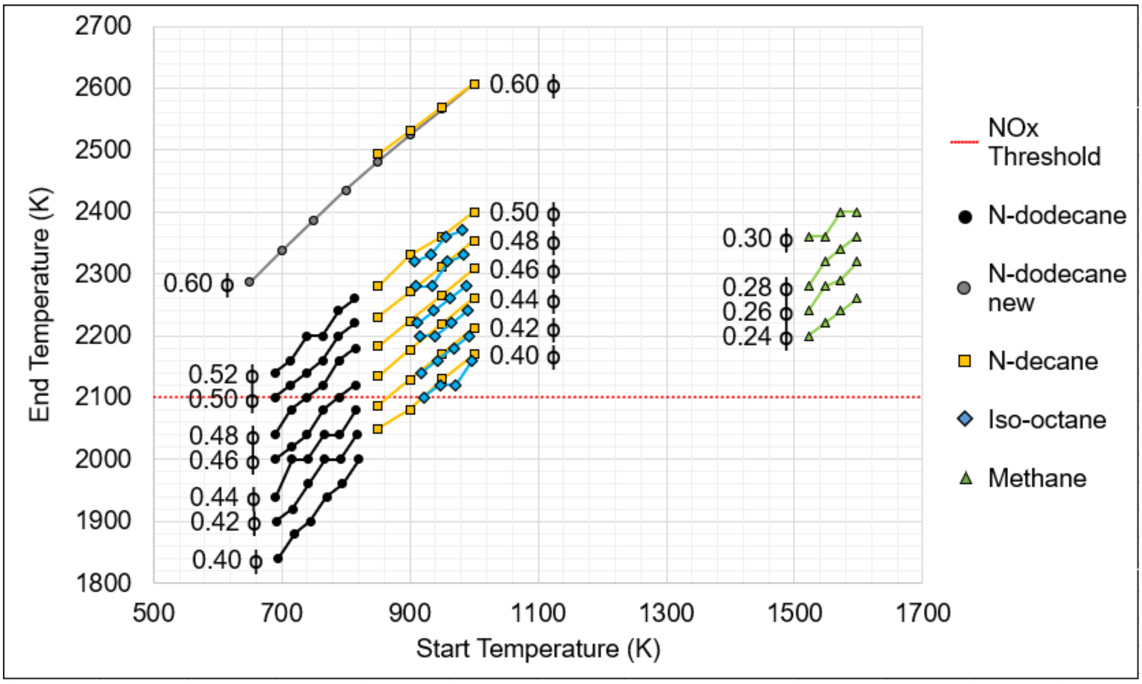

Figure 3.1 End temperature for a range of fuels and equivalence ratios against start temperature. Adapted and modified from Khalid et al [155] *with new additions by the author of N-decane and higher equivalency ratio N-dodecane with higher order schemes.*

The relationship between start and end temperatures for each equivalency ratios should be almost linear, as the energy released by the fuel is divided amongst the mass in the chamber. However, as the initial temperature increases, the heat capacity of air increases (generally above 1,000K for all pressures). This will result in a slightly reducing gradient of end temperature, as more energy is required to heat up the mass in the chamber. This demonstrated that diesel fuel and similar long chain molecules are more suited to producing lower NO_x emissions with autoignition, due to the higher start of combustion temperature required for the same equivalency ratio for shorter chain hydrocarbons.

The new model and analysis conducted by the author also included reaction rate times, represented by the size of the circles in Figure 3.2. The reactions follow the Arrhenius equation (Equation (13)) in that as the start temperature increases the reaction rate also increases. Chemkin can only resolve to the nearest 0.1ms resulting in all the points with 1,000K starting temperature having 2ms reaction time. This approach is limited by imagining the mixture as perfectly mixed and that 100% of the fuel is burned. This will not occur in a real engine but is still a very useful guide for the potential capability of LTC for a given fuel. This piece of work demonstrates although LTC is a challenge to accomplish it does show promise and capability to produce low NO_x emissions combustion systems. The challenges are mostly variable control based, e.g., combustion temperature, and restrictions of operation, e.g., limited engine speed.

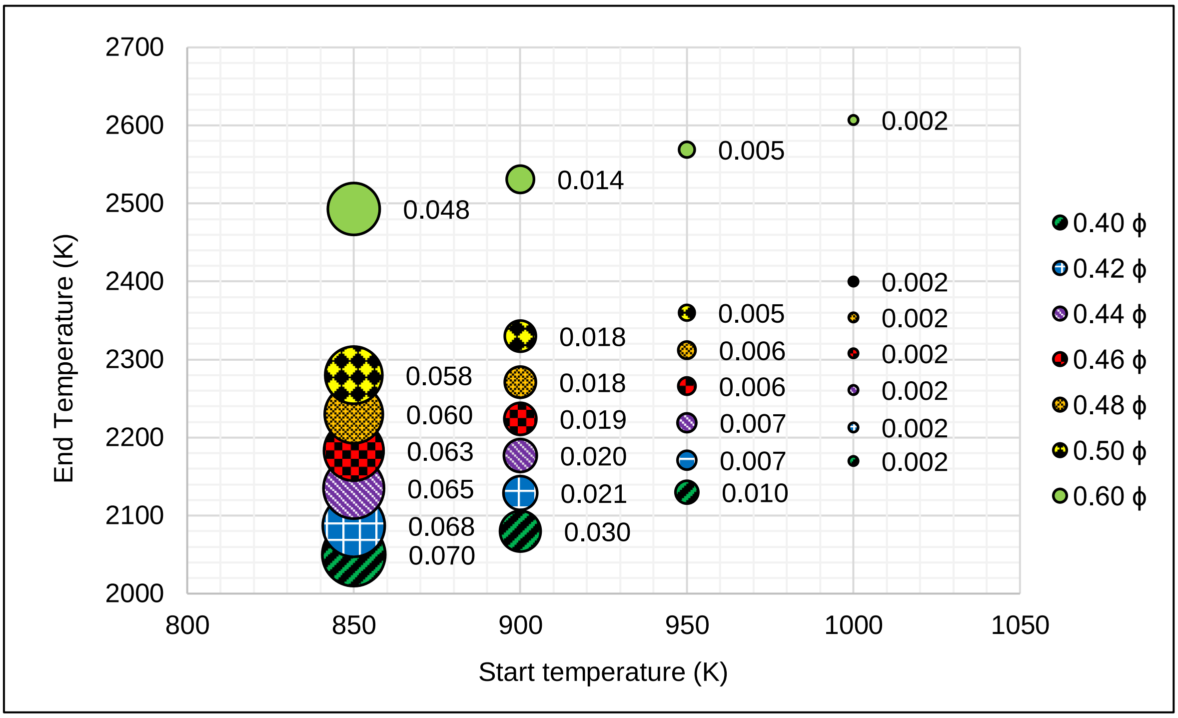

Figure 3.2 End Temperature & reaction times for a range of equivalence ratios & start temperature for decane, with reaction times displayed by the size of the circles and given in the data label in seconds.

Reaction rates are important to consider due to the effects in a real reciprocating expander where there will be a limited window in which the reaction can occur in both time and space. With a lower reaction rate engine speed will play a primary role in time available, followed by piston motion and combustion chamber topology. At 1700 RPM a ~2ms represents a window of 20 CAD.

Ignition systems that do not rely on autoignition for primary ignition is a potential pathway to eliminate this as an issue to utilise fuels with a high autoignition temperature and low start of combustion temperature.

3.4 Adiabatic Flame Temperature & Dilution

Utilising the aforementioned Equations (1) to (8) it is possible to create a simple thermochemical model of adiabatic flame temperatures for an idealised combustion reaction. In the simple adiabatic flame model that will be presented dodecane is utilised as the fuel, and the mixture of reactants, products, and temperature field are assumed to be homogeneous. The ideal dodecane reaction is used as the governing equation for this analysis. This is not a highly detailed chemical model, such as the previously discussed PSR model, as the model only utilises 5 species. However, this model displays the response and trends of the adiabatic flame temperature for the ideal dodecane reaction over a range of dilution, fuel, and temperature conditions simply in a 0D scenario with no timescale.

Four combinations of oxygen concentration and initial temperature were considered. The analysis was run from rich to lean regions. It is assumed in all regions that the chemical reaction is 100% complete dependant on the limiting reactant, i.e., fuel limited in the lean region and oxygen limited in the rich region.

A temperature of 478K was selected as the lower limit for starting temperature, as this is the approximate autoignition temperature of dodecane, and therefore the lowest conceivable temperature at which a reaction could take place without some form of ignition aid for an idealised homogenous mixture. Oxygen concentrations of 21% and 18% by volume were assumed as representative of an engine running without any charge air dilution and an engine with modest dilution – equivalent to approximately 14% exhaust gas recirculation (EGR) by volume. Much higher dilution rates have been proposed [93] but these were not considered due to the impact of high dilution on pumping losses, and hence efficiency, and safe operating procedures with depleted oxygen levels in air for experimental testing. The model assumes dilution is performed by an increase in the balance of nitrogen, this enables simple calculations but does not account for changes such as specific heat capacity ratio of using EGR or other gases as diluents.

The adiabatic model described is shown in Figure 3.3. It is evident from Figure 3.3 that the start temperature plays a major role in the adiabatic flame temperature, with a low start temperature allowing a higher equivalence ratio to be utilised. The greatest difference in flame temperature is at the stoichiometric ratio due to initial temperature and dilution becoming the dominant factors at these conditions as they are not energy limited, as they are at equivalency ratios lower and higher than 1. With higher amounts of energy from combustion more energy is absorbed by the increased fuel or nitrogen quantities compared to at stoichiometric. Dilution and equivalence ratio are also useful tools for achieving low flame temperature. These will be especially key variables to control in the case of fuels with high autoignition temperatures, such as methane and hydrogen.

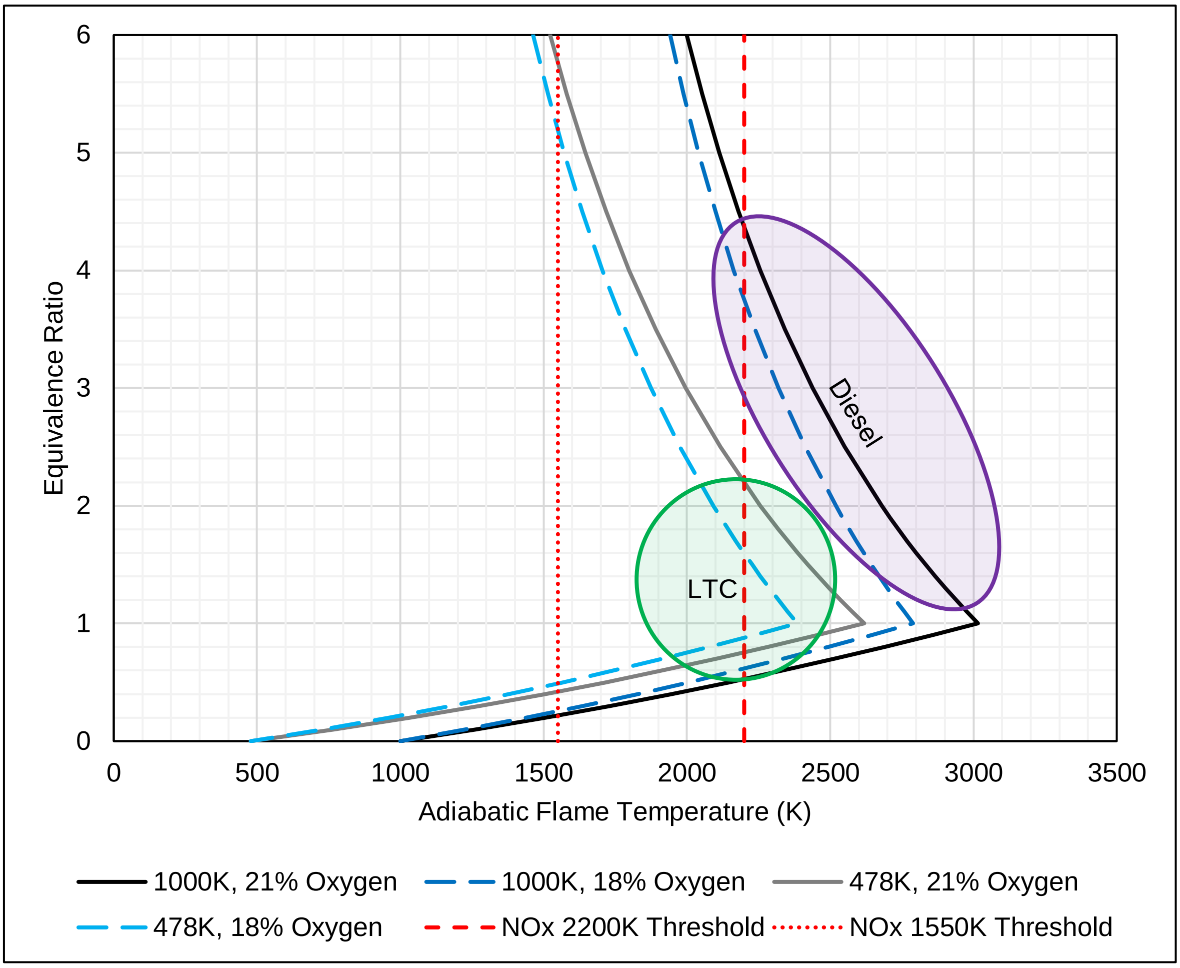

Figure 3.3 Adiabatic flame temperature for an idealised dodecane reaction at start temperatures of 478K & 1,000K and air concentrations of 18% & 21% oxygen by volume.

Similar figures to that of Figure 3.3 have been reported in the past, but they have not presented the changes in adiabatic temperature caused by changes in oxygen levels in the precombustion gas and initial temperature, instead primarily looking at the effects of EGR.

3.5 Efficiency

3.5.1 Introduction

The main methods for reducing energy consumption, and therefore increasing fuel efficiency, for any vehicle are to reduce mass, inertia, aerodynamic drag, tyre friction and to increase the efficiency of the power conversion of the propulsion system. In an ICE vehicle, reducing the energy consumption reduces the amount of carbon dioxide produced per unit of distance, as well as reducing running cost. When analysing the efficiency losses of modern ICE's, it is clear to see that efficiency has become a bottleneck. Increasing the thermodynamic efficiency of an ICE vehicle effects more than just the propulsion system efficiency. As a smaller amount of fuel is required for a task, the mass and size of the vehicle fuel tank can also be reduced for a given range.

3.5.2 Ideal Thermodynamic Efficiencies

3.5.2.1 Carnot and Curzon-Ahlborn

The Carnot efficiency demonstrates the theoretical maximum efficiency of a heat engine, but this theoretical upper limit of efficiency cannot be practically achieved. This is because the conditions of the Carnot efficiency are idealised and do not consider the finite time in which the cycle must exist. It also does not account for unavoidable losses that will be incurred in a real physical engine. However, the Carnot cycle efficiency remains a useful guide for evaluating how efficient an engine is or could be through potential improvement. Equation (14) displays the Carnot efficiency η_{Carnot}, where T_{CS} is the temperature of the cold sink, T_{HS} denotes the temperature of the hot sink, p_{CS} is the pressure of the cold sink, p_{HS} is the pressure of the hot sink, and γ is the heat capacity ratio of the working fluid.

$$\eta_{Carnot} = \frac{T_{HS} - T_{CS}}{T_{HS}} = 1 - \frac{T_{CS}}{T_{HS}} = 1 - \left(\frac{p_{CS}}{p_{HS}}\right)^{\frac{(\gamma-1)}{\gamma}} \qquad (14)$$

Two separate pairs of thermodynamicists, Curzon-Ahlborn and Chambadal-Novikov, discovered Equation (15) for a semi-ideal heat engine. Chambadal-Novikov implicitly discovering this relationship, while Curzon-Ahlborn later derived this relationship, hence the relationship has been generally attributed to Curzon-Ahlborn. Although it is commonly mistaken to be the upper limit of efficiency for practical heat engines, it is proven to be the thermodynamic efficiency of an endoreversible Carnot engine, which gives an thermodynamic efficiency at maximum power [157]. While the Carnot efficiency happens over an infinite amount of time, the Curzon-Ahlborn efficiency considers the finite-time period in which combustion takes place in a real engine. This extension or subset of thermodynamics is generally referred to as finite-time thermodynamics, which has gained interest in the literature at the end of the 20th century [158] but is still in its adolescence as a field of research. As an ideal heat engine is in theory most efficiency at maximum power, the Curzon-Ahlborn efficiency is another useful tool for assessing the theoretical and real efficiencies achievable with a heat engine.

$$\eta_{Curzon-Ahlborn} = 1 - \sqrt{\frac{T_{CS}}{T_{HS}}} = 1 - \sqrt{\left(\frac{p_{CS}}{p_{HS}}\right)^{\frac{(\gamma-1)}{\gamma}}} \tag{15}$$

Considering the maximum temperature imposed by NO_x formation a future heat engine cannot operate at temperatures higher than 2,200K. To understand the impact a temperature limitation would have on efficiency, a plot of Carnot and Curzon-Ahlborn efficiencies over a range of hot source temperatures and a set ambient temperature of 293.15K is shown in Figure 3.4.

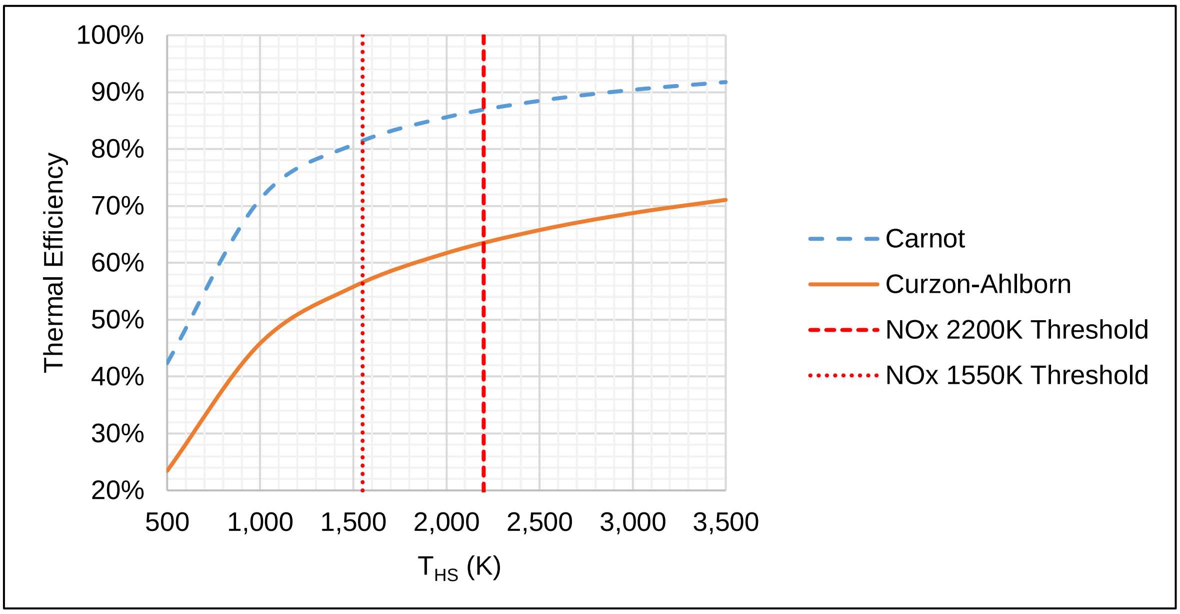

Figure 3.4 Thermal Efficiency for T_{CS} *= 293.15K while varying* T_{HS}*.*

The reverse is also performed, with the set limitation of 2,200K for the hot source temperature and a range of ambient air temperatures on Earth (-60°C to +60°C). A fundamental understanding of the efficiency limits of a low to zero NO_x emissions engine can then be realised, as shown in Figure 3.5. Using the hottest ambient cold sink temperatures present in the world (+60°C) and NO_x threshold hot sink temperature (2,200K) the Curzon-Ahlborn efficiency is 61%, as shown in Figure 3.5. Higher efficiencies are achievable with lower 2,200K is used as the hot sink temperature in the Figure 3.5 as this is where NO_x formation begins to increase exponentially, therefore keeping below this temperature is critical to reduce NO_x emissions. The aim of future low toxic emissions ICEs must be to achieve at least 61% efficiency.

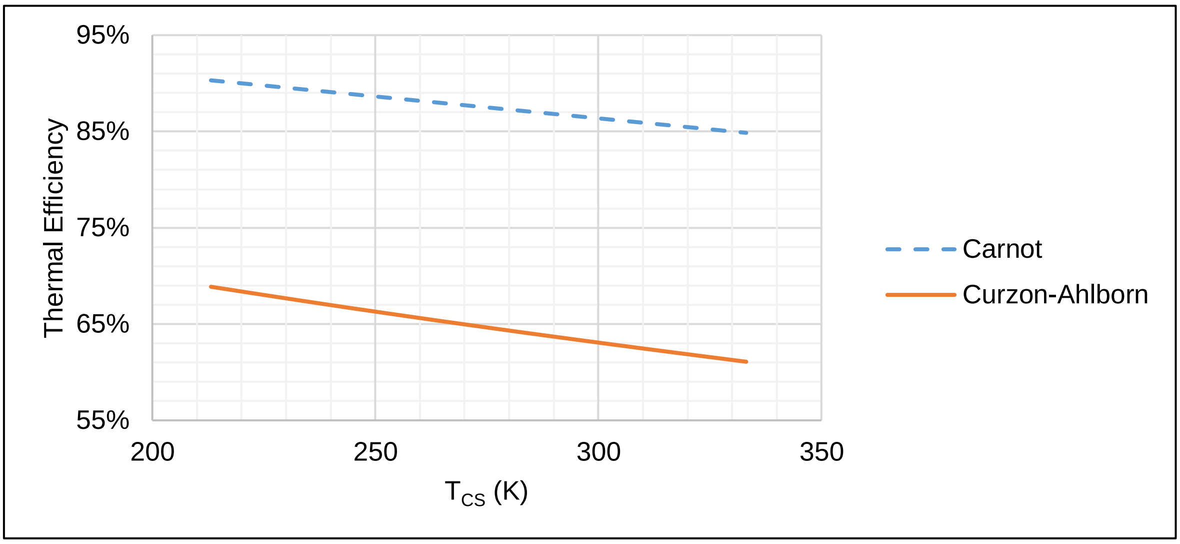

Figure 3.5 Thermal Efficiency for T_{HS} = 2,200K while varying T_{CS}

For an ICE to produce zero NO_x emissions the temperature across the whole of the combustion event must not exceed the formation temperature of NO_2 of approximately 1,550K. This would decrease the maximum theoretical efficiency compared to that of reduced toxic emissions engine, but still shows promise with a Curzon-Ahlborn efficiency of 57% at an ambient air temperature of 293.15K, as shown in Figure 3.4. If the heat sink temperature can be further decreased from ambient air temperatures, there is the potential for efficiencies greater than 60% with zero NO_x production. Alternative heat rejection pathways utilising substances with lower than ambient temperatures could be potential method to increase efficiencies beyond this point.

Equation (16) denotes the formula for pressure ratio. Figure 3.6 displays the Carnot and Curzon-Ahlborn efficiencies against pressure ratio for air (γ = 1.4), utilising the previous discussed Equations (14) and (15). As shown in Figure 3.6, to achieve 57% Curzon-Ahlborn efficiency with air would require a high-pressure ratio of 340 or higher between the hot source and cold sink. Alternatively, a working fluid with a higher ratio of specific heat capacity could reduce the pressure ratio required, but this would require a closed system and potentially a system able to introduce oxygen at much higher concentrations than that of air.

$$Pressure\ Ratio = \frac{p_H}{p_C} \tag{16}$$

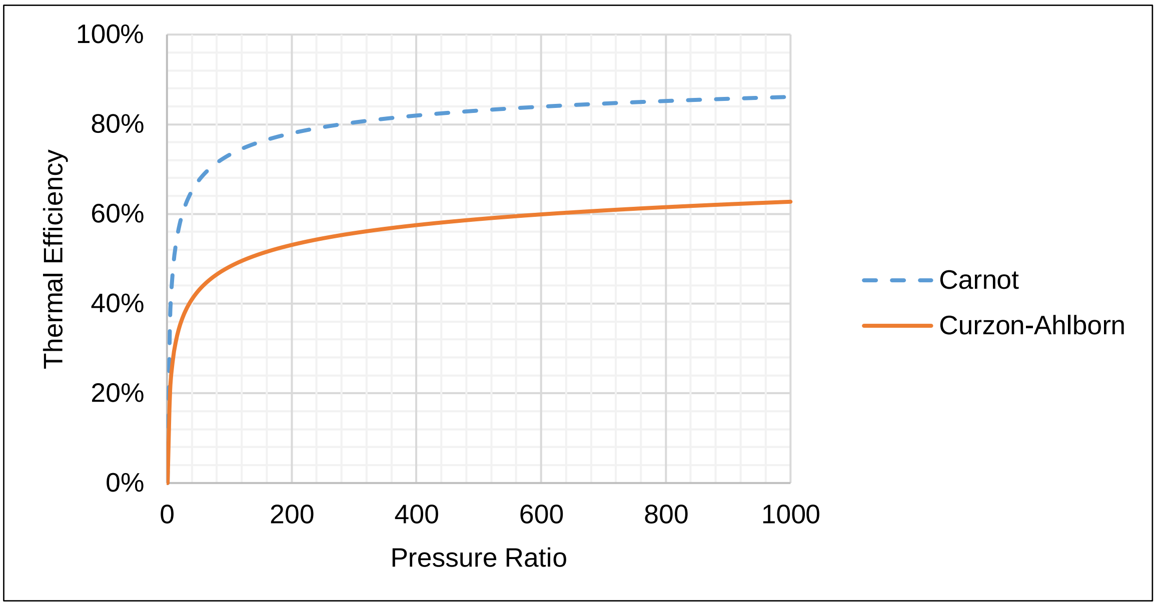

Figure 3.6 Thermal efficiencies vs pressure ratio, utilising air for Curzon-Ahlborn efficiency.

3.5.2.2 Conventional Cycles: Otto, Diesel, & Atkinson

The conventional four stroke thermodynamic cycles have endured the last century. However, there is now a question around whether their fundamental and practical thermal efficiency limitations have been or are close to being achieved. In all cycles compression ratio (CR) and specific heat capacity ratio (γ) are the main variables which dictate ideal efficiency. Equation (17) denotes the formula for CR, where V_{BDC} the volume at bottom dead centre (BDC) and V_{TDC} is the volume at top dead centre (TDC). The corresponding thermal efficiency equations for the cycles are shown in Equations (18)-(20). For an Atkinson cycle, there are differing ratios for expansion and compression. The Atkinson cycle relies on valve timing to generate variations in the effective expansion ratio (ER) and CR of the working fluid.

$$Compression\ Ratio = \frac{V_{BDC}}{V_{TDC}} \tag{17}$$

$$\eta_{Otto} = 1 - \frac{1}{CR^{(\gamma-1)}} \tag{18}$$

$$\eta_{Diesel} = 1 - \left(\frac{1}{CR^{(\gamma-1)}}\right)\left(\frac{\alpha^{\gamma-1} - 1}{\gamma(\alpha - 1)}\right) \tag{19}$$

$$\eta_{Atkinson} = 1 - \frac{\gamma(ER - CR)}{ER^{\gamma} - CR^{\gamma}} \qquad (20)$$

In theory in all cycles by changing the CR, ER, and/or the working fluid, a higher thermal efficiency can be achieved, but this has practical limitations. The main practical CR limitations of reciprocating engine are the architecture, combustion technology, fuel composition, and friction.

The efficiencies of the thermodynamic cycles can be increased by moving away from using air as the working fluid to closed cycles with working fluids with higher specific heat capacity ratios than that of air, such as argon. Using argon as a working fluid is possible with hydrogen as a fuel, as water can be separated from the working fluid. Hydrocarbons could not be utilised as a fuel, as this would require carbon dioxide to be separated, which is currently not viable in vehicles. In an Otto or Atkinson cycle engine running argon, the maximum CR would still be governed by the autoignition temperature of the oxygen and fuel mixture. Necessitating a move to a more “diesel like” combustion system and cycle with direct fuel injection.

A comparison of ideal thermodynamic efficiencies for the Otto, Diesel, and Miller/Atkinson cycle utilising both air and argon as working fluids is shown in Figure 3.7. Ratio of specific heat of air utilised is 1.4 and for argon is 1.66. For Diesel cycle the cut-off ratio (α) of 2 is utilised. For the Miller/Atkinson cycle, the expansion ratio (ER) is assumed to be 1.2 times greater than that of the CR. The Carnot and Curzon-Ahlborn efficiencies, with a source and sink temperatures of 2200K and 293.15K respectively, are overlaid for reference. A range of claimed efficiencies and CR are included for the Otto (Mercedes PU106C & Toyota M20A-FKS), Miller/Atkinson (Toyota 1NZ-FXE), and Diesel (BMW N47 2.0, Volvo D11-72S, &Wärtsilä RT-flex96C) cycle ICEs are shown in the figure. Due to turbocharging of modern ICEs, the Otto and Miller/Atkinson cycle ICEs are further limited below the gasoline knock limit of ~14. A CR of 13 is still a significant achievement with turbocharging, no consistent knock, or substantial low speed pre ignition. However, the premix air fuel combustion system utilised in the original Otto cycle limits any further gains in the thermodynamic cycle through increases in CR. Although the Otto and Miller/Atkinson cycle are more efficient for a given CR in the ideal thermodynamic cycle than the Diesel cycle, in reality diesel ICEs can realise higher efficiencies as they are not limited by the pre ignition and knock constraints of the fuel, as fuel is not premixed. This also allows for higher amounts of turbocharger work to be utilised and optimised accordingly, leading to generally higher efficiency diesel engines.

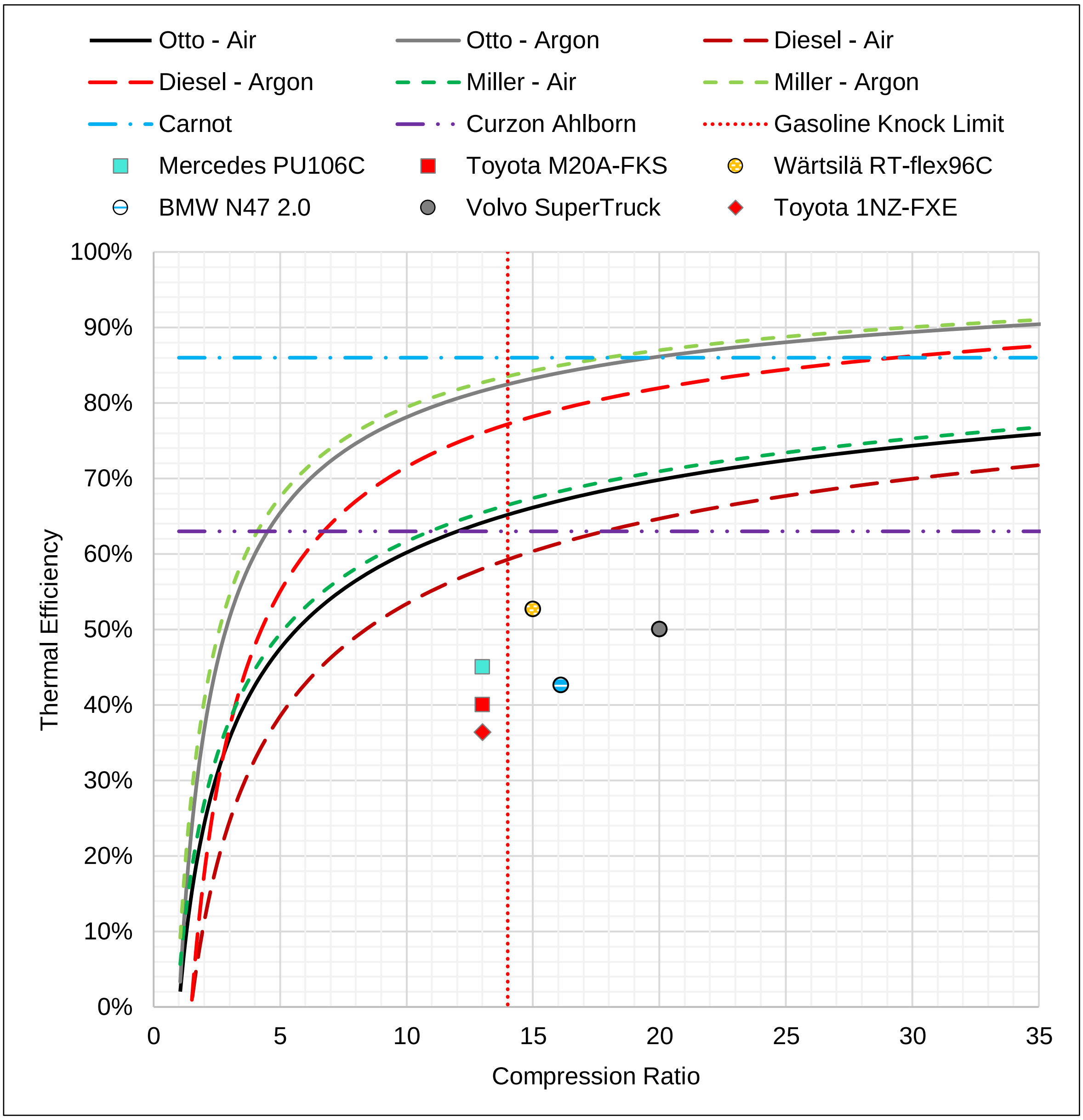

Figure 3.7 A comparison of the ideal thermodynamic efficiencies against compression ratio for the Otto, Diesel, and Miller/Atkinson cycle utilising air and argon as working fluids. With the inclusion of a range of ICE engines and Carnot and Curzon-Ahlborn efficiencies utilising 2100K and 293.15K.

This has led to the development of gasoline engines running more "Diesel like" cycles and combustion systems over the last couple of decades. Such as port and direct injection combustion systems being utilised in gasoline four stroke engines to increase efficiency. However, increasing CR comes with other issues, which will be discussed in the next section.

3.5.3 Losses

A set of equations that are required to calculate losses will be defined, as well as the definitions for MEP are defined in this section. A Sankey diagram illustrating and conversion of fuel energy to useful work is shown in Figure 3.8.

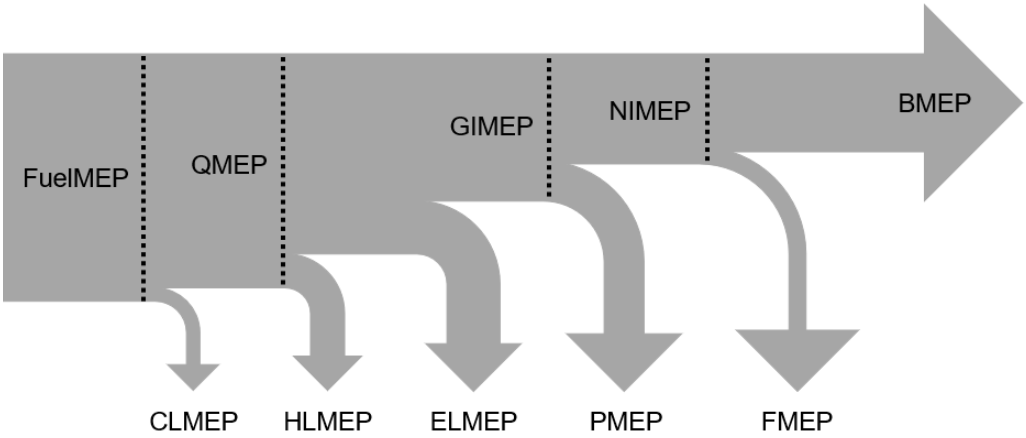

Figure 3.8 Sankey diagram of losses from fuel energy to work. The sizes of arrows are purely illustrative and not to scale.

To calculate the amount of fuel required and energy added to an ICE, the amount of mass of air, fuel and/or AFR must be known. In a reciprocating ICE, the mass of air m_a in the cylinder is dependent on the inlet air pressure p_{Ia}, inlet air temperature T_{Ia}, gas constant R, volumetric efficiency η_V and the in-cylinder volume at IVC V_{IVC}. This is shown in Equation (21).

$$m_a = \eta_V . \frac{V_{IVC} . p_{Ia}}{R . T_{Ia}} \tag{21}$$

This does not incorporate pulsations of the flow field or other phenomena which may reduce or increase the mass of air that is trapped in the cylinder at IVC. The mass of fuel m_f added to the system can then be calculated from the air mass and AFR, shown in Equation (22).

$$m_f = \frac{m_a}{AFR} \tag{22}$$

The energy of the fuel is then simply the mass of the fuel multiplied by the lower heating value of the fuel, shown in Equation (23). The amount of thermal energy Q_T released from the fuel to the system is the fuel energy multiplied by the combustion efficiency η_C, shown in Equation (24)

$$Q_f = m_f.LHV_f \tag{23}$$

$$Q_T = Q_f.\eta_C \tag{24}$$

Mean effective pressure (MEP) is defined as the rate of energy, typically per cycle, divided by the maximum displaced volume. This allows for evaluation of performance of the engine independent of engine displacement. The generally equation for MEP is shown in Equation (25), with specific MEP equations relevant to this piece of work shown in Equations (26)-(28). Where GIMEP is the gross indicated MEP, and QMEP is the thermal energy MEP, FuelMEP is the fuel MEP.

$$MEP = \frac{\dot{W}}{V_d} = \frac{\dot{Q}}{V_d} \tag{25}$$

$$GIMEP = \frac{\dot{W}_G}{V_d} \tag{26}$$

$$QMEP = \frac{\dot{Q}_T}{V_d} \tag{27}$$

$$FuelMEP = \frac{\dot{Q}_f}{V_d} \tag{28}$$

Thermal efficiency η_T is defined as the effectiveness of turning thermal energy Q_T into work, this is defined in Equation (29).

$$\eta_T = \frac{W_G}{Q_T} = \frac{GIMEP}{QMEP} \tag{29}$$

Combustion efficiency is defined as the effectiveness of turning the fuel energy available into thermal energy. This is shown in Equation (30).

$$\eta_C = \frac{Q_T}{Q_f} = \frac{Q_{AHR}}{Q_f} = \frac{QMEP}{FuelMEP} \tag{30}$$

Brake mean effective pressure (BMEP) is described in Equation (31), where $\dot{W}_b$ is the brake power.

$$BMEP = \frac{\dot{W}_b}{V_d} \tag{31}$$

Combustion losses mean effective pressure (CLMEP) is shown in Equation (32).

$$CLMEP = FuelMEP - QMEP = (1 - \eta_C).FuelMEP \tag{32}$$

Equation (33) describes heat transfer loss mean effective pressure (HLMEP), where Q_{ht} is the energy of heat loss.

$$HLMEP = \frac{\dot{Q_{ht}}}{V_d} \tag{33}$$

Exhaust loss mean effective pressure (ELMEP) is presented in Equation (34), where $\dot{Q_{exh}}$ is the rate of energy lost to the exhaust.

$$ELMEP = \frac{\dot{Q_{exh}}}{V_d} \tag{34}$$

Pumping loss mean effective pressure (PMEP) is shown in Equation (35).

$$PMEP = GIMEP - NIMEP \tag{35}$$

Friction loss mean effective pressure (FMEP) is defined is Equation (36).

$$FMEP = NIMEP - BMEP \tag{36}$$

Efficiencies and partial efficiencies are described in this section. Equation (37) demonstrates the gas exchange efficiency η_{GE}.

$$\eta_{GE} = \frac{NIMEP}{GIMEP} = 1 - \frac{PMEP}{GIMEP} \tag{37}$$

Mechanical efficiency η_M is defined in Equation (38).

$$\eta_M = \frac{BMEP}{NIMEP} = 1 - \frac{FMEP}{NIMEP} \tag{38}$$

The equation for brake efficiency is shown in Equation (39).

$$\eta_B = \frac{BMEP}{FuelMEP} = \frac{\dot{W}}{\dot{m}_f . Q_{LHV}} = \eta_C . \eta_T . \eta_{GE} . \eta_M \tag{39}$$

3.5.4 Compression Ratio Limits

Due to high CR leading to high cylinder pressures, the CR in conventional thermodynamic cycles are limited by knock, friction, heat losses, maximum cylinder pressure, or a combination of these factors. As the temperature of the working fluid and fuel mixture is ultimately governed by the CR, the CR is limited by the auto-ignition temperature of the fuel, concentration of oxygen in the mixture, cylinder pressure, and cylinder temperature. However, the Diesel cycle is not constrained by autoignition temperature of the fuel, as the fuel is direct injected around TDC. The real efficiency of the Diesel cycle is limited by other constraints, such as heat, pumping, and friction losses.

Several general models have been proposed for predicting and evaluating the friction and FMEP for an ICE to differing levels of detail. Such as those by Chen et al [159], Sandoval et al [160] , and Rezeka et al [161]. There is agreement that load/cylinder pressure and piston speed are the main influencing factors, with oil viscosity and temperature also of interest in detailed models.

The Chen & Flynn model for friction describes friction as an almost linear relationship with maximum cylinder pressure and mean piston speed [159]. The Chen & Flynn model predicts the FMEP for a reciprocating engine in bar. The formula is shown in Equation (40), where p_{mc} is the maximum cylinder pressure. A, B, C, and D, denote constants for the model and S_f is the engine speed factor, denoted in Equation (41).

$$FMEP_{Chen\,\&\,Flynn} = A_c + B_c . p_{mc} + C_c . S_f + D_c . {S_f}^2 \tag{40}$$

$$S_f = \frac{\omega . s_s}{2} \tag{41}$$

With the correct optimisation of constants, the model has been shown to be accurate when compared to real engines [162]. Without optimisation of the constants, there is low accuracy compared to other models. Due to assumptions of constants which inevitably vary with engine architecture. However, it is still currently widely used due to its simplicity and generalisation. A higher order detailed model was not chosen for this piece of evaluation as the aim was not to produce accurate predictions for a given ICE, but to evaluate issues with ever increasing compression ratios and cylinder pressure. Several initial constants have been used for the values of A, B, C and D. For the calculations in this work values of $A = 0.4$, $B = 0.005$, $C = 0.09$ and $D = 0.000085$ were utilised.

To calculate FMEP the maximum cylinder pressure must be known. To calculate the change in pressure from compression, the initial pressure, specific heat capacity and CR must be known. The equation for isentropic expansion is shown in Equation (42), where γ is the ratio of specific heat capacity. This forms the basis of the ideal gas equation, shown in Equation (43), where T is the temperature.

$$p.V^{\gamma} = Constant \tag{42}$$

$$\frac{p_j}{p_i} = \left(\frac{V_i}{V_j}\right)^{\gamma} = \left(\frac{T_i}{T_j}\right)^{\frac{\gamma}{\gamma-1}} \tag{43}$$

The change in pressure in the cylinder is equal to the calculated the change in pressure due to the change in volume Δp_V and other pressure changes Δp_C. In a conventional engine, this would be pressure due to combustion. This is shown in Equation (44) from Heywood [163, p. 385]. If there is no combustion, Equation (45) can be utilised. If there is combustion, Equation (46) can be utilised. These are rearrangements of the ideal gas Equations shown in (42) and (43) substituted into Equation (44).

$$\Delta p = \Delta p_V + \Delta p_C \tag{44}$$

$$\Delta p_V = p_j - p_i = p_i.\left(\left(\frac{V_i}{V_j}\right)^{\gamma} - 1\right) \tag{45}$$

$$\Delta p_C = p_j.\left(\frac{V_j}{V_i}\right)^{\gamma} - p_i. \tag{46}$$

Calculation of heat release from Heywood [163, p. 388], without crevices and heat transfer calculations, is shown in Equation (47).

$$\frac{dQ}{d\theta} = \frac{\gamma}{\gamma - 1}.p_j.\frac{V_j - V_i}{d\theta} + \frac{V_j}{\gamma - 1}.\frac{p_j - p_i}{d\theta} \tag{47}$$

Over a constant and known difference in crank angle or volume, Equation (47) can be rearranged to calculate the pressure after energy is added to a system. This is shown in Equation (48).

$$p_j = \frac{dQ.(\gamma - 1) + p_i.V_j}{(V_j - V_i).\gamma + V_j} \tag{48}$$

With a known inlet pressure, energy addition from the fuel, and compression ratio, the maximum cylinder pressure can then be calculated from Equation (48) and the energy Equations (21)-(30) from Section 3.2.1. This maximum cylinder pressure will be idealised, as it will be assumed that all the energy is released instantaneously at TDC.

The Equation for Q can be substituted into Equation (48) to produce Equation (49) to calculate the maximum theoretically possible cylinder pressure, p_{mc}, with no losses and instantaneous heat addition. Volumetric and efficiency assumed to be 100% in this instance. R is the universal gas constant with the value of 287J/kgK used in this piece of work.

$$p_{mc} = \frac{\left(\frac{\eta_C.\eta_V.p_i.LHV_f.CR}{R.T_i.AFR}\right).(\gamma - 1) + p_i}{(1 - CR).\gamma + 1} \tag{49}$$

This calculated ideal maximum cylinder pressure can then be used to calculate friction for a given set of conditions using Equation (40).

3.5.5 Comparison of Ideal Efficiency

Figure 3.9 displays a comparison of the ideal thermodynamic efficiencies of the Otto, Diesel, Atkinson, ORC, and RSCE cycles. The thermodynamic efficiencies of the Otto, Diesel, and Atkinson cycle are shown for air and argon as working fluids. The ORC and RSCE cycle are only shown utilising air. For the Otto, Diesel, and Atkinson cycles the same variables are utilised as Figure 3.7. The RSCE efficiency is the ideal efficiency by Dong et al [2] shown in Figure 2.43. With a recuperator effectiveness of 80% and where CR and ER are equal.

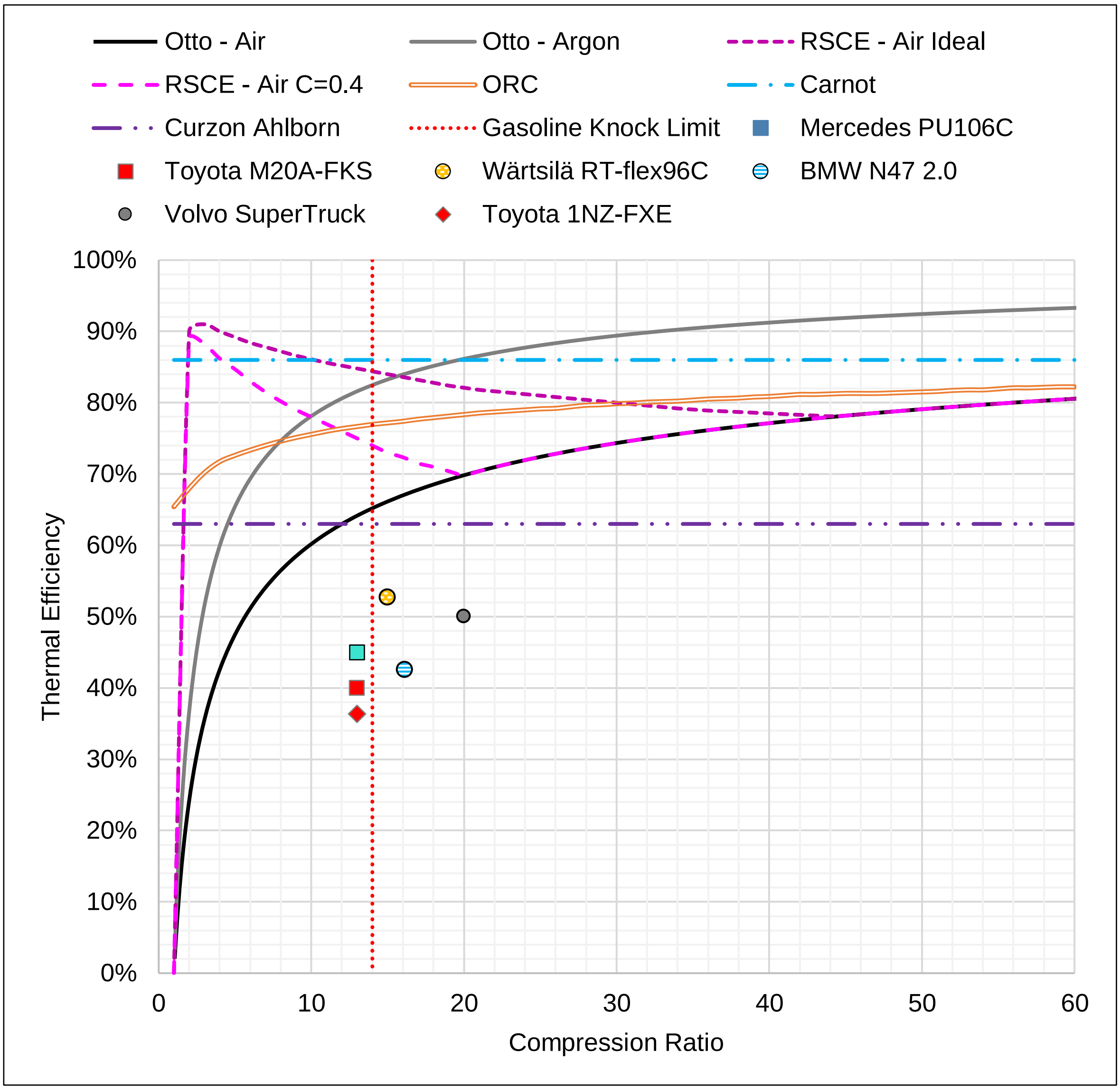

Figure 3.9 Efficiencies of Conventional Cycles, RSCE, ORC, & Real Engines

The RSCE trends towards the Otto efficiency as the recuperator becomes less efficient with lower expansion cylinder out temperatures. The capability for the RSCE thermodynamic cycles to produce high efficiency at low CR is of huge benefit, as the losses incurred for high CR are avoided. This allows the RSCE to achieve not only high thermodynamic efficiency but low heat and friction losses at low CR. There is further potential for higher efficiency with unequal values of CR and ER.

3.6 Discussion

Based on the literature and analysis in this Chapter, the efficiencies of conventional ICE thermodynamic cycles are approaching the practical limits of efficiency even without the constraints of achieving low NO_x emissions. There are likely to be small incremental improvements that can be made, but these are unlikely to give the improvement required to reach ultra-high efficiencies of greater than 60%, at the same time as achieving a reduction in toxic emissions. However, the Curzon-Ahlborn efficiency suggests 61% is possible and therefore there is merit in considering alternative approaches.

Chapter 4 Understanding the RSCE Expander Thermodynamic cycle Efficiency

The thermodynamic cycle, efficiency metrics, and behaviour of an isolated RSCE expander through theory, analysis, and a 0D model.

4.1 Introduction

Before discussing experimentation, it is important to understand the thermodynamic cycle of a RSCE expander. This section will present and explain theory on the thermodynamic efficiency of the RSCE expander and a simple 0D thermodynamic model that was used to understand, investigate, and predict some of the responses of an ideal and quasi-real RSCE expander. Sensitivity studies of the effect of variables, and a study of optimising the Titan expander, will be presented at the end of the chapter.

4.2 A Carnot Efficiency Analysis

This section will differ in analysis to the emissions limited efficiency analysis, as the analysis and discussion will centre on the practical implementation of the cycle and expander. This work builds upon ideas and work that Dong et al presented in their analysis of the and formula for calculating the efficiency of the split cycle engine [2].

There will be two brief Carnot efficiency theoretical analyses of the expander presented, one of the system and one on the expander in isolation. The Carnot efficiency is previously shown in Equation (14). A Carnot upper limit for efficiency dictated by NO_x formation temperature is discussed in Section 3.5.2.1. However, this section discusses the theory on how the expander and the RSCE achieve higher efficiency.

4.2.1 The RSCE System

It is pertinent to revisit the temperature entropy diagram, also known as a T-S diagram, for the RSCE cycle which was briefly discussed in Section 2.7.7. A version created and annotated by the author is shown in Figure 4.1. In the Figure, line a is the quasi-isothermal compression, b is the recuperation, c is the combustion, d is the expansion, and e is the exhaust. The grey dotted lines illustrate the ideal isothermal compression and the ideal heat recuperation from the exhaust.

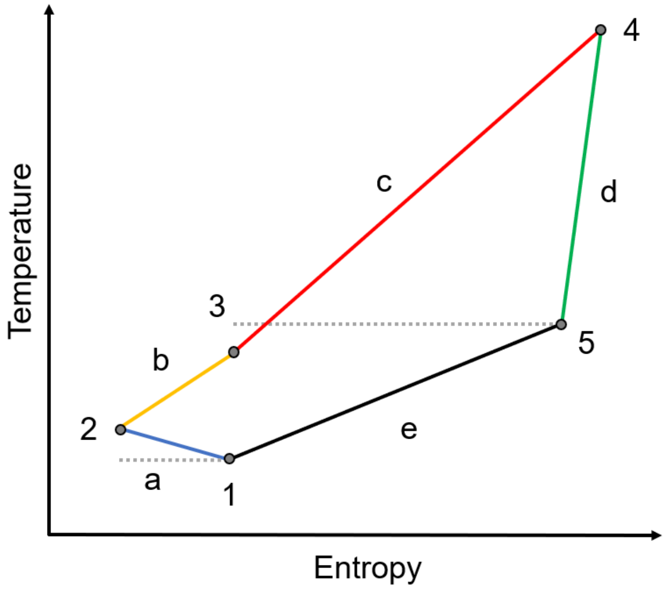

Figure 4.1 Temperature entropy (T-S) diagram of the RSCE (not to scale) annotated with points, steps, and ideals.

The factor that was not discussed in Dong et al’s work, is the interlinking of heat at point 3 in Figure 4.1 and the addition of heat energy from the fuel. As temperature dictates the charge air density and air mass at the start of combustion, there is a direct correlation with air temperature and potential heat addition from the fuel at the start of combustion. Therefore, as the recuperator becomes more efficient, or the exhaust becomes hotter, increasing the temperature of point 3, less energy can be added to the expander, for a given equivalence ratio, pressure, combustion volume, and combustion efficiency. This is shown in Equations (50)-(52).

$$T_4 = T_3 + \frac{Q_T}{c} \tag{50}$$

$$Q_T = \frac{p_3 . V_C . \eta_V . LHV_f . \eta_C}{R . T_3 . AFR} \tag{51}$$

$$T_4 = T_3 + \frac{p_3 . V_C . \eta_V . LHV_f . \eta_C . c}{R . T_3 . AFR} \tag{52}$$

This means as point 3 increases in temperature, the temperature difference provided by heat energy from the fuel must decrease the temperature difference of section c and the temperature of point 4. This can be mitigated through more ideal quasi-isothermal compression, allowing more heat energy to be captured. However, after a certain point increasing recuperator effectiveness will have a negative effect on expander efficiency, as less temperature difference can be realised in the expander.

As the expander ultimately adds fuel energy to the system, there is questionable benefit in increasing temperature higher than necessary to achieve stable, complete, and fast combustion, for a given pressure. Once this has been achieved, increasing recuperator effectiveness or temperature will have a negative effect on efficiency.

It is important to remember that the Carnot efficiency is the difference in temperature between the hot and cold source/sink divided by the hot source temperature. Therefore, if you can maintain the same difference in temperature with a lower hot source temperature, it is possible to achieve a higher efficiency. However, if there is a smaller difference in temperature with the same or lower hot source temperature, the efficiency will decrease.

4.2.2 The Expander in Isolation

When considering the expander in isolation, the only steps and points that need to be considered from Figure 4.1 are points 3-5 and steps c & d. For the purpose of evaluating the expander in isolation, it can be assumed that the recuperator is acting ideal. Therefore, the temperature at points 3 and 5 are equal. The temperature at point 4, T_4, is equal to the temperature at point 3, T_3, plus the heat energy added from the combustion of the fuel Q_C. This is shown in Equation (50). A Carnot analysis for the expander in isolation can then be written by substituting Equation (51) into (53) to create Equation (54).

$$\eta_{Carnot} = \frac{T_4 - T_3}{T_4} \tag{53}$$

$$\eta_{Carnot} = \frac{Q_T}{T_3 + Q_T} = \frac{Q_T}{T_4} = \frac{\left(\frac{p_3.V_C.\eta_V.LHV_f.\eta_C.c}{R.T_3.AFR}\right)}{T_3 + \left(\frac{p_3.V_C.\eta_V.LHV_f.\eta_C.c}{R.T_3.AFR}\right)} \tag{54}$$

Equation (54) demonstrates that to maximise thermal efficiency in the expander, the highest amount of Q needs to be added to the expander to create the largest difference in temperature and the peak temperature needs to be reduced. Operating cold to increase thermal efficiency is unintuitive compared to conventional heat engine thinking, as typically higher heat returns higher efficiency. However, as the source of the initial temperature and heat is provided from the expander and the expander adds fuel energy to the RSCE system, this is not the case for the RSCE expander.

This is a great characteristic for the RSCE, as NO_x emissions should in theory fall, and efficiency should increase with a low start of combustion temperature. Operating colder T_3 temperatures should allow for greater Q and reduce T_4, although the increase in Q could offset the reduction in T_4 temperature caused by reducing T_3. Until combustion can no longer ignite or does not react fast enough. Q can be greater with reducing T_3 by increasing air density and mass in the combustion chamber. There are other potential benefits through running colder. Less heat loss due to lower temperature difference, and less requirements on material properties to withstand high temperatures.

4.3 Equations of Pressure, Work, Efficiency, & Ideal Gas

To calculate the work undertaken or generate by the system work must be calculated, this is shown in Equation (55). Where Work is represented by W, force F, distance s, pressure p, area A, and volume V.

$$W = F.s = p.A.s = p.dV \tag{55}$$

The expander gross work W_G per cycle is defined as the work created over the duration of 360-degree stroke. This is denoted as $\dot{W}_G$. As TDC is the referenced used for CAD in this piece of work, the integral is taken from -180 to 180 CAD ATDC. This expander gross work per cycle is defined in Equation (56).

$$\dot{W}_G = \int_{-180}^{180} p.dV \tag{56}$$

Equations (44)-(48) can be utilised to calculate Q and pressure from Section 3.5.4. However, as the change in pressure during the RSCE expansion cycle can be caused be the introduction of pressure by the intake valves, this is not true in the case of the RSCE expander. The same equations can still be used from Heywood [163, p. 385] to negate the effects of volume pressure change and decipher the change in pressure. While not including the parts of the Equation (47) for crevices reduces the accuracy of the model, this is considered accurate enough for the 0D model to evaluate the expander thermodynamic cycle. Without energy added to the system, Equation (48) can be utilised with dQ at 0, this produces Equation (57).

$$p_j = \frac{p_i.V_j}{(V_j - V_i).\gamma + V_j} \tag{57}$$

Alternatively, the ideal gas Equation can be used in no combustion cases, shown in Equation (58).

$$p_j = p_i.\left(\frac{V_i}{V_j}\right)^{\gamma} \tag{58}$$

Using Equation (47) apparent heat release (AHR) can be calculated with a known change in volume. However, as previously discussed in Section 4.3, there are difficulties in this approach in the expander in a RSCE. As a change in pressure can be caused by either combustion or IVO. For this reason, to calculate the AHR from combustion, an estimate must be made of when SOC begins so as not to include the energy change caused by IVO. AHR is defined in Equation (59) between the CAD for the SOC, and the end of the cycle. Where AHR per cycle is $\dot{Q}_{AHR}$ and θ_{SOC} is the SOC in CAD.

$$\dot{Q}_{AHR} = \sum_{\theta_{SOC}}^{180} \frac{dQ}{d\theta} \tag{59}$$

The rate of thermal energy released is defined as the total thermal energy released by the fuel over the duration of combustion (DOC) in CAD and the resolution of the model. This is shown in Equation (60), where θ_{DOC} is the DOC in CAD and h_θ is the number of steps per CAD in the model.

$$dQ_T = \frac{Q_T}{\theta_{DOC}.h_\theta} \tag{60}$$

This is an averaged heat release approach which does not capture the reality of true heat release and mass fractioned burner of fuel, which has a gradual build up to the fastest heat release before trailing off. However, this is deemed good enough for the model. For the model and studies presented in this piece of work, h_θ will be set at 1 per CAD, this provides adequate resolution for interrogation.

4.4 Model States & Assumptions

Using the equations from the previous sections and setting a crank angle of -180 to 180 degrees as an input, a 0D thermodynamic model of the expander can be created. The states of the model can be split down into three main scenarios or sections:

1. If the exhaust valves are open, in-cylinder pressure is equal to the exhaust pressure.

It is imagined that the exhaust is an infinite volume where the pressure and temperature of the equalisation of the chambers results in the expansion cylinder equalling the set conditions of the exhaust manifold. This is an approximation and ideal process of what occurs. In reality, the cylinder pressure would fall at a rate dependant on valve and exhaust manifold design.

In the expander EVC can act as a method EGR control, trapping any remaining exhaust gas from the previous cycle in the chamber. In this model this is not considered. As long EVC is close to TDC and the intake manifold pressure is much greater than that of the exhaust pressure, the EGR effect will be small. Varying volumetric efficiency could be used as a method of adjusting or investigating the effect EGR would have, as this would in reduce the amount of air available for combustion.

2. If the intake valves are open, the in-cylinder pressure starts to fill by a defined pressure rise rate until achieving intake pressure, which is then held until IVC.

It is imagined that the exhaust is an infinite volume where the pressure and temperature of the equalisation of the chambers results in the expansion cylinder equalling the set conditions of the intake manifold. If start of combustion (SOC) occurs during the IVP, then it is assumed all pressure is absorbed into the inlet manifold, with no increase in pressure in-cylinder. This approximates the real the process which is considered good enough for this model.

In addition, and to make the model more realistic, a PRR due to the intake valves opening is defined in Equation (61). Where p_{IVO} is the in-cylinder pressure at IVO and θ_{DPRI} is the duration in CAD over which the filling occurs. This is not a real representation of the filling from intake manifold into the cylinder, which is dominated by pressure ratio, valve area, valve lift and other effects. However, it provides a simple and good enough approach for the model to examine the effects of increasing the PRR due to valve design quickly and easily.

$$PRR_I = \frac{p_{IVO} - p_{Ia}}{\theta_{DPRI}.h_\theta} \tag{61}$$

3. If all valves are closed, in-cylinder pressure is determined by the pressure of the previous state, movement of the piston and fuel energy added.

In this state the conditions and equations set out in this Chapter drive the model. The overall assumptions of the model are stated below:

- The system is adiabatic.
- Heat capacity ratio is assumed to be a constant value of 1.33.
- Heat release of the fuel is an average over a set number of CAD.
- At EVO until EVC, cylinder pressure instantaneously becomes the set exhaust pressure.
- At IVO, cylinder pressure instantaneously becomes another state.
- In cylinder pressure rise at IVO is defined by Equation (61).

- In cylinder pressure equals intake pressure from end of intake pressure rise until IVC.
- Heat transfer to cylinder walls is not accounted for.
- The effects of crevices inside the chamber and around the piston are not considered.
- The resolution or steps of the model, h_θ, are set a 1 step per CAD.

4.5 The Ideal Cycle

In an ideal expander, the entire upstroke from bottom dead centre (BDC) to top dead centre (TDC) would be dedicated to removing exhaust from the chamber and conditions in the chamber would equal the exhaust manifold conditions instantaneously. IVO, IVC and SOC would all occur at TDC and occur instantaneously. The volume would then begin expansion until EVO at BDC and the cycle repeats again. An ideal split cycle pressure trace created by the 0D model is shown in Figure 4.2. Due to the resolution of the model, IVO and combustion must each occur over 1 CAD, resulting in a slightly off vertical line. In essence and in practicality, the ideal cycle of the expander is the ideal cycle from the Otto cycle with the compression pressure removed and replaced with exhaust manifold pressure.

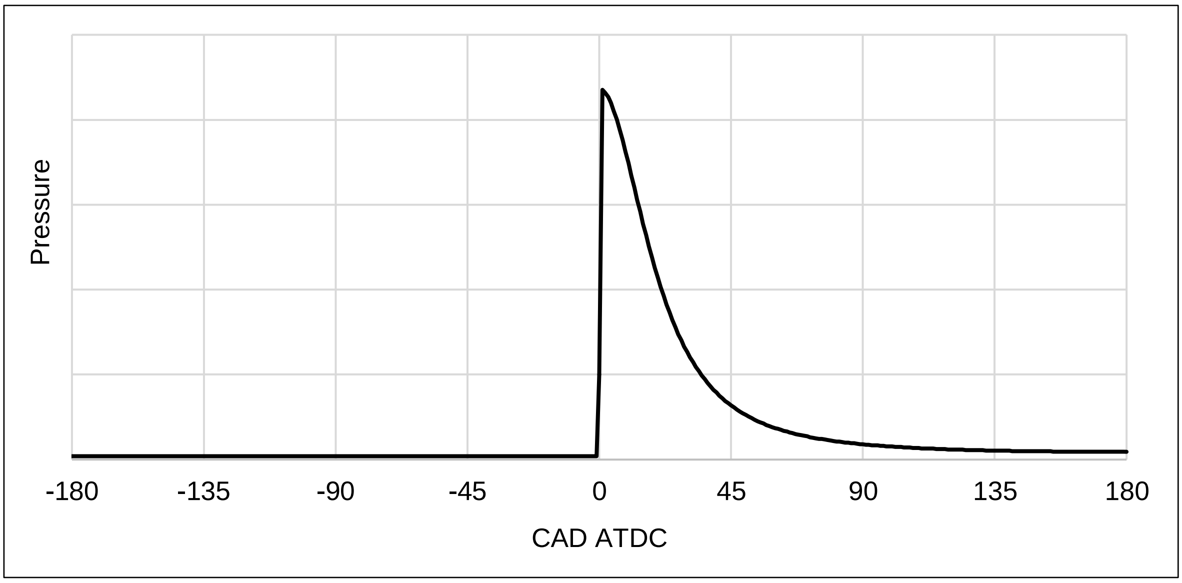

Figure 4.2 An ideal split cycle expander pressure trace.

The PV diagram of the ideal cycle is shown in Figure 4.3. It must be noted that for a RSCE expander to function correctly and provide adequate thermal energy and pressure to the exhaust and recuperator, the end pressure must be greater than the intake pressure to the compressor.

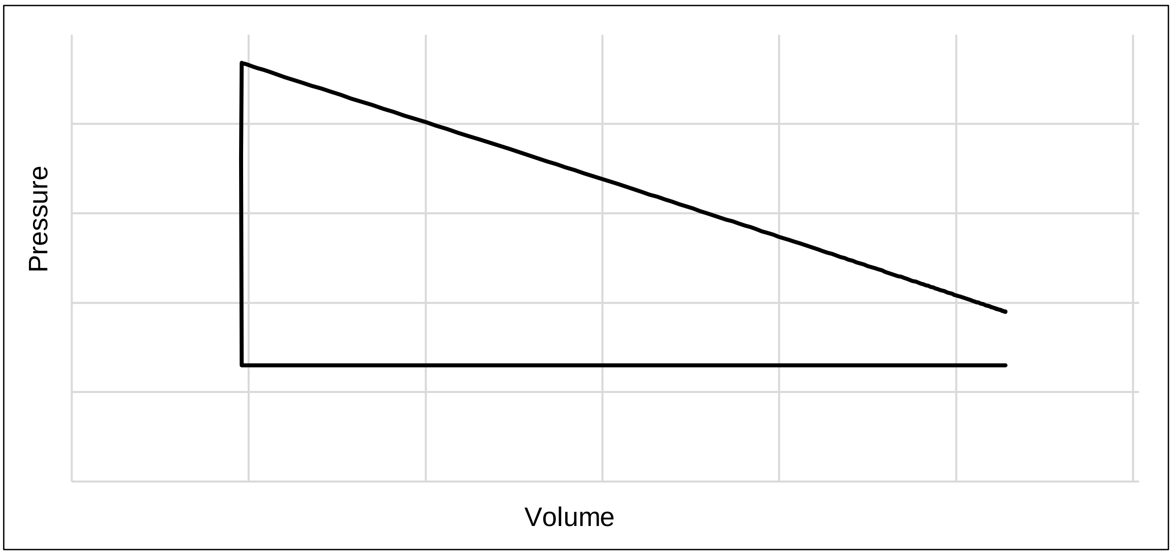

Figure 4.3 An ideal split cycle expander pressure volume diagram, with each axis in a logarithmic scale.

It is not possible to achieve the ideal cycle in the real world, due to the time constraints in which processes such as combustion, heat transfer and valve events must occur. However, in the RSCE there are additional barriers that are not typically considered. Notably it is not possible for instantaneous transfer of intake air. Therefore, there can be inherent disadvantages to valve setup in the expanders of SCE if they are forced to operate with IVO before TDC, as this will create negative torque on the engine by the recompression of previously compressed working fluid.

4.6 The Rankine Cycle Effect

Due to the addition of intake air at IVO, with isobaric conditions during the IVP, the expander in a DCE can be thought of as a Rankine cycle when no fuel is added. As IVP continues past TDC, the expander runs as a Rankine cycle. An ideal example of this is shown from the model in Figure 4.4. Where IVO is at TDC, IVP is set at 30 CAD, and no fuel is added to the system, creating an ideal Rankine cycle.

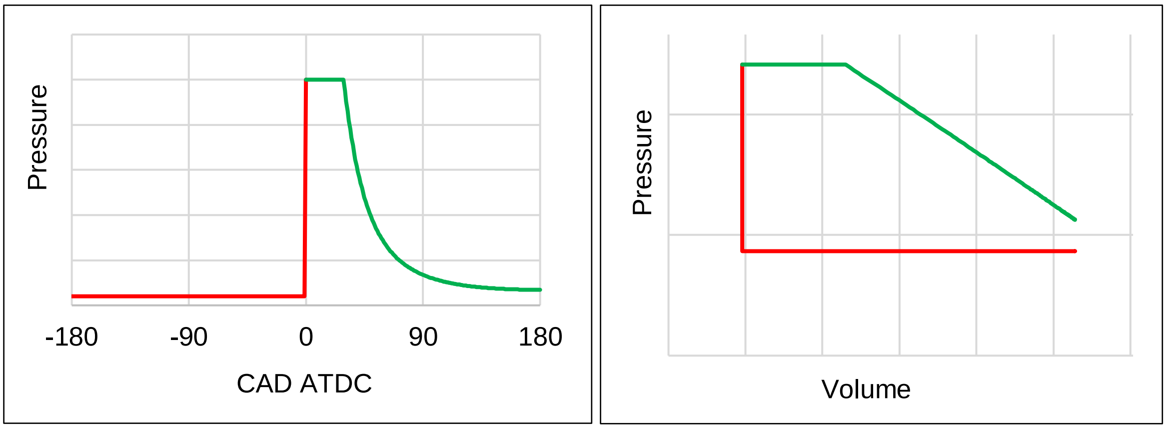

Figure 4.4 Ideal Rankine expander cycle.

Because of this Rankine cycle effect, the apparent thermodynamic efficiency of the expander to tend towards 100% efficiency as fuel added decreases, as work can be generated with no heat addition from fuel and work from the compressor is unaccounted for.

In an ideal conventional engine, the compression and expansion curves are identical. This allows for relatively simple calculation of the work created from combustion, as the compression and expansion work cancel out when the work is summated across the 360 CAD cycle. This is highlighted in Figure 4.5 where the model is utilised to create an ideal Otto cycle with compression, combustion, and Rankine pressure traces.

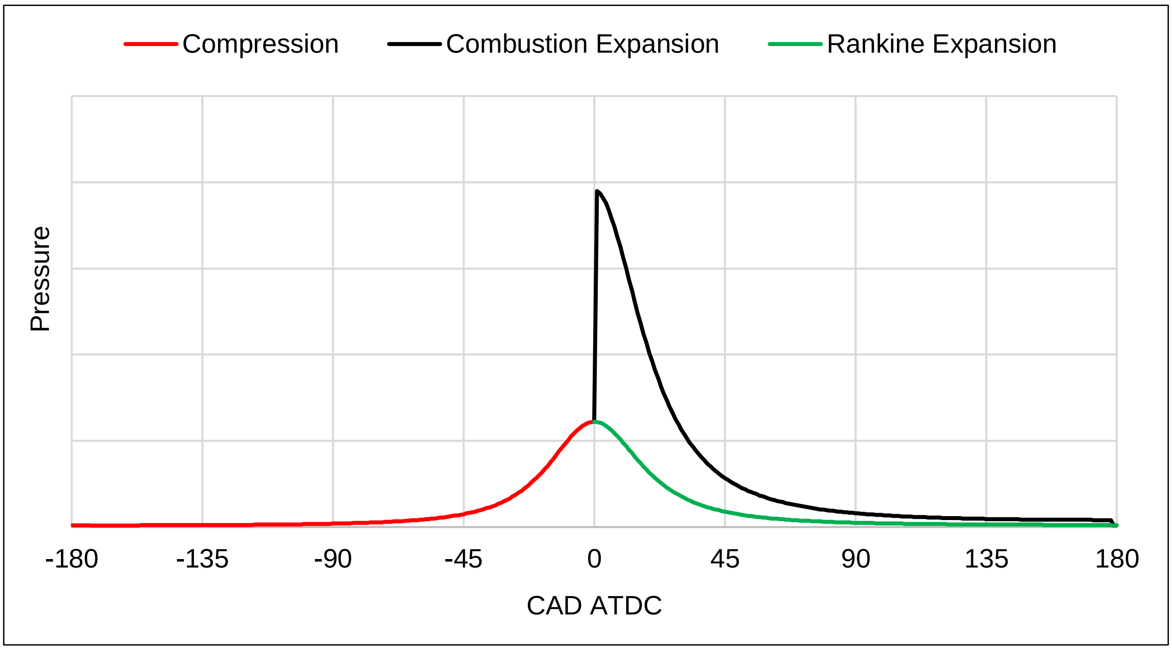

Figure 4.5 Ideal Otto cycle with compression, combustion and Rankine presssure traces.

It is not possible when evaluating the combustion work generated by the expander in isolation to not consider the difference in compression and expansion work, as the compression and expansion curves without fuel are always unequal. For this reason, when evaluating the expander in isolation of the compressor, another method must be used to access how well the expander is producing work from the fuel. Without a compression cylinder to realistically calculate net IMEP, a single metric will not be able to gauge the efficiency of the RSCE expander.

For the RSCE system to be as efficient as possible, compression work must be minimised, and recuperator effectiveness and expander efficiency must be maximised. However, as Rankine work goes up the combustion work will be reduced. Therefore, the goal for the expander is to create the most combustion work from the smallest Rankine work. For this reason, metrics to compare the isentropic expansion work that would occur with no fuel addition must be incorporated when analysing the expander in solitude with no compression cylinder to calculate combustion work. A method for doing this will be explained below and incorporated into the model.

The sections of the cycle can be split into the two areas of where negative and positive work are created, i.e., the recompression and expansion strokes of the expander. Therefore, the following equations are defined. In Equation (62) where $\dot{W}_{RC}$ is the work created during the recompression stroke.

$$\dot{W}_{RC} = \int_{-180}^{0} p.dV \tag{62}$$

With fuel and combustion, Equation (63) defines the work created during expansion of the combustion stroke. Referred to as combustion expansion work $\dot{W}_{CE}$.

$$\dot{W}_{CE} = \int_{0}^{180} p.dV \tag{63}$$

Equation (64) defines the work created during expansion with no fuel or combustion. Referred to as Rankine expansion work $\dot{W}_{RE}$

$$\dot{W}_{RE} = \int_{0}^{180} p.dV \tag{64}$$

The gross work from the expander is the summation of the recompression work W_{RC}, or combustion expansion work W_{CE}, this is shown in Equation (65). The gross Rankine work GRW is the summation of the recompression work and the Rankine expansion work W_{RE}, this is shown in Equation (66).

$$W_G = W_{RC} + W_{CE} \tag{65}$$

$$W_{GR} = W_{RC} + W_{RE} \tag{66}$$

In the same manner as Equation (44), the work created by combustion alone can be calculated from the change with and without combustion present. Therefore, work from combustion can be isolated. This can be calculated by removing the GRW from gross work of the expander. This is shown in Equation (67), where W_C is the combustion work.

$$W_C = W_G - W_{GR} = W_{CE} - W_{RE} \tag{67}$$

An ideal pressure trace of the expander with recompression, Rankine and combustion separated for the same case is shown in Figure 4.6.

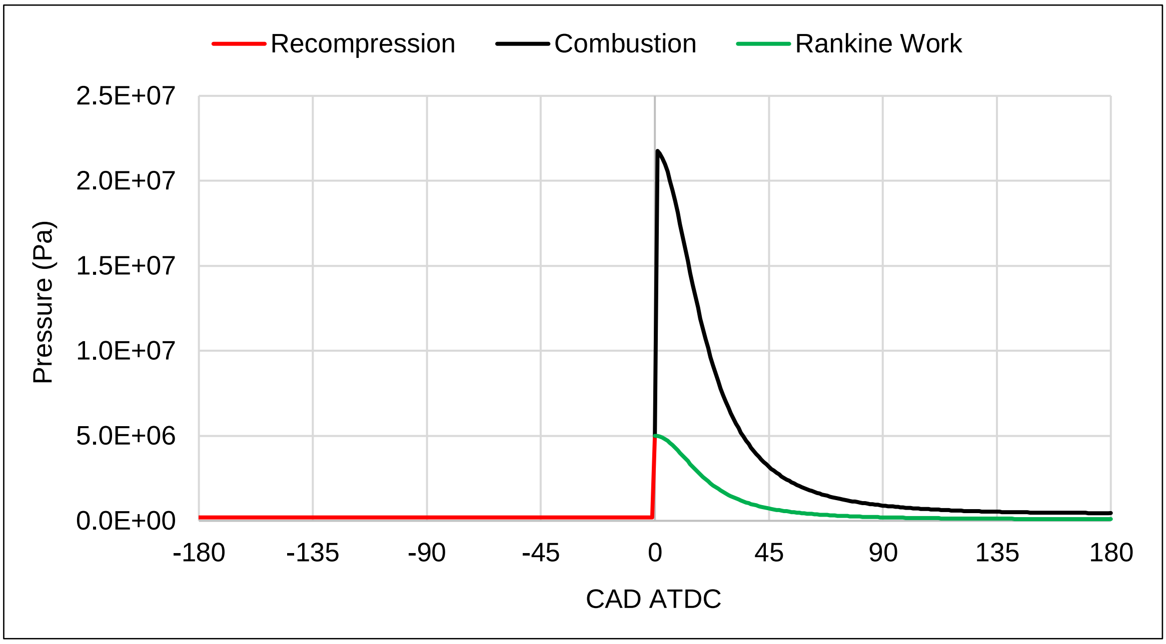

Figure 4.6 The ideal RSCE expander cycle with the lines displaying recompression, combustion, and Rankine work.

Expander adjusted work (EAW) W_{EA} is defined in Equation (68). This metric is useful to understand the double negative work that is required of the recompression work, as it is the minimum work on the compression cylinder as well as work on the combustion cylinder. This metric therefore helps quantify the double negative effect that recompression work has on the system. Without this metric, the effect of increased recompression work would not be captured fully by combustion work.

$$W_{EA} = W_G - W_{RE} = W_{RC} + W_C \qquad (68)$$

Using the definitions for CW and EAW work above, two efficiency metrics that have been used to enable assessment of the efficiency of combustion and are described below. Combustion thermal efficiency (CTE) is shown in Equation (69), where CMEP is the combustion MEP. Expander adjusted thermal efficiency (ETE) is shown in Equation (70), where EAMEP is the expander adjusted MEP.

$$\eta_{CT} = \frac{W_C}{Q_T} = \frac{CMEP}{QMEP} \qquad (69)$$

$$\eta_{ET} = \frac{W_{EA}}{Q_T} = \frac{EAMEP}{QMEP} \qquad (70)$$

An equation to calculate a so-called expander adjusted fuel efficiency (EFE) is described in Equation (71). Ideally this efficiency would include other losses, such as friction, gas exchange, and mechanical efficiencies, but for this simple model these will not be included and are therefore not incorporated into Equation (71).

$$\eta_{EF} = \frac{W_{EA}}{Q_F} = \frac{EAMEP}{FuelMEP} = \eta_{ET}.\eta_C \qquad (71)$$

There are issues with these metric that utilise expander adjusted work if Rankine work is negative. However, if this is remembered and considered in conjunction with thermodynamic efficiency of the expander, these additional metrics serve as useful guidance tools to understand how well the expander is turning fuel into useful work in isolation of the compressor.

4.7 Efficiency Study of a Quasi Real RSCE Expander Cycle

This section will present swings performed on the model to predict impact of key variables on the efficiency of the RSCE expander. The conditions for the initial point of the swing are displayed in Table 4.1. These conditions are based on the Titan SCCRE, which will be discussed in further detail in 0. The initial variable values of IVO, IVP, EVO, EVO, SOC, DOC, intake air, fill rate, AFR, volumetric efficiency and combustion efficiency were chosen for the mid-point to enable the swing. The swings around this point will not produce the most efficient operation of the expander but provide the ability to understand the effect in changes of key variables have on efficiency. An optimised expander will be discussed in the following section.

Table 4.1 Initial conditions for quasi real RSCE expander model efficiency study.

Variable	**Value**	**Unit**
Piston Diameter	0.105	m
Crank Throw	0.0650	m
Con Rod Length	0.2120	m
Expansion Ratio	19.0	-
Gamma	1.33	-
IVO	-20	CAD ATDC
IVP	20	CAD
EVO	-180	CAD ATDC
EVP	140	CAD
SOC	4	CAD ATDC
DOC	10	CAD
Intake Air Temperature	700	K
Intake Air Pressure	5.0	MPa
Fill rate Intake P from IVO	8	CAD
Exhaust Pressure	0.2	MPa
Fuel LHV	45.5	MJ/kg
AFR	21	
Volumetric efficiency	90	%
Combustion Efficiency	90	%

The resultant pressure trace and PV diagram from the model and the midpoint conditions presented in Table 4.1 are shown in Figure 4.7 and Figure 4.8 respectively. It is important to remember that the Rankine work and combustion curves follow the same path until fuel energy is added to the system.

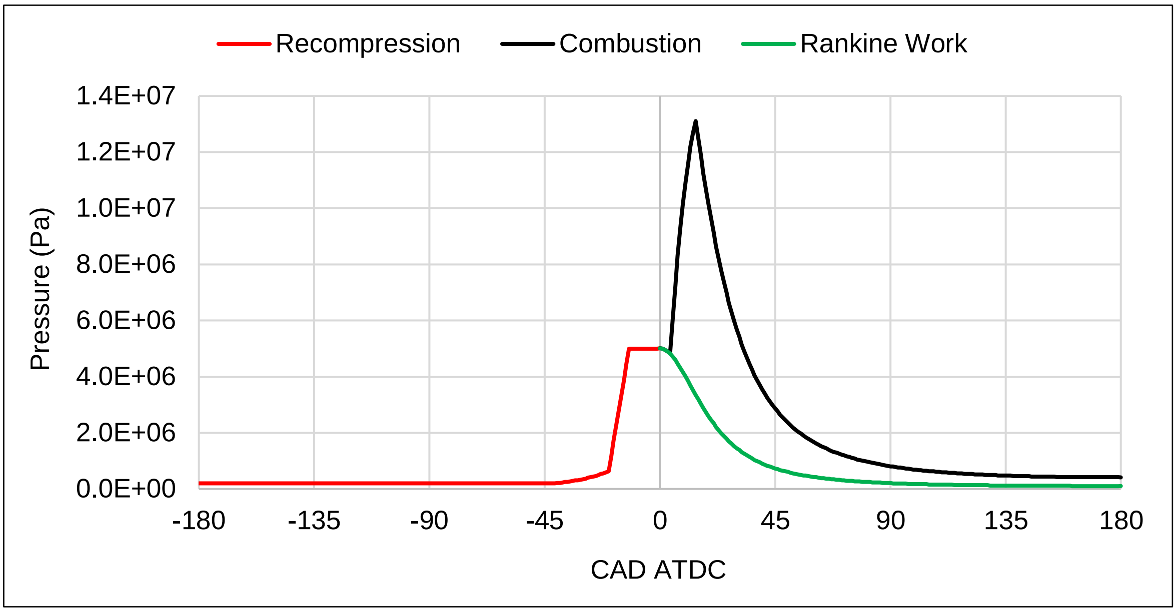

Figure 4.7 The pressure trace for initial point of the efficiency study for the quasi real RSCE expander.

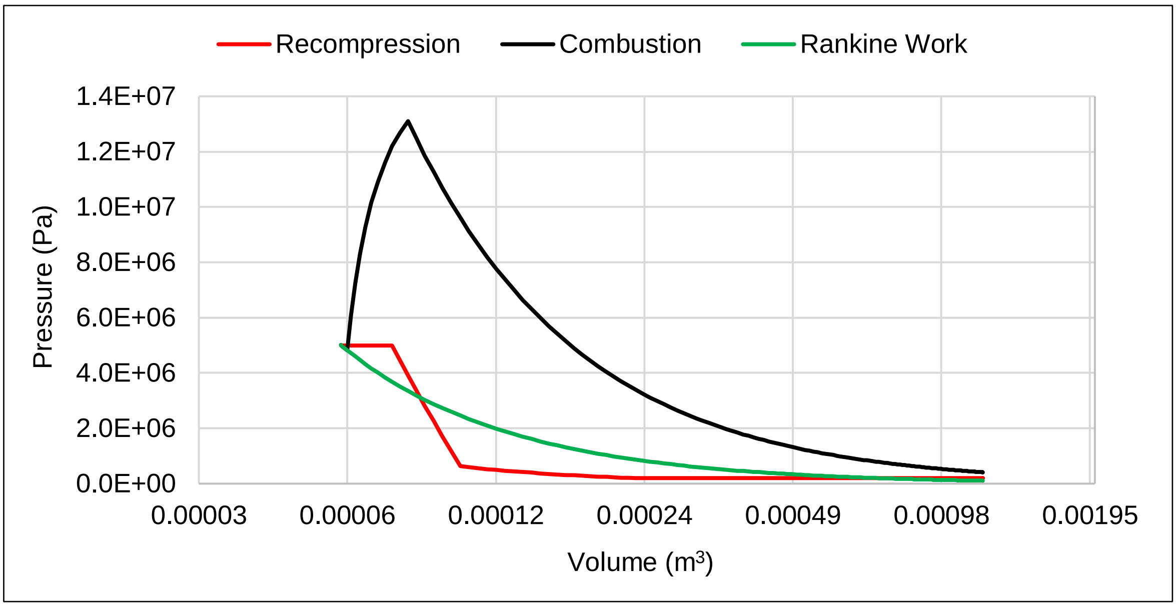

Figure 4.8 PV diagram for the initial point of the efficiency study for the quasi-real RSCE expander.

Figure 4.9 displays the swing in ER and the effect this has on efficiencies. TE and CTE increase linearly with expansion ratio. However, the inverse is true for EFE. This is due to increasing ER reducing the combustion chamber volume for a given IVC, therefore reducing air mass and energy added to the system, and the extra work that is required during recompression at higher ERs. For increasing ER to be a successful method of increasing EFE, intake valve events would need to be retarded to minimise recompression work. However, this has the potential to negatively affect combustion thermal efficiency, as the work created from combustion would have to be retarded so that the intake valves are not open when combustion is occurring. The constant CTE between ER 15 and 17 suggests with a different setup or optimisation of the expander, TE, CTE and EFE can all be increased. It is worth noting that with higher ER, there is not the same issues as friction, as higher ER does not increase maximum cylinder pressure. Which is the case for conventional ICEs utilising a single compression/expansion ratio. High ER can in fact lower the maximum cylinder pressure by increasing the volume from SOC at a faster rate.

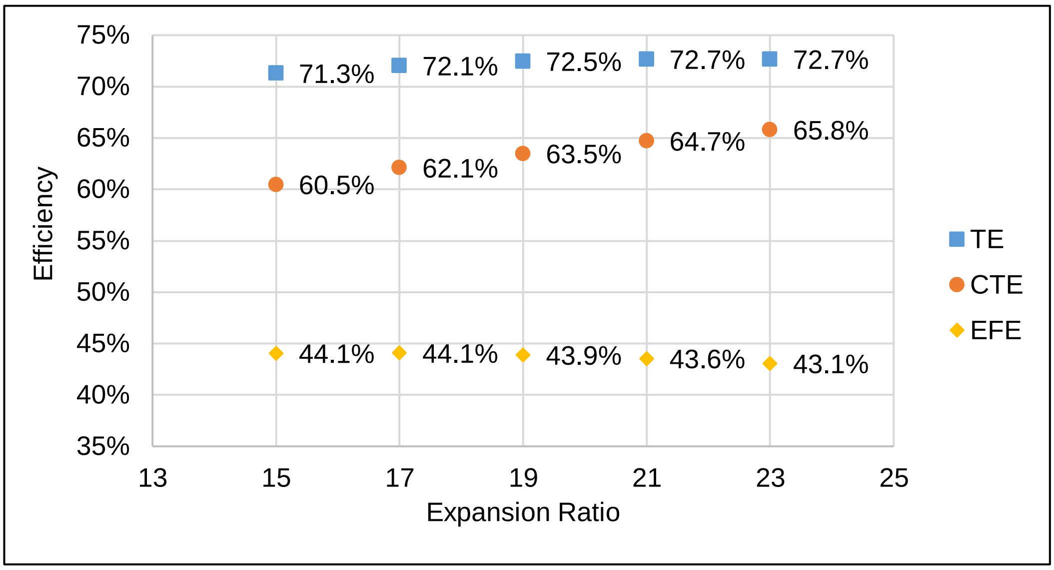

Figure 4.9 Quasi-real expander efficiency study – ER swing.

It is worth remembering that this model does not consider the energy recovered from the recuperator. As exhaust temperature increases with lower ER, the efficiency of the recuperator will increase. As long as the effectiveness of the recuperator is greater than ~77%, system efficiency will increase with lower ER, as shown by Dong et al [2].

Figure 4.10 displays the effect of swinging IVO. In this swing, IVC has no impact on SOC, which remains constant efficiency of 63.5%. TE and EAFE both rise positively with IVO as recompression work is reduced. As IVC moves before and after TDC, there is a change in trapped air mass. TE increases in line with the movement of the piston after TDC, as more “free” Rankine work increases the efficiency, as pressure is maintained a constant rate with a greater volume. This does not affect EFE in the same way, as this is unaffected by the increase in Rankine expansion. Resulting in an almost linear increase in efficiency.

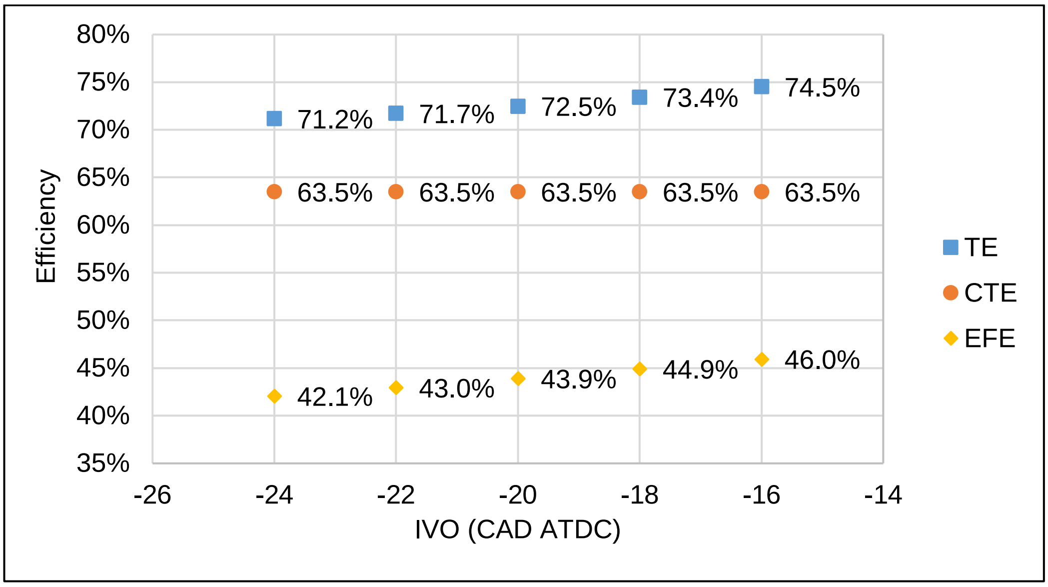

Figure 4.10 Quasi-real expander efficiency study – IVO swing.

Figure 4.11 presents the IVP swing effect on efficiencies. For the same reasons as the swing on IVO, the CTE is unaffected and remains constant at 63.5%. While recompression work is at its highest at 16 CAD IVP, as IVC occurs before TDC, and remains constant from 20 to 24 CAD. TE and EFE follow similar trends, with the minimum efficiencies between 20 and 22 CAD. This is because IVC determines the volume of air that is in the cylinder and IVO is unaffected by IVP and remains constant. Therefore, the effect of IVC dominates, producing a sinusoidal response into variation in IVP alone.

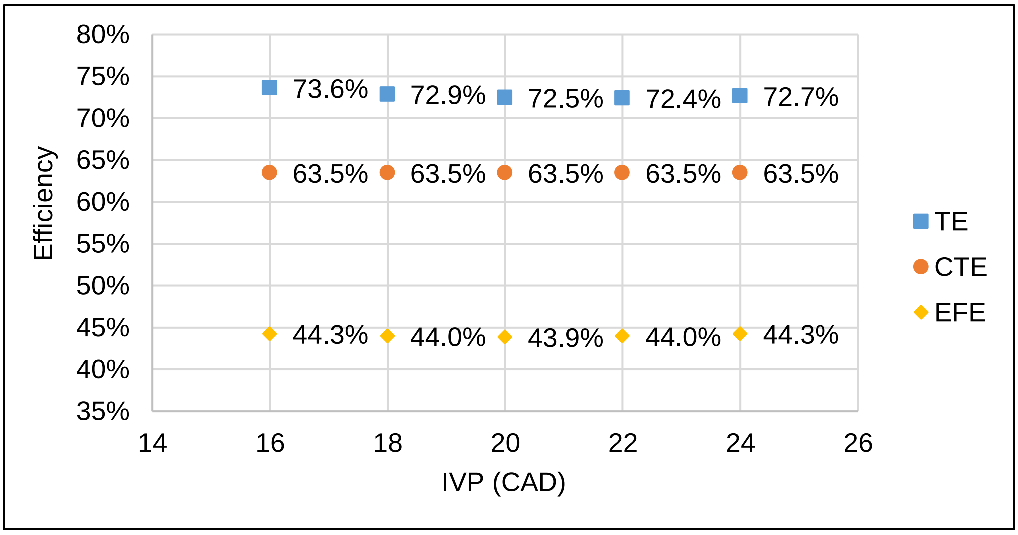

Figure 4.11 Quasi-real expander efficiency study – IVP swing.

Figure 4.12 displays a swing in EVO. Retarding EVO decreases the recompression work that occurs between EVC and IVO, as EVP is constant. EVO before BDC also reduces the amount of expansion that could be converted to work. EVO after BDC creates negative work which begins to be offset by the reduction in recompression between EVC and IVO.

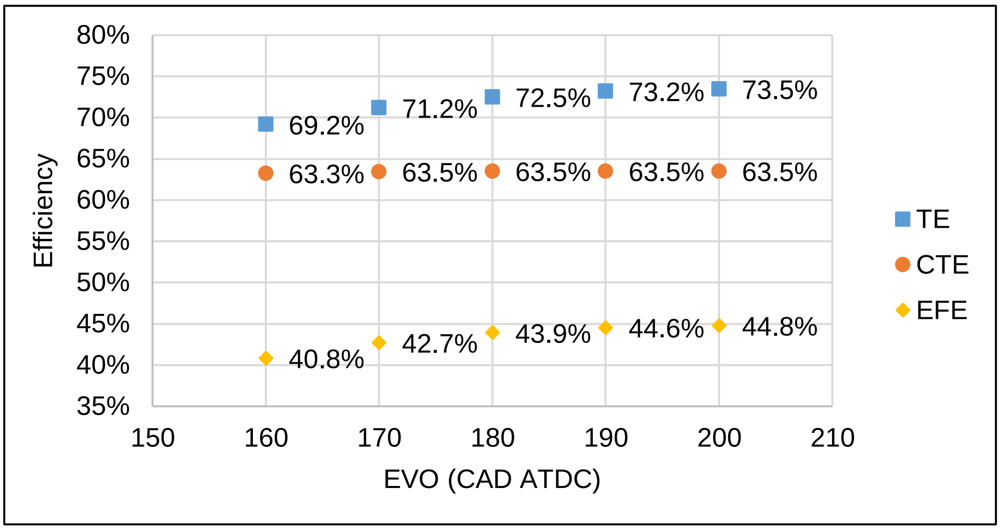

Figure 4.12 Quasi-real expander efficiency study – EVO swing.

Figure 4.13 displays the swing of EVP. Like the swing in EVO, the reduction in recompression work with a longer EVP reducing the gap between EVC and IVO and therefore reducing work. As there is a smaller volume change as the EVC moves closer towards TDC, there is less recompression work that can be removed to increase efficiency. CTE remains constant across the swing as the amount of air, fuel, heat release and expansion is unaffected by this variation in EVP.

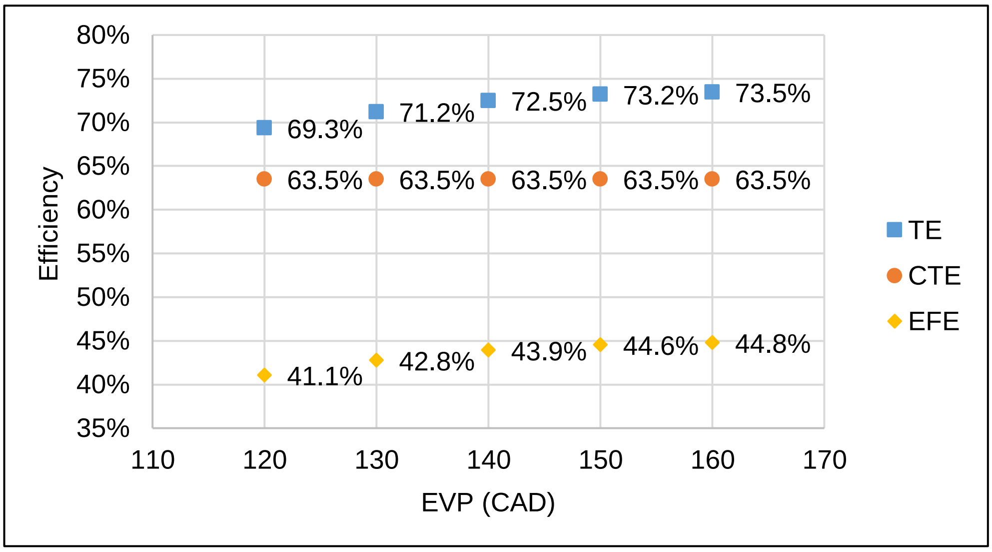

Figure 4.13 Quasi-real expander efficiency study – EVP swing.

Figure 4.14 displays a swing in SOC. In the same manner as conventional engines, if energy is added into the system at larger volumes, less pressure is created in the chamber and there is less distance available to expand to create work from the pressure. Therefore, efficiency in TE, CTE and EFE all follow a negative linear trend as SOC is retarded.

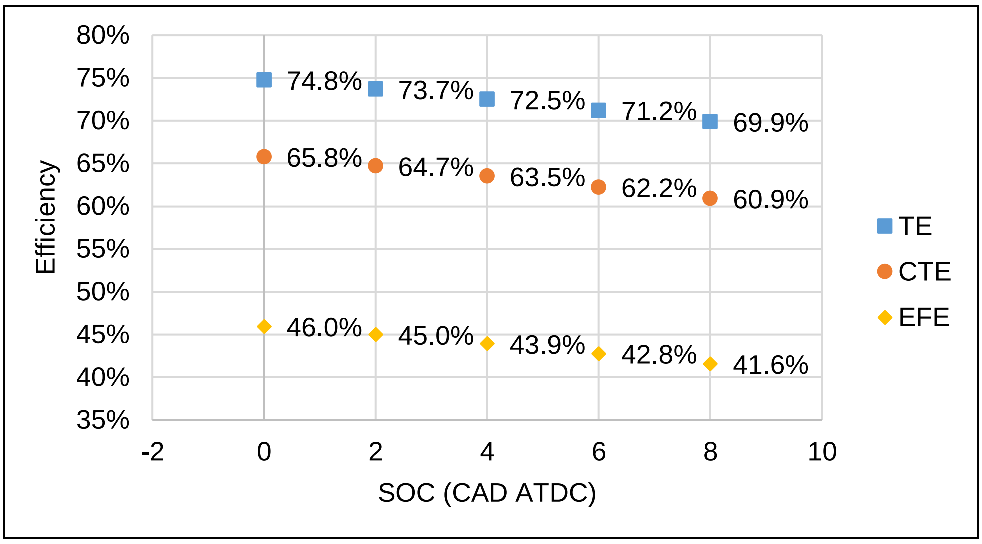

Figure 4.14 Quasi-real expander efficiency study – SOC swing.

Figure 4.15 displays a DOC swing. For the same reasons as outlined in the SOC swing, the later fuel energy is released the less work can be extracted and utilised, resulting in a linear negative trend for all three efficiencies as DOC increases.

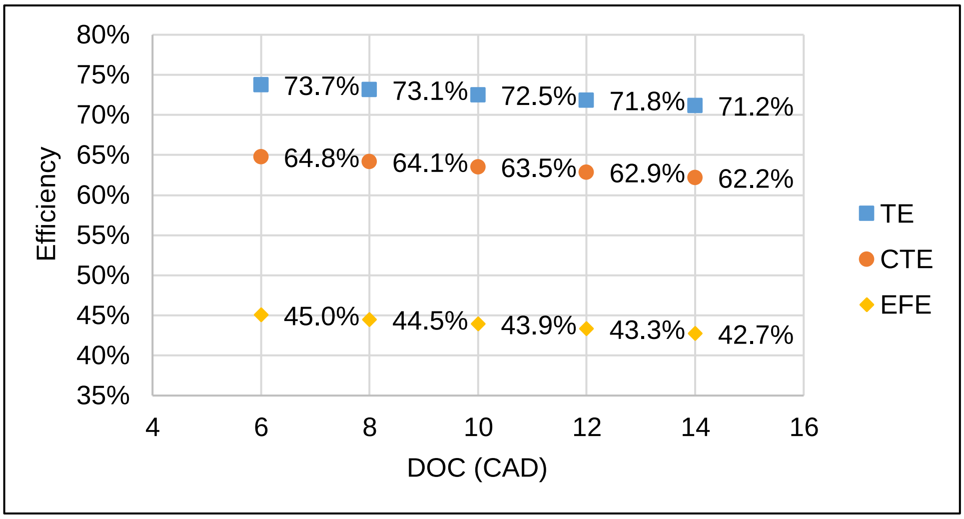

Figure 4.15 Quasi-real expander efficiency study – DOC swing.

Figure 4.16 displays an intake air temperature swing, with TE having a positive correlation, CTE unaffected, and EFE having a negative correlation. As intake temperature increases, less air mass and fuel are introduced to the cylinder.

It is important to note that this a constant Rankine work condition, due to pressure remaining constant. Therefore, more work is extracted from the Rankine work in proportion to combustion work. This increases TE accordingly but has the opposite effect on EFE, and no effect on CTE. EFE decreases as combustion work decreases but the amount of recompression work stays constant.

This matches up with the Carnot analysis and theory presented in Section 4.2, with increasing amounts of energy added it is expected for efficiency to increase. As intake air temperature dictates the amount of mass available for combustion, and therefore maximum cylinder pressure, there is a higher difference in pressure. This means that the expander operates most efficiently at higher loads. However, friction must also be considered, which increases with cylinder pressure.

TE and ETE converge as intake air temperature tends towards zero. This also occurs as AFR changes for the same reason. Underlining the expander would ideally run as cold, high pressure, and as rich AFR as possible. The cold intake air could be a benefit for emissions control and efficiency in the expander.

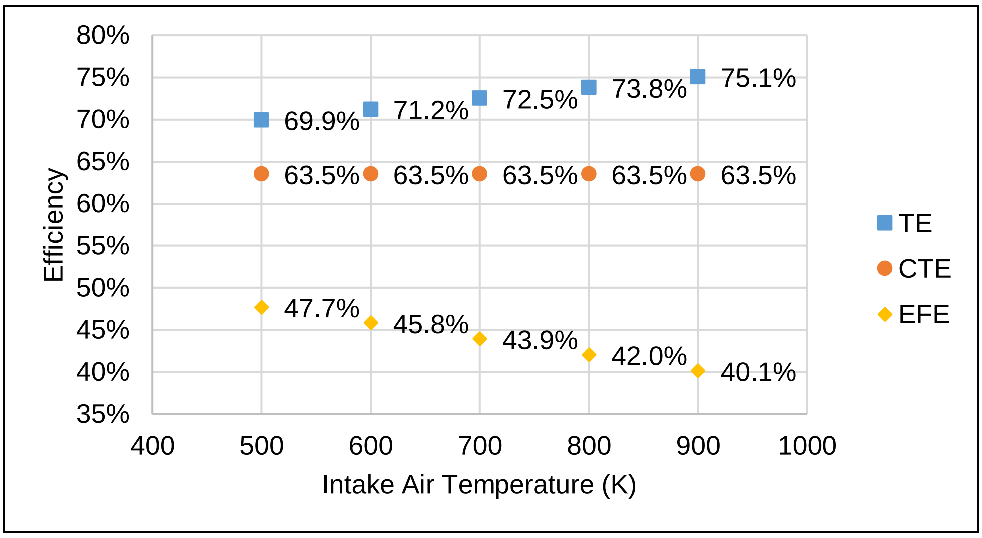

Figure 4.16 Quasi-real expander efficiency study – intake air temperature swing.

Figure 4.17 displays a swing in intake pressure. In this condition both Rankine work and combustion work vary. Both TE and EFE increase positively with intake air pressure. Tending towards an upper limit, dependant on other engine parameters, at higher pressures. CTE remains at a constant 63.5%, as the ratio between Rankine work and combustion work remains constant.

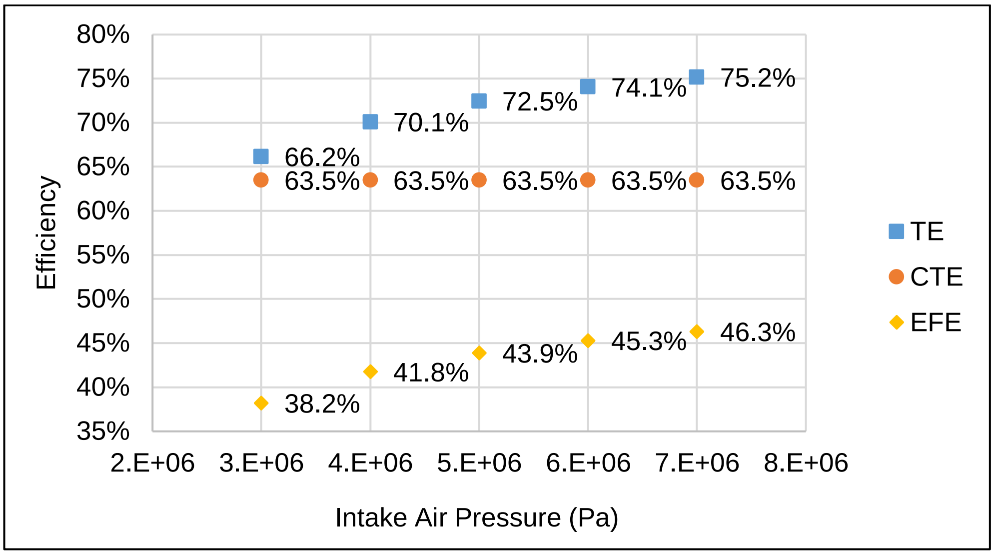

Figure 4.17 Quasi-real expander efficiency study – intake air pressure swing.

Figure 4.18 displays the AFR swing. CTE remains constant as the ratio between Rankine expansion work and combustion expansion work remain constant. TE increases with a reduction in the addition of fuel as a higher proportion of work is extracted from Rankine expansion work compared to combustion expansion work. For a similar reason EFE reduces, as the amount of combustion work reduces but the amount of recompression work remains constant. As EFE more effectively considers the negative recompression work, this results in a negative correlation with AFR.

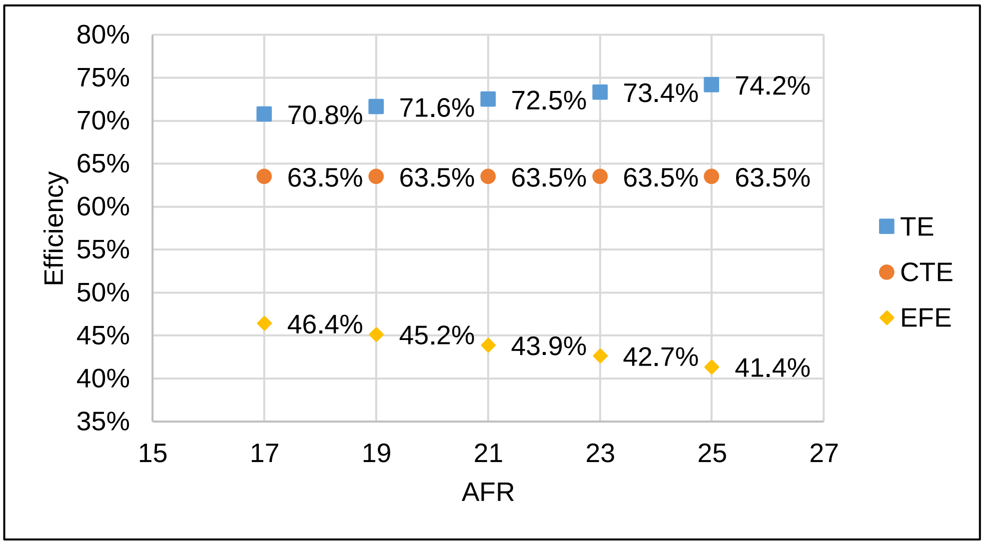

Figure 4.18 Quasi-real expander efficiency study – AFR swing.

Figure 4.19 displays the volumetric efficiency swing. The volumetric efficiency swing has the same responses as the AFR swing. CTE remains constant at 63.5%. TE decreases with increasing AFR as a lower proportion of work is produced from Rankine expansion. EFE increases with AFR as more combustion work is produced while recompression work is constant.

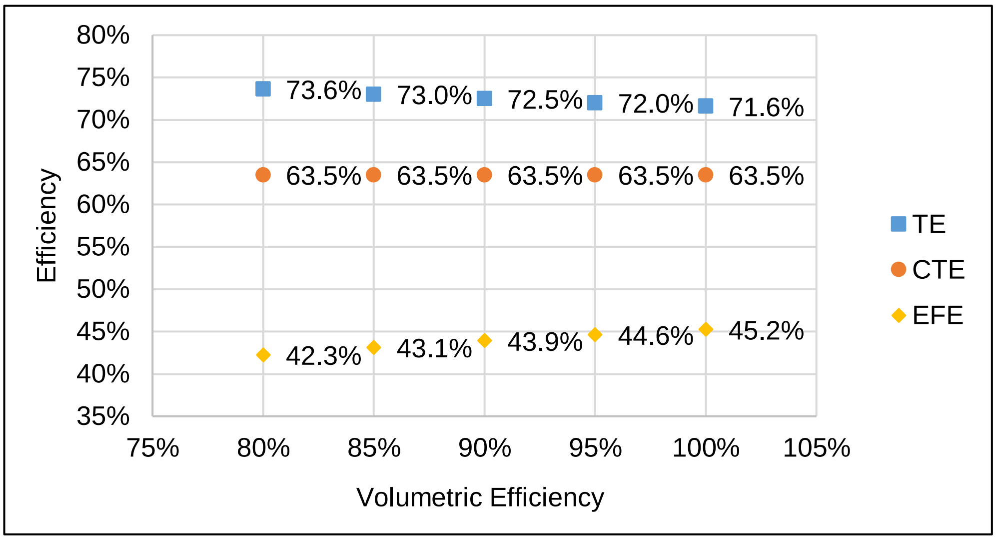

Figure 4.19 Quasi-real expander efficiency study – volumetric efficiency swing.

Figure 4.20 displays the results from the combustion efficiency swing. CTE is unaffected as it is the thermal efficiency of turning thermal energy into work and remains at a constant of 63.5%. TE decreases with combustion efficiency as a lower proportion of work is produced from Rankine work. EFE is directly affected by combustion efficiency, as shown in Equation (71), and therefore reacts positively to increased combustion efficiency.

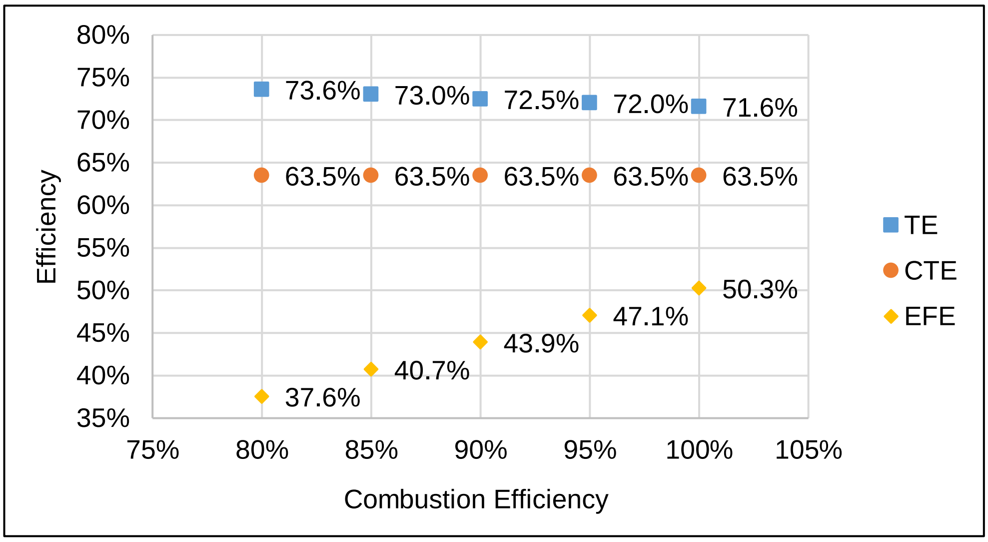

Figure 4.20 Quasi-real expander efficiency study – combustion efficiency swing.

The results from a swing in temperature and pressure with a constant air flow of 24.9kg/m3 (the air flow of the midpoint) is shown in Figure 4.21. This results in constant fuel addition and a constant amount of energy extracted from the fuel as CW. However, Rankine work increases as pressure increase. This results in increasing TE, as the proportion of “free” Rankine work increases. CTE is unaffected, while EFE reduces as there is a larger amount of recompression work with increasing inlet pressure at higher inlet temperatures.

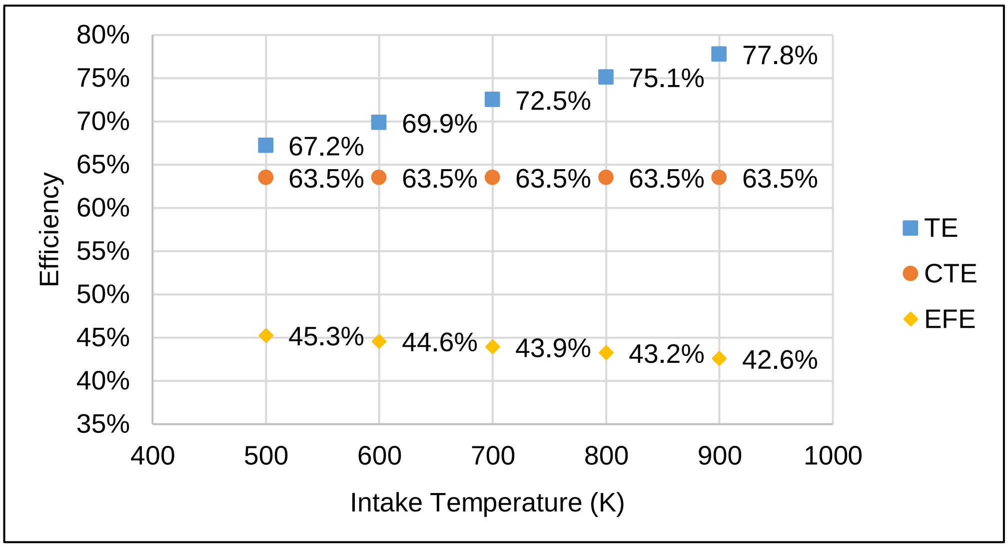

Figure 4.21 Quasi-real expander efficiency study – pressure and temperature swing with constant air flow.

The ideal case for the RSCE expander is to consider the work out required and the temperature of the recuperator. As the recuperator temperature varies transiently with load and speed demand. With a higher recuperator temperature more Rankine work can be captured to increase the efficiency of the expander.

To satisfy this requirement a plot would be required of each load condition, as well as recuperator out temperatures and pressure. For this analysis only one GW condition is considered and shown in Figure 4.22. The GW of the midpoint condition of 1,876J is used as the constant. The figure shows a swing with constant GW against inlet temperature, with pressure varied to achieve constant GW across the swing. The trend show the expected increase in TE, as Rankine work increases and EFE decrease and recompression work increases. This displays the limitation of using EFE which does not consider the recuperation of energy through the recuperator that would be true of a real RSCE. For this to explored accurately and in more detail a full model of the RSCE including the expander and recuperator would need to be considered, as well as the transient and exhaust feedback effects.

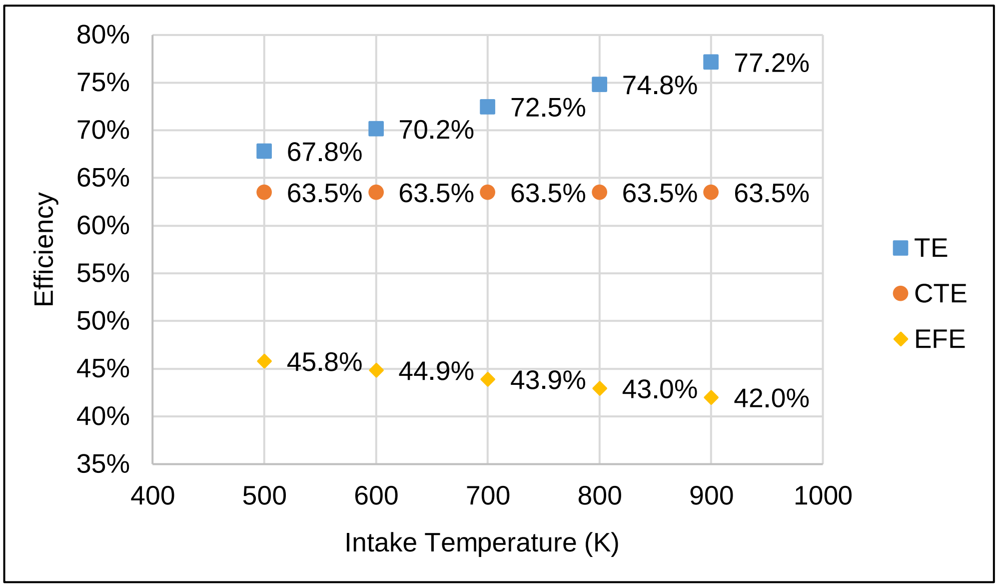

Figure 4.22 Quasi-real expander efficiency study – temperature and pressure swing with constant GW.

Generally, higher CTE leads to higher EFE and TE in all cases, with the exception of the ER swing. This is due to EFE being doubly affected by the extra recompression work caused by increasing ER.

4.8 Optimising A Quasi-Real Expander Cycle

This section will work through optimisation of the quasi-real expander, first concentrating on combustion and valve timings, before discussing engine architecture. For the optimised expander case, piston geometry will initially remain as per the mid-point swing.

4.8.1 Combustion & Valve Events

Several variable limitations were imposed that are considered realistic limits for optimisation of the combustion and valves events. Due to limitations in valvetrain design, the IVP was limited to a minimum value of 16 CAD. IVP must be at least twice that of the intake fill rate in CAD, to allow the intake valves to open and close. The PRR of intake fill rate cannot be less than 8 CAD. DOC cannot be less than 8 CAD.

Table 4.2 summarises the modified conditions that were used for the optimised expander case and the resultant efficiencies. With the changes made, the resulting efficiencies are higher than any shown in Section 4.7, due to multiple variables being optimised at once.

Table 4.2 Modified variables from the midpoint for a quasi-real expander with optimised valve timings & combustion.

Variable	**Value**	**Unit**
IVO	-16	CAD ATDC
IVP	16	CAD
EVO	-180	CAD ATDC
EVP	164	CAD
SOC	0	CAD ATDC
DOC	8	CAD
Intake Air Temperature	600	K
Intake Air Pressure	5.0	MPa
Fill rate Intake P from IVO	8	CAD
Thermodynamic Efficiency	76.8	%
Combustion Thermodynamic Efficiency	66.3	%
Expander Fuel Efficiency	50.8	%

The resultant pressure trace for the optimised combustion and valve events is shown in Figure 4.23. This demonstrates the higher pressures that the combustion event is able to achieve and sustain for a longer period.

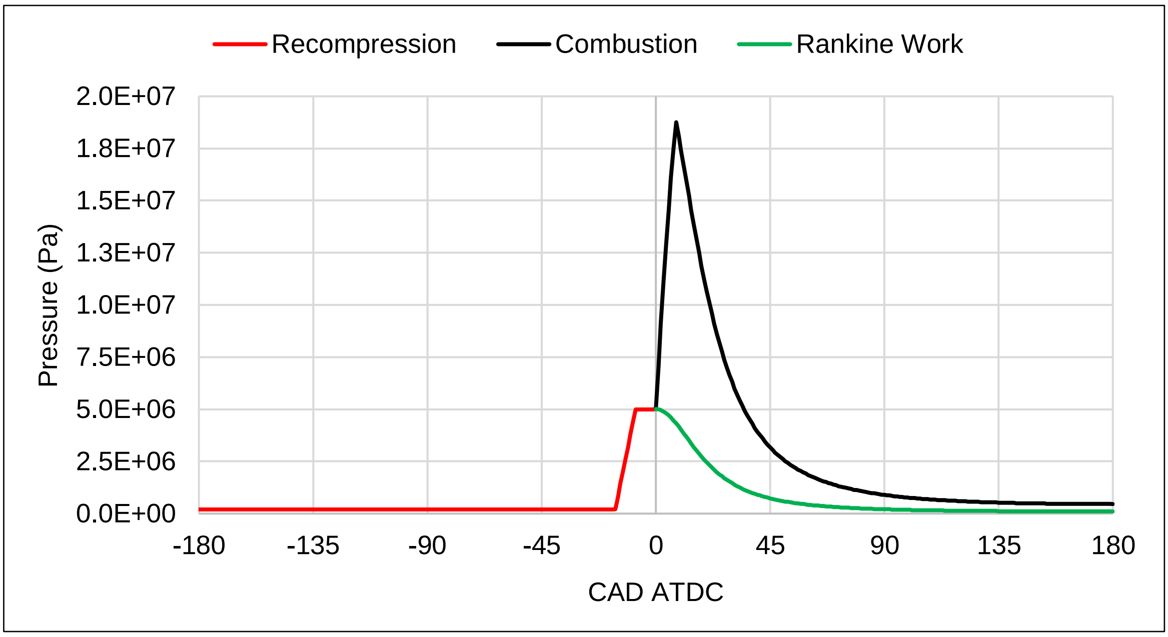

Figure 4.23 Pressure trace for a quasi-real expander with optimised combustion & valve timings

4.8.2 Expander Architecture

Figure 4.24 presents an ER optimisation swing of the quasi-real expander. Efficiencies are highlighted in the graph at 19 ER, the initial ER of the midpoint. 27, where the highest EFE is found at 51.6%. 37, where the highest TE is found at 80.2%. The model was not run at higher than 49 ER, although CTE would continue to increase until recompression work becomes larger than Rankine work, at which point CTE is no longer a useful metric.

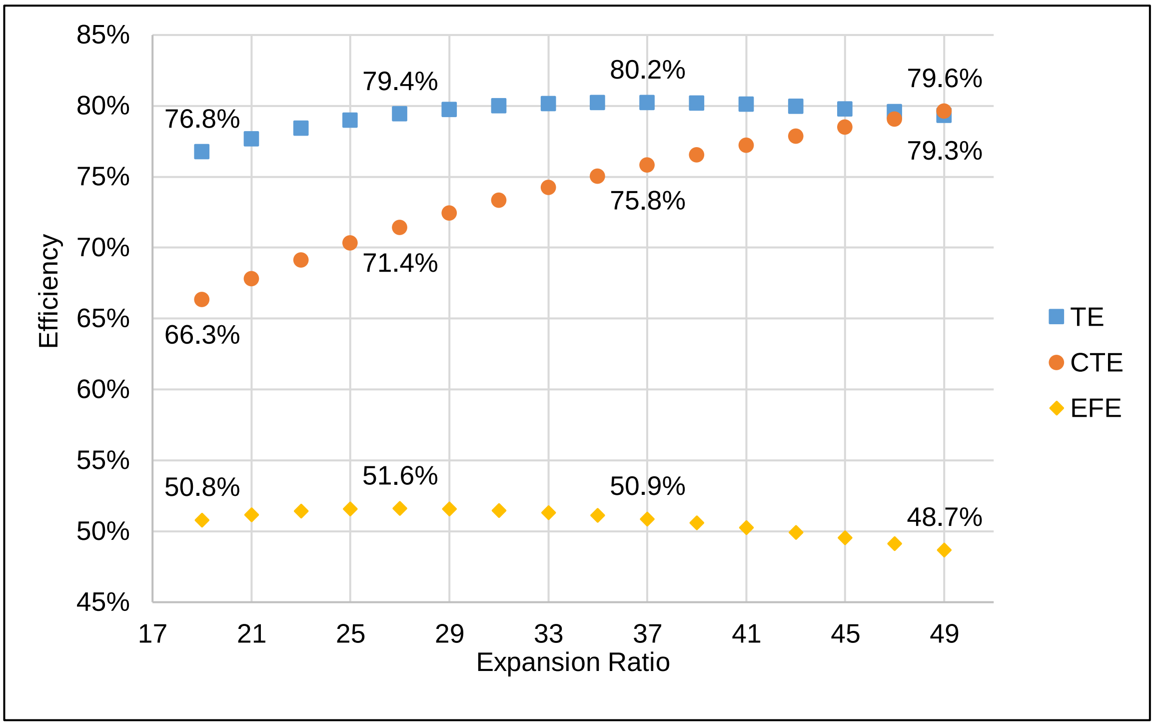

Figure 4.24 A quasi-real expander with optimised valves timings and combustion – ER swing

TE and EFE demonstrate the issues that start to exist with increasing ER. As during IVP there is a constant pressure, with increasing ER there is increasingly more work performed on the recompression stroke. This reaches a tipping point in both TE and EFE, with an earlier tipping point in EFE due to EFE including a correction to remove the “free” Rankine work.

A 3D plot of ER, volumetric efficiency and EFE is shown in Figure 4.25. All other variables outlined in Table 4.2 remain constant. These two variables were chosen as, after valve timings and combustion are optimised, they provide the next step towards further development and optimisation of the expander design. Volumetric efficiency was chosen as one of the variables due to dominated by valve and inlet manifold design and in a real engine is affected by engine speed and part load conditions. While ER is chosen as a this is a key consideration for design of the engine and, as shown in Figure 4.24, it’s intrinsic maximum efficiency. With a low volumetric efficiency of 50%, the optimised ER would be ~16, yielding 43.9% CTE. At the same ER, 90% volumetric efficiency would yield 49.9% EFE. The optimum ER for 90% volumetric efficiency would be ~27, yielding 51.6% EFE. At the same ER, 50% volumetric efficiency would yield 41.5% EFE.

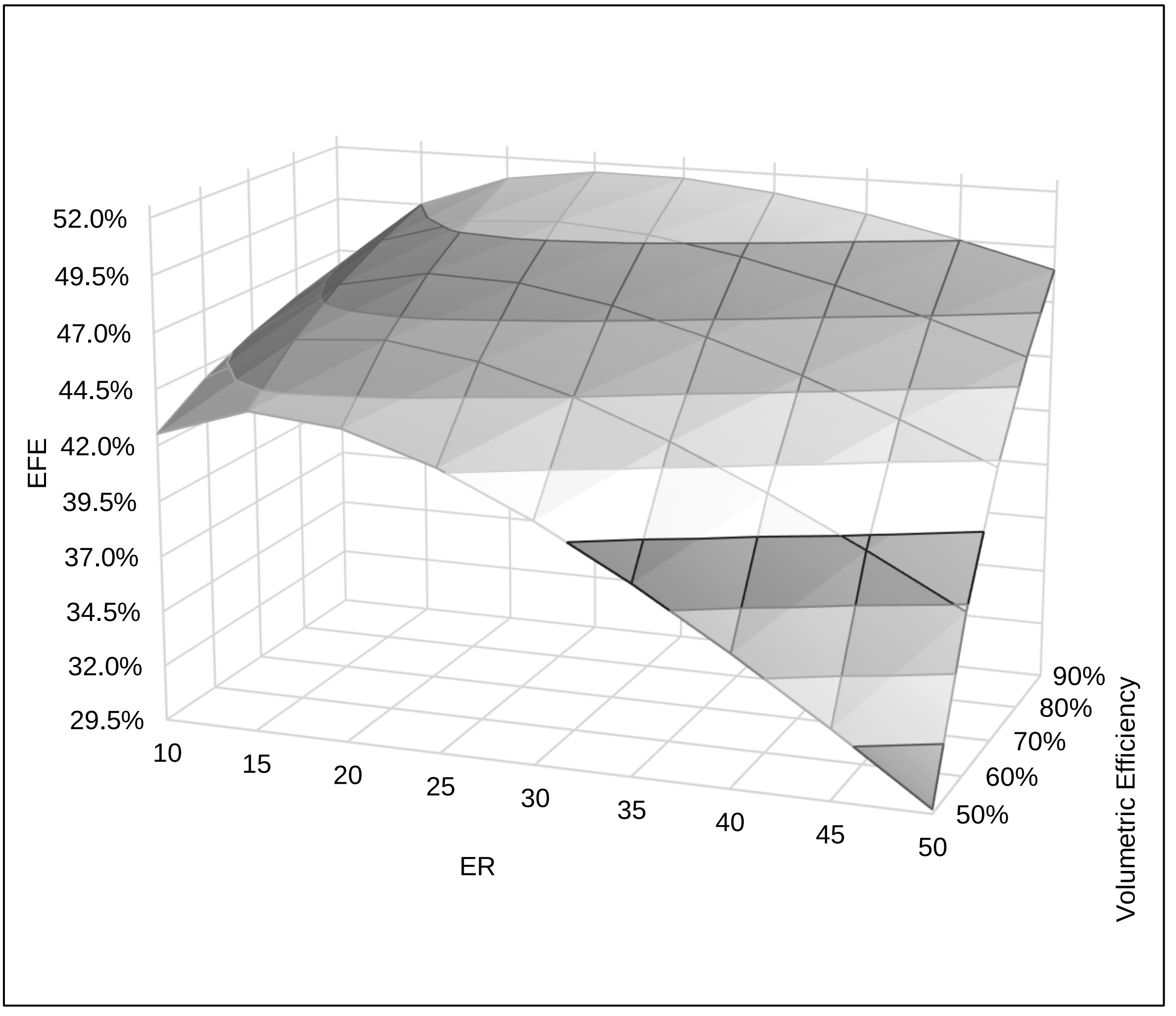

Figure 4.25 A quasi-real expander with optimised valves timings and combustion – 3D plot of ER, volumetric efficiency & CTE

A swing in conrod length occurred from 0.112m to 0.312m in steps of 0.05m, with 0.212m the midpoint. The value of con rod length must be longer than that of the maximum length of the stroke. Figure 4.26 display the effect of con rod length on the change in volume through the cycle. As seen in conventional ICES, increasing con rod length decreases the change in volume near TDC. Increasing the time the piston dwells at TDC. This has a couple of extra benefits for a SCE expander. As there is less change in volume around TDC, there is less losses in the recompression stage of the expansion cycle while the intake valves are open. Engine efficiency would be more forgiving in response changes to intake valve and SOC timings, as the peak change in volume occurs closer towards -90 and 90 CAD ATDC rather than closer towards TDC where it would cause a higher amount of recompression work, as shown Figure 4.26.

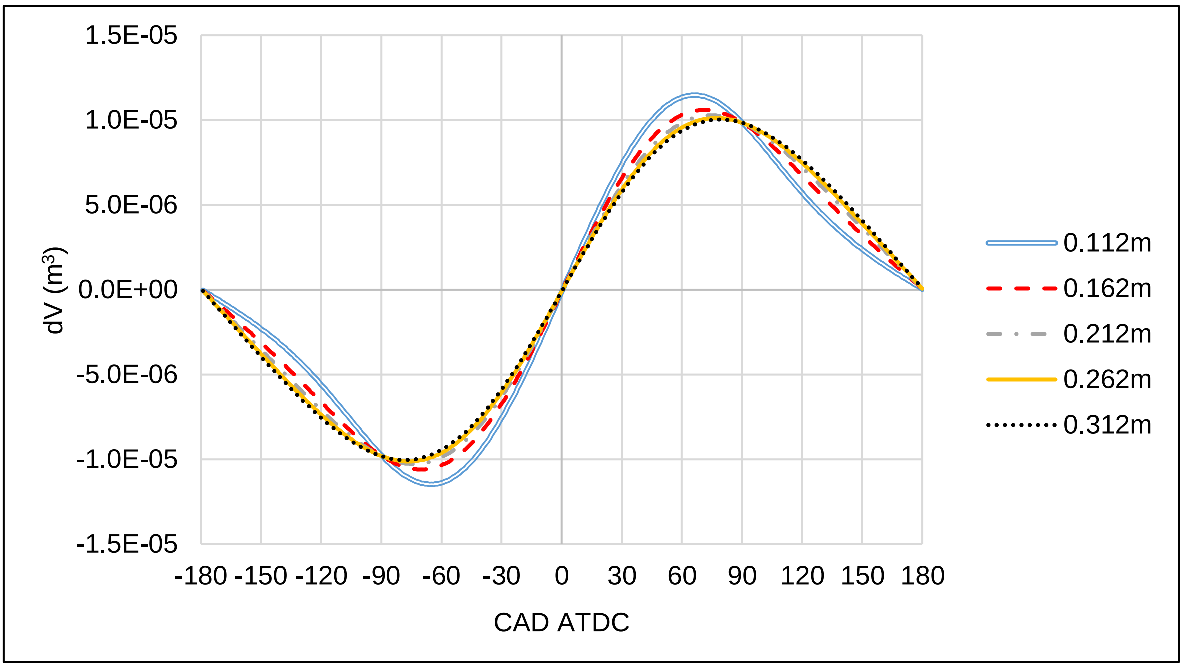

Figure 4.26 A quasi-real expander optimisation – The effect of con rod length on change in volume.

The results of the effect this has on efficiencies are shown in Figure 4.27. CTE decreases as a lower change in volume during peak combustion pressure marginally changes the ratio of Rankine work to combustion work, resulting in a reduction of 0.4% in CTE. As recompression work is reduced, both TE and EFE increase by 0.2% and 0.6% respectively. The reduction in recompression work therefore has a greater impact on efficiency than a slight decrease in combustion work when increasing con rod length. This has associated benefits of longer conrods in conventional reciprocating ICEs, such as reducing the conrod angle and therefore friction between the piston and the cylinder walls.

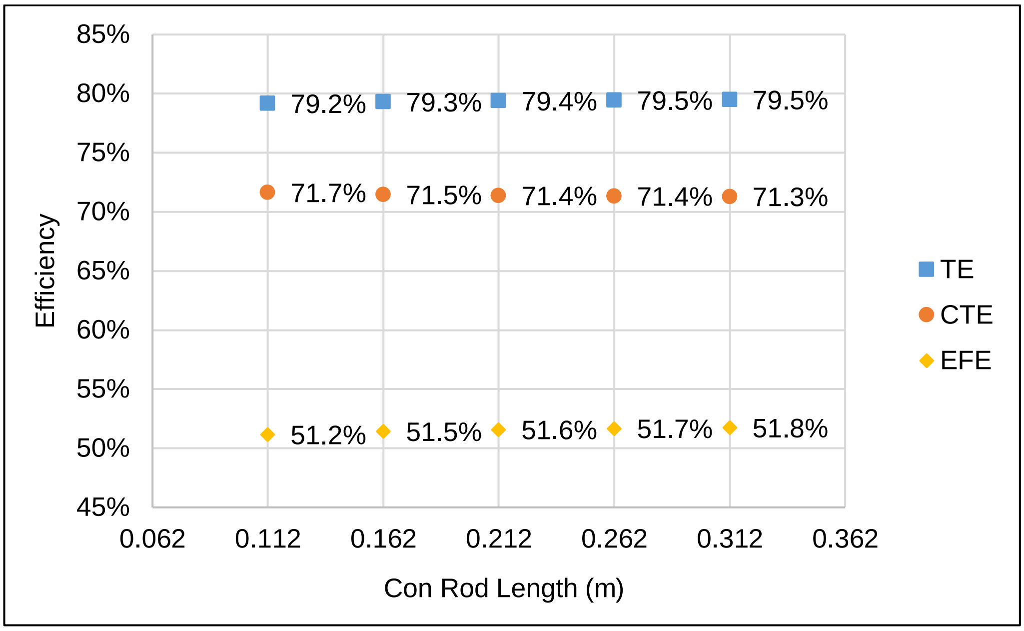

Figure 4.27 A quasi-real expander optimisation – Con rod length swing vs efficiency

For optimisation of crank throw, piston bore varies to maintain a constant 1.26L displacement. The swing occurs from 0.035m to 0.095m over 5 points. Steps of 0.015m were chosen as realistic changes that could be implemented in either direction of the starting midpoint of 0.065m. Similarly to conrod length, the changes to crank throw in the change in volume increases piston dwell at TDC with shorter crank throws, this is shown in Figure 4.28. This also reduces recompression work and is forging in intake valve and combustion timings.

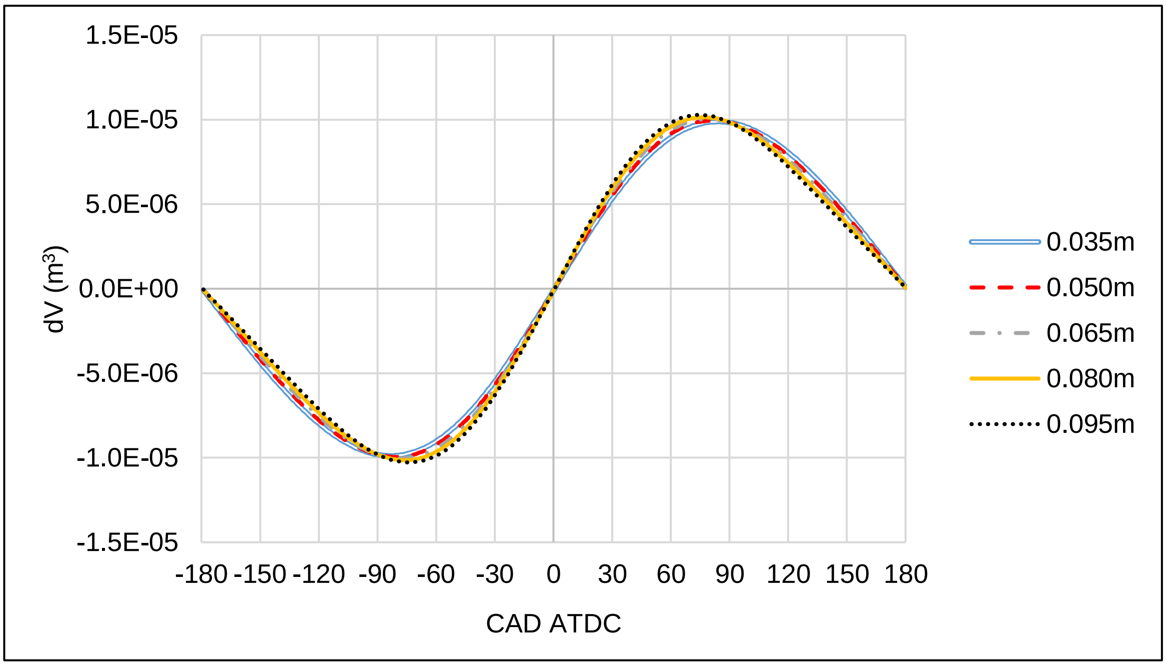

Figure 4.28 A quasi-real expander optimisation – The effect of crank throw length on CAD vs change in volume.

The efficiency responses to the swing in crank throw length are shown in Figure 4.29. With CTE shown to increase with increasing crank throw length, by 0.2% across the swing. TE and EFE both increase with decreasing crank throw length, by 0.2% and 0.3% respectively. This is due to the changes in recompression work and maximising the highest combustion pressure with the greatest change in volume. In this model the engine favours oversquare or short stroke for higher efficiency. However, the increase in efficiency could be negated by an increase in surface area at TDC, leading to higher heat losses. A larger bore is usually beneficial in increasing volumetric efficiency, due to larger available area for the packaging of valves, inlet, and exhaust manifolds.

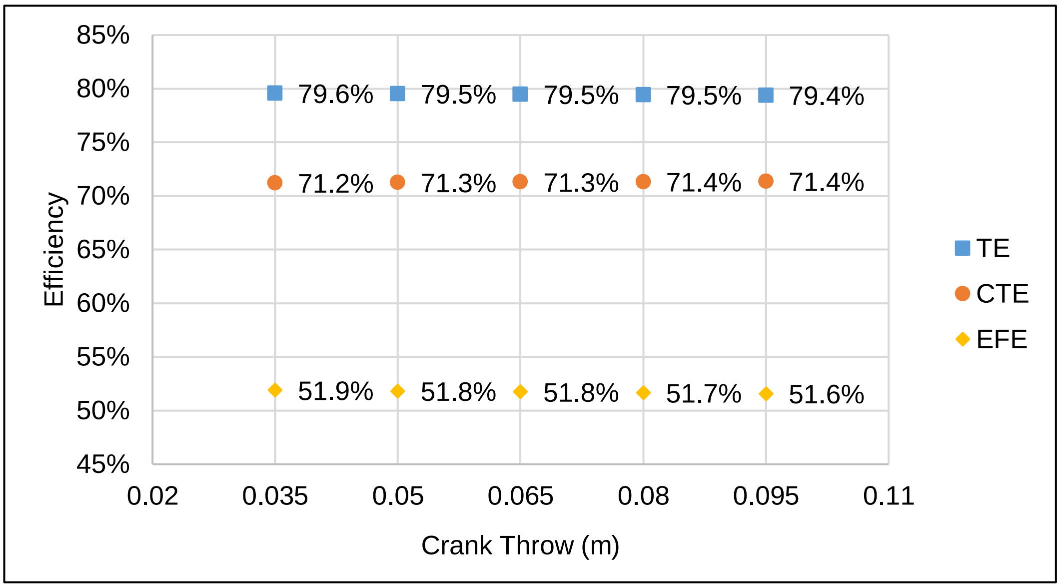

Figure 4.29 A quasi-real expander optimisation – Crank throw length swing vs efficiency

The final variables output from the expander optimisation are shown in Table 4.3.

Table 4.3 Variables for the final optimised expander.

Variable	**Value**	**Unit**
Piston Diameter	0.143	m
Crank Throw	0.035	m
Con Rod Length	0.312	m
Expansion Ratio	27	-
Gamma	1.33	-
IVO	-16	CAD ATDC
IVP	16	CAD
EVO	-180	CAD ATDC
EVP	164	CAD
SOC	0	CAD ATDC

DOC	8	CAD
Intake Air Temperature	600	K
Intake Air Pressure	5.0	MPa
Fill rate Intake P from IVO	8	CAD
Exhaust Pressure	0.2	MPa
Fuel LHV	45.5	MJ/kg
AFR	21	
Volumetric efficiency	90	%
Combustion Efficiency	90	%
Thermodynamic Efficiency	79.6	%
Combustion Thermodynamic Efficiency	71.2	%
Expander Fuel Efficiency	51.9	%

4.9 Comparisons

Table 4.4 displays a summary comparison of the expander optimisation cases/steps that were taken through this chapter, with efficiencies and delta between each step shown. The optimisation of the combustion and valve timing represented the highest change to TE and EFE, 4.3% and 6.9% respectively. CTE shows the highest improvement with optimised ER but still shows a relatively significant improvement with optimisation of combustion and valve timings. Demonstrating combustion and valve timings are key variables to optimise the performance of the expander.

Table 4.4 Efficiency comparison of the initial midpoint and optimised expander cases.

Cases/Steps	**TE**	**ΔTE**	**CTE**	**ΔCTE**	**EFE**	**ΔEFE**
Initial midpoint	72.5%	-	63.5%	-	43.9%	-
+ optimised combustion & valve timing	76.8%	4.3%	66.3%	2.8%	50.8%	6.9%
+ optimised ER	79.4%	2.6%	71.4%	5.1%	51.6%	0.8%
+ optimised engine architecture	79.6%	0.2%	71.2%	-0.2%	51.9%	0.3%

A comparison of the initial and optimised cycle pressure traces is shown in Figure 4.30. Remembering that the area inside the curve represents the work captured from the expander, Figure 4.30 displays the losses from the compression of residuals from the previous cycle, negative work created with IVO before TDC, and lower peak pressures due to combustion happening over several CAD. also displays how a small amount of work could be recovered by acting more “diesel like” with peak pressure occurring at a larger volume later in the cycle in the pseudo-real case.

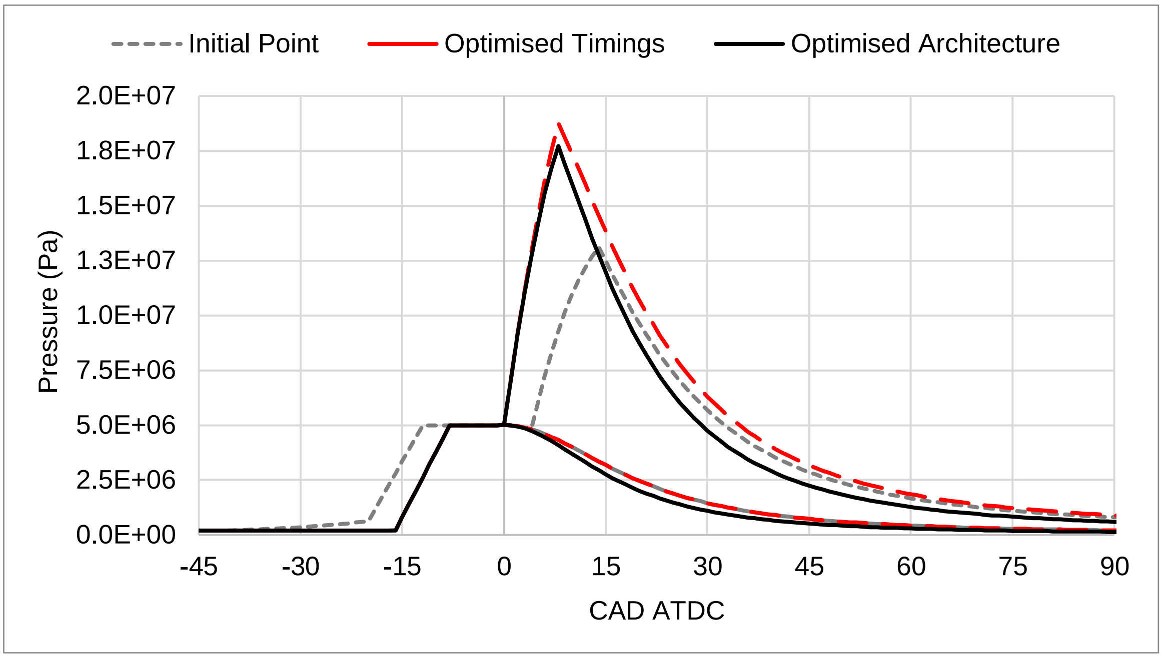

Figure 4.30 Comparison of 0D model pressure traces over three selected stages of optimisation.

Pressure traces show that while the peak pressure is lower, due to increased change in volume smoothing out of the rate of change of volume from engine architecture optimisation, while the overall efficiency increased. A PV diagram highlighting the change in volume is shown in Figure 4.31.

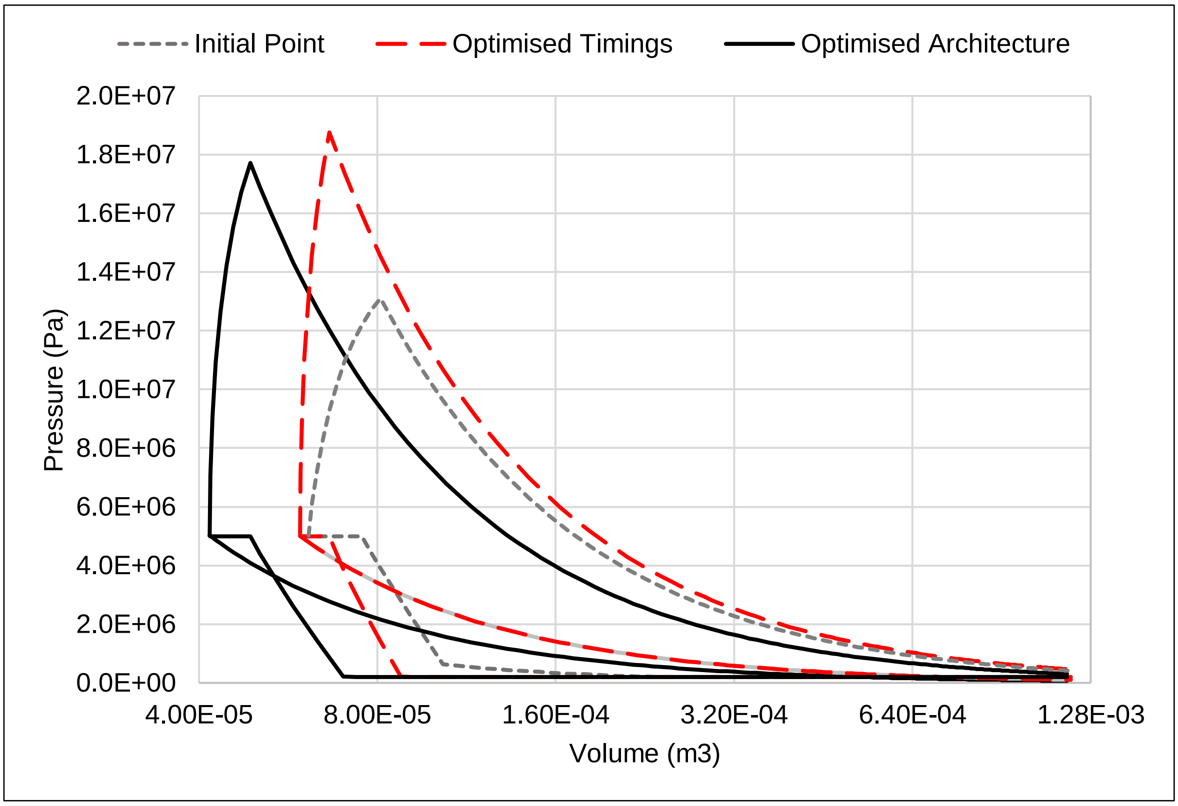

Figure 4.31 Comparison of 0D model PV diagrams over three selected stages of optimisation.

4.10 Discussion

A short evaluation of the cycle and a Carnot analysis were performed in the first part of the chapter. Underlining the potential efficiency benefits of running the overall cycle colder.

A 0D model was created and used as a method of evaluating the RSCE expander. This relatively simple method was used due to the difficulties of separating Rankine work from combustion work in commercial 1D models, such as GT-Suite and Ricardo Wave. The benefits of the 1D commercial applications is that they are more complex and representative of engines, with combustion and losses models more representative than the 0D model demonstrated in the piece of work. However, the 0D model provides a good starting point for interrogation with more complex models or development and provides information on key metrics and differences to conventional cycles.

The model demonstrates that TE alone should not be used as a metric when evaluating the expander in isolation of other systems. As Rankine work is “free” when using TE, this gives deceptive outcomes as to what is the most efficient method of operating the expander. Two metrics are proposed and described, CTE and EFE, which provide can provide a more apt evaluation of how well the expander is truly performing than TE alone.

To maximise efficiency in the expander, volumetric efficiency must be as high as possible, combustion must start early as close to TDC as possible and as fast as possible, in line with conventional engines. In contrast to conventional engines, it is also key to minimise IVP while keeping IVC as close to TDC as possible.

Optimum efficiency is dictated by several extra factors dictated primarily by the changes in valve timings. The optimum expansion ratio is heavily dependent on valve timings, such as IVO due to recompression work. To maximise efficiency over a range of operating conditions, the expander architecture will need to be flexibility in the valve lift and/or timings, and/or variable ER of the expander.

Optimisation of the combustion and valve timings are the key first points to optimise the expander and bring about the highest return on efficiency for a given condition. The compressed air generated from the compressor needs to be transferred or injected as close to TDC as possible to minimise negative torque and maximise the energy extracted from the fuel with minimal penalty. The period in which the expander acts as a “steam engine” should be minimised to ensure the expander does not under expand and maximise efficiency of the expander overall. IVP should only be long enough to allow the cylinder pressure to equalise with the upstream valve conditions. With the correct and optimised timing, the cylinder pressure could be larger than that of the upstream air pressure, due to pressure pulsation/ram air effect.

A larger bore to stroke length is preferable. This should aid breathing and packaging issues, as there is more space for larger diameter or higher number of valves. Minimising IVP as much as physically possible will increase efficiency, as long as volumetric efficiency is maintained or increased.

Running the intake air temperature colder, with high pressure, and high AFR would benefit the efficiency of the expander. Emissions control must be considered with high AFR. However, cold intake gas can mitigate this to an extent, but AFR would need to be limited. The efficiency of the overall RSCE system would need to consider the effectiveness of the recuperator in operating at lower temperature conditions and the cost benefit of the two.

A slightly long conrod is preferable, which in turn can reduce friction but increases mass and overall size. The study suggested this is a relatively small window of optimisation. Shorter crank throws can marginally increase efficiency through optimisation. However, this will reduce torque on the crankshaft. This can be mitigated by larger cylinder bore and higher engine speed to maintain a rated power. There would be high speed engine issues with speed reducing volumetric efficiency and increased friction.

There is merit in further study into offset crank and/or piston pin. This could provide positive efficiency gains through optimisation of the variation in dwell time and change in volume, by minimising the change in volume on the compression side and increasing the change in volume on the expansion side.

To control combustion and maintain high efficiency with varying parameters, such as speed and load, variable valve timing, lift and/or duration will be required. This would allow control of air breathing and pressure and temperature equalisation. As IVP length before TDC is detrimental to efficiency and SOC needs to start as close to TDC as possible, variable valve timing, duration, and lift combined would be the most effective method of control. As with variable lift and duration it is possible to reduce the duration required for a given engine condition. Illustrative examples of this for a given valve lift speed (lift/CAD) are shown in Figure 4.32 for three conditions with the same integral area. High load/speed condition a, medium load/speed condition b, and low load/speed condition c.

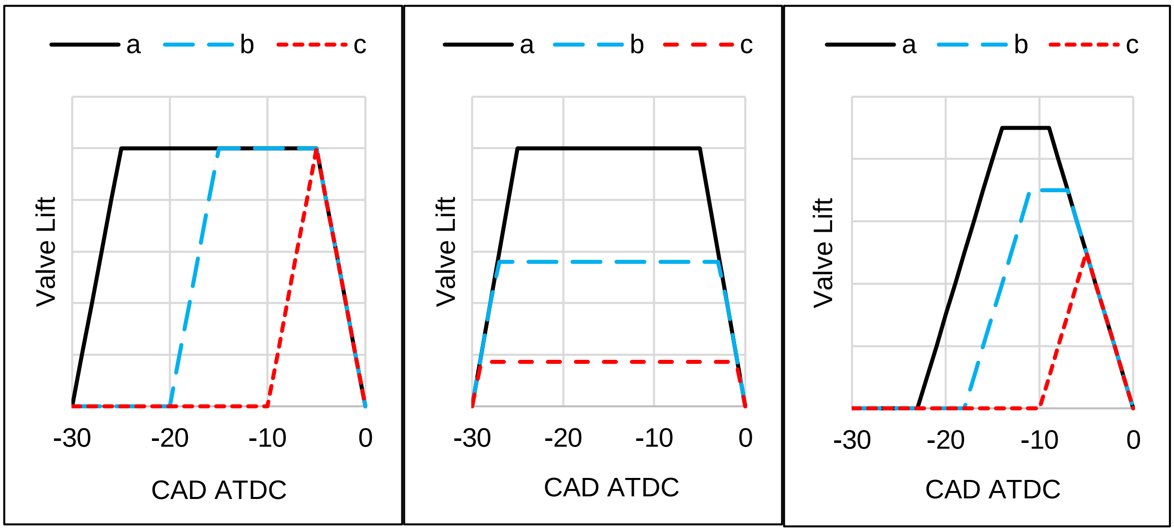

Figure 4.32 Illustrative examples of methods of valve control for conditions of high (a), medium (b) and low (c) speed/load with the same integral area for the three speed/load conditions. With variable duration shown on the left, variable lift centre, and variable duration & lift on the right.

Alternatively, a method of control of air temperature and density would allow variation of load for a fixed valve duration and lift. This could be achieved on the RSCE through a bypass valve route around the recuperator to blend hot air post recuperator and cold air from the compressor. If the exhaust temperature was lower than the compressor out temperature, the bypass would also enable the recuperator to not become a sink of energy that would reduce the overall efficiency of the expander. The other options to avoid this condition would be to decrease ER and improve the isothermal compression of the compressor.

Summary of design considerations to achieve a high efficiency expander:

- Combustion as close to TDC as possible.
- Fast combustion.
- IVP minimised as far as practically possible while still achieving airflow.

- IVC ideally at TDC or after TDC – balance between reducing recompression work and maximising expansion work.
- Low expander intake temperature.
- Air and fuel, as much as possible (high intake pressure, low intake temperature, low AFR, high combustion efficiency, high volumetric efficiency).
- Minimise change in volume on the compression stroke near TDC to reduce compression work.
- Long conrod.
- Short crank throw.

It is worth remembering that this model does not consider the potential reduction in work via quasi-isothermal compression and additional work from exhaust recuperation. If the recuperator can achieve a higher efficiency than the expander, then there is merit in overall system efficiency in decreasing ER, as shown by Dong et al [2]. The combustion power would increase with lower ER, as reducing ER increases the volume and therefore mass of air for a given IVC. However, a full transient system model would be required to understand and balance the competing efficiencies of the system as the exhaust and recuperator temperature changes at various load conditions in the duty cycle. The effects the above variables have on emissions must also be considered, such as AFR, temperature, etc.

Chapter 5 Are the responses of RSCE Expander like that of conventional ICEs?

Investigations and experiments on a single cylinder research rig replicating the RSCE expander.

5.1 Introduction

This chapter primarily explores test bed data from a single cylinder research engine (SCCRE) that replicates the combustion cylinder in a RSCE. The aim of the investigations and experiments were to answer three main questions and aims:

1. Does the RSCE combustion system responds in a similar manner to that of past conventional ICE engines?
2. Are emission responses comparable or lower than that of the of other ICEs?
3. To highlight any differences in responses to that of the conventional ICEs and expected results from the simple 0D model.

It will not interrogate changes to engine architecture, such as ER, piston geometry, conrod length, etc. The variables that can and will be varied during testing will be outlined in the explanation and description of the SCCRE in the next section.

Both emissions and efficiency responses to input variables will be explored in this section. Where possible, comparisons with the predictions from the 0D model will be made and evaluated. Definitively answering which combustion and flame phenomena are occurring will be difficult to achieve but can be discussed and inferred to an extent from responses.

5.2 The Single Cylinder Combustion Research Engine

Test bed parameters, thermodynamic and limited initial test data have been reported to an extent in previous published research by the author and others [2], [3], [152], [164], but will be discussed here in detail. An engine test bed for investigations into the combustion cylinder in the RSCE started testing at The University of Brighton in 2016. Overall front and rear photographs of the SCCRE are displayed in Figure 5.1.

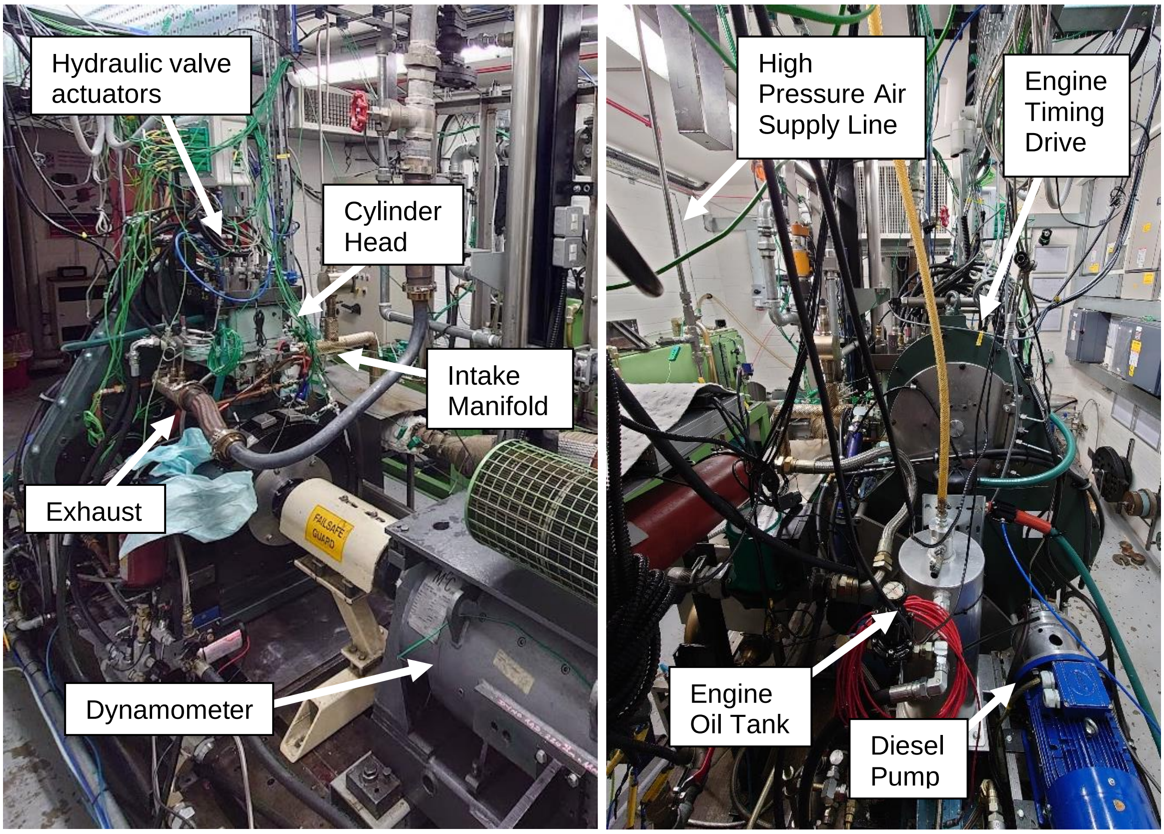

Figure 5.1 Front and Rear photographs of SCCRE and auxillary systems.

The SCCRE is based on a Ricardo Titan single cylinder research engine, which has been modified and fitted with a hydraulic valve actuation system, high pressure intake system, gas burner, recuperator, and accompanying instrumentation. A high-speed hydraulic valve actuation system is utilised on the SCCRE, as this enables full variation of inlet and exhaust valve timings. Modifications to the valve timings can be achieved statically and transiently for testing. Modifications to valve lift can be achieved pretesting through mechanical modifications.

As explained previously, due to the RSCE design, the SCCRE runs a two-stroke cycle, i.e., combustion takes place once every 360 crank angle degrees (CAD). The SCCRE differs from the full RSCE architecture in that compressed air is supplied by an air bank and the recuperator is fed with hot gas from a methane burner. Rather than a compression cylinder feeding the combustion/expansion cylinder and hot exhaust gas feeding the recuperator. This enables a high degree of independent control of key variables that affect the air dynamics and combustion processes in the engine, primarily intake temperature and pressure, allowing isolation of the responses to variable changes. The temperature of the methane burner, and therefore the recuperator, and the air bank inlet pressure, can be varied throughout the testing. Photographs of the 25MPa hydraulic oil system used to control the valves and the gas burner and recuperator systems are shown in Figure 5.2.

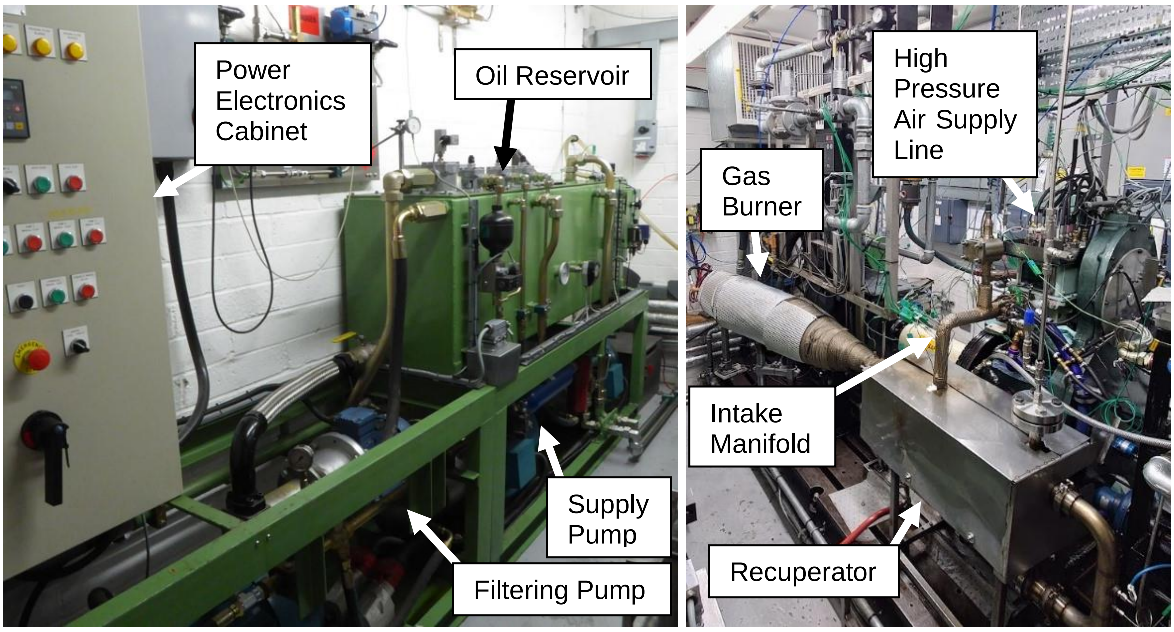

Figure 5.2 Photographs of the hydraulic pack (left), comprising of an oil reservoir and a high pressure and low pressure oil pump, and the gas burner and recuperator (right) systems of the SCCRE.

The SCCRE utilises a ceramic coating of stabilised zirconia to aid insulation of the expander cylinder to minimise heat losses to the surfaces of the piston, upper liner, and valves. This can be seen in the images in Figure 5.3. The details and effectiveness of these coatings will not be discussed, compared, or analysed in this piece of work. However, it is worth noting that these coatings have been utilised to produce the results presented in this chapter.

Figure 5.3 Photographs of the ceramic coating utilised on the surfaces of the piston crown (left), upper liner cuff (left), cylinder head flame plate (middle), valve face (middle), and valve stem (right).

EN590 diesel fuel is utilised in the SCCRE experiments to allow comparison with other known diesel combustion literature. The diesel fuel is supplied through a production common rail direct fuel injection system, with a maximum working pressure of 120MPa (1,200 bar). Utilising a Mercedes Delphi common rail, Delphi 1.5 fuel injector, found on many production Diesel engines, and a separate electric motor driven fuel pump. The Delphi fuel injector has 8 holes and a cone angle of 156°. Baseline SCCRE main parameters are summarised in Table 5.1.

Table 5.1 Initial SCCRE parameters.

Feature	**Value/Description**
Bore	105mm
Stroke	130mm
Compression Ratio	18:1
Injector	Delphi DFI 1.5
Injector Nozzle	8 holes, 156° cone angle
Injector flow at 100 bar	800ml/min
Combustion Chamber	Open shallow bowl
Inlet Valves	Electro-hydraulic, peak lift ~3mm (cold)
Exhaust Valves	Electro-hydraulic, peak lift ~5mm (cold)

A schematic diagram of the compressed air, nitrogen, and exhaust systems for the SCCRE test cell is displayed in Figure 5.4. This demonstrates the two high pressure air banks that feed the SCCRE. A high-pressure compressor fills the air banks overnight to reach maximum pressure (20 MPa) but can also be activated during testing to ensure a longer supply at higher pressures. Typically, the engine is supplied with 2 to 4 MPa air supply to simulate the compressor.

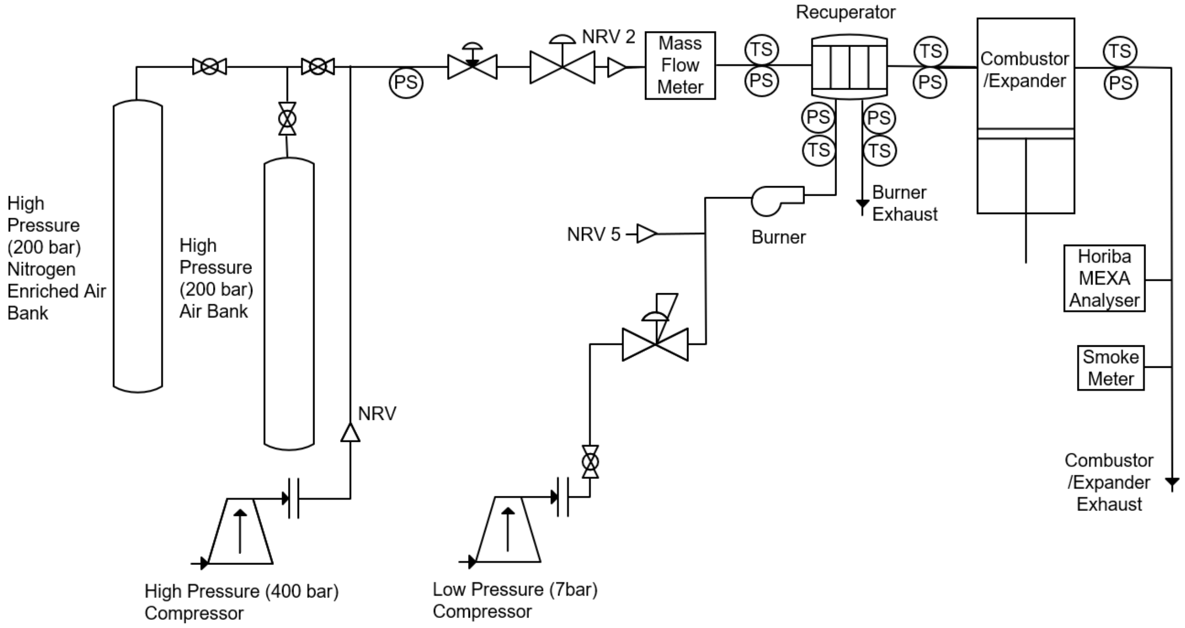

Figure 5.4 Schematic of working fluid and hot recuperator gas supply of the SCCRE test cell.

To simulate nitrogen injection into the compressor and therefore dilution of the intake air, a bank of cylinders can be partially filled with pure nitrogen before filling the remainder with air to reach the desired nitrogen enrichment. A nitrogen dilution of 18% oxygen by volume is typically utilised for nitrogen dilution tests on the SCCRE, as this replicates a modest amount of dilution why keeping above oxygen levels that could potentially cause hypoxia, such as shortness of breath (16%) or loss of consciousness (10%), in unforeseen leakages or worst case events from the large air bank supply to the control room or test cell. Photographs of the two sets of 20MPa air and nitrogen cylinder banks and the Hiflux recuperator are shown in Figure 5.5.

Figure 5.5 Photographs of the two sets of 15 bottle high pressure cylinder banks (left) and the Hiflux recuperator (right) utilised on the SCCRE test bed.

5.3 Data Acquisition & Control Systems

The data acquisition and control system can generally be split into three streams: control systems, high frequency (>1kHz) data acquisition, and low frequency (<10Hz) data acquisition. Several control systems exist for operating and managing the test bed, such as the high-pressure gas supply, methane burner, hydraulic valves, fuel injection, emissions analysers, and other sensors. Some of which are fully independent, such as the hydraulic valves and fuel injection systems. Whereas the others operate at set conditions managed by the main control computer, which runs a version of Horiba STARS Lite Engine test automation software. The Horiba STARS Engine acts as the main test bed controller and data logger, recording all the low frequency data acquisition, such as data from thermocouples, flow meters and emissions analysers. It can also request the IndiCom computer to record high frequency data, which is locally stored on the IndiCom computer.

The separate computer running AVL IndiCom monitors and records the high frequency data from valve position sensors, Kistler pressure sensors operating in the combustion chamber and inlet manifold, and current clamp detecting the injection signal sent from the fuel injection system. A dedicated computer runs Emtronix which controls the fuel injection system, and another dedicated computer runs Ricardo R-Cube and ETAS INCA to control the hydraulic valve system. A diagram providing an overview of the computers, control systems independence, and interconnections is shown in Figure 5.6.

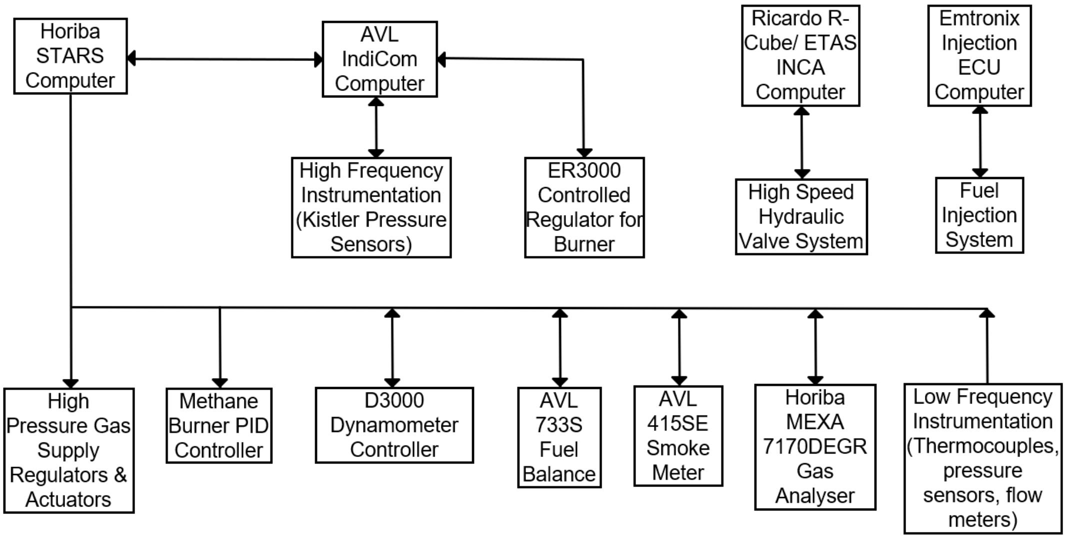

Figure 5.6 Diagram of the interface between data acquisition systems for the SCCRE test bed.

To perform and gather data from the engine test bed, at least two operators are required. One to overseeing the computer running Horiba STARS Lite computer and the other operating the IndiCom, Ricardo R-Cube, and Emtronix computers. Four systems of data collection exist, a paper test cell logbook, an electronic logbook, an electronic engine test request (ETR), a low frequency data log file, and a high frequency data log file. Once an ETR set point has been achieved data collection is started and logged by the operator. Unless otherwise indicated, all tests and data were achieved at stable conditions, enabling reliable data acquisition over the duration of the test logging process.

The STARS computer runs the low frequency (1Hz) data log collecting the average and range of data for each instrument. The STARS logging process takes a log over the course of one minute, first beginning with a purge of the Motor Exhaust Analyser (MEXA) system, before sampling instrument measurements in parallel. The computer running AVL IndiCom records a data set of 100 cycles when requested by the Horiba STARS machine or manually by the operator. From this the average of the 100 cycles, the individual cycles, and other data, such as IMEP, is recorded.

A few key and atypical devices and instrumentation from the SCCRE test bed will be discussed in this section. The list will be non-exhaustive. A David McClure Ltd 130kW 6,000 rpm dynamometer is utilised on the testbed. The dynamometer is operated through a D3000 Digital Dynamometer Controller. An AVL fuel balance 733S is operated to conduct fuel flow measurements. A 1.25kN Novatech F256 load cell it utilised to measure torque. There are two measurements of engine speed; the primary engine speed measurement is provided by a Leine & Linde encoder, with a native resolution of 0.5 CAD which is fed to the AVL Indicom unit. The second is a hall effect sensor located on the flywheel.

A Horiba 7170DEGR MEXA is utilised and measures HC, NO, NOx, CO, CO2, O2, and AFR. An AVL 415SE smoke meter is utilised to measure the filter smoke number (FSN) of the exhaust. Two Kistler pressures are utilised: 6125C measures cylinder pressure. 4007C100 with a cooling jacket measures inlet manifold pressure. A Bronkhorst mass flow meter was utilised; however, this was unreliable for pulsed flow measurements, therefore air mass flow measurements are typically calculated from fuel flow and AFR measurements unless otherwise stated.

Four MOOG E050-807 servo valves were utilised to operate the hydraulic valves. Valve displacement measurement was recorded through four LORD MicroStrain S-DVRT linear displacement sensors. There were reliability issues utilising this approach to measure displacement of the valves. Maintaining calibration was difficult during testing. Therefore, these were primarily used to confirm valve event timings and profile of valve movement but were generally not be relied upon for direct measurement of displacement in distance.

5.4 Equations & Definitions

In addition to the equations discussed in Chapter 4, this section will outline further analytical equations specifically relating to evaluating the SCCRE data from the test bed, as well as definitions. The main additions now that the experiment moves out of the 0D and incorporates emissions testing.

In the expansion cylinder of the RSCE, and other SCE, the capacity is not the swept volume, as in conventional ICEs, instead the volume at TDC, also sometimes referred to as the combustion or “dead” volume, is relevant. The capacity of the expander is a function of the dead volume size, intake pressure, intake temperature, and IVC. Intake valve period (IVP) is defined as the period from intake valve opening (IVO) to the start of intake valve closure (IVC) for the SCCRE testing, as this was the method taken by the engine operators. Exhaust valve period is defined as the period from exhaust valve opening (EVO) to the start of exhaust valve closure (EVC). Exhaust valve inlet valve separation (EVIVS) is defined as the period from EVC to IVO. An illustration of these definitions is shown in Figure 5.7.

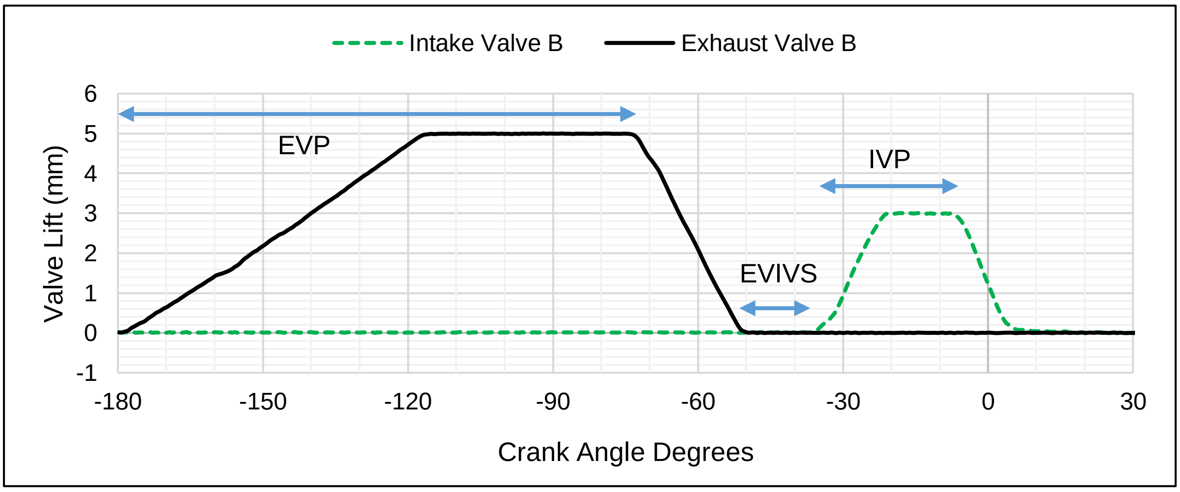

Figure 5.7 Illustration of valve period and separation definitions.

Ignition delay is (IGD) is defined as the difference from the SOI to SOC in CAD. Hydraulic delay is not considered. This is described in Equation (72).

$$\theta_{IGD} = \theta_{SOC} - \theta_{SOI} \tag{72}$$

5.4.1 Normalised Emissions

Angular velocity and power must be defined, as these are prerequisites for calculating power, losses, and normalised emissions. Equation (73) displays the conversion from revolutions per minute n to angular velocity ω. The equation for power $\dot{W}$ is shown in Equation (74), where torque is τ.

$$\omega = \frac{n.2.\pi}{60} \tag{73}$$

$$\dot{W} = \omega.\tau \tag{74}$$

The formula used for mass fraction burned is shown in Equation (75), where m_b denotes the mass burned. As pressure created by IVO can cause a pressure change not created by the change in volume, the mass fraction burned formula is slightly different from the conventional formula, as the calculation starts from the SOC, not from the first logged interval.

$$MFB = \frac{m_{b(i)}}{m_{b(total)}} = \frac{\sum_{\theta_{SOC}}^{i} \Delta p_C}{\sum_{\theta_{SOC}}^{n} \Delta p_C} \tag{75}$$

To normalise emissions from the engine across speed and load ranges, brake specific emissions must be calculated. Therefore, exhaust mass flow must be known. In the absence of direct measurement, exhaust mass flow can be calculated by assuming all fuel, air, and combustion products exit engine through the exhaust. The amount of mass that is missed, such as from soot build up in engine and blowby, from this calculation is negligible. The calculation for exhaust mass flow is given in Equation (76), where $\dot{m}_{exh}$ is the exhaust mass flow, $\dot{m}_f$ is the mass flow of fuel, and $\dot{m}_a$ is the mass flow of air.

$$\dot{m}_{exh} = \dot{m}_f + \dot{m}_a \tag{76}$$

Equation (77) displays conversion from exhaust mass flow to molar exhaust flow rate, $\dot{mol}_{exh}$. A molar mass of 29g/mol is utilised for the exhaust molar mass, MM_{exh}, in this piece of work.

$$\dot{mol}_{exh} = \frac{\dot{m}_{exh}}{MM_{exh}} \tag{77}$$

The equation to calculate the mass flow of the emissions, $\dot{m}_e$, is shown in Equation (78). Where MM_e is the molar mass of the emissions, $VF_{e\,dry}$ is the dry volume fraction of emissions, and k_{hum} is the humidity correction factor. A humidity correction needs to be applied to convert from dry to wet air. As no dynamic intake humidity data is available on the engine and as the engine is supplied by a bank of compressed air cylinders, which is pressurised with an industrial air compressor with a humidity collector before the HP air regulator, there is a set moisture/humidity content that is produced. Therefore, for all data produced from the SCCRE the correction factor is assumed to be constant. 0.9 is used as the assumed value for the humidity correction factor k_{hum}.

$$\dot{m}_e = MM_e.VF_{e\,dry}.\dot{mol}_{exh}.k_{hum} \tag{78}$$

The mass flow of emissions can then be used to calculate the brake specific emissions (BSE). This is displayed in Equation (79), where BS_e is BSE.

$$BS_e = \frac{m_e}{W_b} \tag{79}$$

As previously discussed in Chapter 4, the work created from the expander can be misleading when evaluating the expander in isolation of the compressor. Therefore, a further calculation for the expander specific emissions (ESE) is shown in Equation (80), where ES_e is the ESE. This will not fully capture the losses but is another useful metric for evaluation of the engine.

$$ES_e = \frac{m_e}{W_{EA}} \tag{80}$$

Brake specific fuel consumption (BSFC) is displayed in (81), where BS_{FC} is the BSFC.

$$BS_{FC} = \frac{m_f}{W_b} \tag{81}$$

Expander specific fuel consumption (ESFC) is displayed in (82), where ES_{FC} is the ESFC.

$$ES_{FC} = \frac{m_f}{W_{EA}} \tag{82}$$

5.5 Comparison & Evaluation of Real Expander Pressure Trace Data

In this section, selected experimental results from the SCCRE will be reviewed and compared to illustrate the fundamental differences brought on by combusting at the representative conditions of a real RSCE expander engine. Some of results have been reported in past research [164] but will be discussed here in more detail and compared to conventional a Diesel ICE and the 0D model to highlight the key questions regarding how the RSCE combustion system operates. The two comparisons will be discussed in this section.

5.5.1 Comparison with Conventional Engine Data

A comparison of three pressure traces can be seen in Figure 5.8, a comparison of PRR and ignition delay is also shown in Table 5.2. One pressure trace is that of a conventional Diesel cycle from a Ricardo Hydra single cylinder research engine at 2,000 RPM, air fuel ratio (AFR) of 21 and 140MPa rail pressure. The two other pressure traces are from the SCCRE and are of differing intake pressures (3.85MPa and 2.89MPa) at 1,200RPM, 21 AFR and 120MPa rail pressure. The valve events for the SCCRE are noted at the bottom of Figure 5.8, the valve events of the conventional Diesel pressure trace are not noted. All tests displayed in Figure 5.8 have the same start of injection (SOI) timing of -4 CAD.

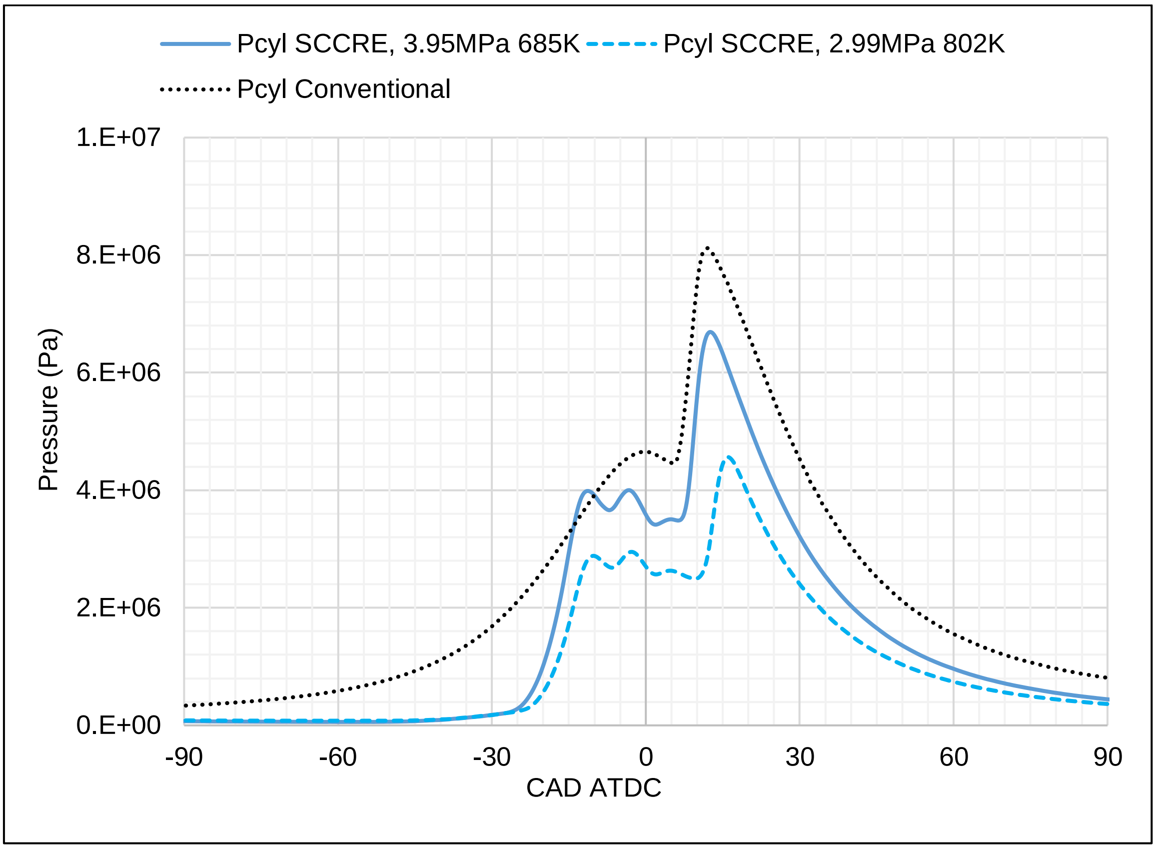

Figure 5.8 Comparison of three pressure traces. Two from the SCCRE at 1,200 RPM and one from a conventional Diesel engine at 2,000RPM. All at 0.69 equivalence ratio (21 AFR). SCCRE data previously reported in [164].

It can be seen in Figure 5.8 that the two pressure traces of the SCCRE do not resemble that of conventional Diesel or Otto ICEs pressure traces. There is a small increase in pressure at -35 CAD as a small amount of residuals from the previous cycle are compressed. Before a sudden large increase in pressure at intake valve opening (IVO) is recorded, as air is introduced into the chamber and equalises to the set inlet manifold pressure. Pressure equalisation occurs before the maximum valve lift of 3mm is achieved. The intake valves close (IVC) after TDC when expansion is already underway and, depending on the case, combustion may already be occurring. A more detailed investigation of the air motion during these steps will be covered in Chapter 6.

Table 5.2 Comparison of maximum PRR and ignition delay of the three pressure traces presented in Figure 5.8.

Pressure Trace	Maximum PRR (MPa/CAD)	Ignition Delay (CAD)
SCCRE 3.95MPa	1.0	11
SCCRE 2.99MPa	0.6	14
Conventional Diesel	1.0	9

Comparing first the two SCCRE pressure traces: Both cases have identical valve timings, injection timings, operating at 1,200RPM, 120 MPa rail pressure and an AFR of 21. However, they differ in manifold pressure and intake temperature. As the methane burner that feeds the recuperator is at the same set temperature (~1,080K) in both cases and the mass flow of air through the recuperator increased with pressure, this led to a variation in temperature between the two cases. The 3.95MPa intake pressure case has a decreased ignition delay of approximately 3 CAD and increased PRR of 0.2MPa/CAD compared to the lower 2.99MPa case. Both cases display a small increase in pressure around 3 CAD with similar PRR. This is most likely the result of reflected pressure waves in the cylinder but could be a small initial heat release. This is followed by the main heat release, with an earlier and faster burn in the 3.95MPa intake manifold pressure test point.

Comparing the conventional Diesel and 3.95MPa case: Both the 3.95MPa SCCRE and conventional Diesel pressure traces have similar maximum PRR of approximately 1.0MPa/CAD, with the 2.99MPa displaying a slightly lower maximum PRR of 0.8MPa/CAD. Similarly, the higher pressure SCCRE case and conventional Diesel differ marginally in ignition delay, with ignition delays of 11CAD and 9CAD, respectively. The lower pressure 2.99MPa case displayed a longer ignition delay of 14CAD. However, once the differences in RPM are considered, the Diesel pressure case demonstrates that the higher temperature and pressure in the conventional Diesel trace is resulting in almost 167% increase in PRR. Both comparisons demonstrate that increased PRR, and therefore reactivity, is still primarily dictated by pressure and temperature conditions of the charge air.

5.5.2 Comparison with the 0D Model

To compare a real data case with the 0D model, first a few inputs and assumptions are required to from the real data case. Two key inputs are temperature and pressure. The pressure of the intake is 2.99MPa. Temperature is 802K out of the recuperator. There are caveats with the temperature measurement, as this is the measured gas temperature out of the recuperator and may not be fully representative of the temperature of the gas in the chamber once it has equalised with the pressure upstream of the valves.

For this case, SOC is assumed to begin at 9.4 CAD. It is not possible to say accurately whether combustion occurs before this point without optical data. However, as SOI begins before IVC, it is likely there is a small amount of combustion occurring before this point that cannot be detected.

The valve timings, intake pressure fill rate, DOC are then best fit to provide a comparison with the 0D model in this first case. Figure 5.9 demonstrates real pressure data compared with a best fit of the 0D model.

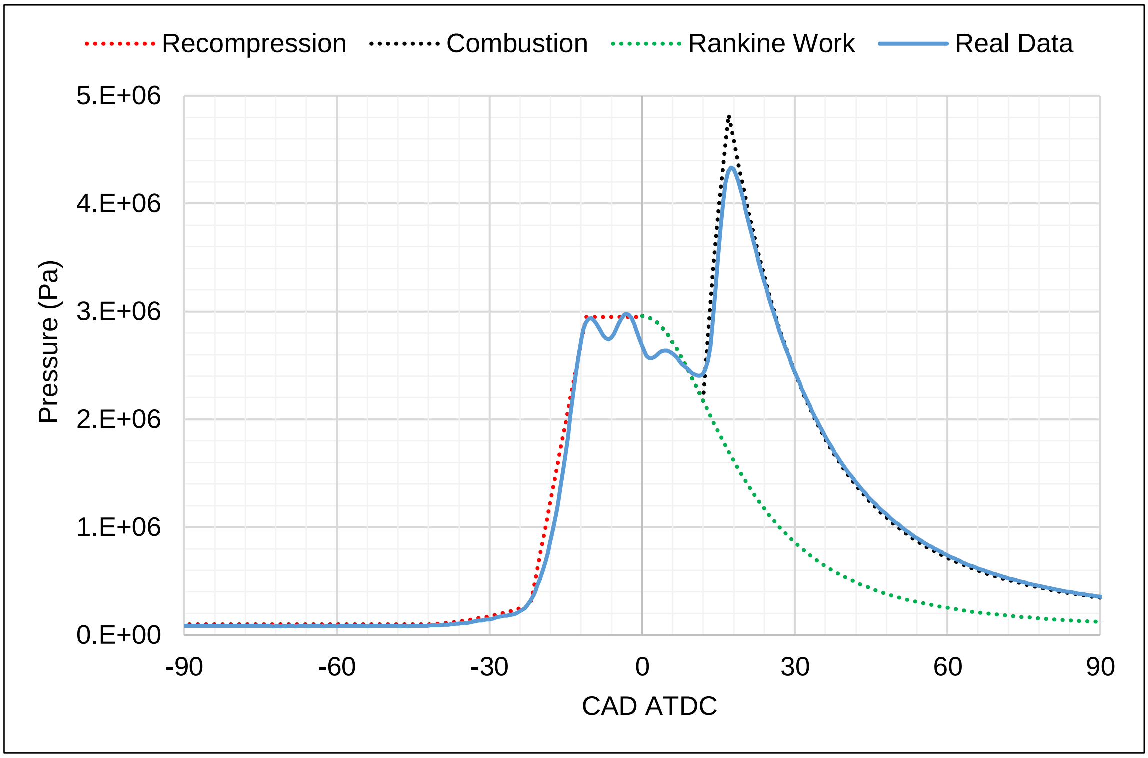

Figure 5.9 Example of best fit approach of 0D model with real pressure data.

A pressure volume (PV) diagram is shown in Figure 5.10 below of the real and best fit data. This comparison begins to highlight some of the issues with the best fit approach, such as at which point SOC begins. The high-pressure pumping loop is clear from the real data. Ideally this would be minimised or eliminated to maximise efficiency. There are issues with the best fit approach for evaluating the combustion work, Rankine work, and performance of the expander. Valve timings do not fully match, due to valve size, valve movement, differential pressure and mass flow rate calculations are not incorporated in the 0D model.

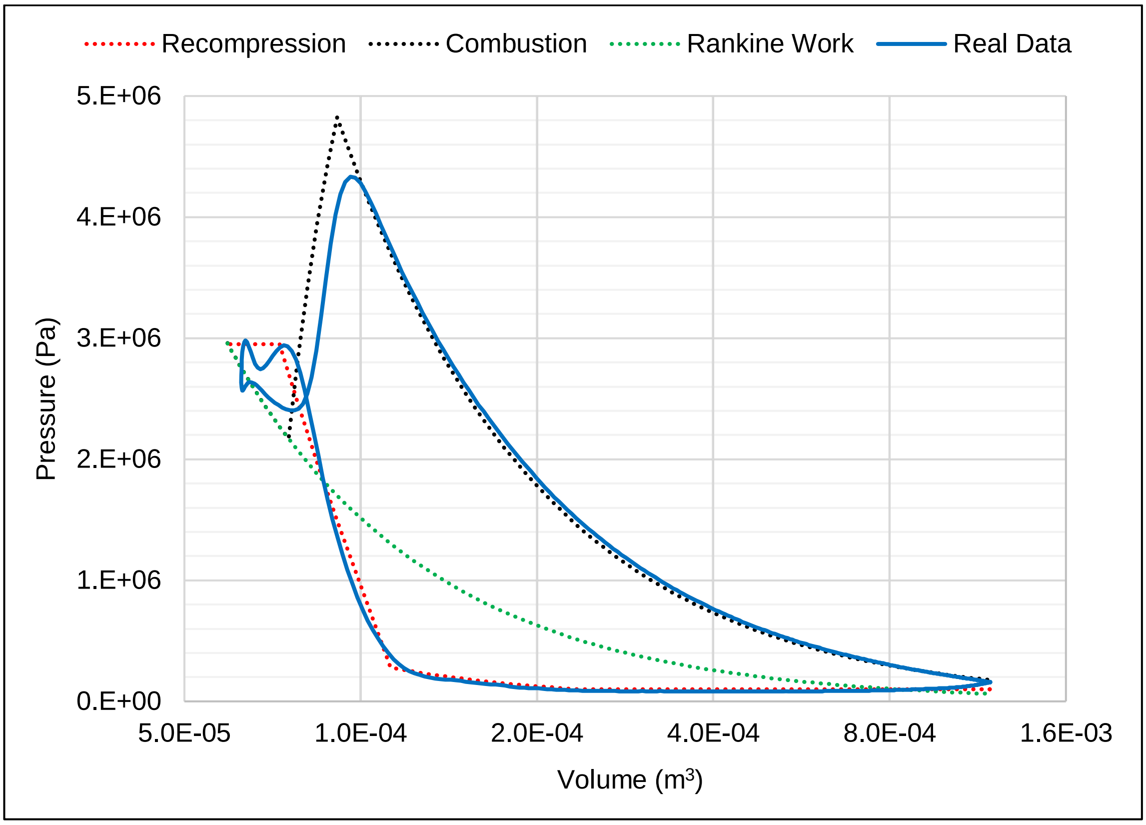

Figure 5.10 PV diagram comparison of best fit approach and real data.

There are issues with inlet pressure fluctuations and combustion pressure which are not captured accurately. These issues are evident when comparing the pressure change not created by changing volume between the real and best fit case, shown in Figure 5.11. The Figure shows a variable rate of PRR would have made an improved comparison for initial chamber filling, dependant on valve geometry and movement. A fluctuation could have been added for the period between chamber filling and SOC. Though this would need to be tuned. Instead of a DOC producing a constant heat release, a heat release map with increasing heat release around 50% burn would have yielded better comparisons. However, the aim was not to create a high precision model but to investigate the effects of major variables. Comparing the GW from the best fit (709.17J) vs the real case (714.09J) shown in this section, the best fit approach achieves a high accuracy, within 0.7% of the real case.

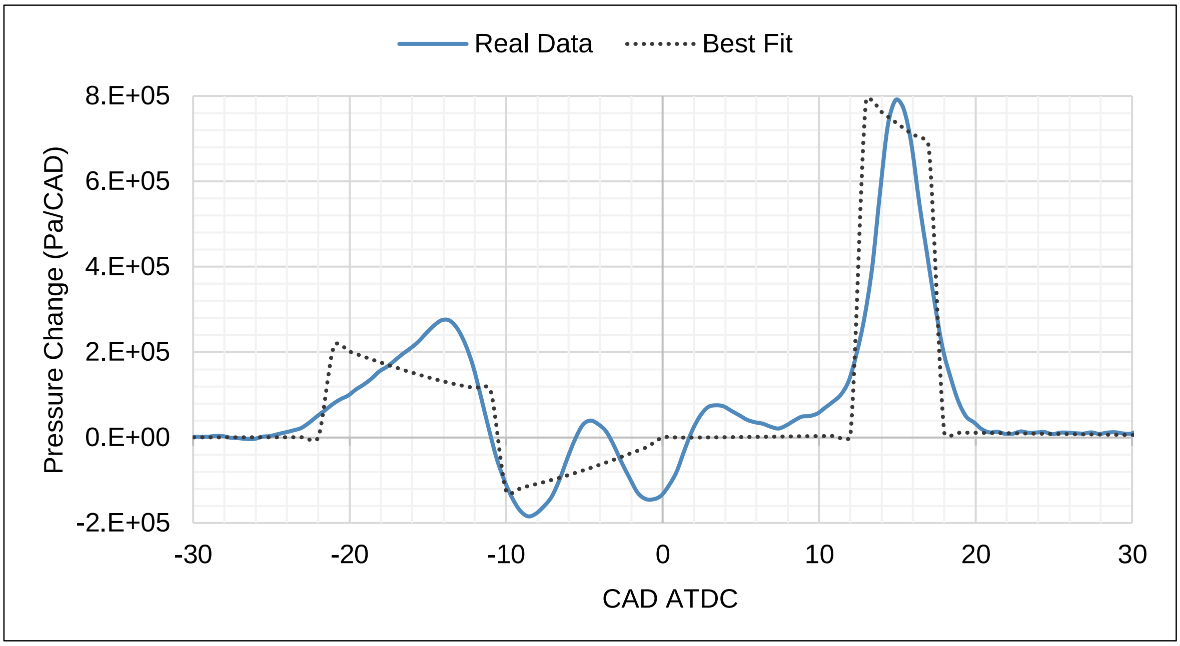

Figure 5.11 Comparison of 0D model best fit with real pressure change data.

For a real case to evaluate Rankine work, combustion, and efficiencies realistically, accurately, and quickly, the pressure data from the real case will be used up until SOC. Rankine expansion pressure will then be calculated from the change in volume after SOC using Equation (57). Which can then be utilised to generate work and efficiencies. An example using the data presented in shown in Figure 5.12.

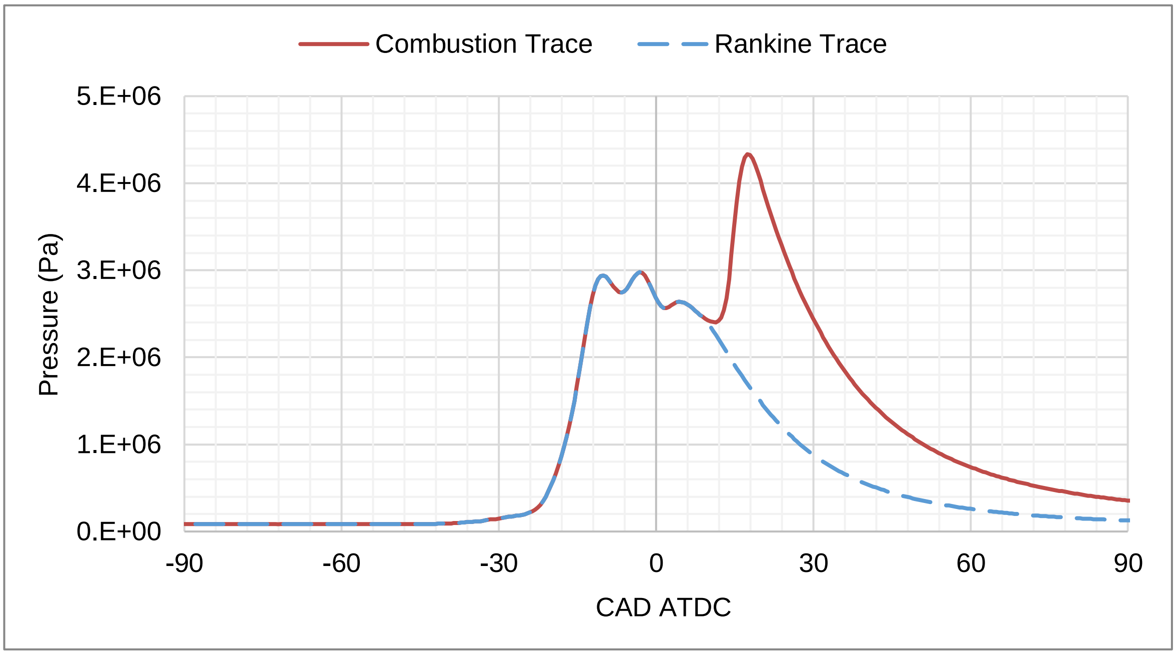

Figure 5.12 Example of approach to calculate Rankine work from real pressure data.

There remains an issue of deciding at which point SOC begins when looking at a combustion trace, such as the one shown in Figure 5.12, to calculate the Rankine pressure trace without combustion. Once IVC has occurred it can be assumed that any pressure change after IVC can be attributed to pressure created by combustion. However, pressure waves detected by the pressure sensor still make this an estimate with ~1-2 CAD accuracy. This typically only has a small effect on work (0-20J) created as combustion and Rankine work, which is acceptable. If fuel is injected before IVO and ignites before IVC, it will not be possible to capture this from the pressure trace.

The difference and improvement of the best fit approach compared to that of calculating pressure change due to volume from SOC is shown in Table 5.3. Gross Rankine work (GRW) showed the greatest difference between the two methods, with a 10.5% decrease in in the volume after SOC method compared to the best fit approach.

Table 5.3 Comparison of best of fit approach and volume method after SOC.

Metric	**Best Fit Approach (J)**	**Volume after SOC Method (J)**	**Difference (J)**	**Percentage Difference**
Gross Rankine Work	170.06	153.91	16.15	10.5%
Recompression Work	-196.04	-207.94	11.90	6.1%
Combustion Expansion Work	544.03	555.26	11.23	2.1%
Expansion Work	347.99	327.32	20.67	6.3%

For analysis of the rest of the cases presented in this chapter, the approach of calculating the pressure trace from volume after estimated SOC will be used to evaluate Rankine work. Rather than a best fit approach utilising the 0D model, this will enable higher accuracy and produce a faster result.

5.6 Injection Timing Swing

5.6.1 Aim

Injection timing swings have been shown to be a useful tool for lowering NOx emissions in conventional engines, due to late combustion phasing enabling lower peak combustion temperatures. However, they have typically incurred a trade off with efficiency, and increasing fuel consumption. As demonstrated in the 0D model and in conventional engines, combustion closer to TDC creates higher pressures and temperatures, this allows for a greater expansion and therefore captured work.

The aim of this swing was not to produce positive work or high efficiency, but to investigate the combustion sensitivity to injection timing, and its effect on emissions.

Therefore, a relatively early IVO and long IVP is utilised to give a stable condition to operate within.

5.6.1 Data Quality

Issues were present with the high-speed cylinder pressure data in this set of testing. Unresolved, this would affect the pressure and combustion calculations. However, this does not impact low speed data and other areas and evaluation of ignition delay can still be interrogated. There were questions on whether this data is real and produced from other phenomena such as Helmholtz resonance, detonation, knock, or other type of combustion. However, the presence of this noise throughout the signal, presence in the non-combusting periods of the pressure trace, and consistent oscillation attributed this to damage to the sensor or possibly a consistent source of unknown noise.

For the high-speed cylinder pressure data for this set of testing, a centred moving mean average (CMA) was applied to reduce noise and produce a smoother signal from the data. The length of the average was minimised as much as possible to avoid eliminating accuracy and fidelity from the high-speed data. The CMA was taken over 3 data points. Summing the previous and following data point for the CMA. The data is recorded from Indicom at intervals of 0.5 CAD. Therefore, the average is over 1.5 CAD. An example of the raw cylinder pressure data compared to the 3-point CMA is shown in Figure 5.13. The graph focuses on the intake pressure waves and combustion as this is the location of the highest amount of noise.

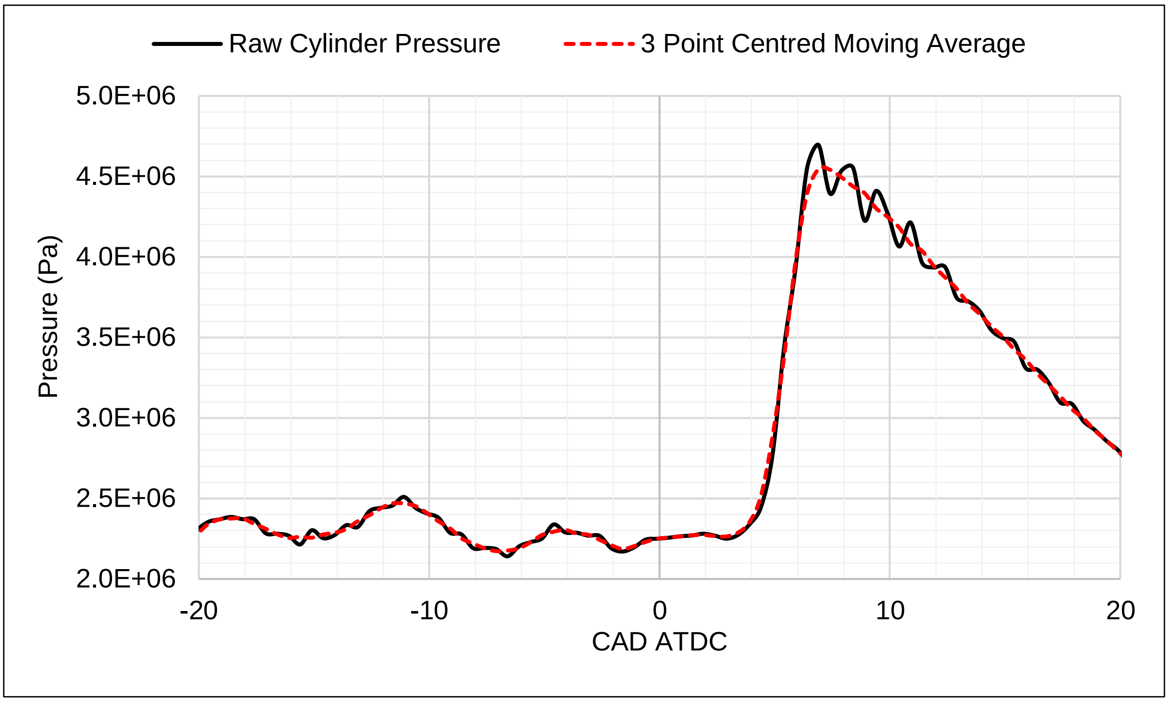

Figure 5.13 Injection Timing Swing – Raw cylinder pressure data compared with the 3 point centred moving average.

This is not a perfect solution, as some fidelity and accuracy is lost on SOC and lowers peak pressure, but this provides a more realistic dataset to be utilised to calculate pressure changes, work, and efficiency. There remains a small amount of noise in the 3-point CMA data, most notably just after peak cylinder pressure.

The improvement the CMA brings when analysing the data is clear when comparing the calculated pressure change from the raw data and several CMAs of differing lengths. Figure 5.14 displays a comparison of the raw data with CMA of lengths of 3, 5 and 7 points. There is a significant improvement in noise reduction from the 3 point CMA, with lower improvements when increasing to 5 and then 7 point CMA. However, there is a large effect on the peak cylinder pressure at 5 and 7 CMA. For these reasons, the 3 point CMA was chosen as the optical to use for the data.

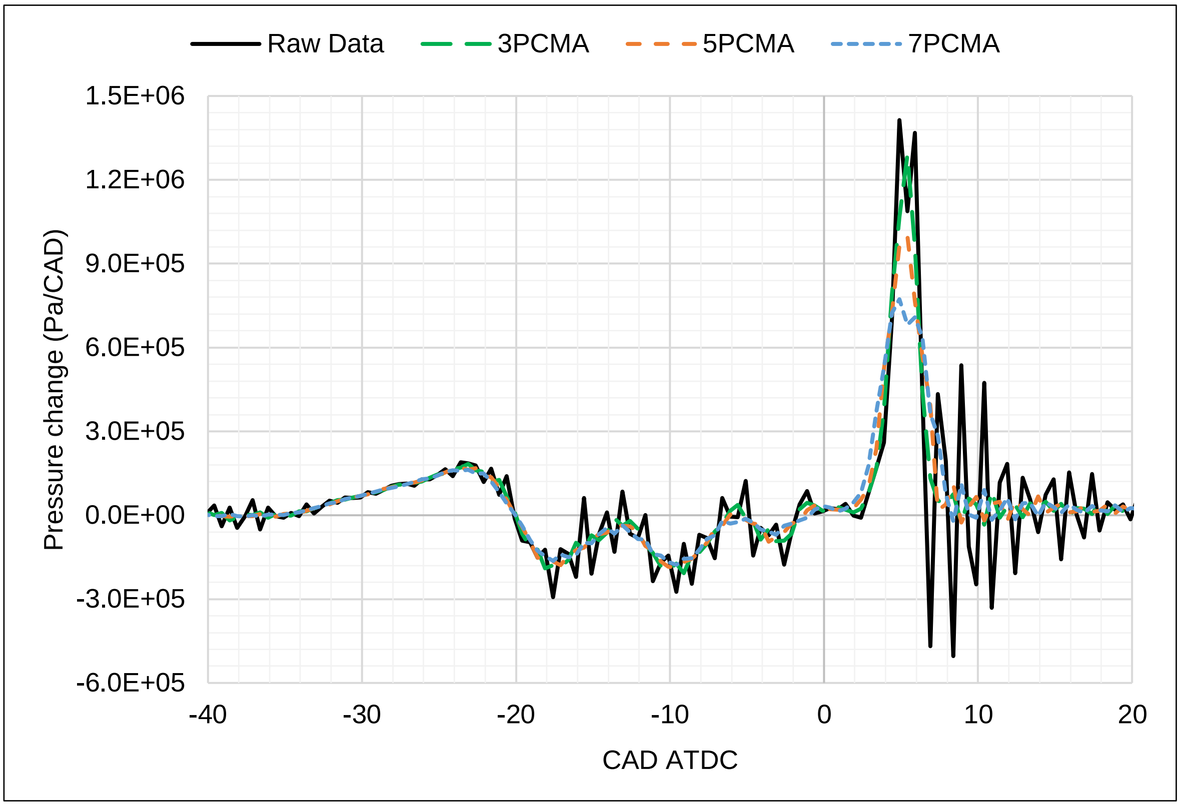

Figure 5.14 Injection Timing Swing – Pressure change calculated from raw data, 3 point CMA (3PCMA), 5 point CMA (5PCMA), and 7 point CMA (7PCMA).

All of the cylinder pressures and resulting calculations in the rest of Section 5.6 Injection Timing Swing will utilise the 3-point CMA approach on the test data.

5.6.2 Initial Conditions

The initial conditions for the SOI swing are shown in Table 5.4.

Table 5.4 Initial conditions of the injection timing swing tests.

Quantity	Value	Units
Intake Pressure	2.5	MPa
Rail Pressure	80	MPa
Engine Speed	1200	RPM
AFR	21	-
Intake Valve Opening	-35	CAD ATDC
Intake Valve Period	30	CAD
Exhaust Valve to Intake Valve Separation	15	CAD
Exhaust Valve Opening	175	CAD ATDC
Gas Burner Temperature	1073	K

Figure 5.15 displays the valve setup for the injection swing.

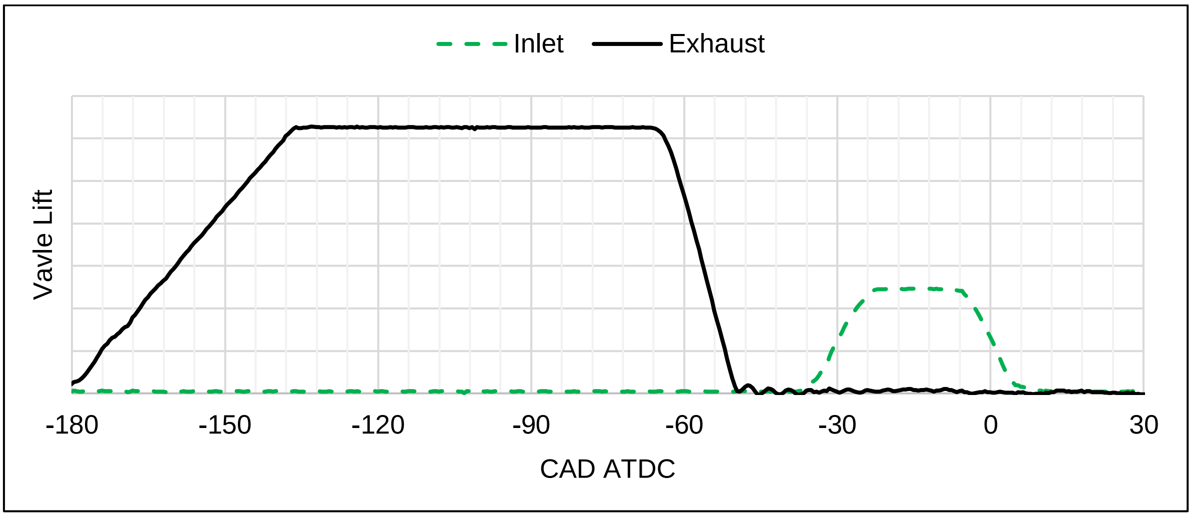

Figure 5.15 Injection Timing Swing – Valve profiles.

Table 5.5 displays the test number with the differences in SOI. SOC, IGD, GIMEP mean and GIMEP standard deviation (SD) is also shown.

Table 5.5 Injection timing swing tests.

Test Number	SOI (CAD ATDC)	SOC (CAD ATDC)	IGN Delay (CAD)	GIMEP Mean (Pa)	GIMEP SD (Pa)
1	-6.0	4.4	10.4	394,627	12,816
2	-5.0	4.9	9.9	394,233	8,351
3	-4.0	7.4	11.4	395,944	11,689
4	-3.0	10.0	13.0	393,541	7,997
5	-2.5	9.4	11.9	383,862	9,074
6	-6.0	4.4	10.4	395,386	11,219
7	-7.0	2.4	9.4	393,895	12,238
8	-8.0	2.0	10.0	394,307	6,234

5.6.3 Results & Analysis

5.6.3.1 Cylinder Pressure

The pressure traces of an injection timings swing are displayed in Figure 5.16. The SOI swing is performed from -8.0 to -2.5 CAD ATDC.

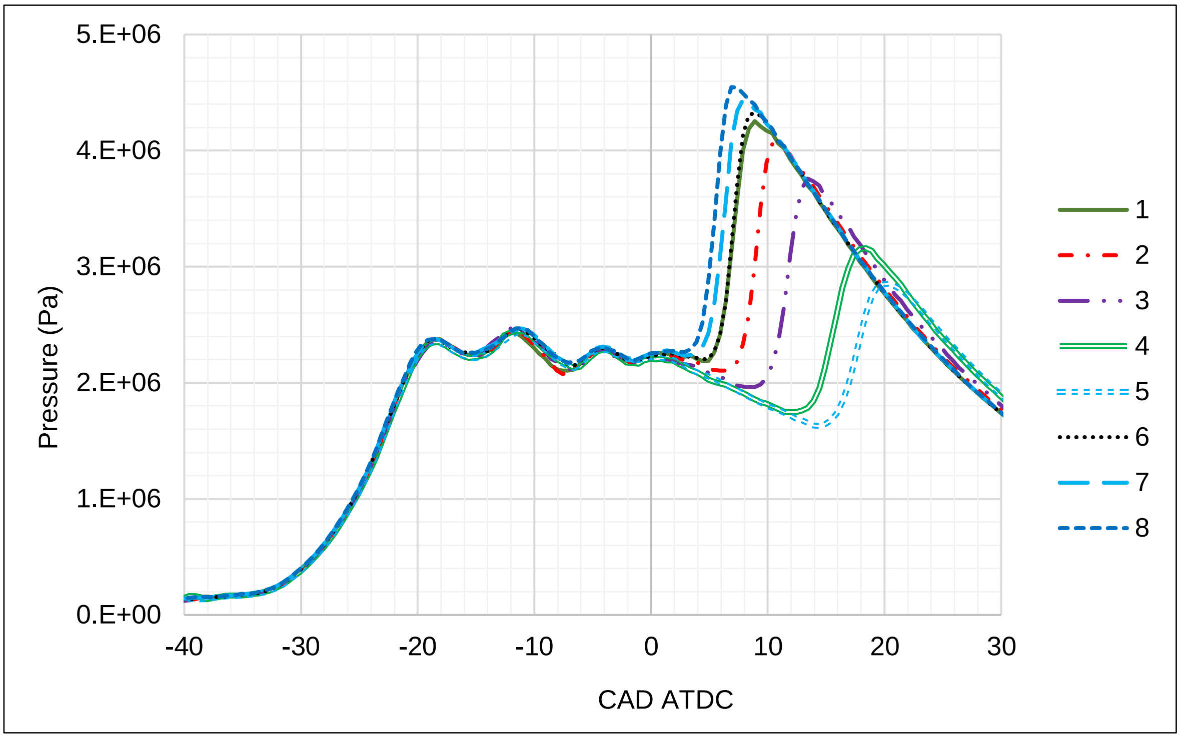

Figure 5.16 Injection Timing Swing – Cylinder pressure traces

Figure 5.17 displays the Rankine pressure traces for all 7 test points. In theory all of the Rankine pressure traces should be identical. However, due to pressure sensor error, the variation in start of SOC, and therefore variation at which point the change in volume method begins, there is a variation in the Rankine pressure trace. There are small variations in recompression work of 6.3J, 9.4J in Rankine expansion, and 6.5J in GRW. This results in a worst-case variation of 2% in recompression work and 3% in Rankine expansion work. This variation is considered small and acceptable across the test points.

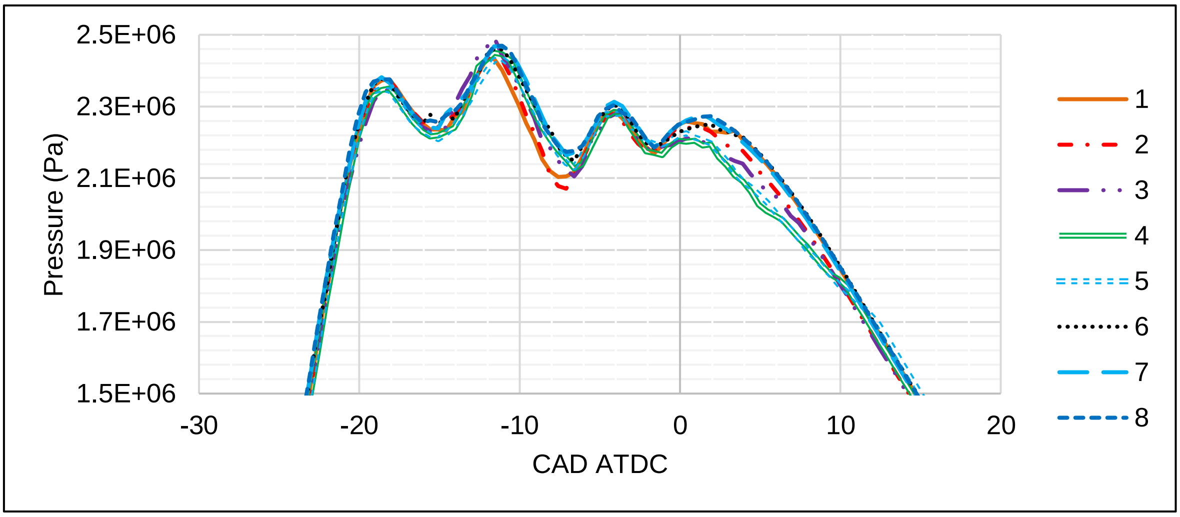

Figure 5.17 Injection timing swing – Difference in Rankine pressure traces

The PV diagrams for the test points are shown in Figure 5.18. This figure highlights a reduction in high pressure pumping loop work across the test points. With earlier ignitions resulting in almost no high-pressure pumping loop.

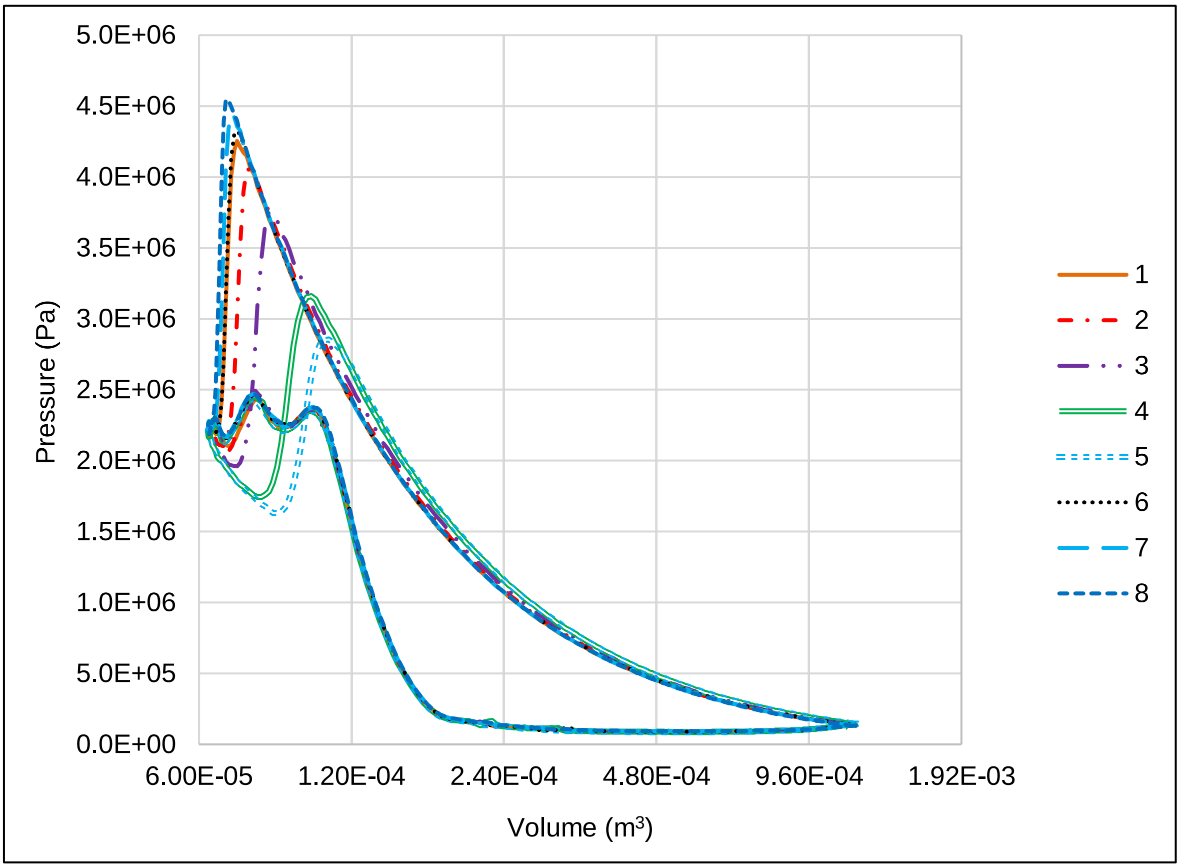

Figure 5.18 Injection timing swing – PV diagrams

5.6.3.2 Ignition & Combustion

The trend in ignition delay remains constant from -8 to -6 CAD SOI timings, before increasing at a steady rate between -6 and -2.5 CAD. The approximate ignition delay can be seen in Figure 5.19. The ignition delay of 11.7 CAD can be attributed as the fastest rate of ignition at the set experimental conditions, while the late combustion phasing is expected to decrease as the bulk of the fuel burns later in the chamber. The sinusoidal movement of the piston is expected to quickly reduce the temperature and pressure and therefore reaction times, as the piston no longer moves out of the dwell zone at TDC. It is for the same reason that burn angle and PRR are seen to follow the same trend, i.e., the reaction rate has an inverse relationship with ignition delay with decelerating reaction time and accelerating ignition delay time.

Although the general trend is positive, test points with -7, -5 and -2.5 SOI have a slightly lower ignition delay than the preceding SOI timing. These couple of CAD changes roughly match that of the pulsations of inlet pressure. The variation in ignition and CE could be the result of changing air dynamics occurring around the varying points of SOI, with higher pulsations and turbulence at points after IVO. However, this result on its own is not enough evidence, especially with the resolution of a 1 CAD change is not enough and without repetition of the test points.

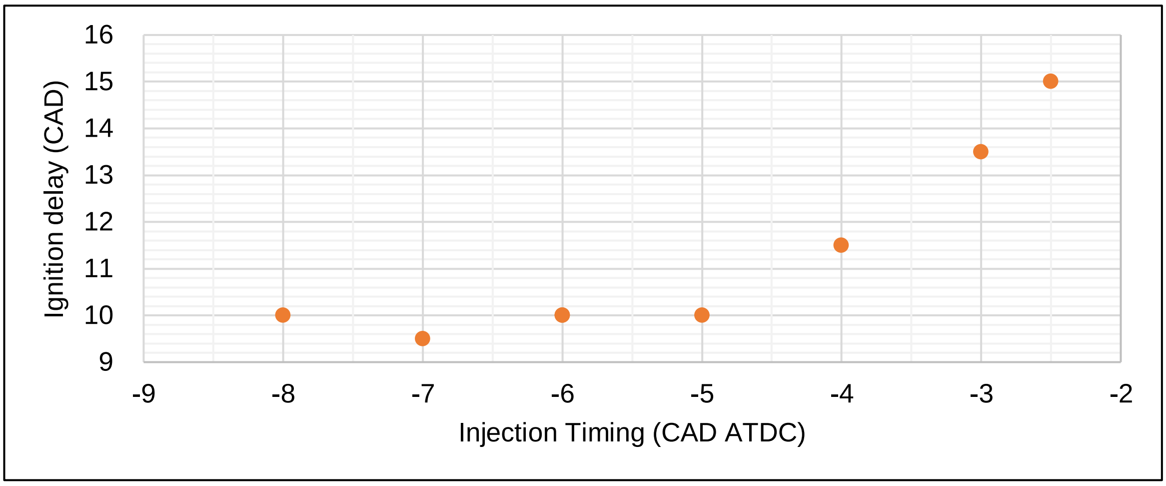

Figure 5.19 Injection timing swing – Ignition delay

Mass fraction burned is shown in Figure 5.20. This again highlights the earlier ignition with earlier injection. The mass fraction burned shows the burn rate is faster in the earlier injection cases. There are two potential main causes of this. Due to SOC starting later in the cycle, a degree of expansion of the gas has already occurred. Leading to lower combustion temperatures, as well as shorter duration of sustained higher temperatures, as the cylinder and expansion accelerate. As the SOI moves further away from IVC, there may be lower mixing and kinetic potential available to break up and accelerate atomisation of the fuel spray.

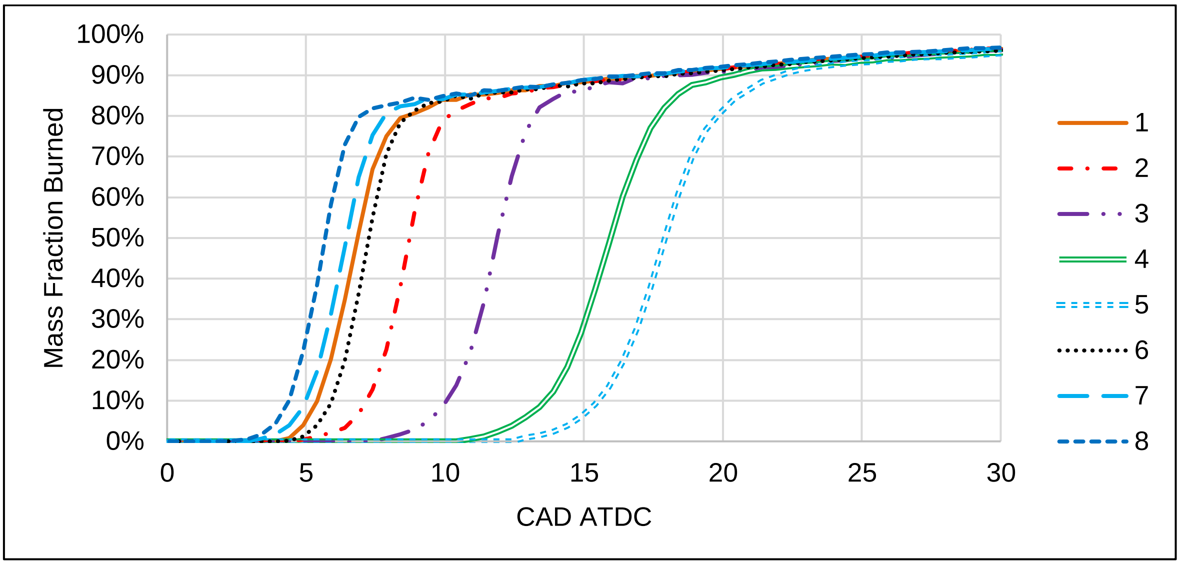

Figure 5.20 Injection timing swing – mass fraction burned.

5.6.3.3 Efficiencies

Figure 5.21 displays the CE for the test points. There is not a consistent response in CE to injection timing. There is a relatively large variation in CE, from 49 to 63% overall. As CE can only be calculated after IVC, there will likely be some combustion occurring while the inlet valves are open which is missed, especially in the earliest injection cases. Following the earlier suggestions of effects of temperature and atomisation, it would have been expected that both causes would lead to increased CE. However, it may be the case that with earlier SOI there is an increased amount of burning before IVC, leading to less pressure build up and therefore a higher amount of fuel being uncaptured as a pressure rise in the cylinder.

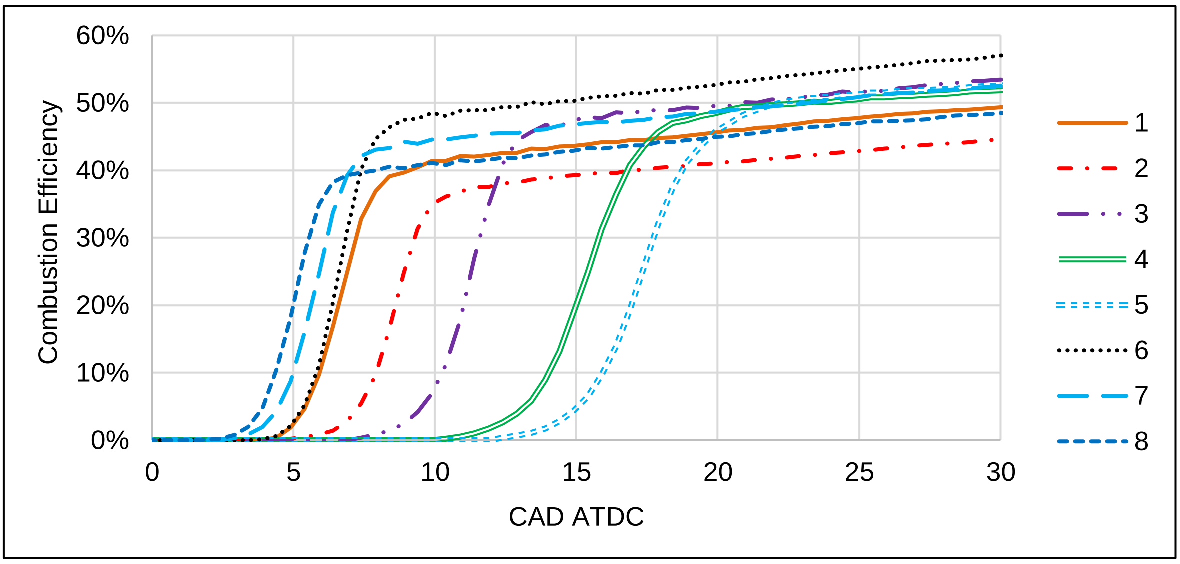

Figure 5.21 Injection timing swing – Combustion efficiency

A comparison of efficiencies against SOI is displayed in Figure 5.22. EAW is negative in these cases, due to the large amount of recompression work required in these test points, therefore EFE is not reported. There is a small increase in CTE and CE from -8 to -6 CAD ATDC. This is either due to less combustion occurring while the intake valves are open, and/or there is an increase in air fuel mixing. TE remains high, due to "free" Rankine work, at between 55.2 and 62.5%. TE and CTE both decline with retarding SOI timings, this is expected with later and lower peak pressures and the high-pressure pumping loops with later SOI timings. BE is between 20.4 and 26.9%, there is an inconsistent response which is due to the variability of CE.

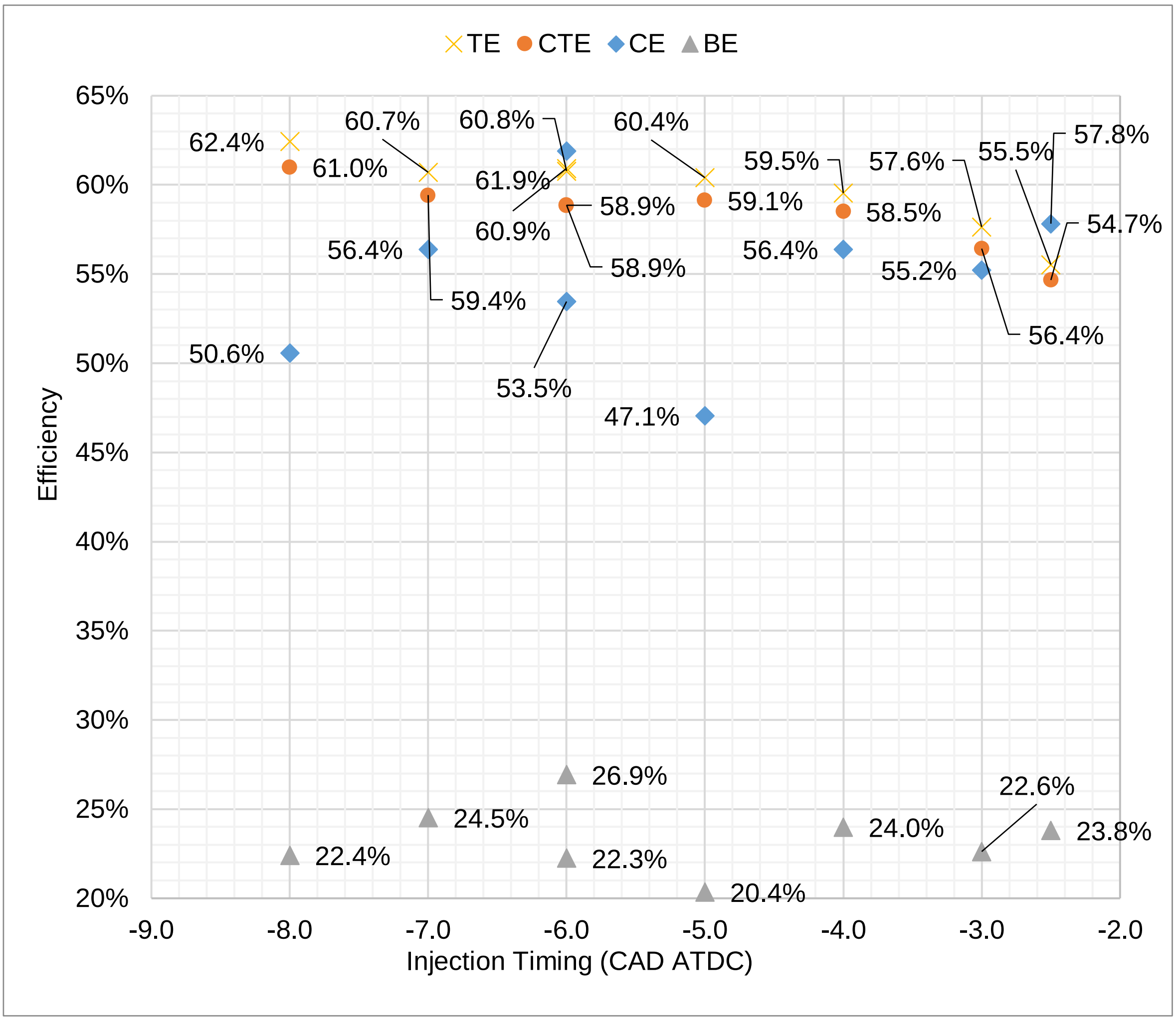

Figure 5.22 Injection timing swing – Efficiencies

5.6.3.4 Emissions

Figure 5.23 displays the NO_x and FSN responses to the SOI swing. The NO_x follows the expected response of decreasing with retarded injection timing, as there is a lower temperature. However, there is a slight increase in NO_x at -3 CAD. This could be attributed to a slight increase in AFR at this condition. The FSN is relatively high in this setup, suggesting poor mixing or atomisation at these conditions, and decreases with SOI. This suggests that the conventional NO_x soot trade-off is not occurring in these test conditions. The flat or trending downwards $BSNO_x$ could be attributed to lower temperatures at the SOC in combination with increased mixing rate. This may explain why FSN has started to decrease. As SOI occurs while the inlet valves are open, earlier combustion may be impeding the turbulent kinetic energy and flow created by the intake valves. Fuel consumption and NO_x trade-off is still present with SOI timing changes.

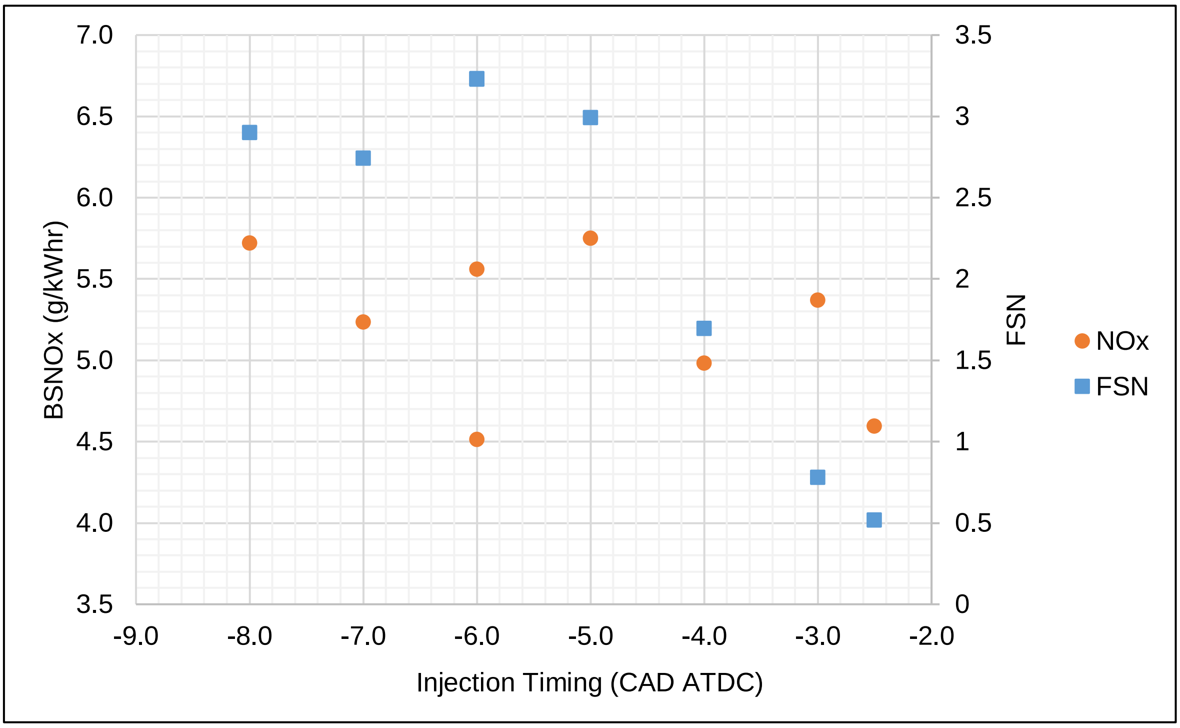

Figure 5.23 Injection Timing Swing – NOx and FSN response

Figure 5.24 displays the BSHC. Generally, BSHC increases with later SOI timing. This is due to relatively constant power output of the engine over the swing, higher HC emissions with later SOI, and the variability of CE that was previously discussed. There appears to be a trade-off in FSN vs BSHC, with retarded SOI producing higher BHSC and lower FSN. This suggests there may be a phenomena decreasing the mixing rate at a certain point, this may again be the result of combustion during IVP impeding bulk mixing or other mixing motion.

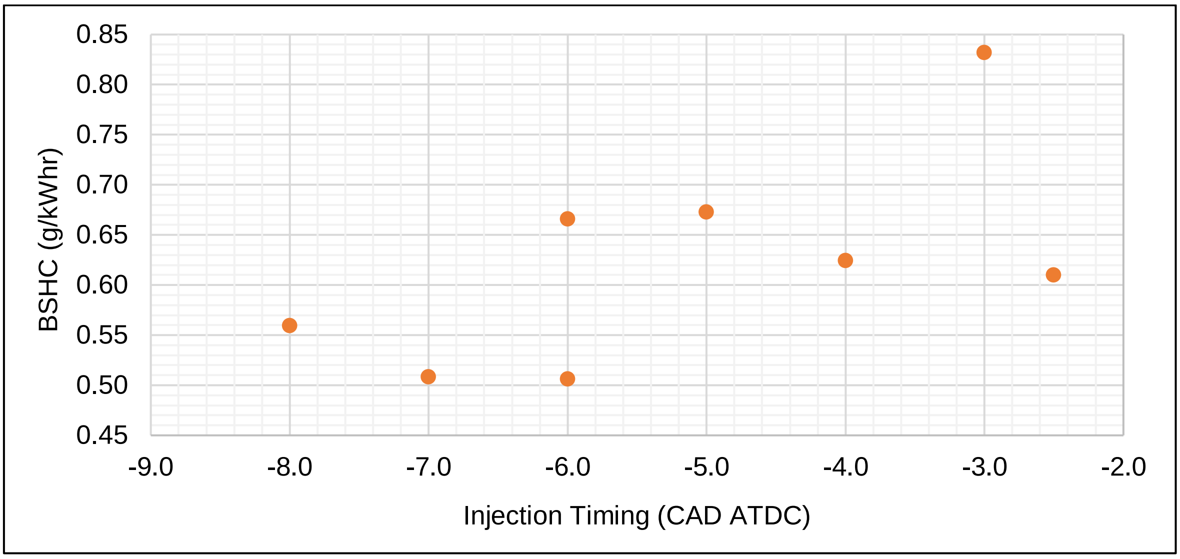

Figure 5.24 Injection timing swing – BSHC response

5.6.3.5 Other Variables

It must be noted that heat in the recuperator can vary depending on the load and thermal mass. Figure 5.25 displays the high-pressure inlet air temperature post recuperator. The effect of residual heat in the recuperator can be seen in when comparing Figure 5.25. There is a loss in recuperator outlet temperature as the tests are performed. This can be seen in Figure 5.25, where the repeated initial point (-6 CAD ATDC) shows a 50K loss between the start and end of the swing. This does not appear to have had affected the response to NO_x, FSN and HC during the injection swing. It would be expected that the NO_x would be lower at lower inlet temperatures but NO_x at -8 SOI is higher than that of -2.5 SOI.

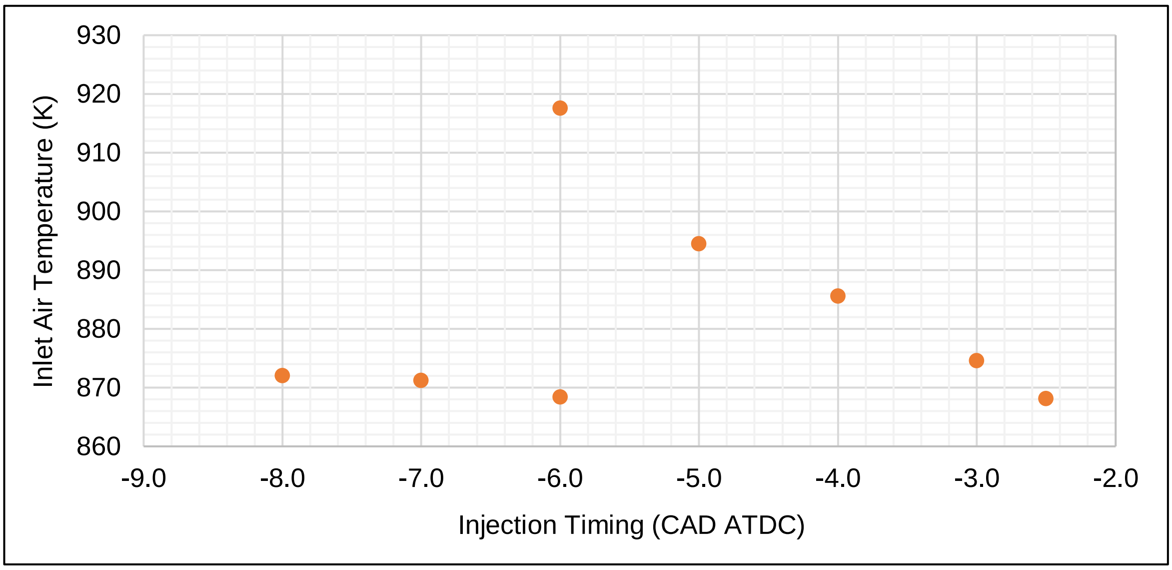

Figure 5.25 Injection timing swing – Inlet temperature

The AFR is shown across the swing in Figure 5.26. This generally has an acceptably small variation of ±0.25 from -8 to -3 SOI. However, the AFR drops to 20.1 at -2.5 SOI. However, this has not affected the BSHC and FSN at -2.5 SOI.

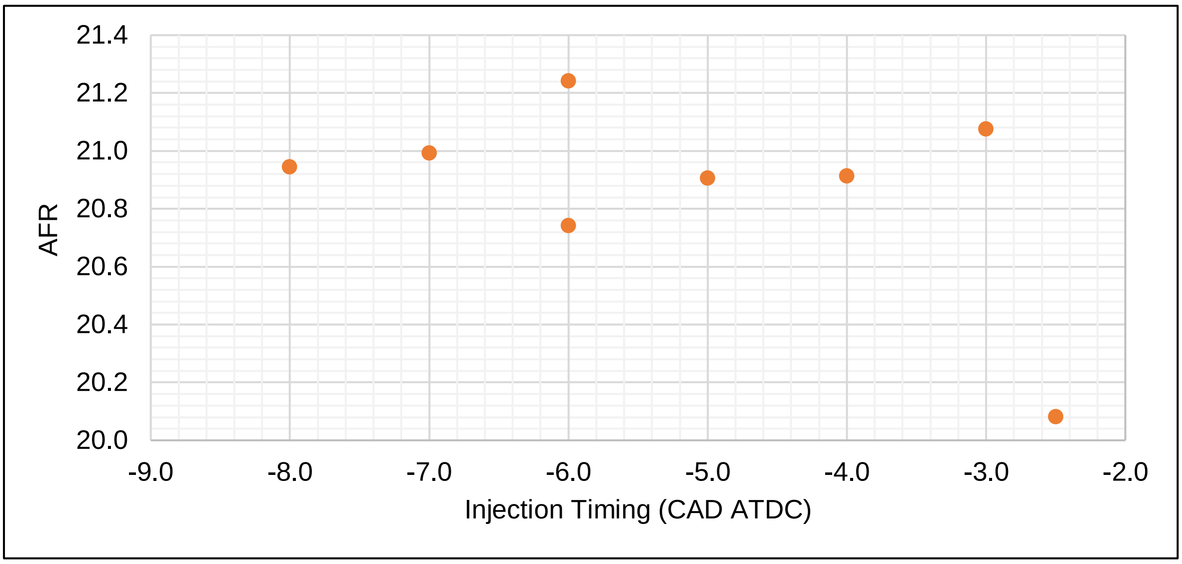

Figure 5.26 Injection timing swing – AFR

Figure 5.27 displays the mass flow rate calculated from the AFR and fuel flow rate. While the inlet air temperature may vary throughout a test due to the thermal energy in the recuperator, the pressure remains fairly constant. Combustion before IVC will also impede air flow into the engine.

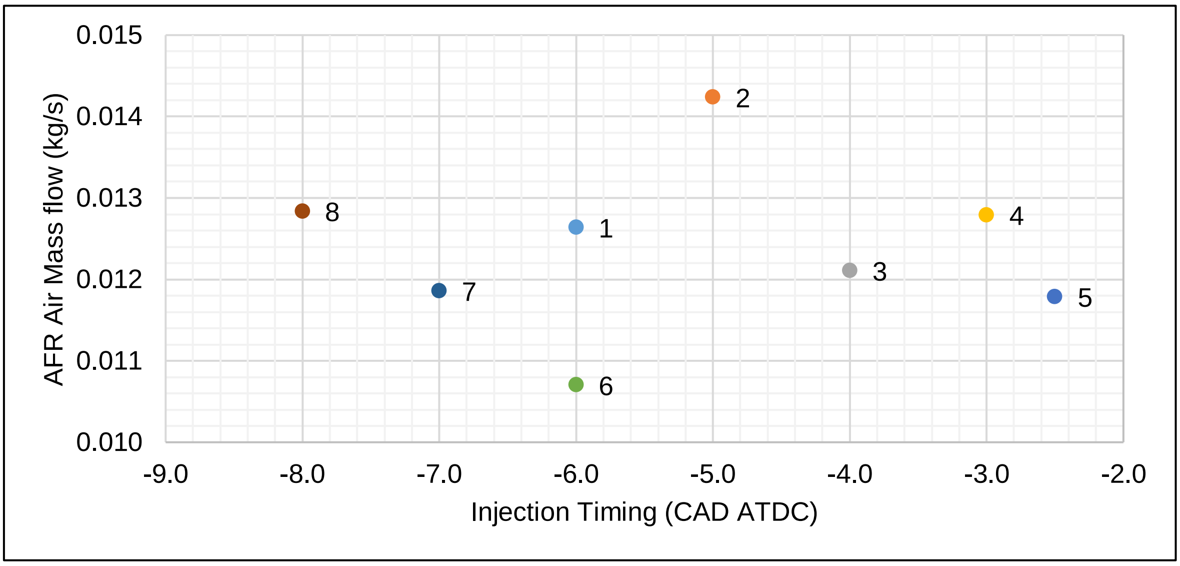

Figure 5.27 Injection timing swing – AFR calculated mass flow rate.

Figure 5.28 displays the exhaust temperature response to the injection timing swing. Retarding the injection timing increases exhaust temperature from 814 to 865K displaying a strong positive correlation with SOI. This could be due to fuel burning in the exhaust, but does not have a clear relationship with NO_x, FSN, or HC. As it would be expected that more fuel combustion in the exhaust would produce lower FSN and HC, as well as higher NO_x. This effect could be purely a result of later combustion phasing and a slightly lower effective ER.

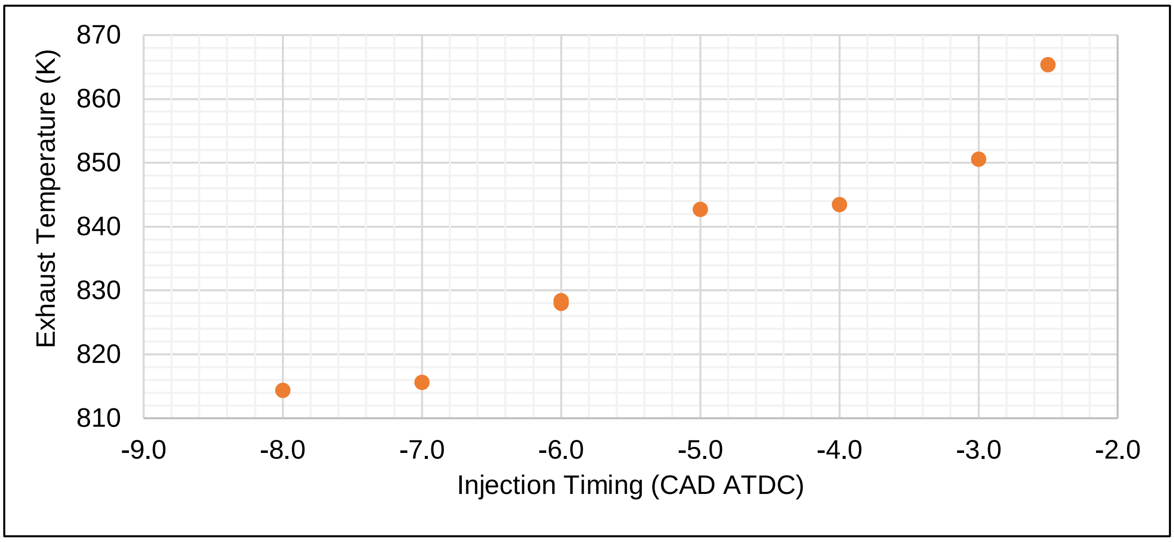

Figure 5.28 Injection timing swing – Exhaust temperature

There is a small difference in torque which can be attributed to the changes in AFR and airflow, this can be seen in Figure 5.29. However, torque and power are almost constant throughout the test points. With a range of 48.3 to 51.0Nm.

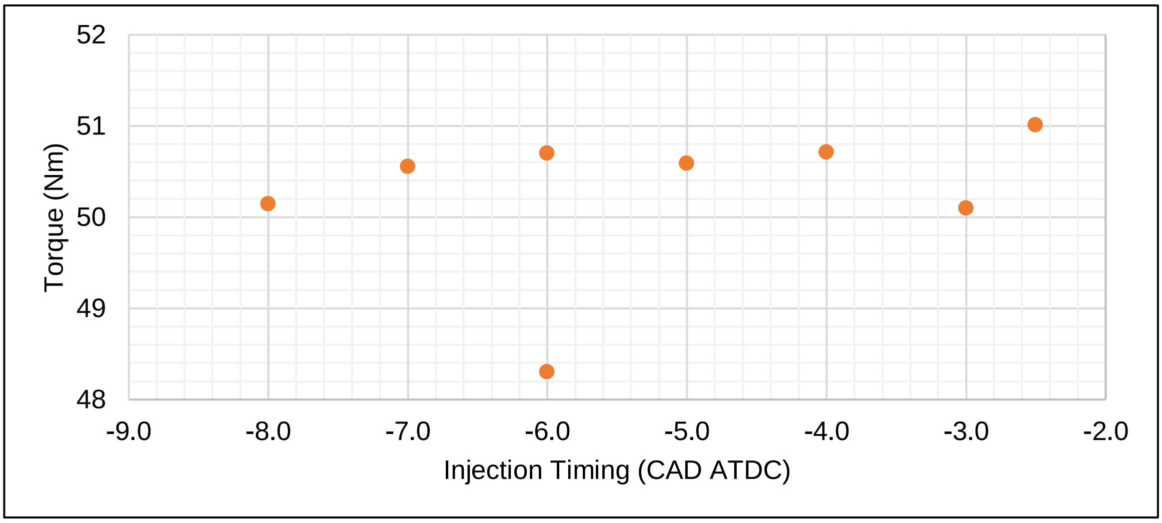

Figure 5.29 Injection timing swing - Torque

5.7 Intake Valve Opening & Exhaust Valve Separation Swings

5.7.1 Aim

As first discussed in Chapter 4, due to the induction event of the RSCE and SCCRE occurring near TDC, the valve timings have a much greater effect on efficiency and combustion than those of conventional engines. As IVC occurs near the end of the exhaust stroke or at the beginning of the combustion stroke, small changes to the position of the piston relative to IVC can have a major effect on the volume available to fill. Therefore, effecting the residual gas from the previous cycle (EGR) and the oxygen mass available for combustion. This can have an effect not only dilution but residual temperature within the chamber. In cases where IVC occurs after TDC, a large amount of air can continue to enter the chamber as the chamber attempts to equalise with the upstream pressure which can cause a further drop in temperature of the chamber gas on top of the expansion of the chamber.

Earlier IVO has a negative effect on work output from the engine as the compressed gas entering before TDC is compressed again. Likewise, if IVC occurs after TDC this can inflate the work output from the engine. Ideally IVO needs to occur at as late of timing as possible to still enable effective transfer and equalisation of high-pressure gas and heat from the recuperator. If IVO only occurred after TDC, the gas would undergo expansion and never equalise in temperature, leading to no autoignition due to low temperature conditions.

As IVO and EVC occur over the same stroke, the period between EVC and IVO (EVIV) directly affects the amount of residual exhaust gas in the chamber from the previous cycle, acting as a method of EGR variability and control.

5.7.2 Initial Conditions

The constant set conditions for the intake valve opening and exhaust valve separation swings are shown in Table 5.6.

Table 5.6 Initial conditions of the intake valve opening and exhaust valve separation swing tests.

Quantity	Value	Units
Intake Pressure	3.0	MPa
Rail Pressure	120	MPa
Engine Speed	1200	RPM
AFR	21	-

Intake Valve Period	20	CAD
Exhaust Valve Opening	180	CAD ATDC
Gas Burner Temperature	1073	K

The four valve profiles for the first four test points are shown in Figure 5.30. The intake valve profiles remain the same for the other 8 test points, however the exhaust valve profiles are advanced according to the EVIV separation.

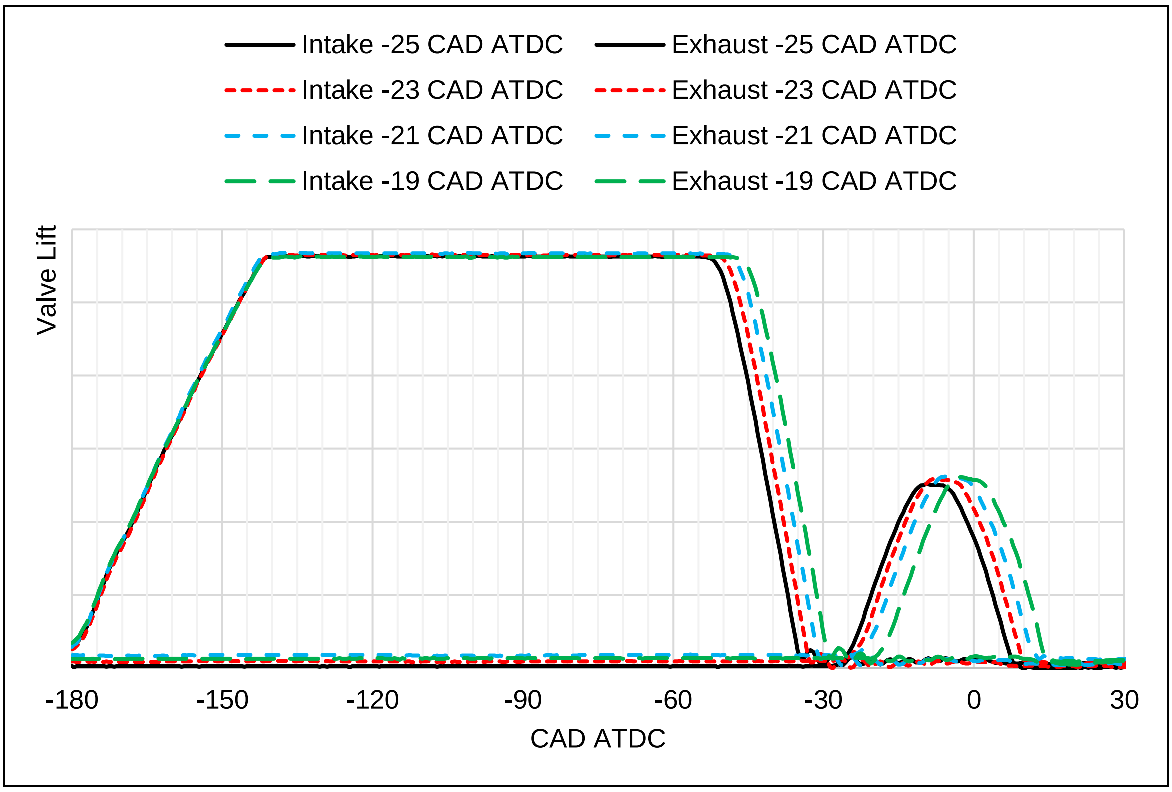

Figure 5.30 IVO & EVIV Swing – Valve Profiles

SOI aimed to be constant throughout the swing. However, changes had to be made to the injection timing to ensure adequate and stable combustion throughout the entire swing of valve timings. This resulted in a 3 CAD variation in SOI across the test points, this is shown in Table 5.7. This is not an ideal comparison due to the change in SOI that was necessitated to maintain nominal combustion, but comparisons will still be interrogated to understand the effect IVO and EVIVS. This variation is captured to an extent in the ignition delay.

Table 5.7 IVO & EVIV separation test points

Test Number	**IVO (CAD ATDC)**	**EVIV Sep (CAD ATDC)**	**SOI (CAD ATDC)**	**SOC (CAD ATDC)**	**IGN Delay (CAD)**	**GIMEP Mean (Pa)**	**GIMEP SD (Pa)**
1	-25	10	-3.0	7.4	11.4	634,368	15,364
2	-23	10	-3.0	9.4	13.4	712,123	17,170
3	-21	10	-3.0	10.5	14.5	785,262	18,251
4	-19	10	-3.0	6.5	10.5	729,204	24,443

5	-25	15	-4.0	7.4	13.4	644,454	17,541
6	-23	15	-4.0	9.4	15.4	709,658	20,434
7	-21	15	-3.5	9.4	14.4	767,513	18,383
8	-19	15	-3.5	7.0	11.0	855,115	23,016
9	-25	20	-5.0	7.5	15.5	626,497	13,068
10	-23	20	-5.0	7.0	15.0	683,965	18,356
11	-21	20	-4.5	4.9	11.9	720,159	15,597
12	-19	20	-2.0	6.4	8.4	794,716	14,150

IVO, EVIVS, and SOI are shown in Figure 5.31. This displays that as EVIV separation increased SOI was retarded to ensure stable and reliable combustion for each test point. As EVIVS increased, and at IVOs of -21 and -19 CAD ATDC, SOI was increasingly retarded. This could be the results of increased residuals and temperature, leading to decreased ignition delay and earlier SOC. This will be further evaluated in the next section.

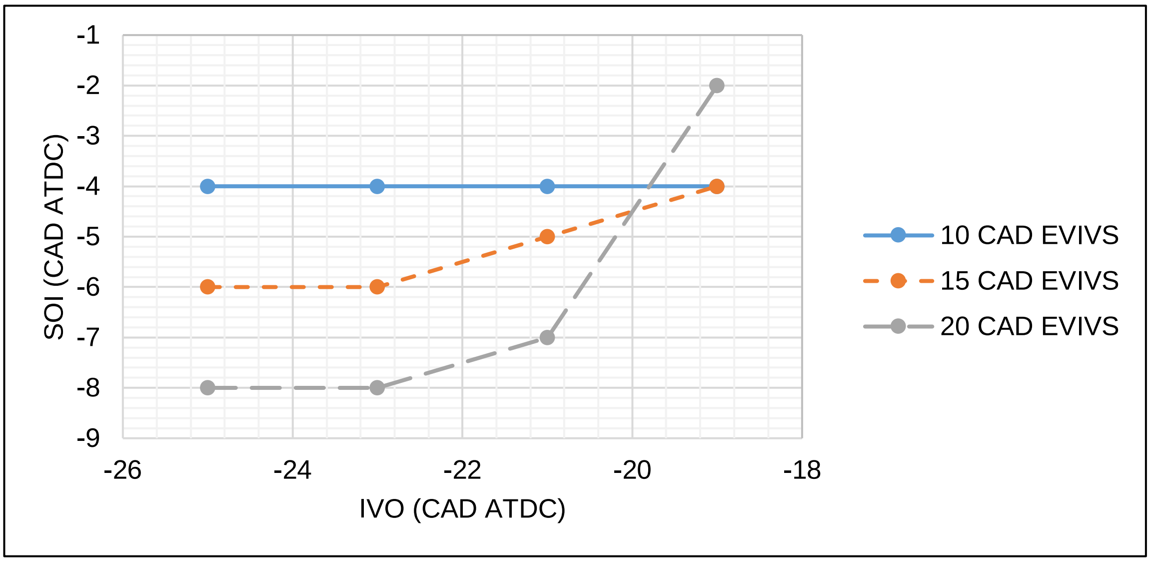

Figure 5.31 IVO & EVIV Swing – SOI timing.

5.7.3 Results & Analysis

5.7.3.1 Cylinder Pressure

First, only test points 1-4 will be discussed to describe the effect seen on the PV diagram with the variation in IVO, shown in Figure 5.32. As previously discussed, retarded IVO creates a greater PV area and therefore amount of work to be captured due to the reduction in recompression work. It is clear from Figure 5.32 that test point 4 should produce the highest efficiency due to the later IVO and an earlier SOC. It is worth remembering the consistent SOI (-4 CAD ATDC) that was achieved during these first 4 test points.

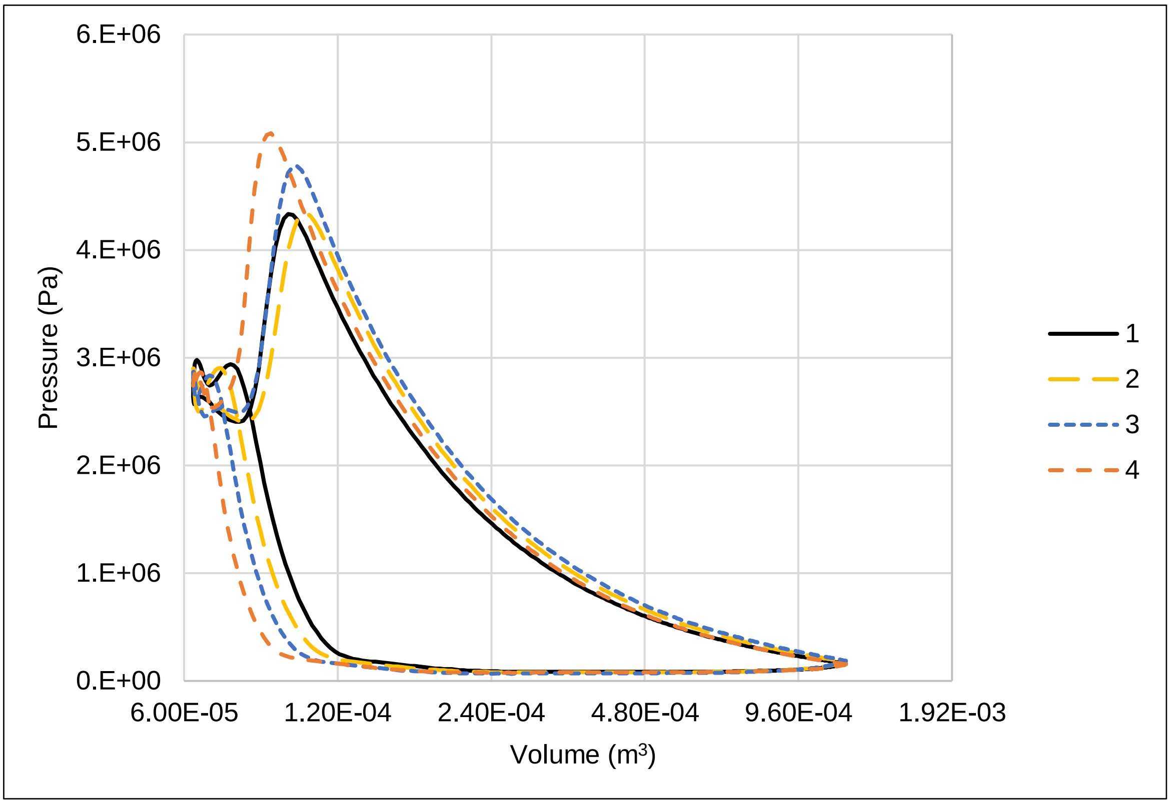

Figure 5.32 IVO & EVIV Swing – Test points 1-4

Interrogating the pressure trace further by eliminating the change in pressure due to the change in cylinder volume is shown in Figure 5.33. This figure shows the difference in pressure change caused by the changes in IVO and displays the earlier onset of combustion that occurs in the -19 IVO case for 10 EVIV separation. The -19 CAD case demonstrates lower ignition delay and higher PRR. There is an increase in the maximum pressure change of roughly 0.2MPa compared to the other three test cases. This could be attributed to moving towards a higher turbulence region or into another phenomena that is enhancing the atomisation and leading to a higher PRR. Theoretically this is an ideal scenario for expander efficiency, as this reduces the expander recompression work at the same time as creating conditions which reduce ignition delay and reduces the combustion duration of the fuel.

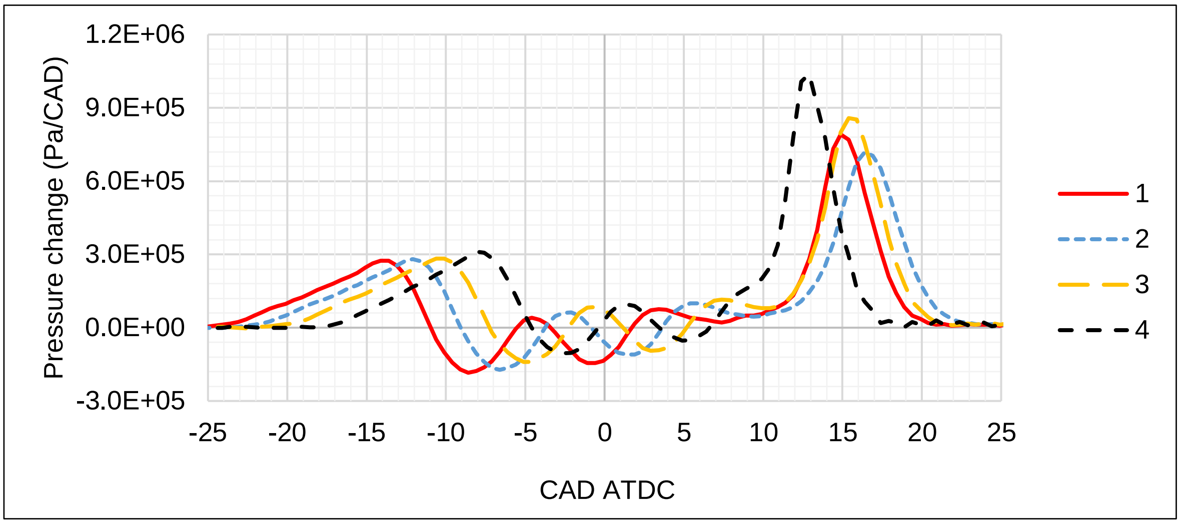

Figure 5.33 IVO and EVIV swing – Pressure changes for test points 1-4.

Figure 5.34 displays the pressure change for test points 5-8. Test points 5-7 have a higher PRR than that of test points 1-3 but are similar in terms of max pressure change. There is a fairly consistent SOC and PRR among tests 5-7, with most retarded IVO having the latest SOC. These conditions are comparable to that of test point 4 in terms of PRR, but not in terms of maximum pressure change. Test 8 however appears to have an early SOC around 9 CAD ATDC, before all of the other cases, but with a lower PRR that results in a later combustion. It is possible that pre combustion during IVP is causing a decrease in overall combustion PRR, impeding mixing and/or the flame propagation. Although there would be an increase in mixing, as SOI is closer to IVO, even with some retard of a couple of degrees in this case and increase in temperature due to residuals from the previous case.

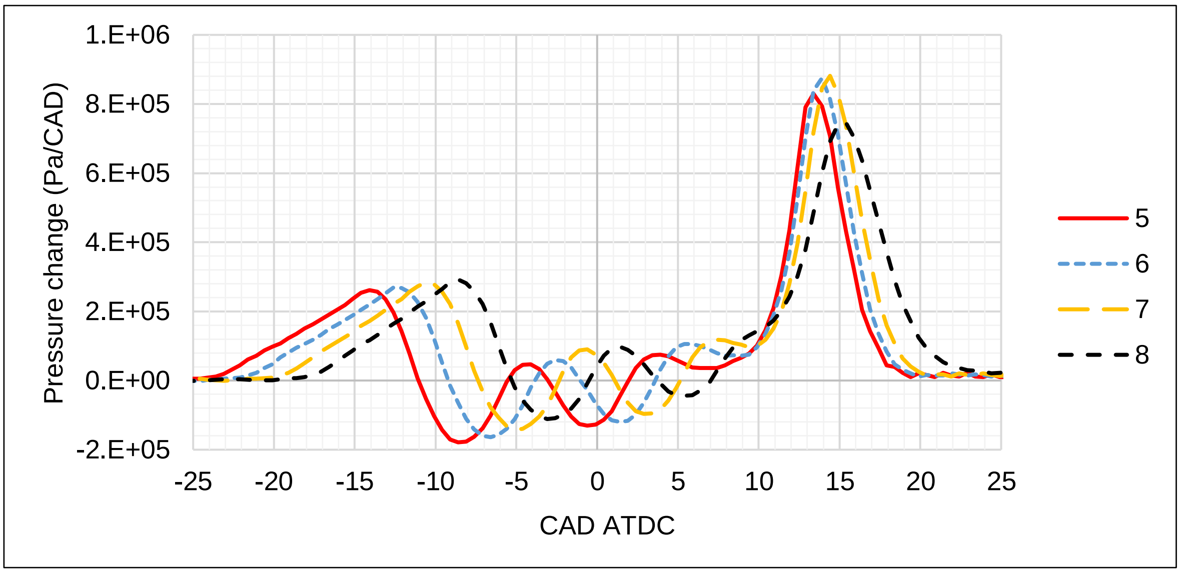

Figure 5.34 IVO and EVIV swing – Pressure changes for tests 5-8.

Figure 5.35 displays the pressure change from tests 9 to 12. Test points 10 and 11 display similar PRR and responses to that of 5-7, but with a slightly lower peak pressure change. This is expected with a higher degree of residuals in the chamber.

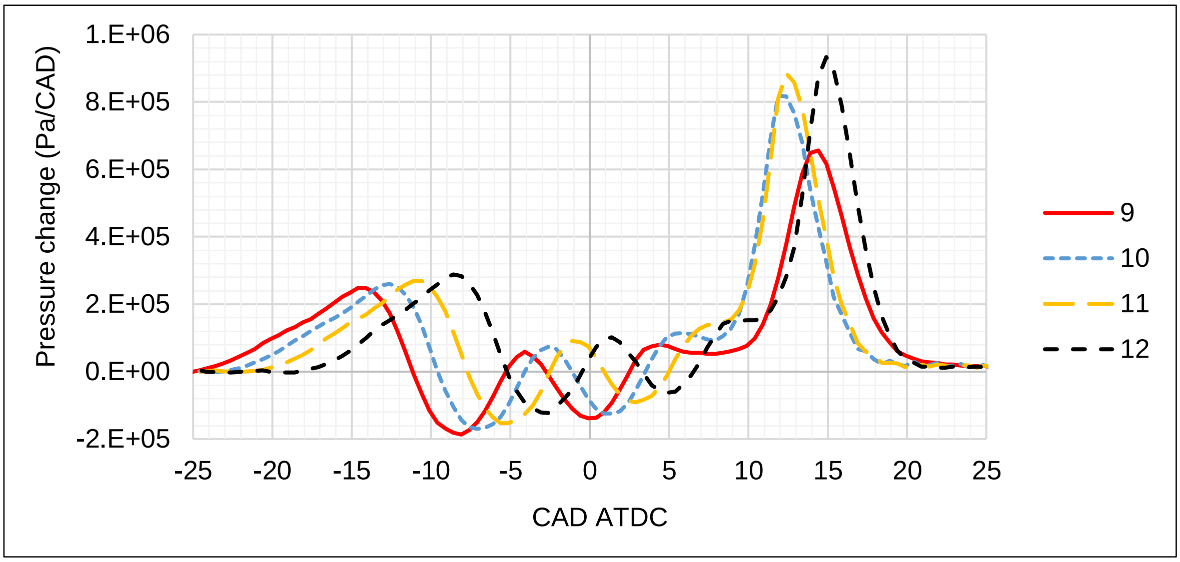

Figure 5.35 IVO and EVIV swing – Pressure changes for tests 9-12.

From these cases it is possible that there is an optimum zone where fast or a premix style of air fuel preparation can occur, followed by ignition and combustion. Where there is just enough time to mix to form a premix style of combustion, but not enough energy to ignite early and ruin the formation of the premix. The EGR effect could aid in managing this by effecting both the temperature and the reaction chemistry.

5.7.3.2 Ignition & Combustion

The ignition delay is displayed in Figure 5.36, as well as previously shown in Table 5.7. Due to the changes in SOI, ignition delay across the cases are not comparable like for like. However, it is notable that ignition delay is lowest in all cases at -19 CAD ATDC. With the lowest ignition delay in the -19 CAD IVO 20 CAD EVIV separation and the second lowest in the -19 CAD IVO 5 CAD EVIV separation case, reversing the expected result shown at -25 CAD ATDC. There appears to be a trough in ignition delay that is present with no SOI change (10 CAD EVIV) and with changes in SOI. This trough is impacted by EVIV effects on residuals and gas temperature.

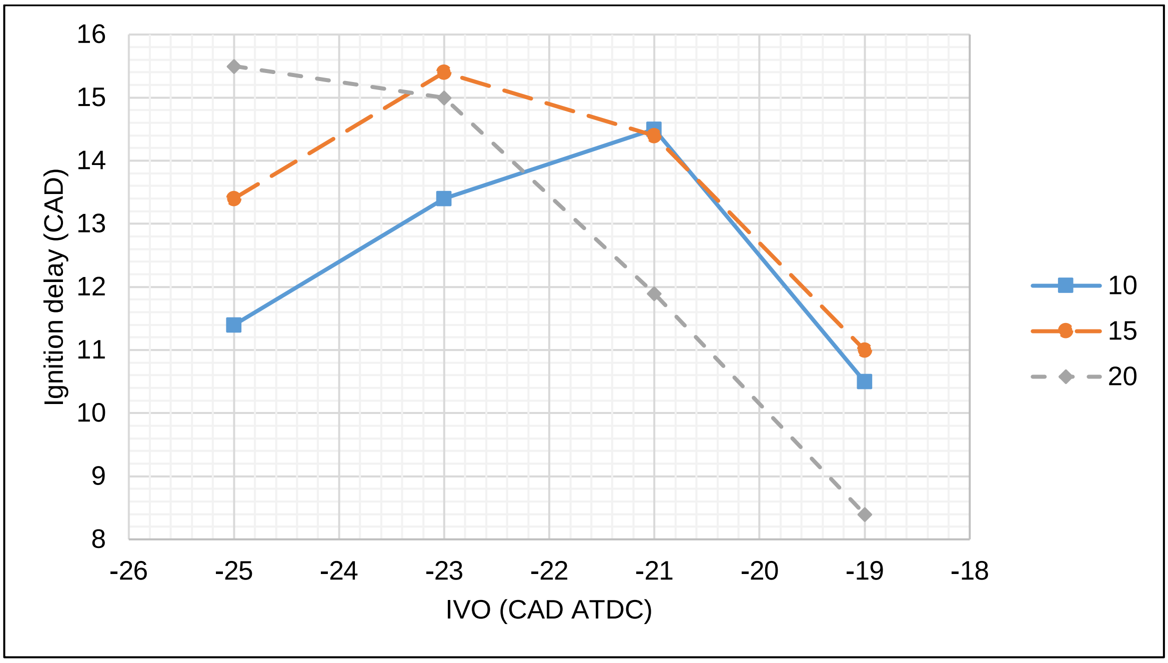

Figure 5.36 IVO and EVIV swing – Ignition delay

Lower temperatures would be expected as IVC goes further past TDC. Increasing EVIV separation would help retain an increasing amount of heat in the chamber, resisting unstable combustion at more retarded IVC timings. This is shown to have an effect in Figure 5.36. However, what is not anticipated is that ignition delay decreases to below that of the earliest IVO cases at -21 and -19 CAD.

5.7.3.1 Efficiencies

The effects of earlier ignition with retarded IVO is reflected when interrogating the efficiencies. Efficiencies for test points 1-4 are shown in Figure 5.37. TE increases as expected, as recompression work is minimised and more REW is generated. This is also why ETE and EFE continue to rise. CTE is highest in the cases with the earliest and highest PRR. Therefore, CTE is highest in the -19 CAD IVO case. These points are true for the rest of the test points in this swing. However, CE is low (64.3-67.9%) across these test points and decreases with retarded IVO. Part of this can be attributed to unoptimized SOI, but this could be explained by a drop in temperature reducing reactivity throughout the combustion event as IVO is retarded and introduces more air post TDC. Interestingly, although test point 4 has the highest reaction rate, as shown in Figure 5.33, CE is lowest in this swing. This could be due to SOC occurring earlier than the other cases and possible ignition before

IVC. It is notable that there is a substantial benefit to be had if CE increased to result in EFE close to the ETE efficiencies of 40.2-50.6%.

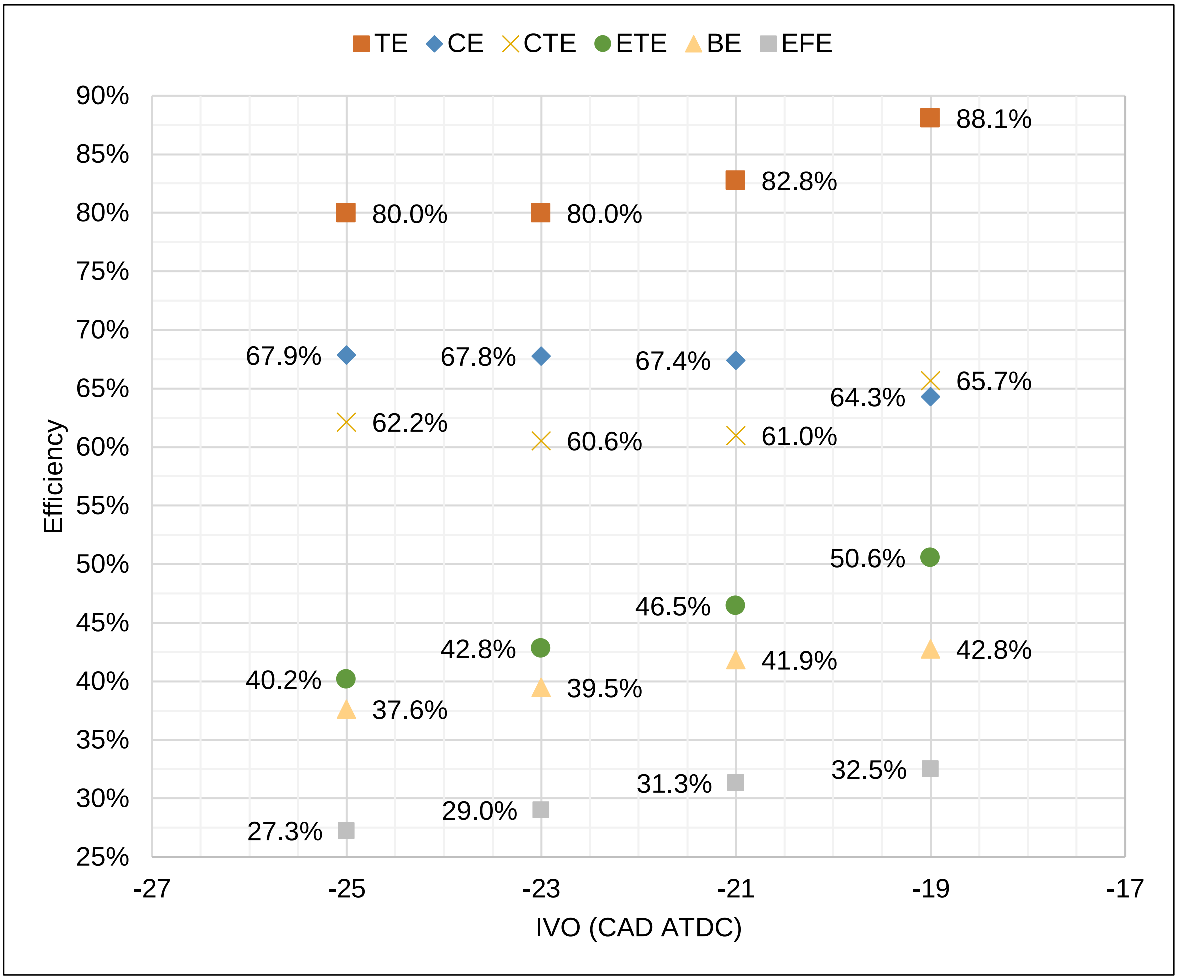

Figure 5.37 IVO and EVIV swing – Efficiencies for Test points 1-4, 10 CAD EVIV separation.

Figure 5.38 display the efficiencies for test points 5-8. Late SOC of test point 8 contributes to lowest TE and CTE. However, CE is highest in this test point. Generally, BE and EFE have increased in comparison to tests 1-4. This is due to an increase in CE for tests 5-8, with only a small change in ETE. A higher CE could be due to trapped residuals retaining heat contributing to a higher reaction rate in test cases 5-7, and a slightly lower reaction rate in test point 8, as shown in Figure 5.34. This differs from the 10 CAD EVIV cases in that SOC occurs at a similar point across the 15 CAD EVIV cases. Although dilution is also higher in these set of cases which should act against the increase in temperature to a lesser extent. Because of the dilution, overall ETE drops slightly in comparisons to the 10 CAD EVIV cases, as there is less air and fuel added compared to the corresponding IVO case. Highest

ETE is lower than Test point 4, however, highest EFE is higher due to 7.4% increase in CE.

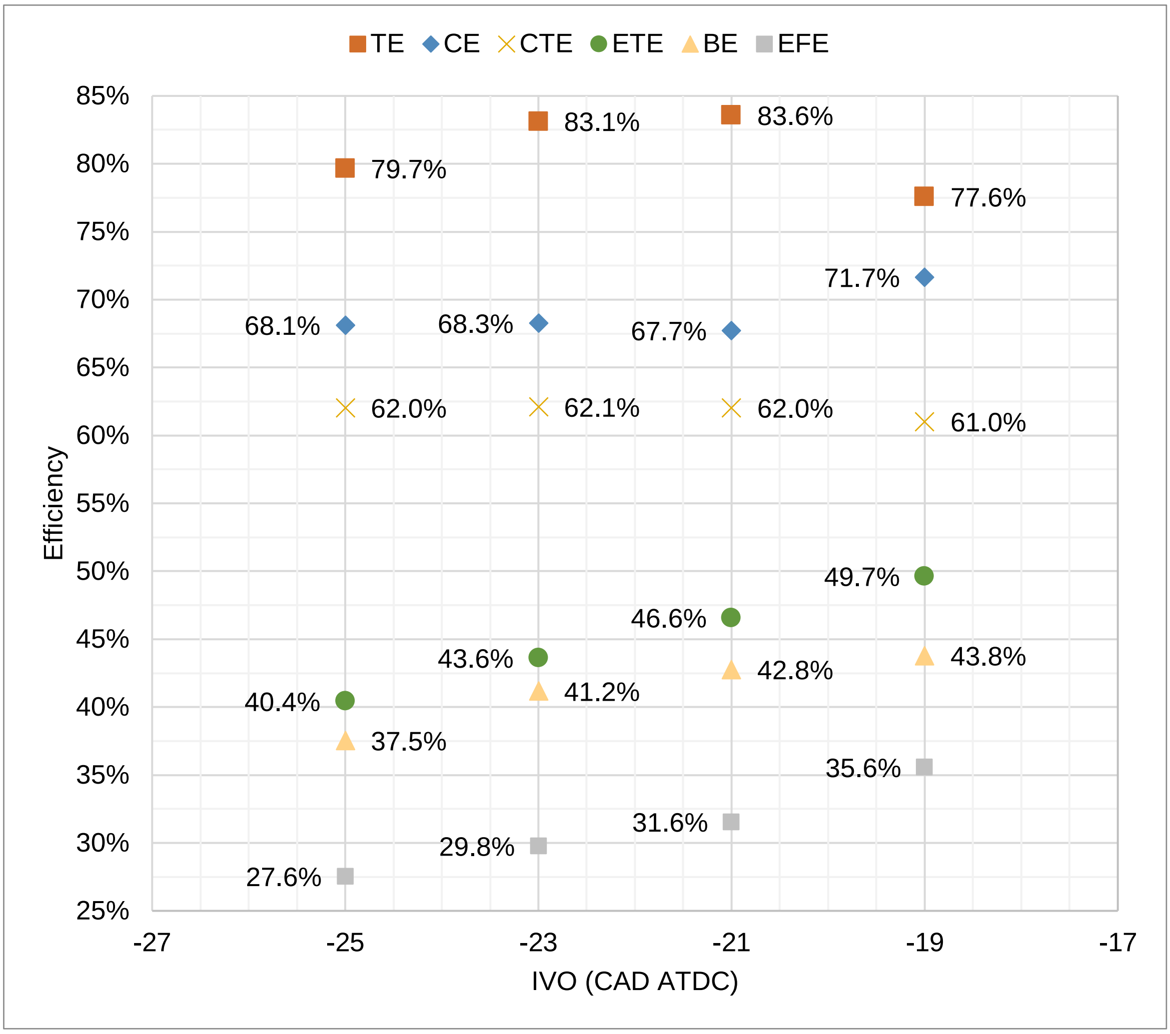

Figure 5.38 IVO and EVIV swing – Efficiencies for Test points 5-8, 15 CAD EVIV separation.

Figure 5.39 displays the efficiencies for test points 9-12. Notable CE has again generally improved with increasing EVIV. However, the benefit this previously had on ETE and BE is now less than the negative effect on ETE. Resulting in a small reduction or stagnation in EFE across the points in comparison to the 15 CAD EVIV test points.

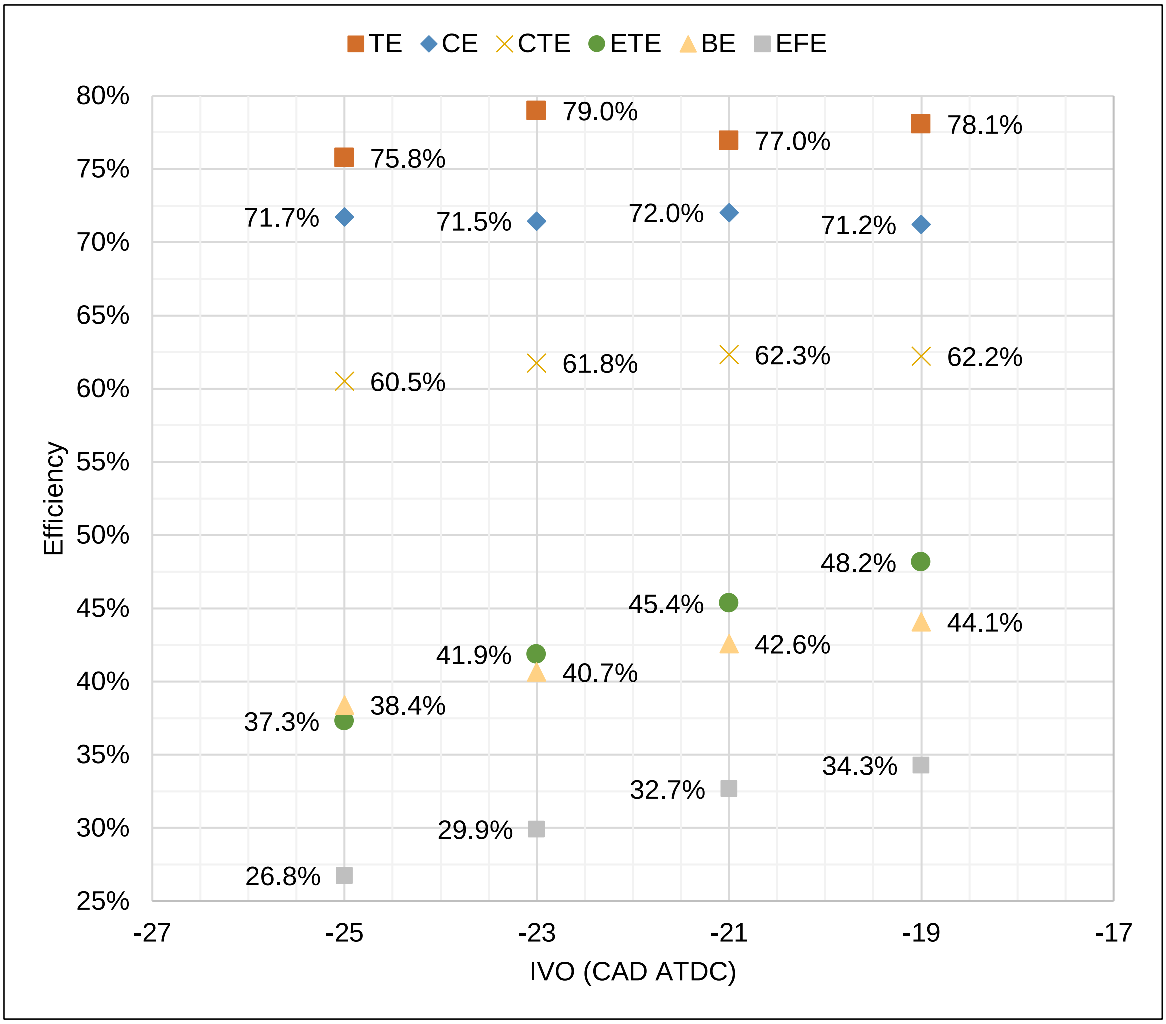

Figure 5.39 IVO and EVIV swing – Efficiencies for Test points 9-12, 20 CAD EVIV separation.

5.7.3.2 Emissions

As IVO is delayed there are a couple of effects that are effecting SOC temperature. The later IVO is post TDC, the greater the Joule-Thomson cooling effect as the cylinder volume expands. Less effective compression of residuals due to the piston slowing down closer to TDC, resulting in lower residual temperature. However, exhaust temperature from previous cycle will play a larger effect. It is likely that SOC temperature is lower because of the dominance of the air compared to residuals, and the amount of dilution will also reduce with later IVOs. This should result in an increase in ignition delay, FSN, and torque, as well as a reduction in NO_x. Air flow should continue to increase as the intake valves start to close closer to TDC. As the separation between EVO and IVO is increased, it would be expected that ignition delay and FSN increase, with air flow and NO_x decreasing. This is due to the EGR dilution decreasing the amount of air available to mix and combust, reducing the mass of air that can enter the cylinder, and reducing the differential pressure between the intake manifold and cylinder.

The FSN response for all of the test cases is shown in Figure 5.40. The response follows the expected trend, with FSN increasing due to lower availability of oxygen and lower combustion temperatures.

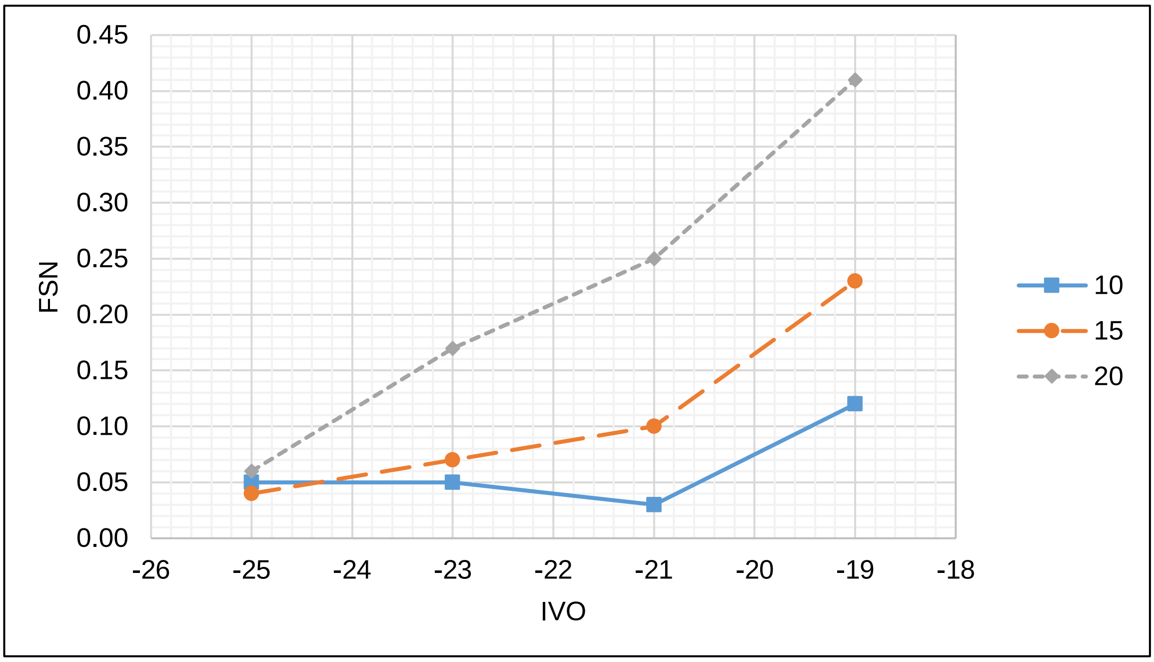

Figure 5.40 IVO and EVIV swing – FSN response.

Figure 5.41 displays the BSNO$_x$ and ESNO$_x$ responses from the test points. There is a general trend between test three sets of cases for EVIV separation, with 10 CAD EVIV producing highest specific NO$_x$, followed by 15 CAD EVIV, and 20 CAD EVIV the lowest. This is expected to an extent due to lower available energy to increase temperature and produce NO$_x$ from the new incoming air. There is not a clear general trend across all of the test points in response to IVO. There appears to be an outlier in the 10 CAD EVIV -23 IVO case (test point 2), when compared to the general linear upward trend of the rest of the 10 CAD EVIV and 20 CAD EVIV cases. However, there is a much flatter response for the 15 CAD EVIV cases.

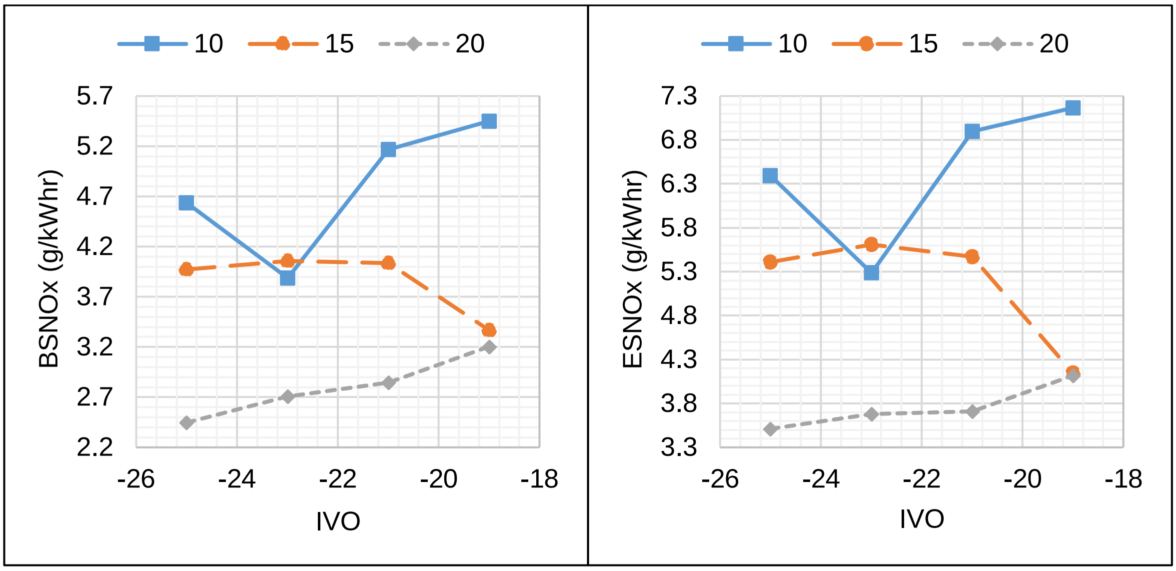

Figure 5.41 IVO and EVIV swing – NOx responses.

Figure 5.42 displays the HC responses from the test points. There again seems to be an outlier in the test point 2, suggesting there may have been an issue with the MEXA emissions readings recorded at that test point. The rest of the test points appear to follow a trend of decline from -25 to -21 CAD ATDC for IVO, before an increase at -19. This is an interesting trend when compared to that of CE and FSN. It would be expected for HC content to increase with FSN or remain fairly flat due to small variations in CE. It may be that mixing and/or combustion are not uniformly occurring across the chamber. Resulting in local areas of high mixing that do not combust and/or areas of poor mixing that do combust.

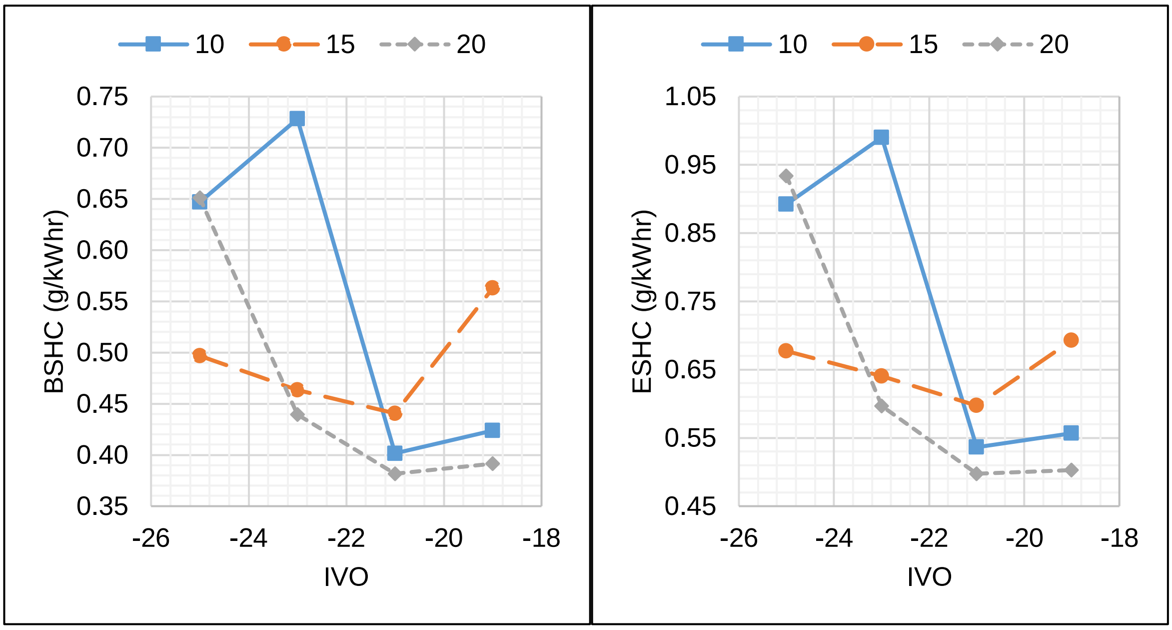

Figure 5.42 IVO and EVIV swing – HC responses

5.7.3.3 Other Variables

Figure 5.43 displays the graphs for calculated air flow and torque across the swing. As expected, air flow and torque increase in line with each other as IVO is retarded and decreases with EVIV separation across all cases, with the exception of the 10 CAD EVIV -19 CAD ATDC case. This is likely due to the reduced ignition delay and interference of the SOC with IVC. Combustion occurring earlier and before IVC would impede the breathing of the expander as air is either not able to flow due to the flow of combustion products upstream of the intake valves, or lower differential pressure between the intake manifold and the expansion cylinder.

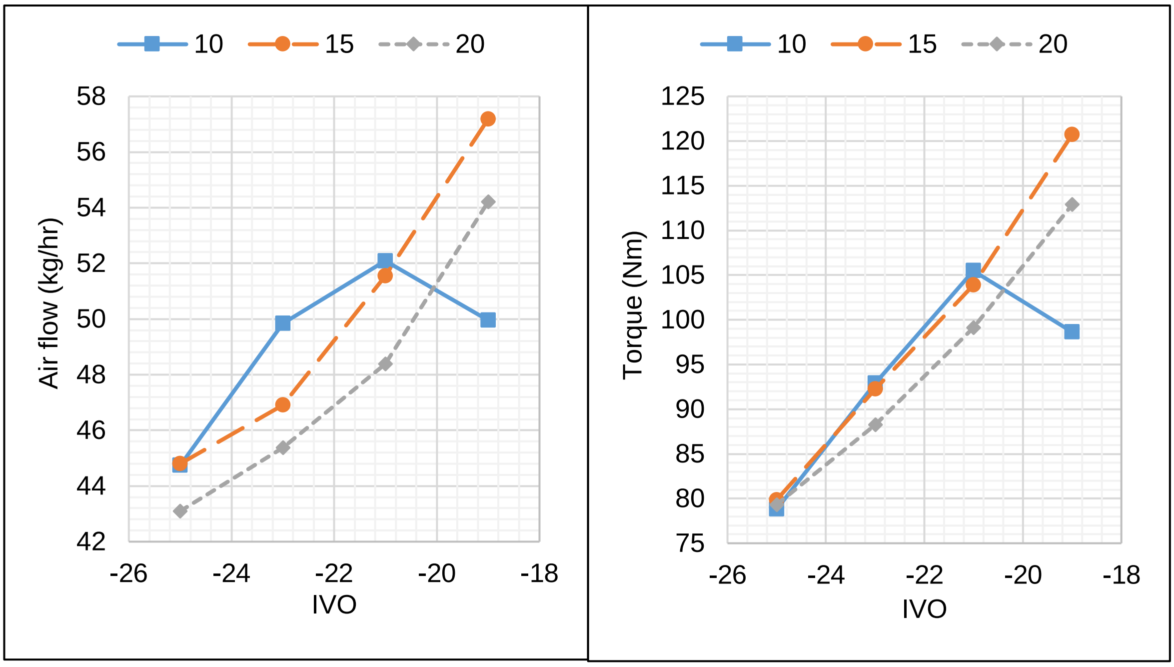

Figure 5.43 IVO and EVIV swing – Air flow (AFR) and Torque

The inlet and exhaust temperature across the test points is shown in Figure 5.44. A variation of 468°C to 624°C can be seen on the recuperator outlet temperatures. This is not ideal due to changes that this will undoubtedly have on the combustion proves. Why the temperature respond as it does is not obvious. It could be theorised that with increasing air flow rate and the same gas burner set conditions that the inlet temperature would reduce. However, this appears to only be the case for the 15 CAD EVIV test points. The only other explanation would be transient behaviour of the recuperator thermal mass over time due to the test point conditions. With the exception of the 10 CAD EVIV swing, the exhaust temperature increases with airflow and fuel as expected.

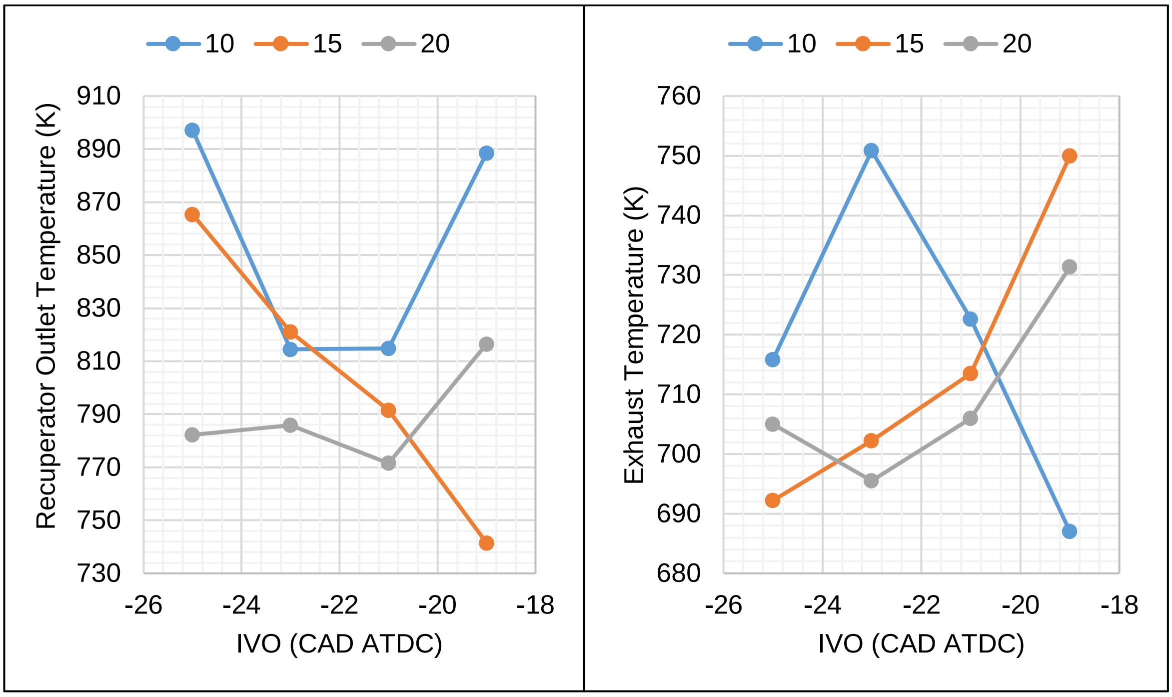

Figure 5.44 IVO and EVIV swing – Reuperator outlet (left) and exhaust (right) temperatures

A key consideration at these conditions is that the inlet temperature is greater than that of the exhaust, therefore there would need to be a reduction in inlet temperature or ER to be achievable on a real RSCE. The objective of this swing was to investigate combustion response and efficiency and therefore exhaust temperature was not a concern.

5.7.3.4 Discussion

The low CE across all cases displays that there remains room for further development and optimisation of the combustion system to increase CE. If a CE of 95+% can be achieved, in line with conventional ICE combustion systems, then the SCCRE could achieve 50% in line with ETEs reported for these set of conditions. These set of test point swings are only for a medium pressure of 30 bar intake air, if this can also be further raised without impacting CE, further efficiency gains could be made.

5.8 Inlet Pressure & Temperature Swing

5.8.1 Aim

The temperatures at TDC in the SCCRE is dictated by the intake temperature. The intake temperatures have a wider range and overall lower compared to temperatures at TDC of conventional Diesel ICEs, 500 to 1,000K compared with 800 to 1,200K. The highest intake temperature in the SCCRE is limited by the heat supplied by the gas burner and recuperator. Whereas in conventional engines this is a function of intake temperature and CR. The pressures are generally lower in the SCCRE compared to a conventional Diesel, 2 to 7MPa compared to 6 to 12MPa.

As previously discussed in Chapter 2, whereas LTC is forced on conventional ICEs through EGR and high AFR, the RSCE and SCCRE can theoretically achieve LTC through lowering initial temperature and late combustion phasing. This ensures expansion and combustion processes occur after TDC, thereby limiting the maximum temperature that the combustion gas can achieve during the combustion process. As well as having the potential to eliminate the negative effects EGR and high AFR have on efficiency, as well as being a much more effective method of LTC.

In the RSCE the point of ignition can be as much as 30 crank angle degrees (CAD) after TDC, where some cooling of the charge will have occurred through heat losses and expansion of the compressed intake air. Additional reductions can also be with low adiabatic flame temperatures by dilution with EGR or nitrogen.

The aim of this swing is to understand the combustion and emissions over the range of pressures and temperatures. The conditions will not be phased late after TDC to allow low intake temperatures to be achieved.

5.8.1 Data Quality

In the same manner as Section 5.6, a high amount of noise was present on cylinder pressure data. In addition, the pressure sensor reading dropping below zero after adjustment to absolute pressure. This made interpretation and calculations from the high speed pressure data impossible. Therefore, high speed cylinder pressure data will not be reported in the section, including calculations that rely on cylinder pressure data such as TE, CE, ETE, ignition delay, etc.

5.8.2 Initial Conditions

Test set conditions of the swing are shown in Table 5.8. EVIV separation is set at 0 CAD to minimise the effect of residuals as much as possible. SOI is allowed to float to maintain combustion throughout the swing but is set a stable nominal position for each test point.

Table 5.8 Initial conditions of the inlet pressure and temperature swing studies.

Quantity	Value	Units
Rail Pressure	120	MPa
Engine Speed	1200	RPM
AFR	21	-
Intake Valve Opening	-30	CAD ATDC
Intake Valve Period	20	CAD
Exhaust Valve to Intake Valve Separation	0	CAD
Exhaust Valve Opening	180	CAD ATDC

The valve setup used for the intake pressure and temperatures swing is shown in Figure 5.45.

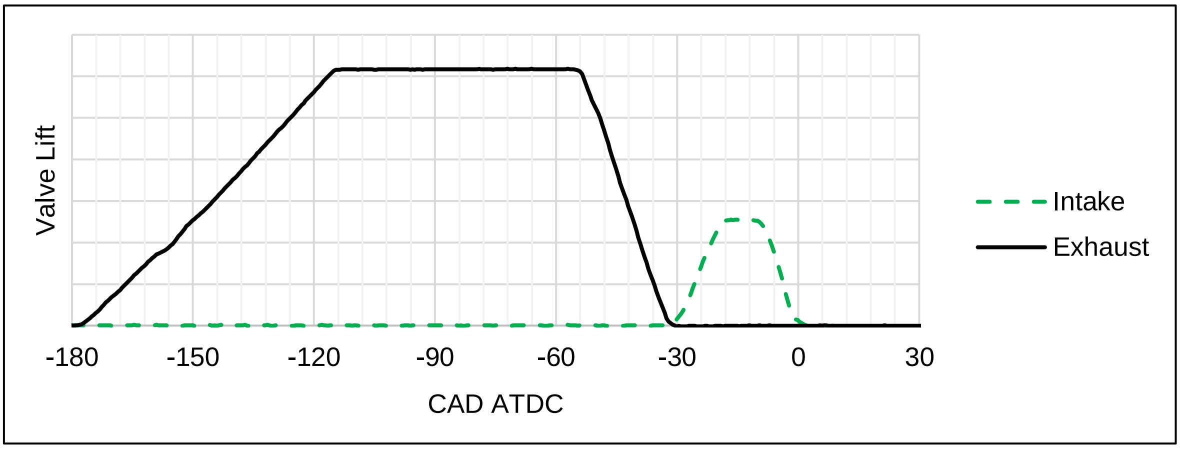

Figure 5.45 Inlet pressure and temperature swing – valve setup.

The desired and measured inlet temperatures and pressures for the 26 test points are shown in Table 5.9. In this experiment the methane burner was run at the maximum operating temperature and reduced by 25-50K for each test condition, over a range of pressures from 2 MPa to 4 MPa at 0.5 MPa intervals.

Table 5.9 Inlet pressure and temperature swing – test points.

Test Number	Desired Inlet Pressure (MPa)	Measured Pressure (Gauge MPa)	Burner Set Temperature (K)	Measured Inlet Temperature (K)
1	2.0	2.04	1073	802
2	2.0	2.04	1073	815
3	2.0	2.05	1023	751
4	2.0	2.05	973	667
5	2.0	2.05	923	600
6	2.0	2.06	873	544
7	2.0	2.06	848	512
8	2.5	2.49	1073	822
9	2.5	2.49	1023	723

10	2.5	2.49	1023	717
11	2.5	2.49	973	629
12	2.5	2.49	923	564
13	3.0	3.00	1073	718
14	3.0	3.00	1023	633
15	3.0	3.00	973	566
16	3.0	3.00	948	537
17	3.5	3.41	1073	667
18	3.5	3.42	1048	623
19	3.5	3.42	1023	585
20	3.5	3.42	998	550
21	3.5	3.43	973	521
22	3.5	3.43	973	519
23	4.0	3.93	1023	532
24	4.0	3.94	1048	555
25	4.0	3.90	1073	589
26	4.0	3.98	1023	529

The maximum inlet temperature achievable is limited by the heat transfer from the methane gas burner to the recuperator. The gas burner has a maximum operating temperature of 800°C. The heat transfer rate is limited by this upper temperature limit and the mass flow through the burner, which is a constant rate for each set temperature condition.

The measured test point temperature and pressure conditions are shown in Figure 5.46. Due to the higher heat transfer rate required to remain above the ignition point at greater mas flow rates, there is a decreasing number of test points for each pressure condition, i.e., at 2MPa bar there are 7 test points, while there are 4 test points at 4 MPa.

The true temperature of the air in the chamber will be lower than that of the measured recuperator outlet temperature due to heat losses to the chamber, and energy loss due to choked flow conditions from the Joule-Thomson effect.

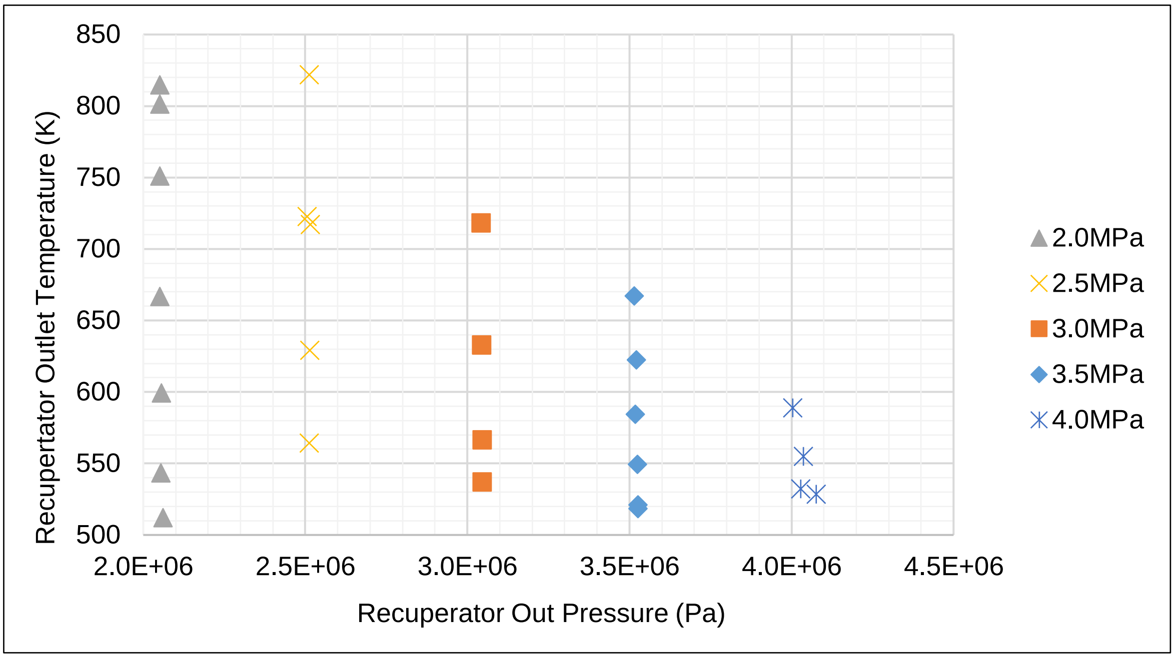

Figure 5.46 Inlet Pressure & Temperature Swing – Measured recuperator outlet pressure and temperature

5.8.3 Results & Analysis

5.8.3.1 Efficiencies

Due to the issues with data quality previously mentioned, only BE will be discussed and evaluated in this section. The BE for the test points is shown in Figure 5.47. As air flow and fuel is added to the system BE increases as expected. The 0.2MPa swing shows a drop in CE at and below 544K recuperator outlet. As the autoignition temperature of diesel fuel is approximately 500K at standard conditions, it is likely caused by reducing CE, as less of the fuel auto ignites.

As pressure increase, the autoignition temperature reduces. This may play a part in why there is not the same level of reduction in BE at lower temperatures for the swings higher than 0.2MPa. Steps of 25K gas burner temperature did not provide high enough resolution to capture if there was a fall below ~525K for the rest of the cases, as any lower provided an unstable combustion or none at all. Interestingly the highest temperature cases for 3.5 and 4.0 MPa appear to buck the trend and increase at the higher temperature. There is not enough information to access whether this is real.

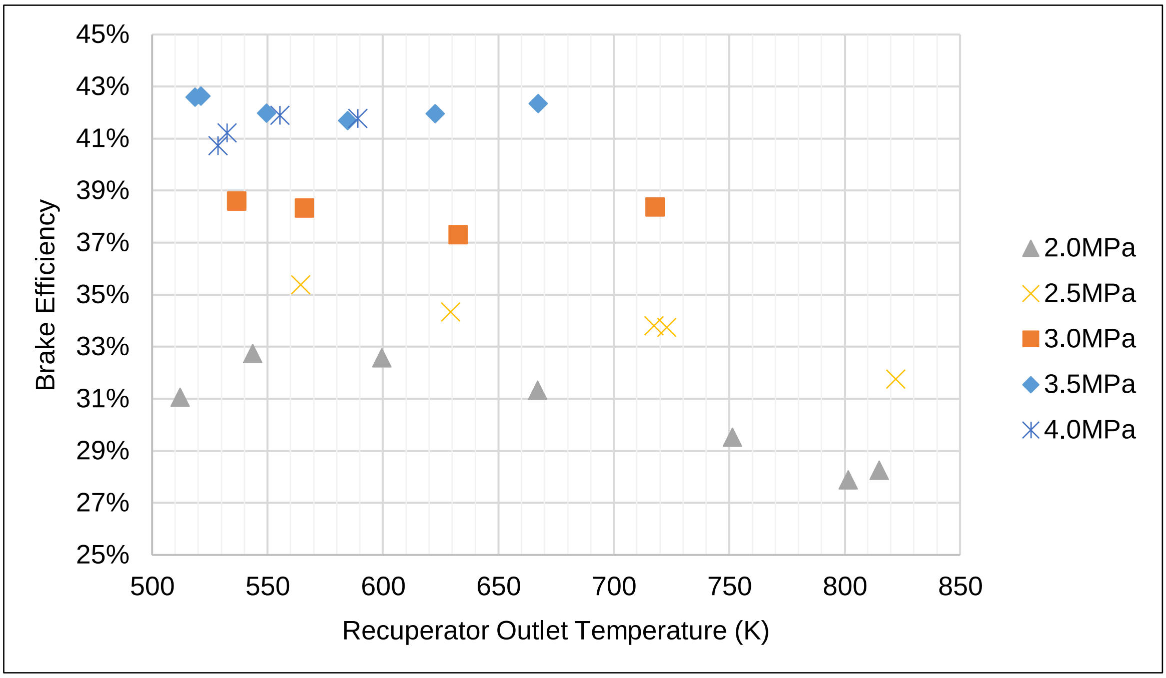

Figure 5.47 Inlet Pressure & Temperature Swing – Brake efficiency.

As the recuperator is fed independently from the exhaust, the effectiveness of the recuperator can be assessed by comparing the energy available from the exhaust and the amount of energy added by the burner. This is not a true measure of recuperator effectiveness, as a theoretical value is required to compare potential energy. For example, as the exhaust is not cooled, the theoretical energy available compared to the ambient temperature can be used to assess potential energy available. In a similar manner, as the air for the SCCRE is fed by a bank of pressurised cylinders which is regulated down, the air temperature entering the recuperator is typically below ambient temperature. Therefore, a theoretical value of ambient temperature can be used to understand how much energy is required to heat the air from ambient to the measured recuperator out temperature. Equation (83) displays the formula used for the so-called quasi-recuperator efficiency, η_{QR}. For the analysis, constants for the specific heat of air and exhaust were used. Where C_{air}= 1,100J/kgK and C_{exh}= 1,063J/kgK. T_a is the ambient temperature, which in this analysis was 298.15K, T_{ro} is the recuperator air outlet temperature, T_{exh} is the exhaust temperature, and η_{QR} is the quasi-recuperator efficiency.

$$\eta_{QR} = \frac{\dot{m}_{air}.\, c_{air}.\, (T_{ro} - T_a)}{\dot{m}_{exh}.\, c_{exh}.\, (T_{exh} - T_a)} \qquad (83)$$

The BE for the test points against quasi-recuperator efficiency is shown in Figure 5.48. It is possible for the quasi-recuperator efficiency to be greater than 100% due to the separation of the exhaust from the recuperator and inclusion of the burner. It must be noted that this only considers the effect recuperator efficiency has on the expander and does not consider the benefit of recuperation on the system level of the RSCE. However, the cost of increased recuperation must be understood for the overall cycle.

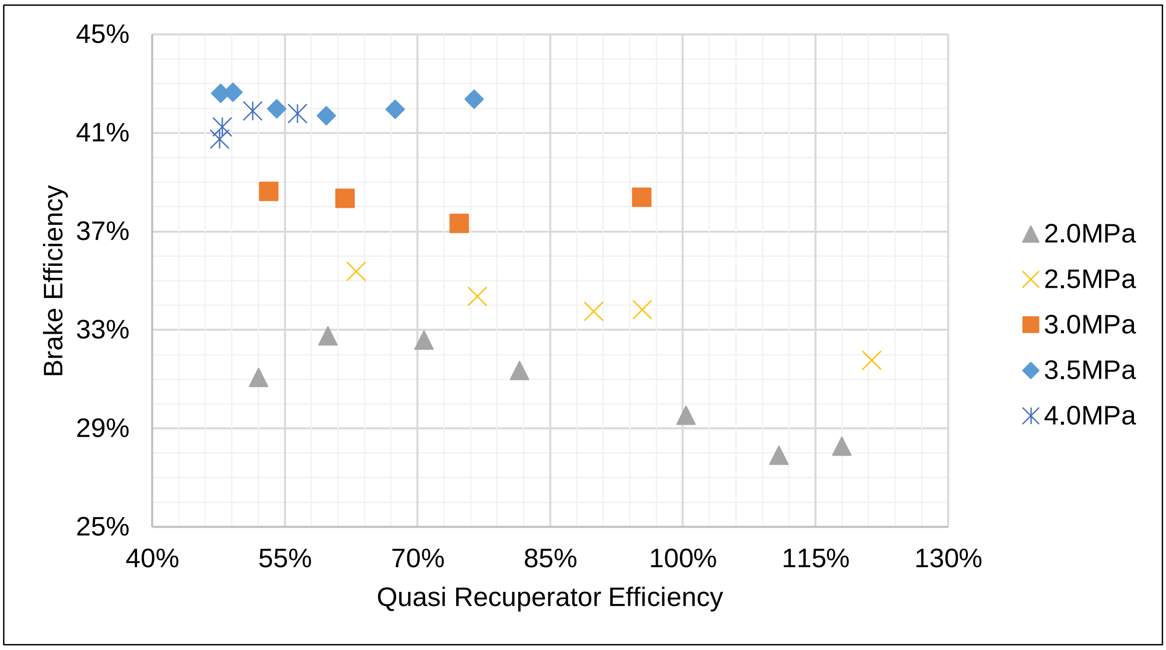

Figure 5.48 Inlet Pressure & Temperature Swing – BE against quasi-recuperator efficiency.

Graphs of BE plotted against calculated air flow and torque are displayed in Figure 5.49. BE should increase with airflow, as with a constant AFR more energy is added to the system. However, the gradient of BE increase decreases with increasing pressure. With a drop in BE from the 3.5MPa to 4.0 MPa test points. This suggest CE is falling at these elevated pressure conditions. As torque is directly related to airflow, the same reasoning applies to the torque case.

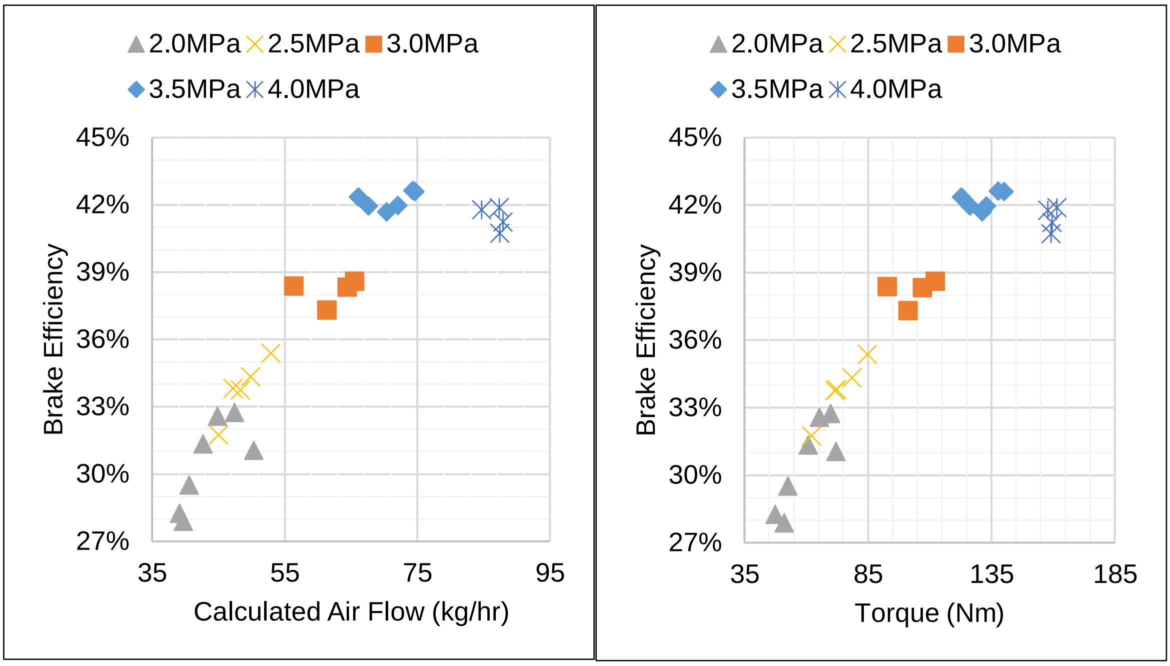

Figure 5.49 Inlet Pressure & Temperature Swing – BE against calculated air flow (left) and torque (right).

5.8.3.2 Emissions

The FSN response to the swing is shown in Figure 5.50. As temperature increases, the reactivity and vaporisation of the fuel increases. Therefore, it is expected that FSN decreases with increasing temperature, and this is generally shown to be the case throughout all of the pressures for the swing. However, there is a slightly flatter response at lower temperatures for the 2.0 and 2.5 MPa cases. This may suggest there is another form of ignition of combustion occurring in the high temperature, low pressure, and therefore low density cases. At these conditions it is possible that there is impingement of fuel spray into the piston resulting in surface ignition driven combustion.

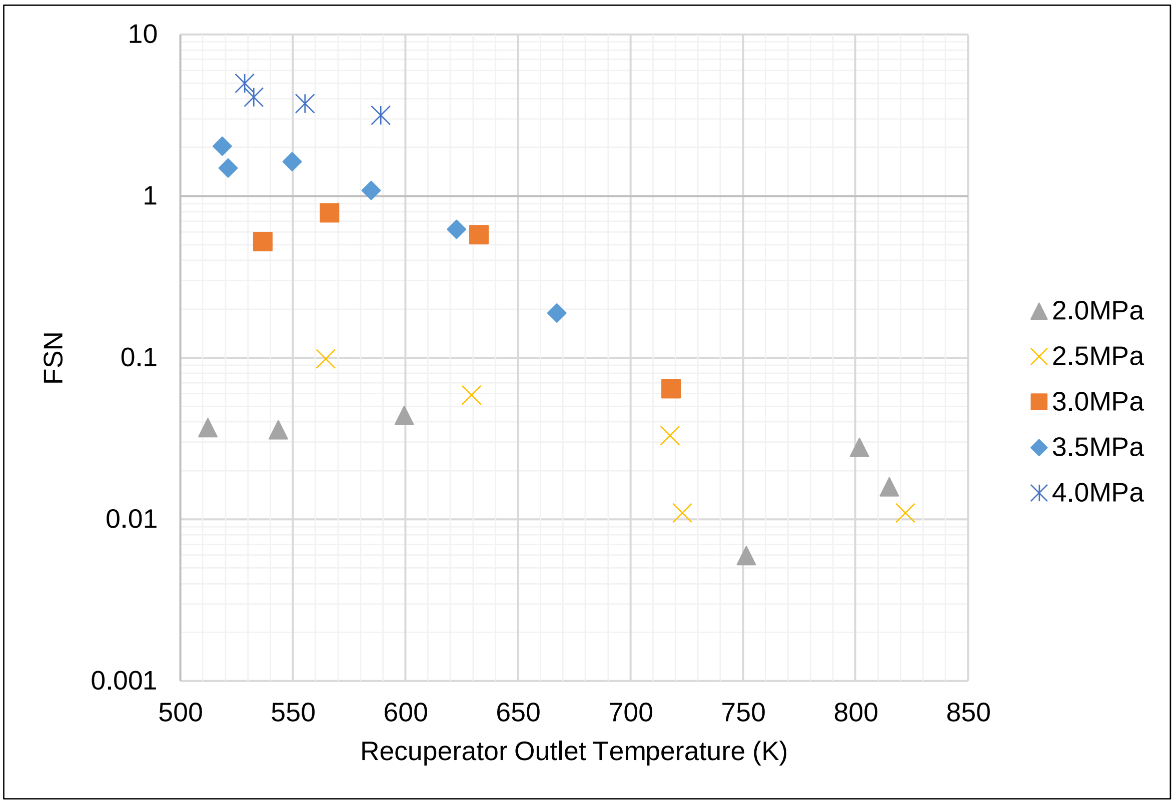

Figure 5.50 Inlet Pressure & Temperature Swing – FSN against recuperator outlet temperature.

An alternative graph is shown in Figure 5.51, in which FSN is plotted against the calculated density at the recuperator outlet. This more accurately captures the variation in measured temperature and pressure. This suggests a strong trend of exponential increase in FSN with density. However, this may not represent a complete picture due to the gas burner limitations. Resulting in the highest temperature of 315°C in the recuperator outlet at 4.0MPa, compared to 549°C in the highest 2.5MPa case.

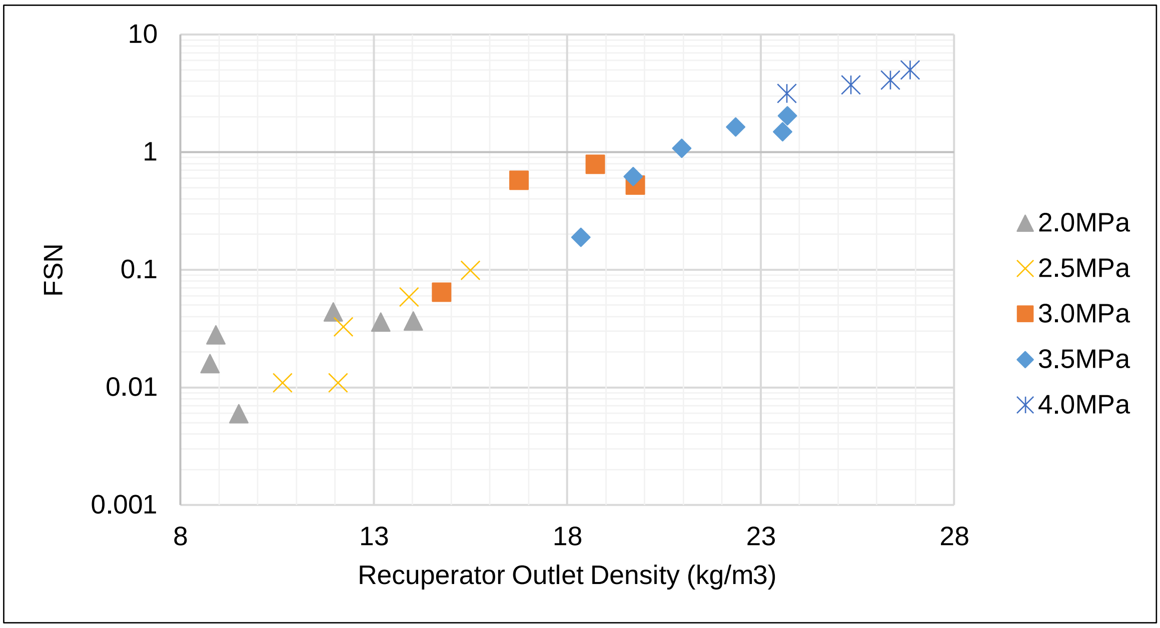

Figure 5.51 Inlet Pressure & Temperature Swing – FSN against recuperator outlet density.

The trend with density is still not expected, as with higher density it would be assumed that atomisation would increase and therefore there would be a lower FSN. Each pressure swing has a near constant gradient with FSN, with the gradient increasing with pressure. This suggests there is a pressure related phenomena that is causing a change in the gradient. A cause for this could be that the bulk and localised air motion changes at high pressure, which does not create the same air fuel conditions as lower pressure conditions, causing localisation of fuel mixture resulting in higher FSN.

The BSNO$_x$ response against temperature for the test points can be seen in Figure 5.52. Overall, engine out NO$_x$ production for the entire swing is low (< 8g/kWhr) over the range of inlet temperatures tested, compared to conventional ICEs. However, this does not subtract the “free” Rankine work and therefore the specific NO$_x$ will be higher once this is accounted for. With the exception of the two lowest temperature 2.0MPa cases, there is a linear trend of BSNO$_x$ against recuperator outlet temperature, which would be expected. However, there is not enough test points at high temperature and high pressure to confirm that the cases follow the same trend at high temperature. The difference in BSNO$_x$ response at sub 650K suggests there is poor localised mixing at higher pressures, as NO$_x$ should more readily produce in the higher pressure conditions if other variables are maintained.

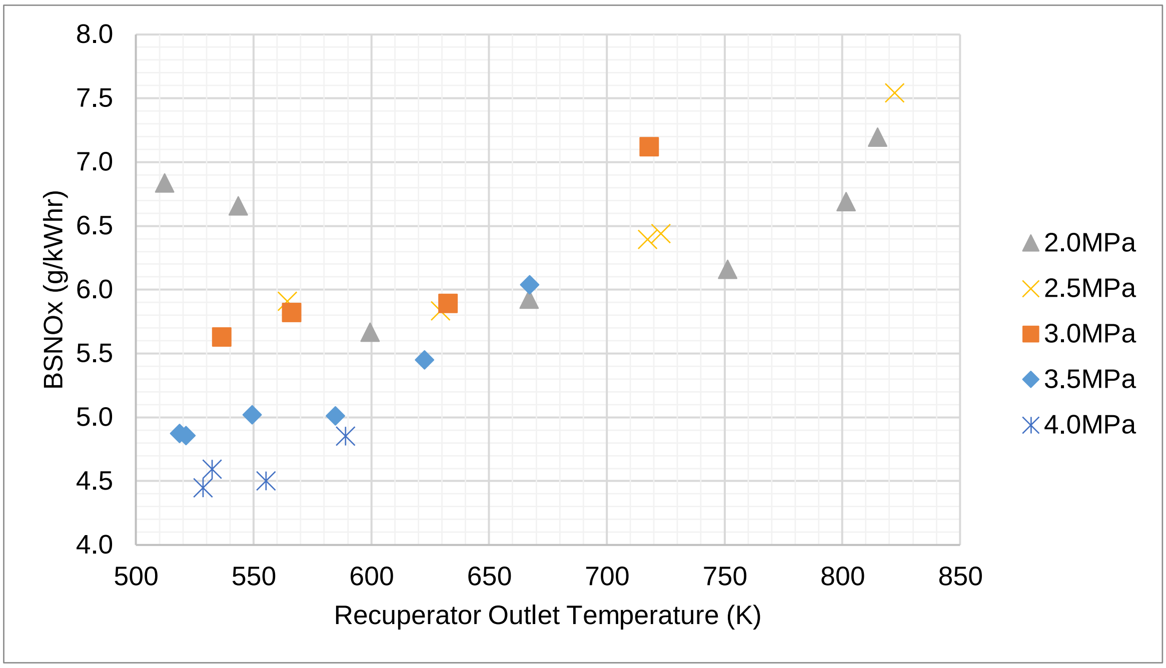

Figure 5.52 Inlet Pressure & Temperature Swing – BSNOx against recuperator outlet temperature.

$BSNO_x$ plotted against recuperator outlet density can be seen in Figure 5.53. With the exception of the two highest density 2.0MPa test points, when plotted against density it appears that the 2.0, 2.5, and 3.0 MPa cases have similar responses, with the highest density cases of each producing similar $BSNO_x$ of around 5.7 g/kWhr. However, this is not the case for the 3.0 and 4.0 MPa cases, suggesting localised mixing is falling at elevated pressures, in line with the increased FSN responses.

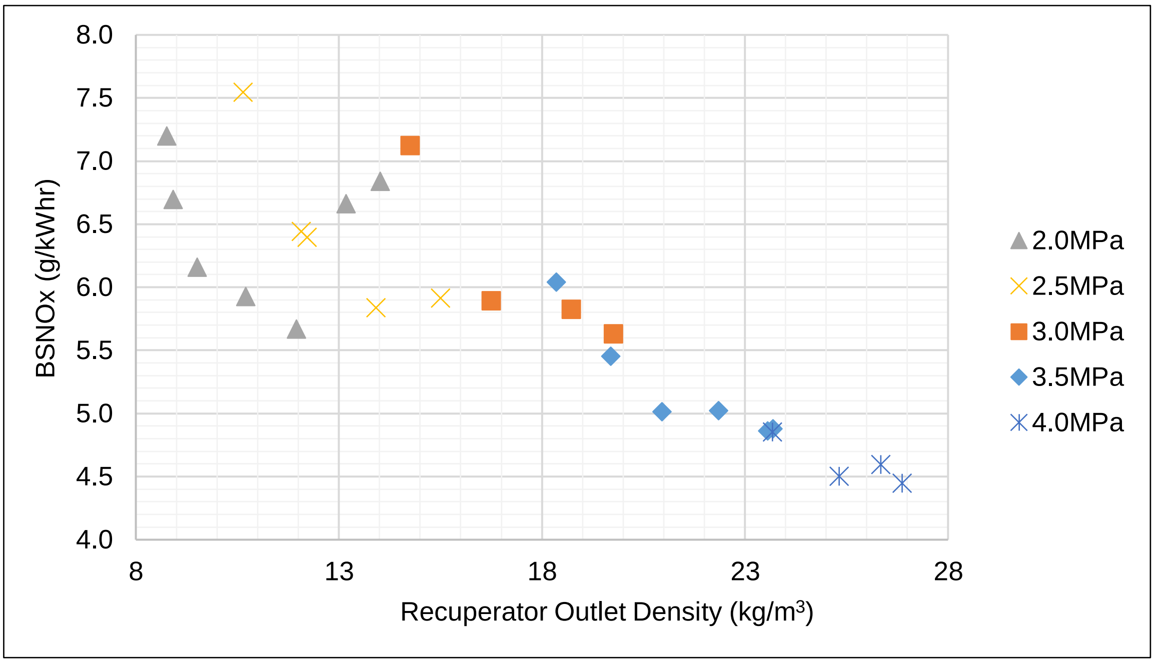

Figure 5.53 Inlet Pressure & Temperature Swing – BSNOx against recuperator outlet density.

The importance initial temperature plays in NO_x formation is underlined when looking at $BSNO_x$, shown in Figure 5.54. This displays that increasing exhaust temperature is not a prerequisite for NO_x formation. This graph underlines again a difference in the 3.5 and 4.0MPa cases.

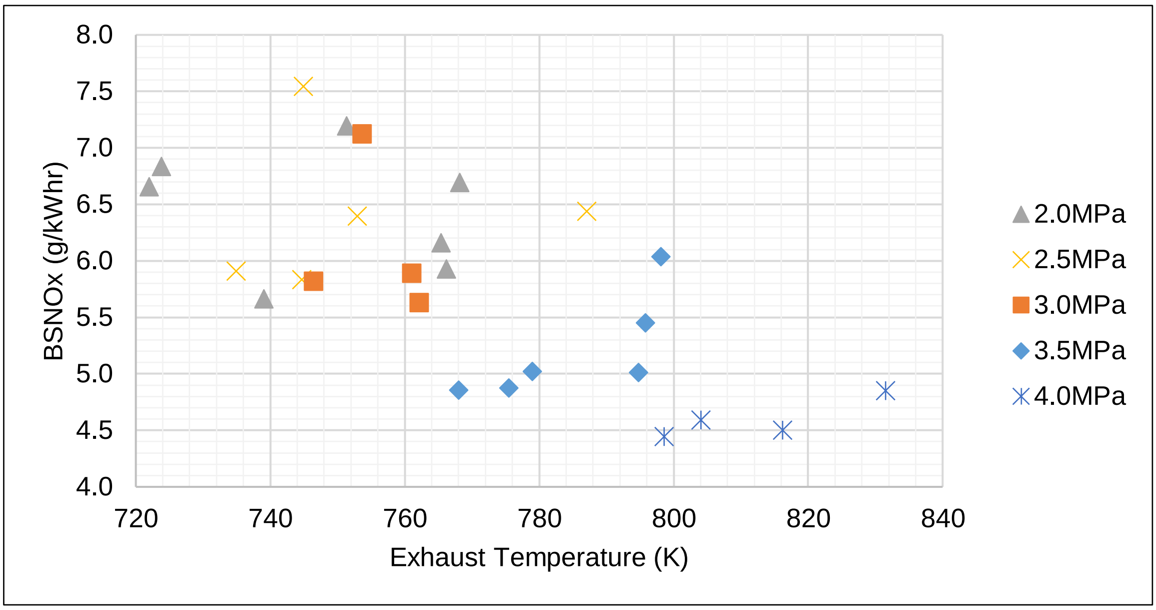

Figure 5.54 Inlet Pressure & Temperature Swing – BSNOx against exhaust temperature.

The BSHC response against recuperator outlet temperature is displayed in Figure 5.55. Interestingly the 2.0MPa swing displays a different response to that of the other cases, which large follow a lower linear positive trend, whereas the 2.0MPa case displays a negative linear trend with increasing recuperator outlet temperature.

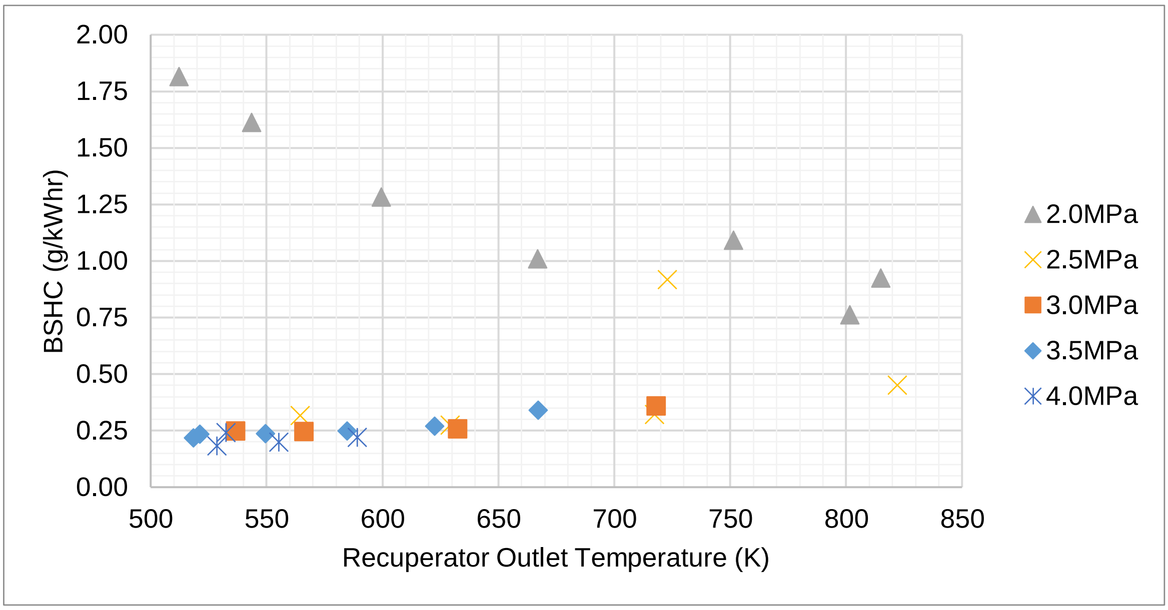

Figure 5.55 Inlet Pressure & Temperature Swing – BSHC against recuperator outlet temperature.

5.8.3.3 Other Variables

SOI against recuperator outlet temperature is shown in Figure 5.56. This display a guide for plotting the SOI required to provide stable combustion across this valve timing and engine speed for a wide range of pressures and temperatures. In the absence of high frequency pressure data to accurately access ignition delay, a rough assumption can be made by looking into SOI used during testing to maintain stable combustion. There is a linear trend in each pressure condition, with SOI requiring advancing with reducing recuperator outlet temperature. As well as SOI requiring retarding for a given intake temperature with increasing pressure. These both follow the expected responses as reaction rate increases with both increasing temperature and pressure. However, there is very limited change in SOI when comparing the 3.5 and 4.0 MPa cases. Suggesting and agreeing with previous data that poor air fuel mixing or another factor is impeding the overall reaction.

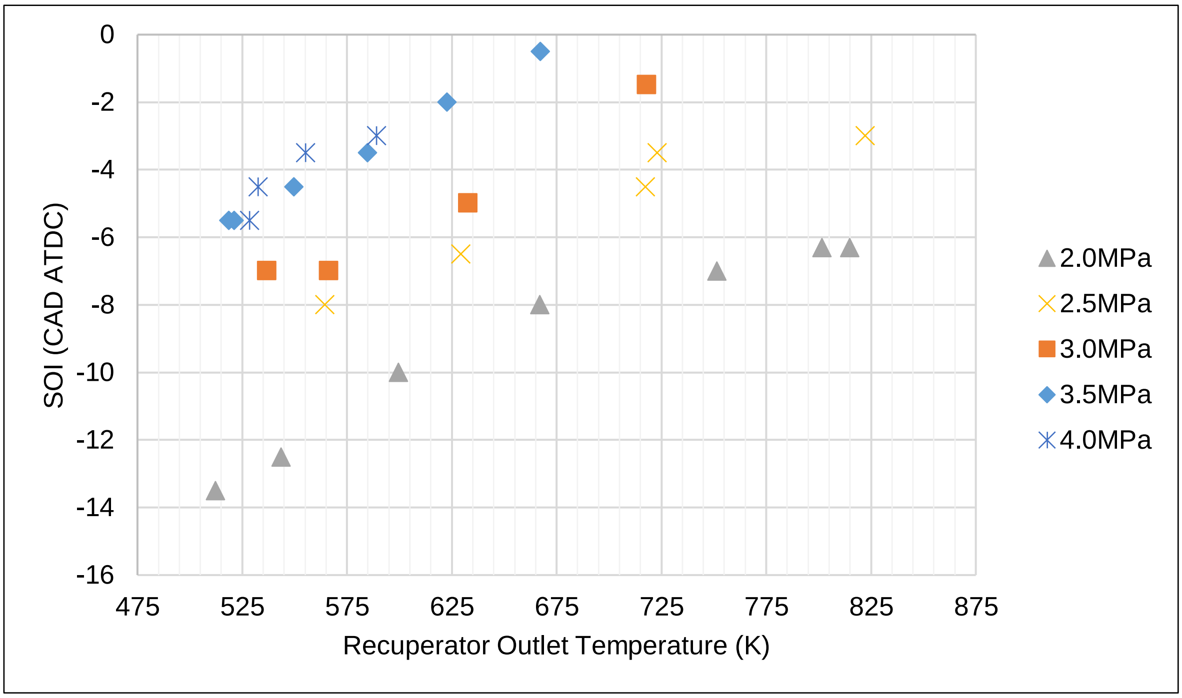

Figure 5.56 Inlet Pressure & Temperature Swing – SOI against recuperator outlet temperature.

Comparing the mass flow graphs from the Bronkhorst air mass flow meter and the calculated air mass flow from AFR and fuel mass flow, shown in Figure 5.57, clearly displays the issue with the Bronkhorst mass flow meter. The mass flow must increase with density, as shown in the calculated air flow graph. However, this is not picked up by the Bronkhorst mass flow meter, which reads the gradient incorrectly and low. Demonstrating that this cannot be relied upon.

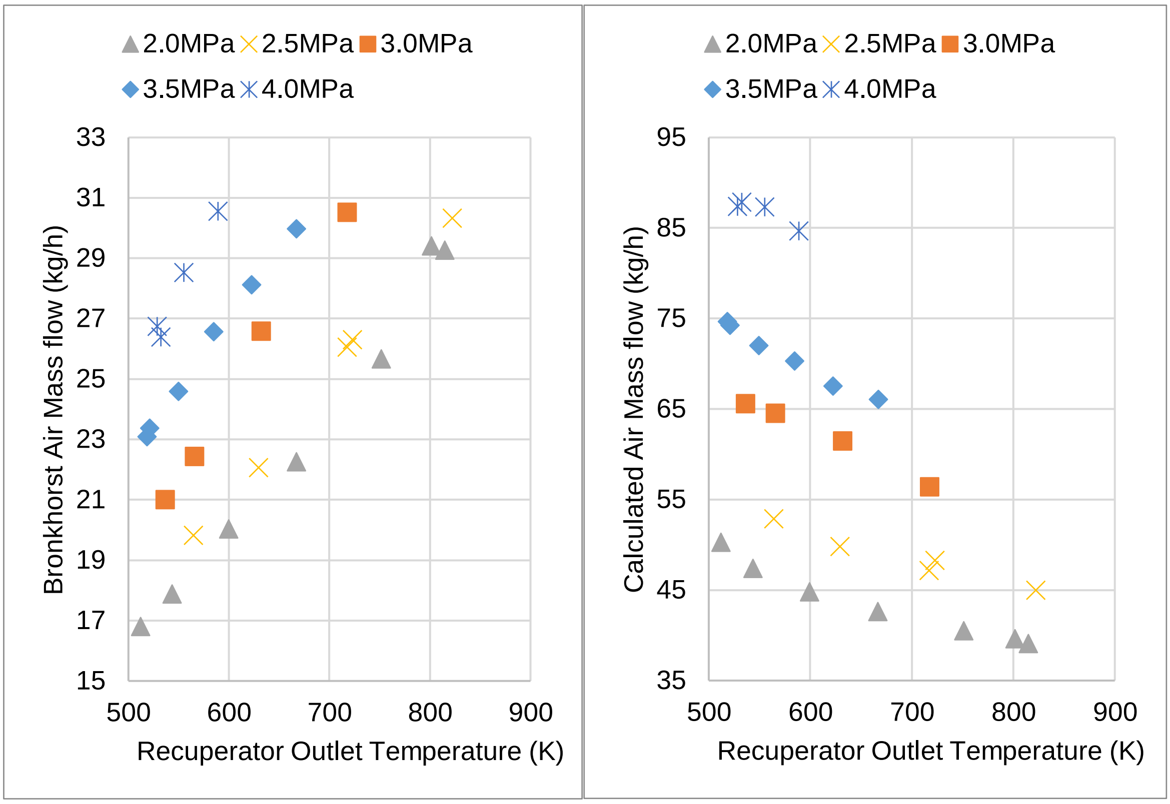

Figure 5.57 Inlet Pressure & Temperature Swing – Graphs of air mass flow against recuperator outlet temperature. Measured directly with a Bronkhorst air mass flow meter (left) and calculated using AFR and fuel flow (right).

5.8.4 Discussion

The inlet pressure and temperature swing suggests there are three fairly distinct combustion modes this set of testing:

1. The lowest pressure 2.0MPa swing indicates relatively good mixing but poor combustion reaction rate.
2. The medium pressure 2.5 and 3.0 MPa swings indicate both relatively good mixing and fast combustion rate.
3. The highest pressure 3.5 and 4.0 MPa swings indicate relatively poor mixing but fast combustion rate.

Optimisation and design of the combustion system required to enable the higher pressure cases to achieve a good level of mixing to reduce FSN and improve BE. A potential avenue for increased mixing and penetration for the high pressure cases could be to increase mixing.

5.9 Rail Pressure Swing

5.9.1 Aim

This set of test points aimed to understand if rail pressure has significant benefit to fuel atomisation and combustion in the same manner as conventional ICEs.

5.9.2 Initial Conditions

The set initial operating conditions of the SCCRE for the test points are shown in Table 5.10.

Table 5.10 Initial conditions of the injection timing swing tests.

Quantity	Value	Units
Intake Pressure	3.0	MPa
Engine Speed	1200	RPM
AFR	21	-
Intake Valve Opening	-35	CAD ATDC
Intake Valve Period	30	CAD
Exhaust Valve to Intake Valve Separation	15	CAD
Exhaust Valve Opening	180	CAD ATDC
Gas Burner Temperature	1073	K

The intake and exhaust valve profiles utilised for the swing are shown in Figure 5.58.

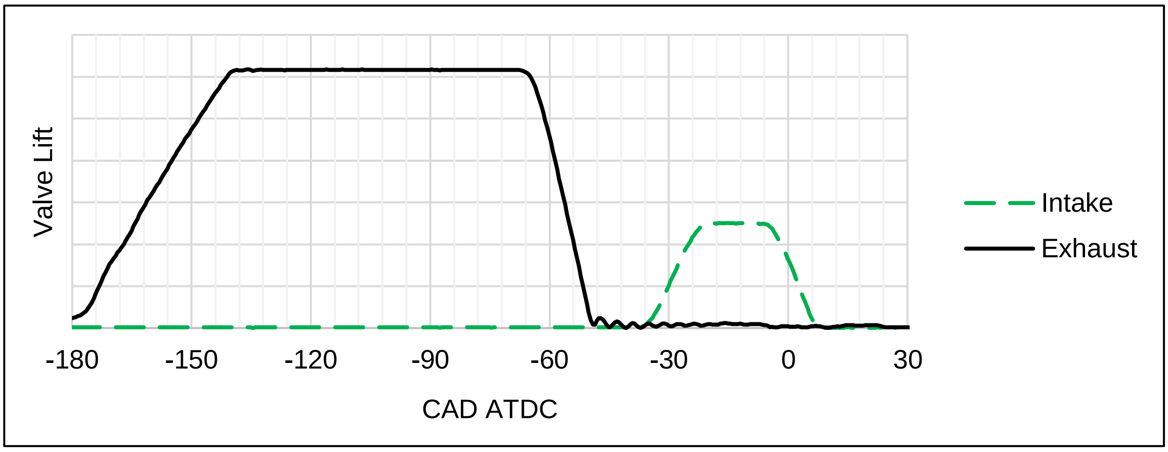

Figure 5.58 Rail Pressure Swing – Valve setup.

The SCCRE operating conditions across all rail pressure swing test points are shown in Table 5.11. A constant SOI of -6 CAD ATDC was utilised throughout the swing. AFR aimed to be 24, inlet pressure of 3.0 MPa, and a gas burner temperature of 1073K. SOC may begin earlier than can be seen in the high frequency cylinder pressure data, as the intake valves begin to close around -5 CAD ATDC and do not fully close until 5 CAD ATDC, this can be assessed in the CE data.

Table 5.11 SCCRE rail pressure swing operating conditions across all test points.

Test Number	Rail Pressure (MPa)	SOC (CAD ATDC)	IGN Delay (CAD)	GIMEP Mean (Pa)	GIMEP SD (Pa)
1	40	8.0	14	440,702	12,485
2	60	5.0	11	457,363	10,234
3	80	4.0	12	467,403	9,179
4	100	4.0	10	461,446	8,703
5	120	4.0	10	462,914	9,187

5.9.3 Results & Analysis

5.9.3.1 Cylinder Pressure

The recompression and calculated Rankine work are shown in Figure 5.59, there is minimal difference between the five test points. It is notable at this condition there is a relatively large high pressure pumping loop which will make these set of test points inefficient. However, they provide a stable point for assessing the effect of rail pressure, with SOC near TDC, combustion is stable across a range of rail pressures with a constant SOI.

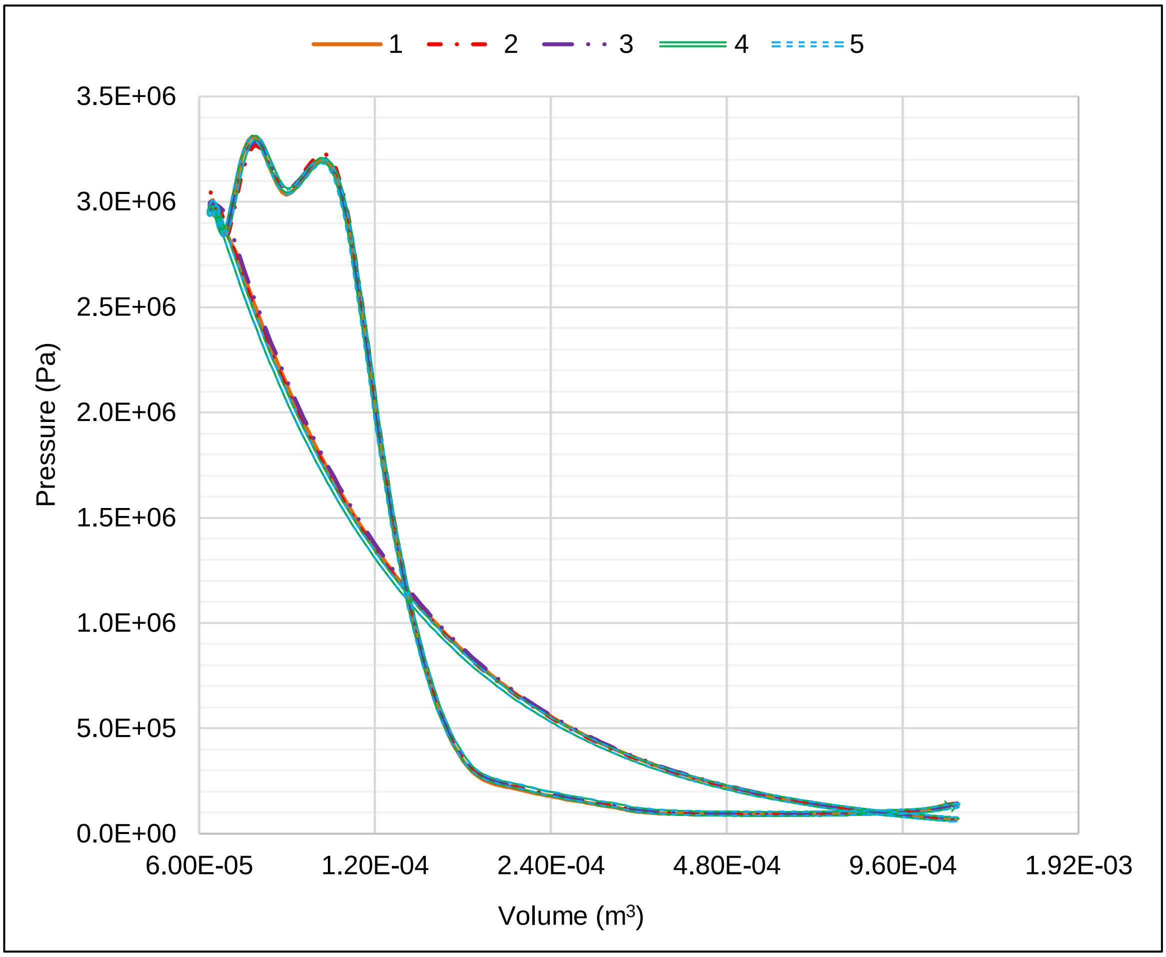

Figure 5.59 Rail Pressure Swing – Rankine PV traces.

Pressure traces initially suggest that there is still a mixing benefit in increasing rail pressure, as shown in Figure 5.60, with the 120 MPa rail pressure case having the highest peak cylinder pressure of 5.3MPa.

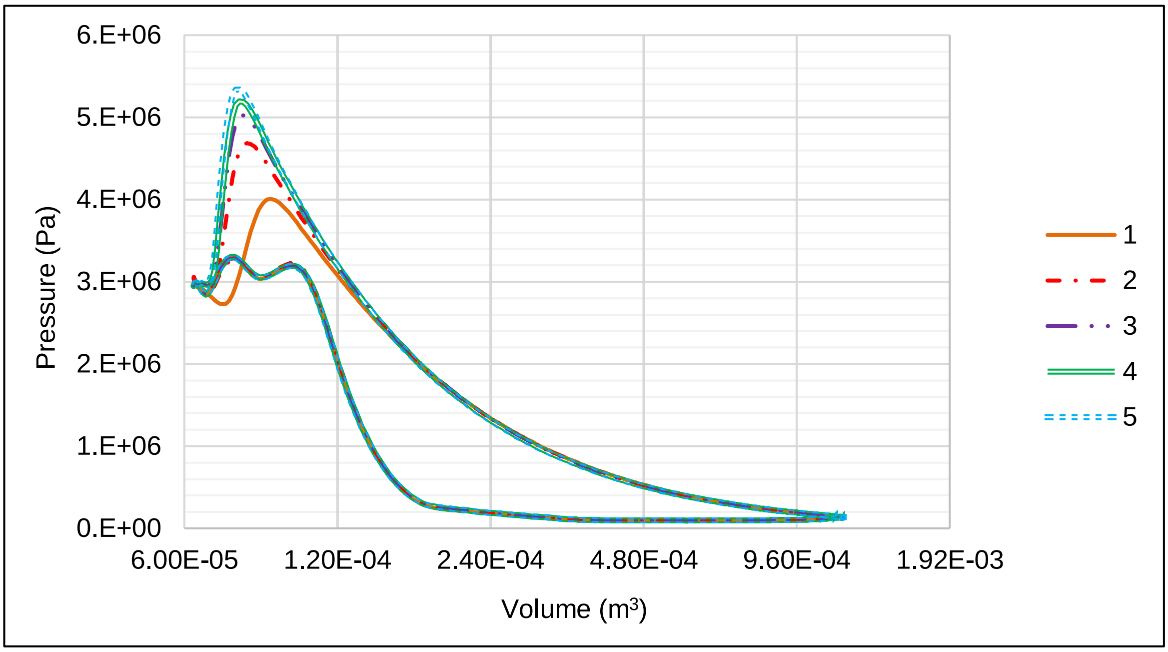

Figure 5.60 Rail Pressure Swing – PV diagrams.

5.9.3.2 Ignition & Combustion

The mass fraction burned is displayed in Figure 5.61. There is an improved rate of heat release and decrease in ignition delay with higher rail pressure that. However, the rate of improvement decreases until there is a marginal improvement between test point 4 and 5.

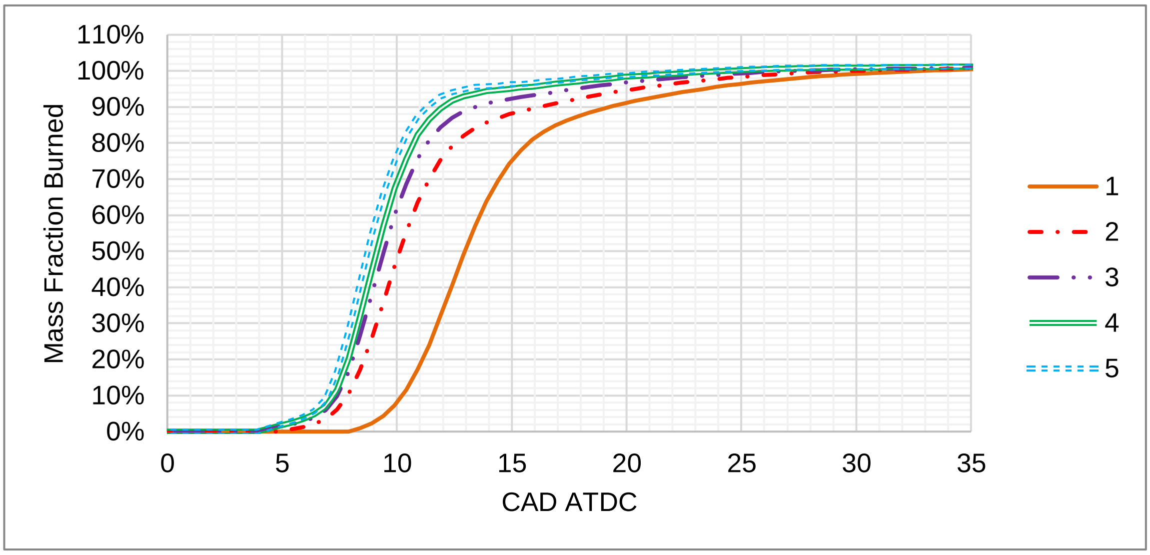

Figure 5.61 Rail Pressure Swing – Mass fraction burned.

5.9.3.3 Efficiencies

When looking at the combustion efficiency vs CAD, shown in Figure 5.62, the same reasoning can be applied as for the mass fraction burned. Again, there is little difference between 4 and 5, with 5 also displaying higher reduction or apparent heat loss after the combustion event, leading to a lower CE at 90 CAD ATDC.

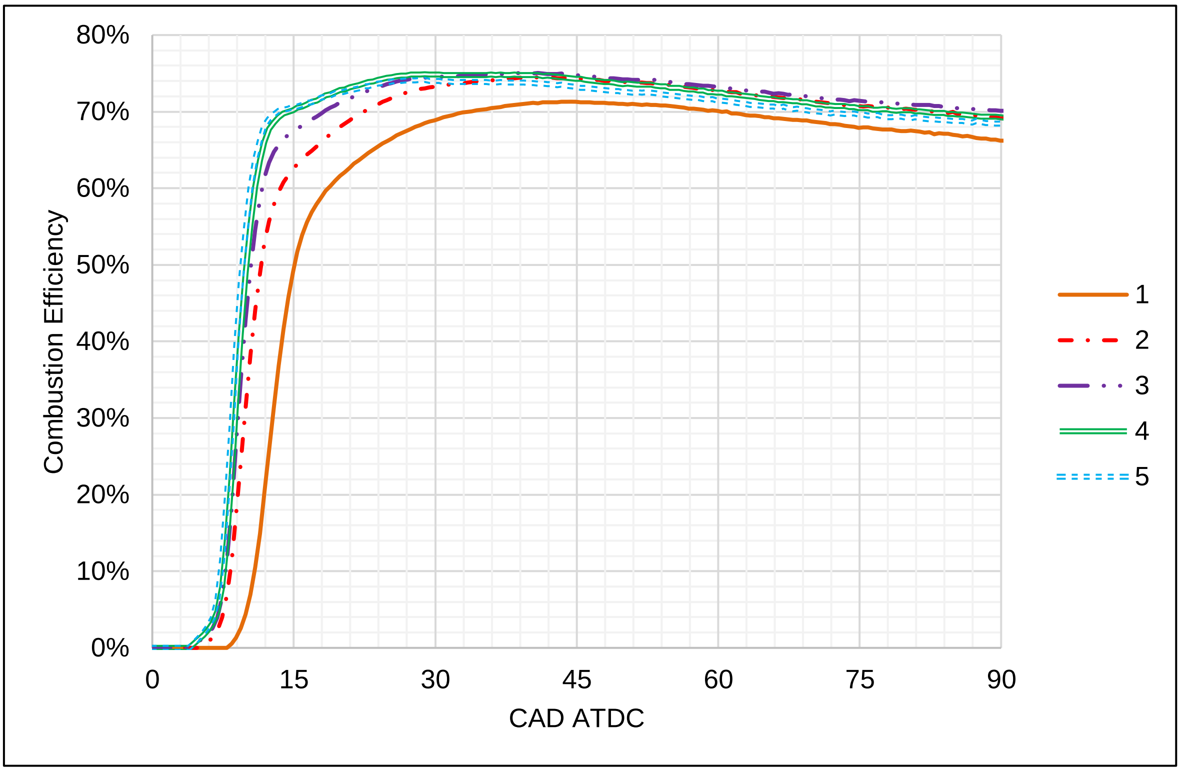

Figure 5.62 Rail Pressure Swing – Combustion efficiency.

The efficiencies for each test point are shown in Figure 5.63. The broadly consistent CE suggests there is not a significant portion of fuel combustion before IVC, as has been seen in other swings, such as in the injection timing swing in Section 5.6. However, the slight drop in CE at each point from 80 to 120 MPa suggests a small amount may be combusting before IVC. TE and CTE increase with rail pressure, due to the earlier ignition and faster heat release rate shown in MFB and CE plots. ETE increase up to 80MPa rail pressure, before stagnating due to no improvement in CW at the higher conditions, this is due to little difference in SOC and heat release rate at these conditions. EFE and BE increase for the same reasons of ETE, but also consider the slight drop in CE at pressures above 80MPa. Therefore, there is a stagnation and slight drop in EFE and BE at 100 and 120 MPa compared to the 80MPa test point.

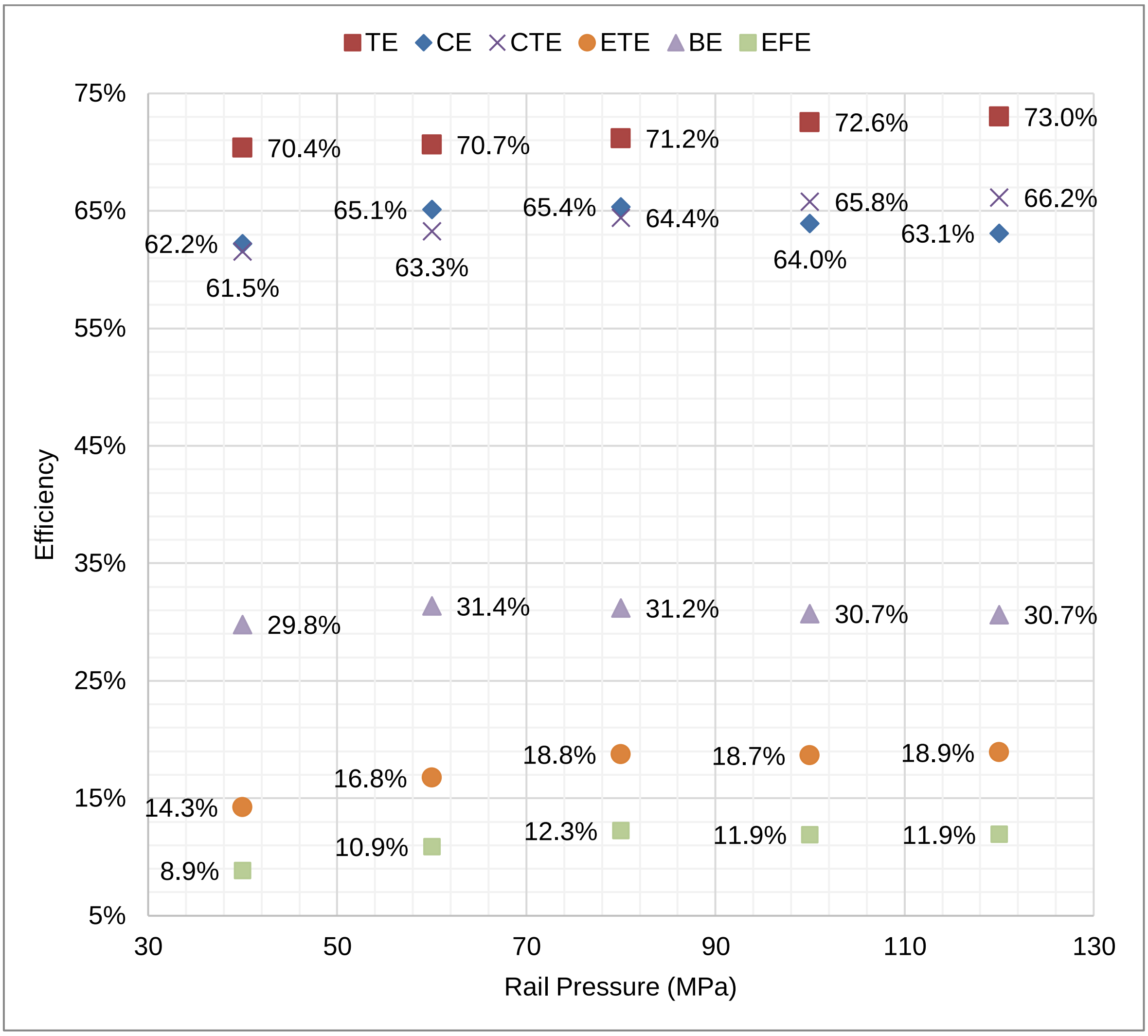

Figure 5.63 Rail Pressure Swing – Efficiencies

5.9.3.1 Emissions

Figure 5.64 presents a comparison of rail pressure swings from the SCCRE and a conventional Diesel single cylinder research engine (Ricardo Proteus). FSN was observed to plateau at a lower rail pressure condition of approximately 100 MPa in the SCCRE, compared to the convention-al Diesel engines rail pressures of approximately 180 MPa. NO_x emissions increased with increased rail pressure in the case of the SCCRE, suggesting the dependence is still in line with that of conventional engines. This is expected in both scenarios, as with higher temperatures carbonaceous matter is more likely to combust and NO_x is more likely to be produced. However, as rail pressure increases to very high pressures (>100 MPa) it would be expected in conventional engines for NO_x to begin to flatten out. The linear response suggests that the local premixed air and fuel is closer to stoichiometric, rather than rich local equivalence ratio in Diesel engines.

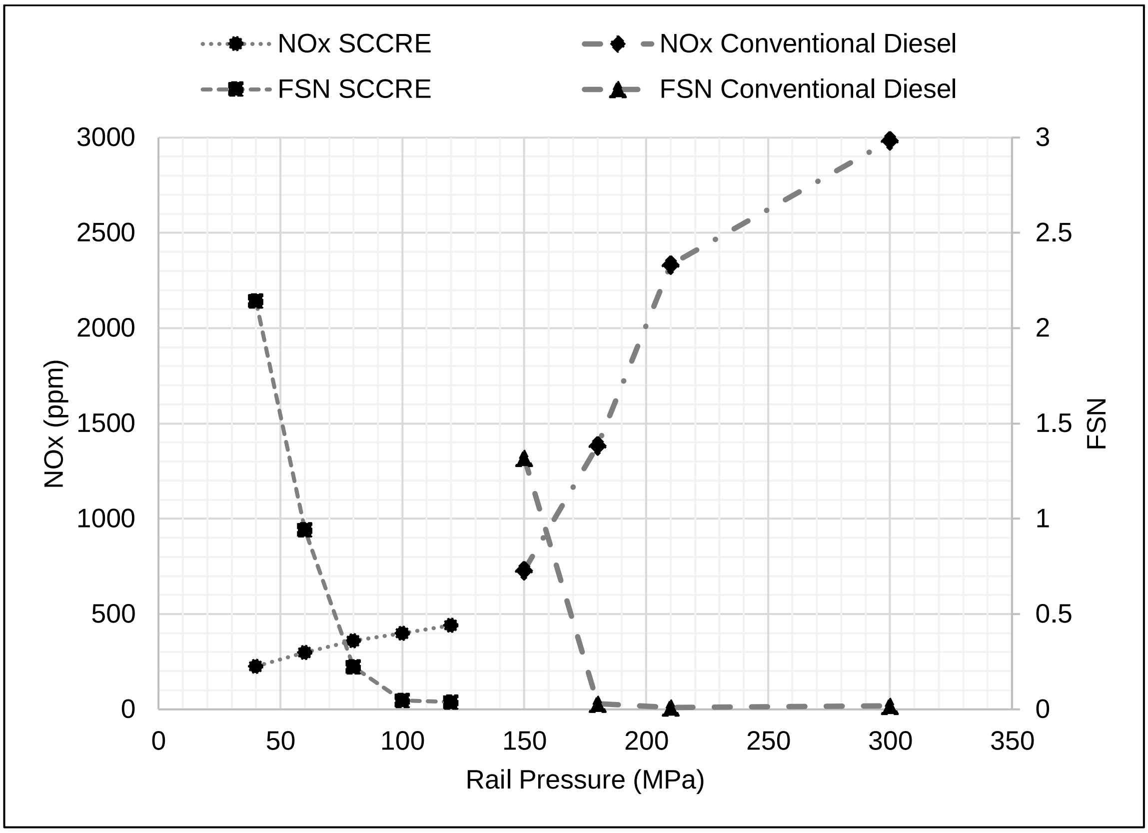

Figure 5.64 Rail Pressure Swing – NOx and FSN vs rail pressure from the SCCRE at 1,200 RPM and 0.69 equivalence ratio (21 AFR) and from the Proteus at 1,250 RPM and 0.66 equivalence ratio (22 AFR). Data previously reported in [8].

The earlier plateauing of FSN with rail pressure, increasing NO_x with rail pressure, and high PRR (relative to the low temperature and pressure conditions), suggests there is an amplified or new phenomenon enhancing the air fuel mixing before combustion in comparison to conventional Diesel combustion systems. The two sets of data suggest that mixing has been amplified while reactivity has declined. The decline in reactivity can be attributed to the lower peak pressures and temperatures, however the increased mixing warrants further investigation.

Specific NO_x results are displayed in Figure 5.65. The effect of removing Rankine and compressor work for the $ESNO_x$ is apparent when comparing the specific NO_x response for these test points, as over half of the work is lost accounting for this. However, as previously discussed, the aim was not to produce a highly efficient and high power test point but to analyse the response to rail pressure. As rail pressure increases it would be expected for NO_x emissions to increase as higher amounts of local mixing and combustion occur. This is shown to be the case in the specific NO_x in line with the ppm shown in Figure 5.64. This does suggest there may still be further gains to be had from increasing rail pressure beyond 120MPa.

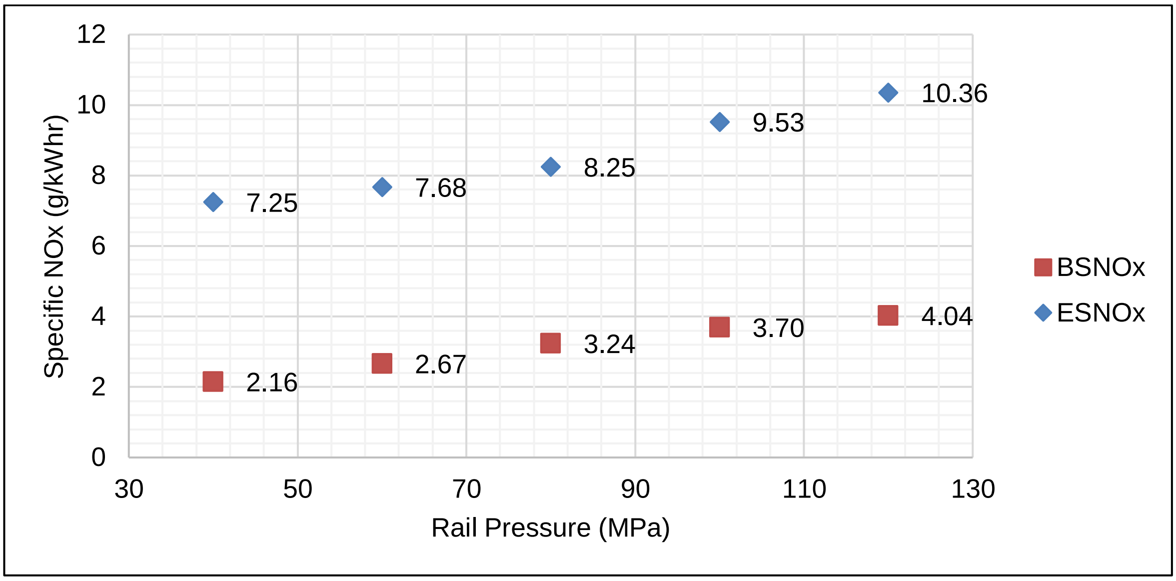

Figure 5.65 Rail Pressure Swing – Specific NOx.

Specific HC response is shown in Figure 5.66. Specific HC is shown to reduce from 40 to 80 MPa and stagnate from 80 to 120 MPa. It would be expected for HC emissions to decrease as atomisation and combustion improve. The stagnation from 80 to 120 MPa suggests there is not an additional benefit.

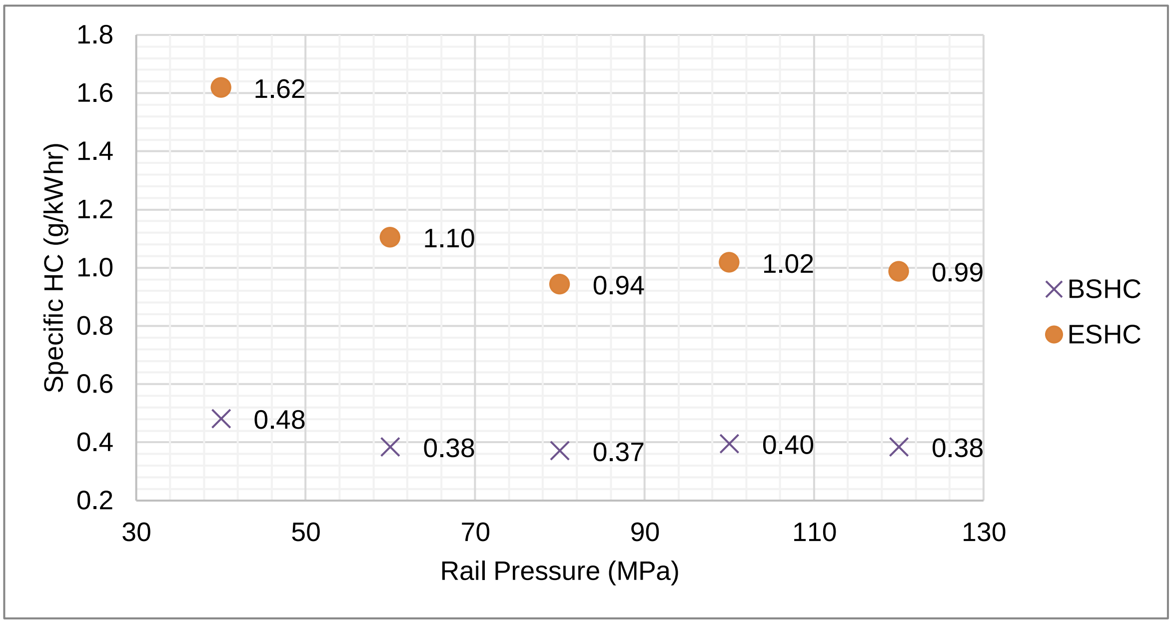

Figure 5.66 Rail Pressure Swing – Specific HC.

5.9.3.2 Other Variables

Figure 5.67 displays the average IMEP over 100 cycles for each test point over the rail pressure swing. This displays the highest IMEP of 4.67 bar at 80 MPa before dropping for 100 and 120 MPa rail pressure.

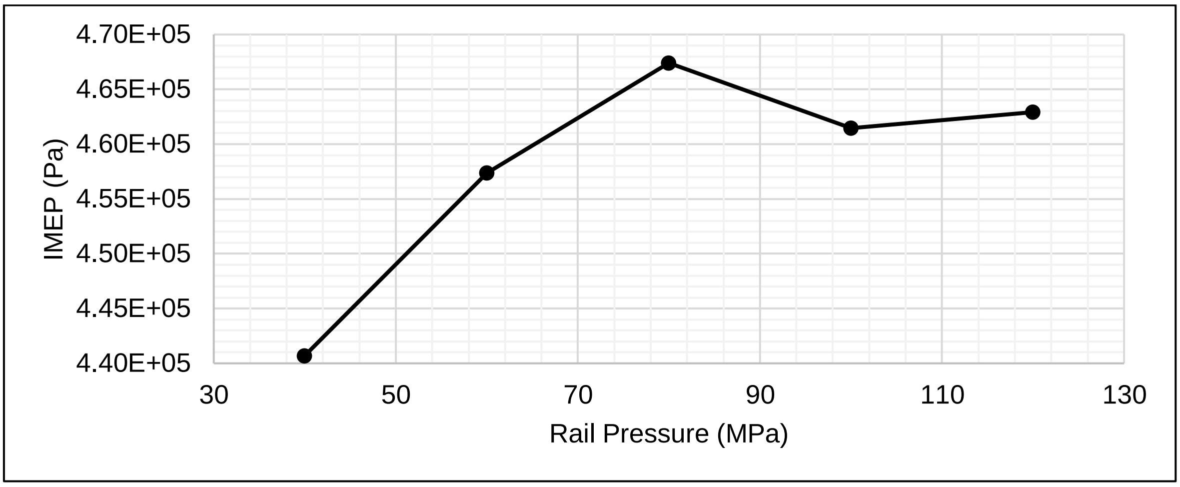

Figure 5.67 Rail Pressure Swing - IMEP

Air flow vs rail pressure is shown in Figure 5.68. There is a decrease in air flow from 40 to 60 MPa, before an increase at 80 MPa followed by a plateau from 80 to 120 MPa. Typically, it would be expected for air flow to be an indicator of torque at a set speed, with a higher mass flow of air allowing more fuel to combust for the same air fuel ratio. This is still the caser in the SCCRE and RSCE, however the variation in air inlet temperature must be considered as this can vary by a large amount, affecting the air flow and torque in the engine.

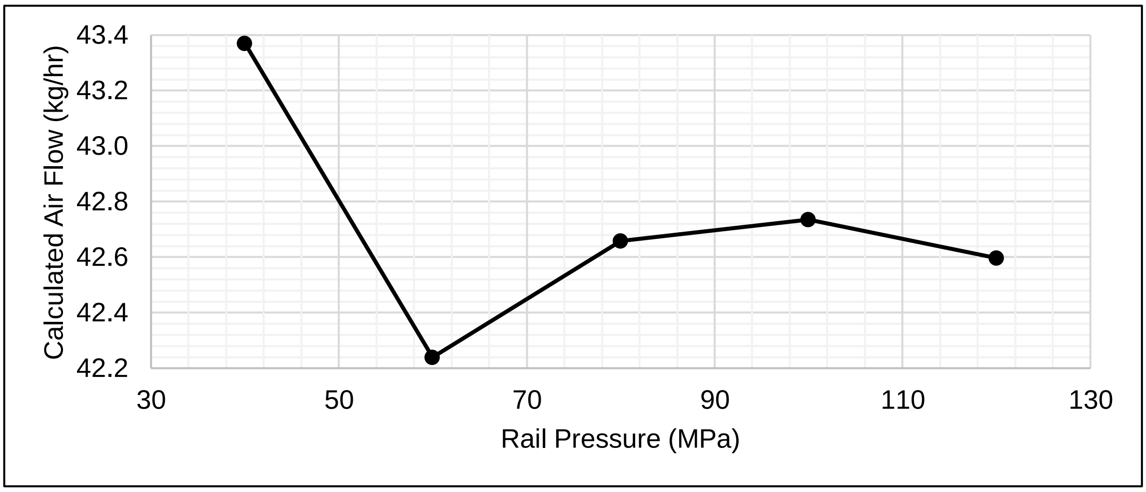

Figure 5.68 Rail Pressure Swing – Air flow (calculated from AFR)

The variation in recuperator out temperature over the rail pressure swing is shown in Figure 5.69. Although the burner that feeds the recuperator is at a set temperature for these tests, the HP air out temperature of the recuperator varies depending on the air flow and temperature of the recuperator. A relatively minor variation of only ~20K is observed during this swing, suggesting this has little impact on the results.

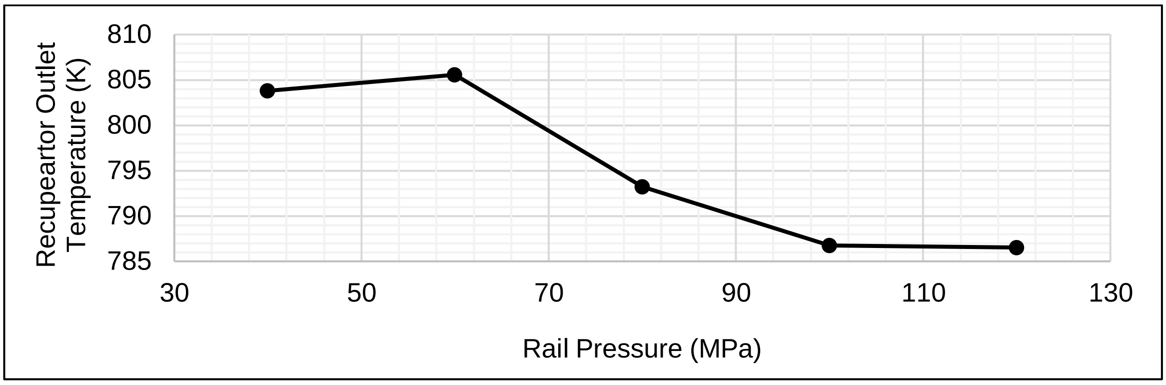

Figure 5.69 Rail Pressure Swing - Recuperator HP out temperature

Figure 5.70 displays the rail pressure swing vs high pressure recuperator out density. It would be expected that with the higher air density in the cylinder that fuel atomisation would increase. However, the change in cylinder air density is relatively small, with a difference of only 0.32kg/m^3 from the lowest density (13.32kg/m^3) and highest density (13.64kg/m^3) in the rail pressure swing cases.

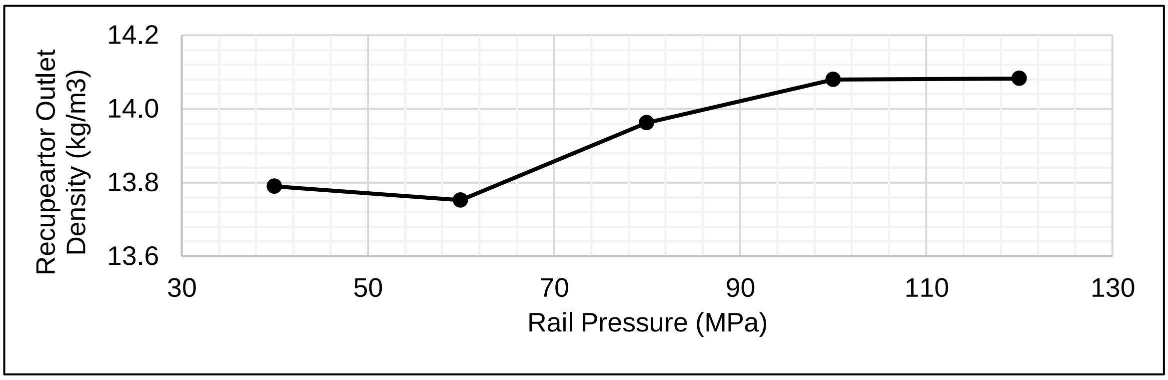

Figure 5.70 Rail Pressure Swing - Recuperator HP out density

Figure 5.71 displays the torque output for the rail pressure swings. Combined with CE and IMEP, this confirms the 40 MPa case has the poorest combustion but there is less variation amongst the other cases.

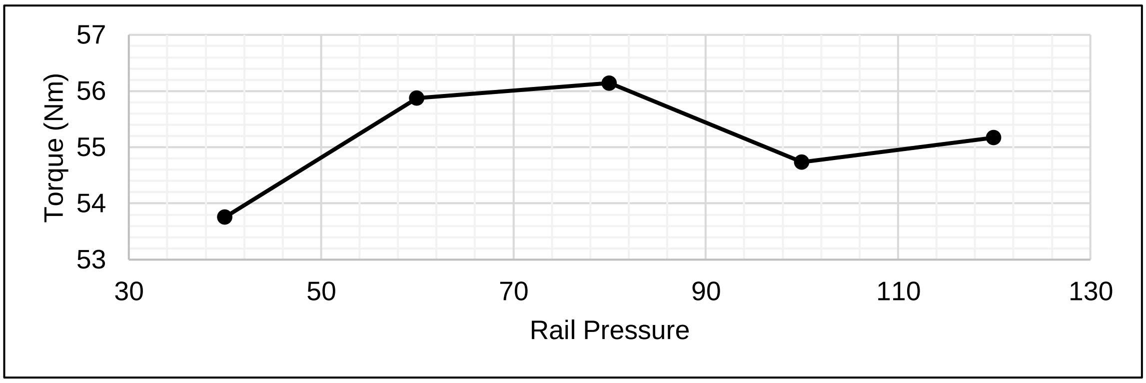

Figure 5.71 Rail Pressure Swing – Torque

5.10 Nitrogen Dilution

5.10.1 Aim

As previously discussed in Chapter 3, dilution is another method of decreasing the formation of NO_x, reducing the combustion temperatures and adiabatic flame temperature. Whereas this has been achieved previously through EGR, dilution using nitrogen is an alternative method to achieving oxygen dilution which has a negligible impact on the specific heat capacity of the working fluid and can be used as a coolant, if LN2 is utilised, to achieve isothermal compression in a RSCE. LN2 can be green source of endothermic coolant and diluent if produced from renewable electricity.

5.10.2 Initial Conditions

The initial conditions for the nitrogen dilution tests are shown in Table 5.12.

Table 5.12 Initial conditions of the nitrogen dilution tests.

Quantity	Value	Units
Intake Pressure	4.0	MPa
Engine Speed	1200	RPM
AFR	21	-
Intake Valve Opening	-30	CAD ATDC
Intake Valve Period	25	CAD
Exhaust Valve to Intake Valve Separation	15	CAD
Exhaust Valve Opening	175	CAD ATDC
Gas Burner Temperature	1073	K

Three nitrogen dilution test points will be presented with a comparative atmospheric air condition test point. While not completely identical in conditions, the comparative test point has a valve profiles close to that of the nitrogen dilution case, as well as similar AFR, air flow, torque, and inlet temperatures. The test point valve setups vary by a couple of degrees, as shown in Figure 5.72, due to operator error from the manual setup of the valves. The peaks seen in the exhaust profiles are due to issues with the displacement assembly during testing.

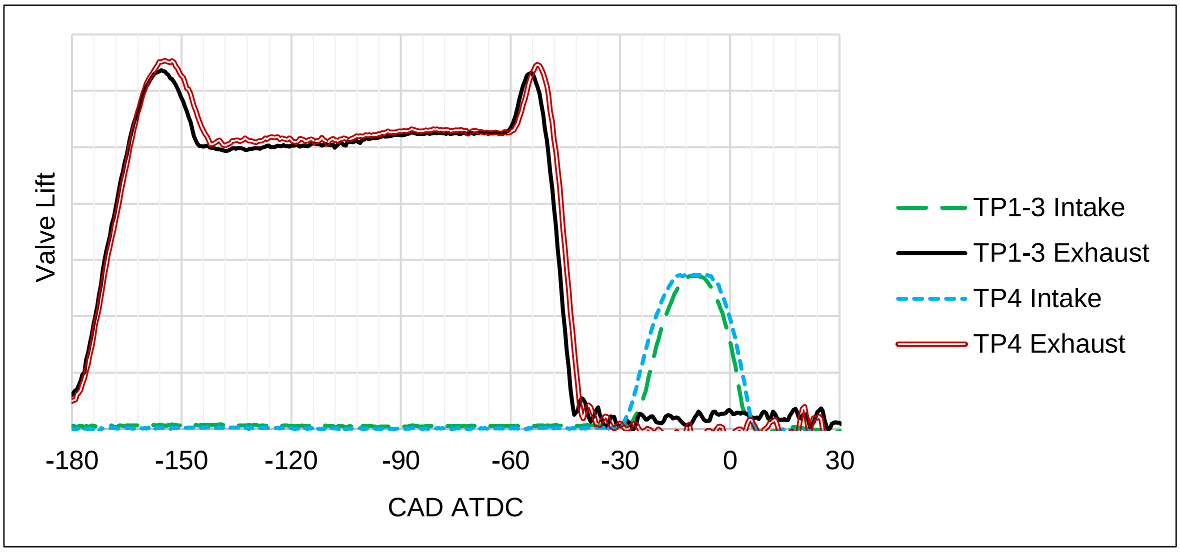

Figure 5.72 Nitrogen Dilution – Valve setups for test points 1-3 and the comparative test point 4.

The rail pressure and SOI for the 4 test points is shown in Table 5.13. There was a small swing in rail pressure for the nitrogen dilution cases. SOI aimed to produce a normalised stable combustion and therefore varied accordingly by the operator.

Table 5.13 Nitrogen dilution test points 1-3 and comparative test point 4.

Test Number	**Rail Pressure (MPa)**	**SOI (CAD ATDC)**	**GIMEP Mean (Pa)**	**GIMEP SD (Pa)**
1	120	-6.6	898,571	15,555
2	100	-7.6	893,358	14,231
3	140	-8.0	894,727	17,101
4	120	-4.0	881,893	14,253

Air is diluted with pure nitrogen to obtain 18% oxygen by volume in the nitrogen diluted cases. The measured AFR and recuperator outlet temperatures are shown in Figure 5.73. The is a minor variation in AFR of 0.3 across all 4 test points. There is a minor variation in temperature of 6K, however test point 4 is 70K higher than test points 1-3.

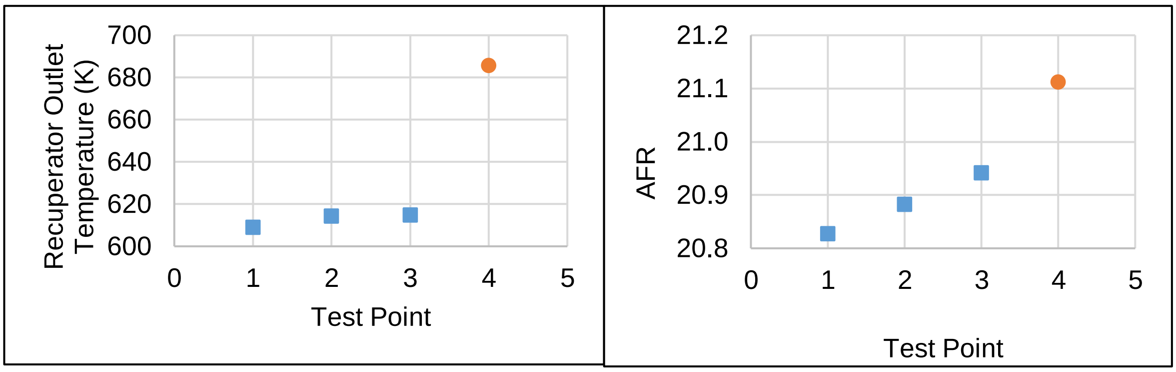

Figure 5.73 Nitrogen Dilution – Recuperator outlet temperature (left) and AFR (right) conditions obtained for the test points.

5.10.3 Results & Analysis

5.10.3.1 Cylinder Pressure

The cylinder pressure data for the three test points are presented in Figure 5.74. The effect the small change in IVO can be seen from the earlier cylinder pressure rise for test point 4. This also effects the timing of the pressure waves in the chamber, resulting in less airflow as IVC occurs during the pressure pulsation trough.

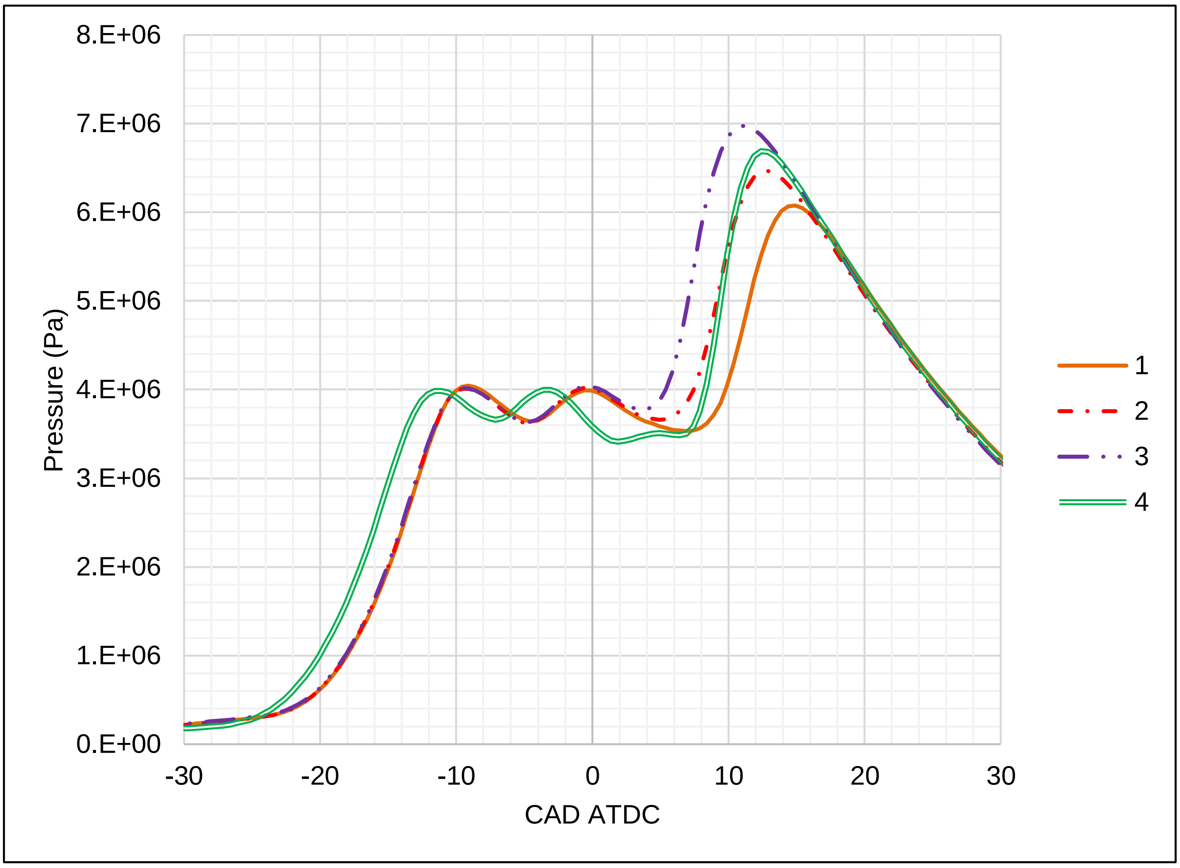

Figure 5.74 Nitrogen Dilution – Cylinder pressure vs CAD.

The earlier valve timing inefficiency can be seen when comparing test point 4 to the nitrogen dilution cases in Figure 5.75. Test point 3 can be seen to have the highest peak pressure due to having the earliest SOC.

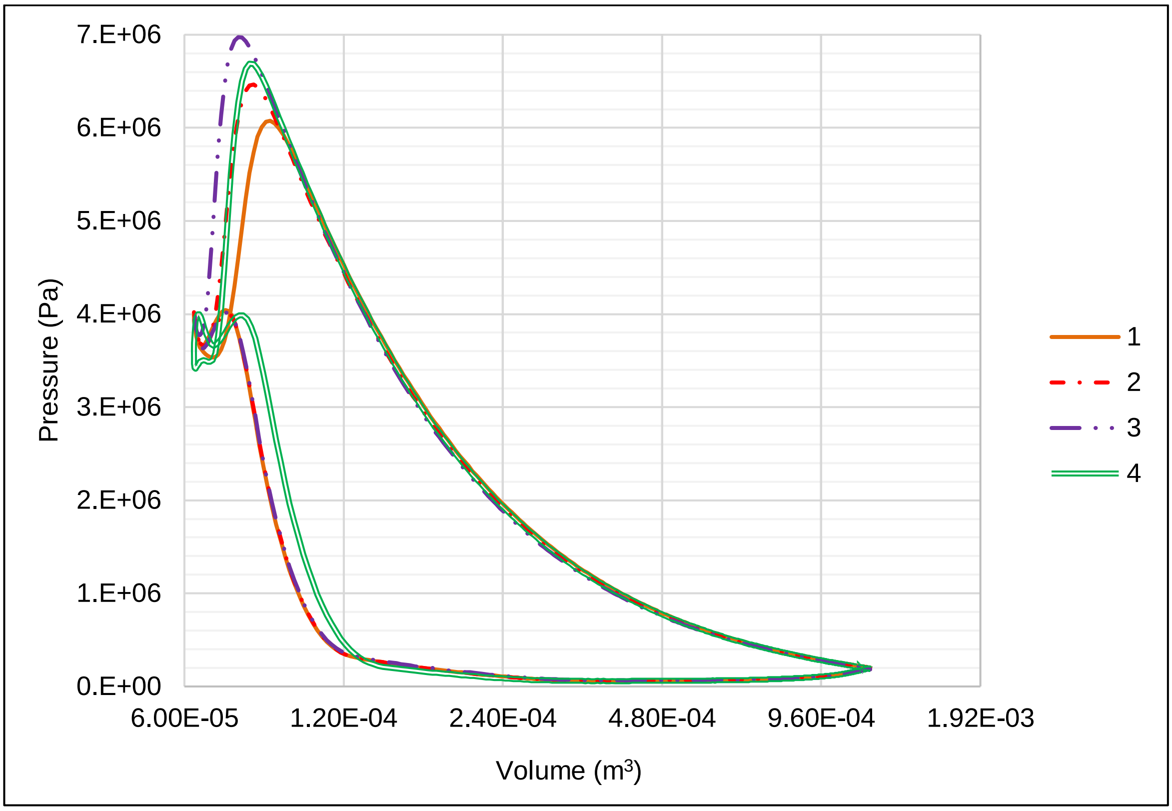

Figure 5.75 Nitrogen Dilution – PV diagrams.

5.10.3.2 Ignition & Combustion

The mass fraction burned is presented in Figure 5.76. Again, the earlier SOC for test point 3 is observed. The faster combustion of test point 4 can be seen compared to test point 2. Although test point 2 has an earlier SOC, the faster heat release of test point 4 results in a similar 50% burn point for both cases. This is expected due to the higher amount of energy available in the standard air case compared to the N2 dilution case, due to the consistent AFR.

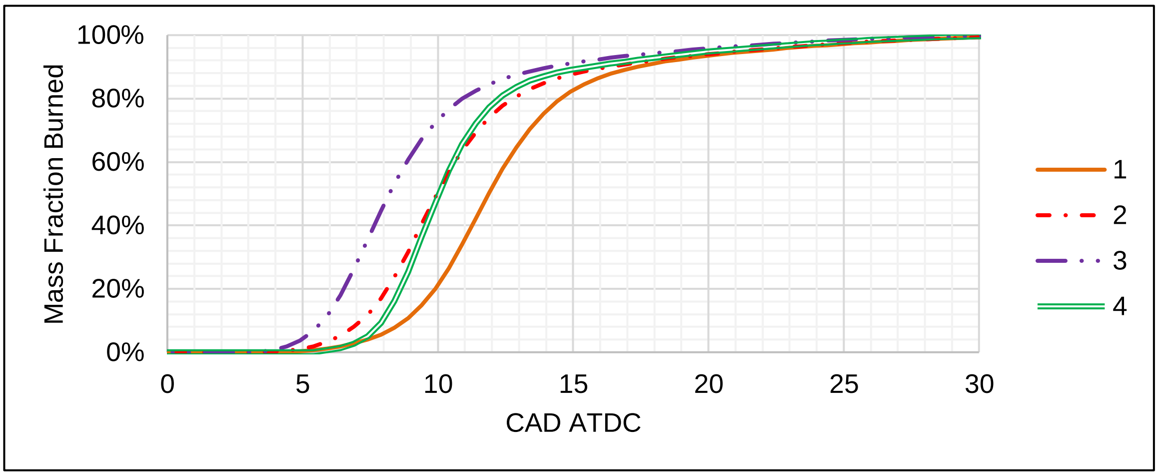

Figure 5.76 Nitrogen Dilution – Mass fraction burned.

The AHR is shown in Figure 5.77. It is clear from Figure 5.77 that test case 4 adds more energy to the system. However, as seen in Figure 5.74 and Figure 5.75, this does not result in the highest cylinder pressure due to the retarded SOC compared to test point 3. Test points1-3 show increasing initial AHR rates with earlier SOC due to the combustion phasing into areas of lower cylinder volume change.

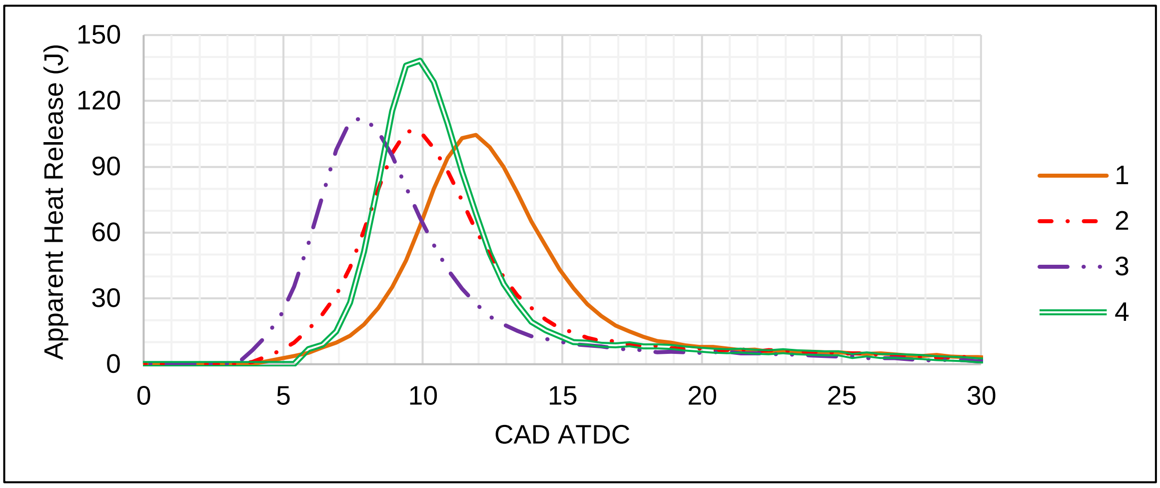

Figure 5.77 Nitrogen Dilution – Apparent heat release.

5.10.3.3 Efficiencies

The efficiencies for the 4 test points are shown in Figure 5.78. By introducing dilution and lowering the quantity of fuel energy due to the constant AFR, TE will increase as a higher proportion of total work is performed by “free” Rankine work, in the same manner as increasing AFR. Even with a slightly lower heat release rate, this results in 1.4% increase in TE for test point 3 compared to test point 4. Test point 3 has the highest CTE due to early SOC and fast combustion, followed by test point 4. The CE for test points 1-3 are fairly constant within 0.9%. However, there is a drop in test point 4 of ~3%. Lower density due to slightly higher temperature likely reduced fuel atomisation. The nitrogen dilution may also allow a longer mixing time before ignition and during the combustion event. ETE is lowest in test point 4 at 46.5%, with test point 3 the highest at 47.8%. The highest ETE is explained again by the early SOC compared to the rest of the nitrogen dilution cases. Test point 4 is lower than the comparative test point 2 case due to the effect of valve timing, with the small difference resulting in increased recompression work that negates the positive effect of rapid heat release. BE is fairly flat with the nitrogen dilution cases with only a minimal difference of 0.4%. However, test point 4 is once again slightly lower due to the recompression work.

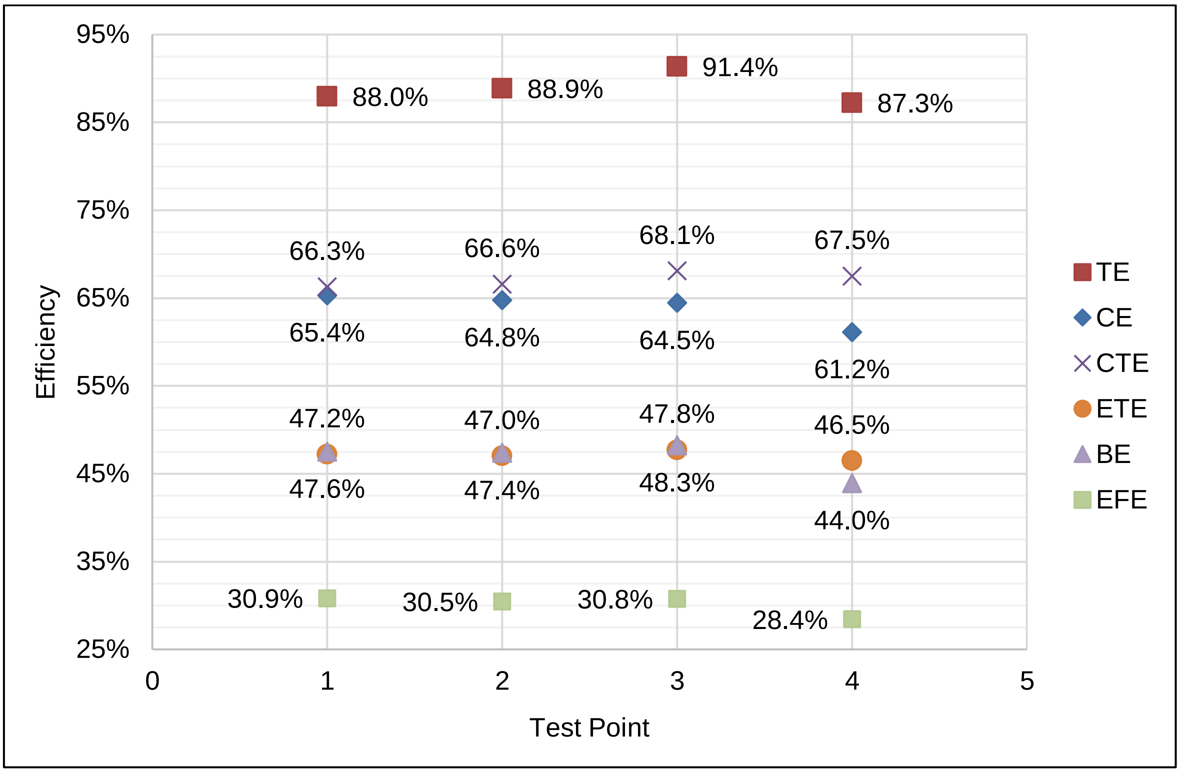

Figure 5.78 Nitrogen Dilution – Efficiencies.

5.10.3.4 Emissions

The FSN response for the 4 test points is shown in Figure 5.79. Not unexpectedly FSN increased for all of the nitrogen dilution cases, as there is less oxygen present in the mixture to react, compared to test point 4. With almost 3.5 times the FSN in test point 2 compared to test point 4. The fairly low recuperator outlet temperature of all the test points (608-694K) will have also played a role in increasing FSN. Interestingly FSN increased in test points 2 and 3 compared to test point 1. It is not obvious what has caused this difference. Overall FSN is still fairly high among all points and suggests there is improvements to be made in mixing and the reaction.

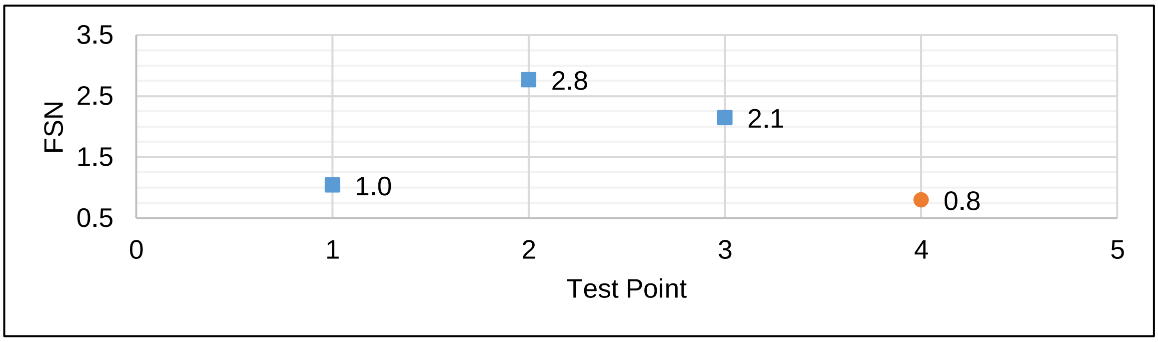

Figure 5.79 Nitrogen Dilution – FSN.

The specific NO$_x$ results are shown in Figure 5.80. There is a large reduction in specific NO$_x$ in the nitrogen dilution case compared to test point 4, as well as generally compared to other specific NO$_x$ results from all swings. With an 84% reduction in ESNOx from test point 4 to 1. This is explained by the effect of dilution on adiabatic flame temperature.

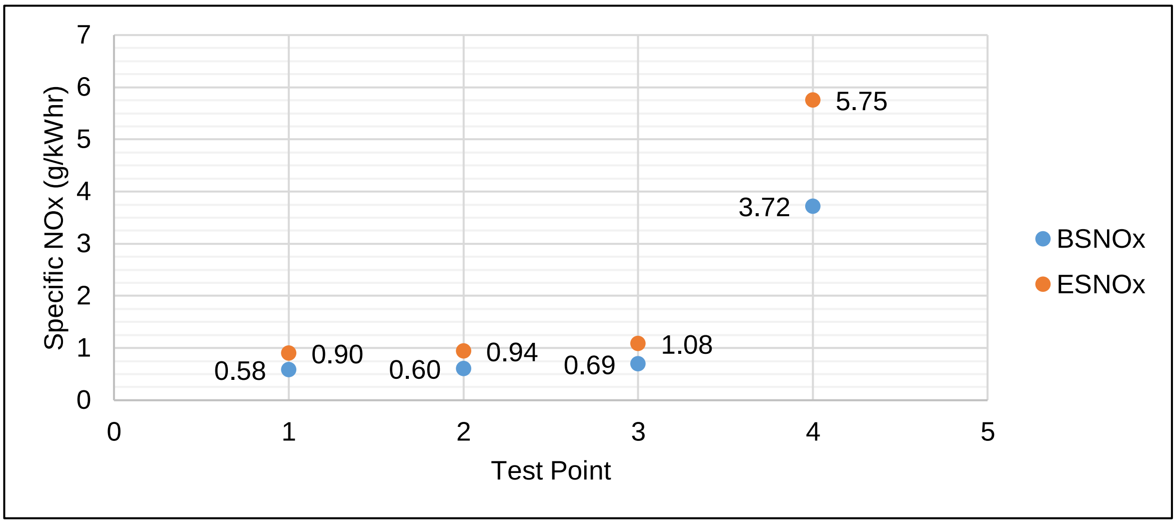

Figure 5.80 Nitrogen Dilution – Specific NOx.

The specific HC emissions are shown in Figure 5.81. It would be expected for HC emissions to rise as the lower presence of oxygen leads to a lower number of interactions with oxygen. This is displayed in Figure 5.81, with test point 4 displaying a ~62% reduction in both BSNO$_x$ and ESNO$_x$. However, the higher recuperator outlet temperature in test point 4 will have also helped reduce HC emissions.

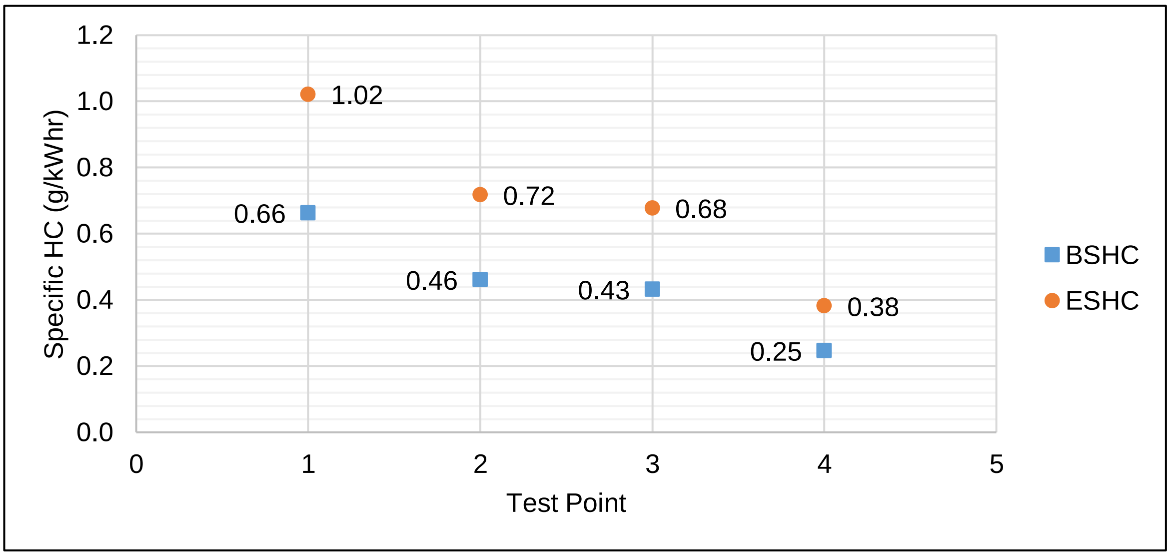

Figure 5.81 Nitrogen Dilution – Specific HC.

5.10.3.5 Other Variables

The airflow and torque for the test points are presented in Figure 5.82. The torque drop is a direct response to the drop in airflow. Airflow and torque fall in test point 4 due to the difference in timing and increased recuperator out temperature.

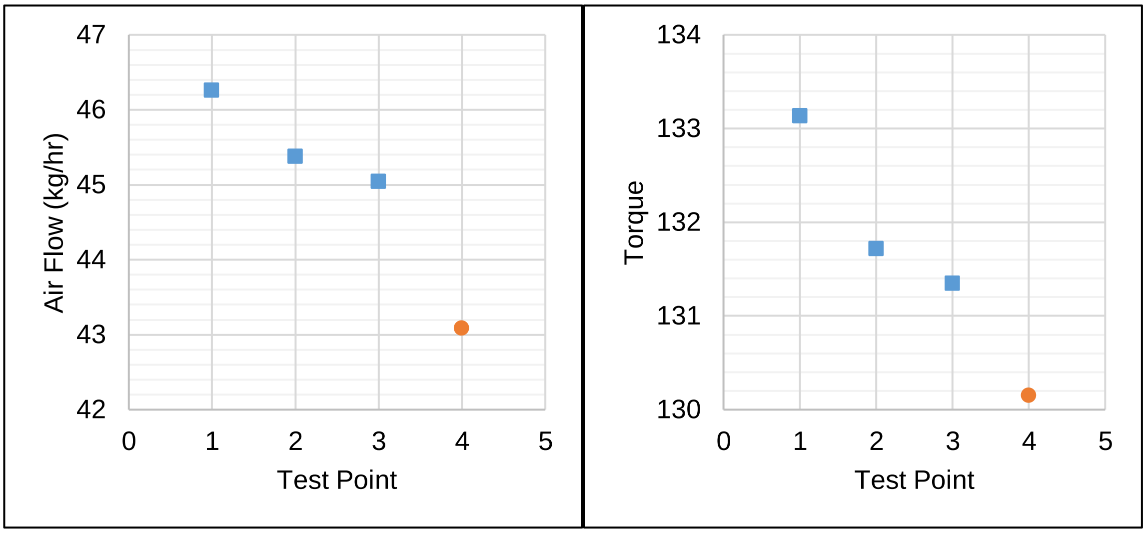

Figure 5.82 Nitrogen Dilution – Air flow (left) and torque (right).

5.11 Summary & Discussion

The SCCRE suggests that the combustion responses in the RSCE are similar to those of conventional ICE responses. However, there are key differences in emissions characteristics and responses. NO_x emissions specifically show a curve and response that suggest a local premixed style of combustion is occurring in some conditions. This is seemingly confirmed by a relatively high PRR with low CE. However, there is some inconsistent operation through a number of swings. This suggests that only part of the mixture is achieving a premix style combustion and there is a high degree of incomplete or uncombusted fuel. There are also high FSN conditions with low NO_x, again suggesting low homogeneity throughout the combustion chamber.

The efficiency results suggest it there is potential to achieve ultra-high TE of ~90%, however this does not consider the work performed by the burner. If there is a thermal store or mass of energy from a previous operating point, there is the possibility of achieving this efficiency for a period in a real engine.

Removing the Rankine work, the SCCRE shows proven ability to meet 50% ETE, even with the unoptimised expander system. However, poor combustion efficiency of 60-70% is currently limiting the potential overall efficiency. With a combustion system optimised and a fuel air mixing strategy utilised which capitalises on the architecture and operation of the engine, of EFE 50% can be realised. Coupled with a recuperator heat and quasi-isothermal compression, system efficiencies of greater than 50% are realistically achievable.

Overall specific emissions demonstrated a range of NO_x results from 2 to 10 g/kWhr, with the nitrogen dilution cases demonstrating a significant further reduction down to sub 1g/kWhr. With combustion optimisation and aftertreatment this has the potential to be further reduced with increases in power and mixture homogeneity.

Chapter 6 How does the induction RSCE process function?

Hypotheses and experiments on an optical flow rig investigating the air dynamics pre-combustion in the RSCE expander.

6.1 Introduction

The experimental results in the previous chapter prompted thoughts and ideas on the RSCE induction process. With questions over what is currently happening and how could the differences in the induction process be capitalised on to enhance the combustion process and achieve higher CE and lower emissions. This chapter present some concepts on the air transfer process and some initial experiments that were captured on an optical flow rig replicating the cylinder head of the SCCRE.

6.2 Conceptual Air Transfer Process

The transfer of the charge air from the inlet port to the combustion chamber in a RSCE is a very different process to that in a conventional ICE. In a conventional engine, the expanding volume of the combustion chamber during the induction stroke draws air into the combustion chamber. In the RSCE, the air is “injected” due to the high-pressure difference upstream and downstream of the combustion cylinder intake valves. This creates a unique air injection event in SCEs not typically found in reciprocating ICEs.

Air assisted fuel injectors have been mooted in the past [165]–[172], where the aim has been to impinge high speed and density air with the fuel spray. In these studies, air assisted atomisation displayed promise for enhancing fuel atomisation, but adoption of air assisted atomisation in a conventional ICE architecture has so far been deemed prohibitive by manufacturers, possibly due to the potential gain versus the complexity and cost of adding and operating an auxiliary high pressure air system. The RSCE architecture lends itself to a form of high-pressure air assisted fuel atomisation, as a high-pressure working fluid source is readily available. However, the case in the RSCE differs from the air assisted atomisation literature [165]–[172], as the chamber pressure is low at the start of the air and fuel injection, and the air is heated by exhaust gas. This enables a higher-pressure difference than performed in the assist air literature to date and creates a lag in temperature equalisation, as the air expands and then compresses downstream of the poppet valves. Theories and hypotheses on the dynamics of this process will be described in this section.

At the start of IVO, the pressure difference across the intake valves in the RSCE is up to 7.0MPa, varying depending on load conditions. These high differential pressures can create a choked flow at IVO which continues until the pressure ratio between the chamber and manifold is below 1.893 for dry air, a simple illustration of this is presented in Figure 6.1. The choked flow initially limits the mass flow into the combustion chamber, causing it to accelerate to supersonic speeds after the poppet valve constriction and display supersonic phenomena, such as shocks. As the air pressure equalises between the upstream and downstream conditions after IVO, the flow is no longer choked as the pressure ratio lowers. This occurs approximately over 5 to 10 CAD, depending on IVO and EVC timings and intake manifold pressure. This causes the air to experience a large expansion initially at IVO followed by a compression, as the air pressure equalises between the manifold and the combustion chamber. Therefore, there is a large variation in the state, density, and temperature of the air in the chamber as it first expands and then compresses during the air injection and pressure equalisation events.

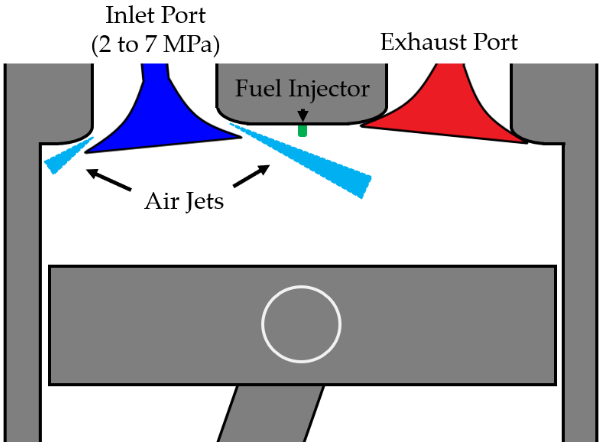

Figure 6.1 Simple 2D diagram of combustion chamber with inlet air jets in SCCRE.

It is difficult and computationally expensive to model the full conditions in the RSCE, due to the potential supersonic and/or supercritical conditions prevailing the air flow dynamics, moving geometry, fuel injection and combustion dynamics. For this reason, CFD studies to date have been simplified, utilising steady upstream flow conditions, static geometries and/or 2D models [81], [173]. For the same reasons, an experimental approach was taken using test rigs to investigate and describe the induction event in the engine. Previous CFD studies indicated that the injected air is at supersonic conditions at the beginning of IVO and predicted high turbulent kinetic energy in the combustion chamber [81]. Air velocities were predicted to be 150 to 500 m/s [81] compared to the 10 to 30 m/s typically observed in conventional ICEs. This creates unique flow dynamics across the whole chamber but specifically around the inlet valves, close to the injection point and on the cylinder walls.

6.3 Hypotheses

It is proposed the atomisation and combustion processes in the SCCRE, and therefore the RSCE and other SCEs, are primarily driven by the unique air dynamics. This is thought to causes the air fuel mixture to have a high amount of premix (regardless of the direct injection of the fuel) before combustion, giving rise to low emissions and rapid mixing of the fuel producing the PRR, NO_x, and FSN responses presented in Chapter 4. The exact physical phenomena that have caused this increased mixing are unknown. From analysis of test bed data and the literature relevant to various jet dynamics, three hypotheses are proposed here that alone or in combination could contribute to the enhanced mixing observed.

6.3.1 Hypothesis 1: Increased Mixing Driven by Increased Charge Air Bulk Velocity, Swirl & Turbulences

Atomisation and combustion dynamics in modern diesel fuelled engines are primarily driven by high fuel injection pressures and low swirl ratios (<2). Mixing is largely driven by high injection pressures, usually in excess of 200 MPa with some systems approaching 400 MPa [174], promoting atomisation of the fuel jet and mixing with the charge air. Bulk structured air motion via swirl contributes to air-fuel mixing but to a lesser degree than that of the high injection pressure of the liquid fuel spray.

It is proposed that in the case of the RSCE the opposite is true, leading to fuel injection pressures of 100 MPa being sufficient. With high air velocities from injection of air into the combustion chamber resulting in large scale flow structures and higher turbulence, directly affecting the Weber number and thus the atomisation processes. The high-pressure ratios, of up to 70 to 1, between the inlet duct and combustion chamber will cause higher air velocities and could induce swirl or tumble like motion in the combustion chamber. Enhancing swirl has been shown to decrease ignition delay and combustion duration but typically incurs higher pumping losses in Diesel ICE [175]. In the Aumet Z engine, another SCE variant, novel valves were utilised to generate air flow conditions with high swirl ratios (20-40), high velocities (> $100 ms^{-1}$) and low NO_x emissions reported [128], [176]. This suggests similar inlet air driven mixing could be occurring in the SCCRE.

It is proposed the high velocities induced during air induction in a RSCE result in residual air motion still present at the start of injection of the fuel. This promotes enhanced mixing before ignition and a high fraction of the fuel reacts from a lean dilute mixture resulting in low NO_x emissions and a high rate of heat release.

Lean premixed combustion in swirling flames has shown potential to reduce NO_x emissions in non-engine experiments, resulting in a blue ‘cool’ flame [177], [178]. Characterisation of these diffusive flames have been performed on methane and hydrogen low swirl burners but there is little experimental literature characterising blue “cool” swirling flames with a Diesel fuel [175], [177], [178]. The small initial PRR after TDC could be an indication of blue “cool” flame kinetics before the main autoignition, due to a lean to stoichiometric local equivalency ratio air fuel mixture, high swirl, and turbulence in the chamber. However, further research is needed before this can be said with any certainty.

6.3.2 Hypothesis 2: Increased Mixing Driven by Impinging Jet, Airblast & Crossflow Atomisation

The very high-pressure ratios create inlet air conditions that are expected to be closer to that of a rocket injector than that of a conventional ICE. This creates a curtain jet of air past the constriction of the poppet valves of high density and velocity air, which would only occur when the air flow through the valve is choked, i.e., above the minimum pressure ratio (1.893 for dry air). The fuel injector is located centrally, and the fuel spray injects into the area where this air jet curtain would materialise. Potentially producing impinging, crossflow, or transverse jet atomisation effects, as the fuel jet interacts with this high velocity air flow field. A simple diagram showing how these two flows may interact is shown in Figure 6.2.

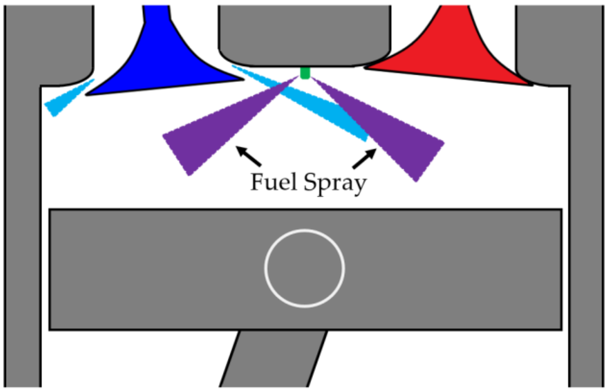

Figure 6.2 Simple 2D diagram of combustion chamber with fuel and air jets in SCCRE.

Impinging jet atomisation has been shown to produce rapid atomisation of the fuel spray but has typically focussed on liquid nitrogen and/or liquid oxygen mixtures at sub to supercritical conditions into sub to supercritical environments [95]. It is proposed that if the air jet is still present at the start of injection, the interaction of the two jets would promote rapid breakup of the fuel spray, mixing and combustion.

As discussed in Section 2.5, there is little literature on air assisted atomisation in ICEs and typically they have been at low air injection pressures (<1.0MPa). Air blast atomisation and crossflow atomisation at high pressures (>1.0MPa) have seen wider experimentation in literature associated with applications such as rockets, ramjet, scramjet, and gas turbine combustors [96], [98], [179]–[183]. Generally higher pressure and velocity conditions have demonstrated enhanced mixing, with high velocity subsonic and supersonic crossflow conditions producing rapid mixing in comparison to coaxial jet injection [179]. Both primarily utilised relative velocity and density as a route to increased mixing. However, as the high pressure research has typically been focussed on rocket and ramjet applications, the experiments involved an open volume and have had difficulties in combustion stability and performance in the past, with the physiochemical mechanisms at supersonic conditions still not well understood [183].

The conditions in the RSCE differ from that of other comparable high-pressure impinging jet literature, as a liquid diesel fuel spray is injected into a high-pressure gaseous air jet [95]. By virtue of being in a reciprocating engine the flow air flow field is further complicated by a closed volume compressing and expanding. At certain conditions and areas, the air may also be in a supercritical state.

6.3.3 Hypothesis 3: Increased Mixing Driven by Pressure & Shockwaves

As discussed in the previous section, at certain locations in the cylinder the flow field (most notably around the intake valves) the air may be supersonic and induce shockwaves, at least initially at IVO and while the pressure ratio is exceeded. These pressure waves could reflect off in-cylinder surfaces, superimpose, and affect the fuel breakup as they interface with the fuel spray. Chehroudi *et al* demonstrated that acoustic waves can affect jet breakup substantially, depending on the initial conditions of the fluid and chamber [184]. The research [184] utilised cryogenic nitrogen, injecting into chambers of 1.46 – 4.86 MPa and pressure ratios of 0.43 – 1.43, with the acoustic wave induced by an oscillator at the injector at 161 to 171 db and two set frequencies of 2,700 and 4,800 Hz. Research has also shown that lower temperatures enhance shockwave propagation while higher densities inhibit this. Shockwaves have been shown to be induced by the fuel injector at low enough temperatures and charge air densities by Kook *et al* [185]. These could in theory propagate to a higher extent in the SCCRE and RSCE due to the lower temperatures and charge air densities. However, the shockwave induced by the injector will be of a lower magnitude than that of shockwave generated by that of the inlet valves. Other works have been produced studying shockwaves generated by the spray and the effect this has on spray penetration [186]. However, there is no research on the effect of sprays interacting with shockwaves or reflected waves generated from another source in a closed volume.

It is hypothesised that the choked flow conditions are enabling pressure and shock waves to form and enhance the breakup of the fuel spray in the SCCRE, as the spray interfaces with these induced reflected pressure waves in the cylinder. Forcing the spray and/or droplets to increase mixing due to the pulsating translational movement caused by these waves.

6.3.4 Of Note – Diffusive Mixing

After the primary jet breakup, that is mostly driven by Kelvin Helmholtz instabilities based on stripping of the potential core, diffusive mixing may become an important contributing factor in the secondary breakup of the liquid fuel, instead of "catastrophic breakup" based on Rayleigh Taylor instabilities common in diesel jets. Diffusive, transcritical and supercritical mixing has been shown to occur above supercritical pressure conditions in impinging jet atomisation experiments involving gaseous-gaseous interfaces [95], [187], [188]. Research by Manin *et al*. [101] has shown that injection conditions need to exceed that of the critical conditions of diesel (618K, 2.1MPa for decane) and air (133K, 3.8MPa) to exhibit transcritical or supercritical diffusive mixing phenomena while utilising a liquid diesel fuel. Surface tension forces were shown to diminish at these elevated conditions. If ligaments and droplets are already of a smaller size after the first stage of mixing, due to one of the hypothesis increasing atomisation, diffusive mixing could promote further rapid mixing in the second stage of atomisation that is not typically seen in conventional Diesel engines at low chamber pressures and temperatures (< 133K, < 3.8MPa).

6.3.5 Comparison to Dec & Extended Dec Models

Using the conceptual models created and extended by Dec and Musculus et al as a comparators [82], [94], it is expected that the standard Dec model is not a good comparison when LTC conditions are present in the RSCE. The Musculus et al extended Dec model is the most comparable [82]. However, in certain valve train and injection setups that the injection plume does not readily hold position, leading to greater spread and breakup of the first stage of ignition.

6.4 A Study of RSCE Expander Head Air Flow

In the previous section three hypotheses were proposed that could be improving the mixing and combustion in the SCCRE. The hypotheses were formed purely on the operating conditions and evidence in the literature. In this section a test programme performed in collaboration with the Sheffield Advanced Manufacturing Research Centre (AMRC) will be described.

AMRC designed a flow rig in collaboration with Dolphin N2 to flow and analyse the replicated cylinder head of the SCCRE with access windows below to an open volume. The author setup and conducted the Schlieren optical investigation and set the test conditions laid out in this chapter.

The test programme was performed to optically capture the flow around the valve in order to study the processes taking place and validate the hypotheses. The collected data can help visualise the phenomena taking place through the air-fuel interaction in the RSCE and thus begin unpicking which of the phenomena described in the previous section are dominant and which are secondary. The flow rig replicates the valve geometry of the SCCRE, with no fuel injection or combustion, and static positions of valves. Several tests were conducted with varying valve lift and high-pressure conditions captured optically using a Z Schlieren setup. The optical work focussed on the near field flow around the valve seat at IVO. This was of interest to better understand the flow field that is created by the unique choked flow conditions around the poppet valve in the SCCRE. In the SCCRE the maximum valve lift is 3mm and pressure equalisation between the combustion chamber and the inlet manifold occurs before full valve lift is achieved. For this reason, this initial study will concentrate on valve lifts at 1mm and under. As there is no fuel injection and an open volume is used in this experiment, the effects these conditions have on the fuel spray and the effect of pressurisation cannot be ascertained from this first initial experiment alone.

In the experiment high pressure tanks are filled with air before discharging through a regulator at a set pressure to a digital control valve. Before then passing through an air mass flow meter to the cylinder head. After passing through the head and past the valves, the air is discharged to atmosphere through a muffler. This does not capture any possible flow interactions and reflections that will occur in a closed volume with a piston. The air jet curtain and mass flow were the main source of interest in this initial test. Optical access is below the head with two flat windows either side for imaging. Figure 6.3 to Figure 6.5 illustrate the experimental setup.

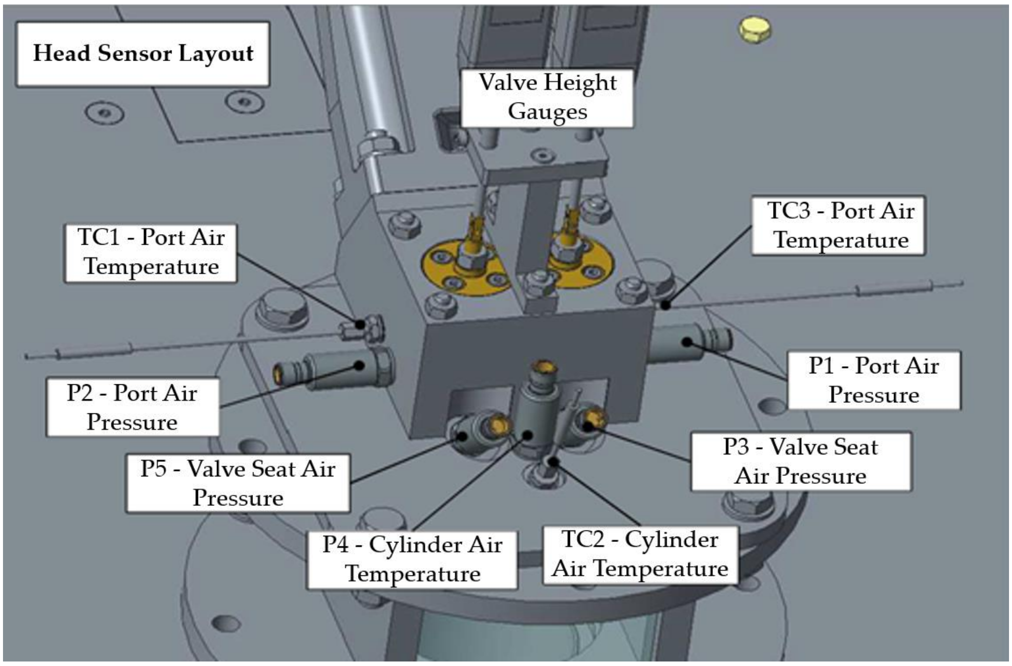

Figure 6.3 ARMC flow rig head sensor layout. Credit to AMRC.

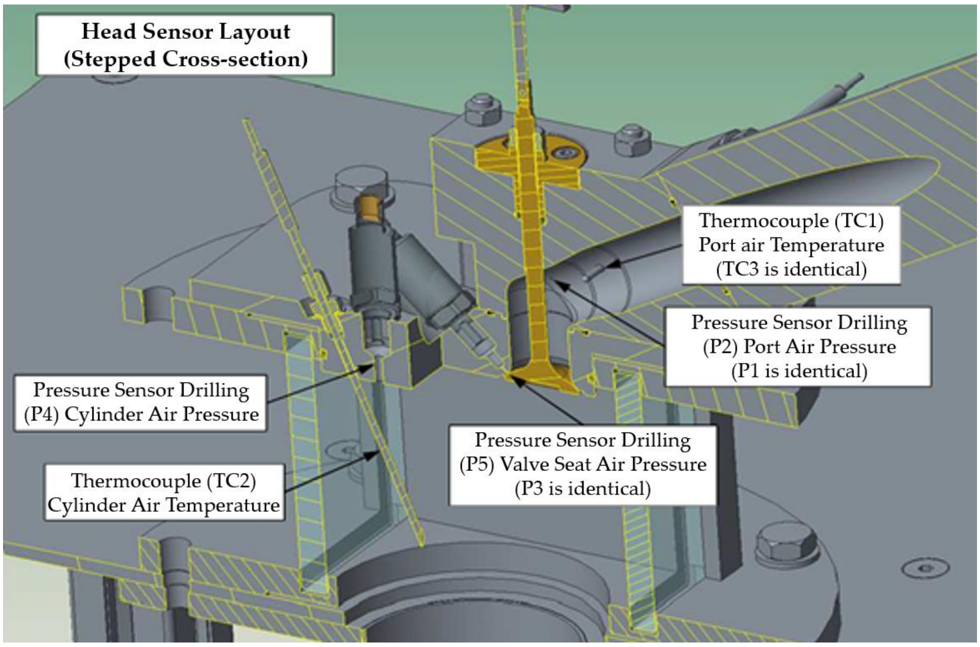

Figure 6.4 AMRC flow rig head sensor layout (stepped cross-section). Credit to AMRC.

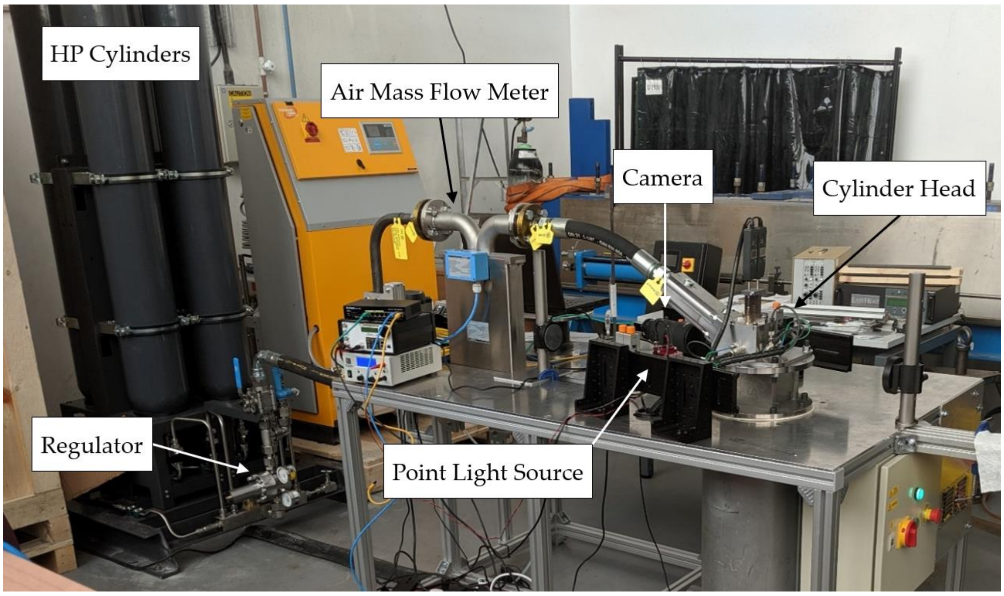

Figure 6.5 Overview of AMRC flow rig experiment setup.

The camera utilised for the experimental studies is a Basler acA1920-40gm which utilise a monochrome sensor with a resolution of 1920 by 1200 pixels and a frame rate of 42 fps. This is considered fast enough and with a higher enough resolution for the this set of tests where the interest is focussed on the steady state conditions with a set valve lift and pressure conditions. The point light source utilised was a CREE XT-E royal blue LED with a custom driver.

A range of pressures from 1.5MPa to 8.0MPa are tested at 1mm valve lift, with a further small number of tests at the maximum regulator pressure (8.0MPa) and decreasing valves lift, as well as number of valves open. The test schedule is shown in Table 6.1.

Table 6.1 AMRC flow rig test schedule.

Test	Valves Open	Lift (mm)	Regulator Pressure (MPa)
1	2	1.0	1.5
2	2	1.0	1.5
3	2	1.0	2.5
4	2	1.0	2.5
5	2	1.0	2.5
6	2	1.0	5.0
7	2	1.0	8.0
8	2	0.5	8.0
9	2	0.2	8.0
10	1	0.2	8.0
11	1	0.1	8.0
12	1	0.1	8.0

There is an expected drop in pressure between the regulator and the port, primarily due to the mass flow meter, but generally the pressure is consistent over the first 2s of the experiments for all test cases. Figure 6.6 displays the measured mass flow from the Coriolis flow meter against time from the start of the command to open the electronic next to the regulator, measured at 0.1s intervals. There is a sudden increase in mass flow around 0.6 – 0.7s due in most of the readings due to the amount of air mass is required to pressurise the column of air between the cylinder head and the valve. Over the 1mm valve lift tests there is an expected larger increase of mass flow rate with pressure, as a larger amount of mass is required to bring the volume between the regulator and the valves up to higher pressure.

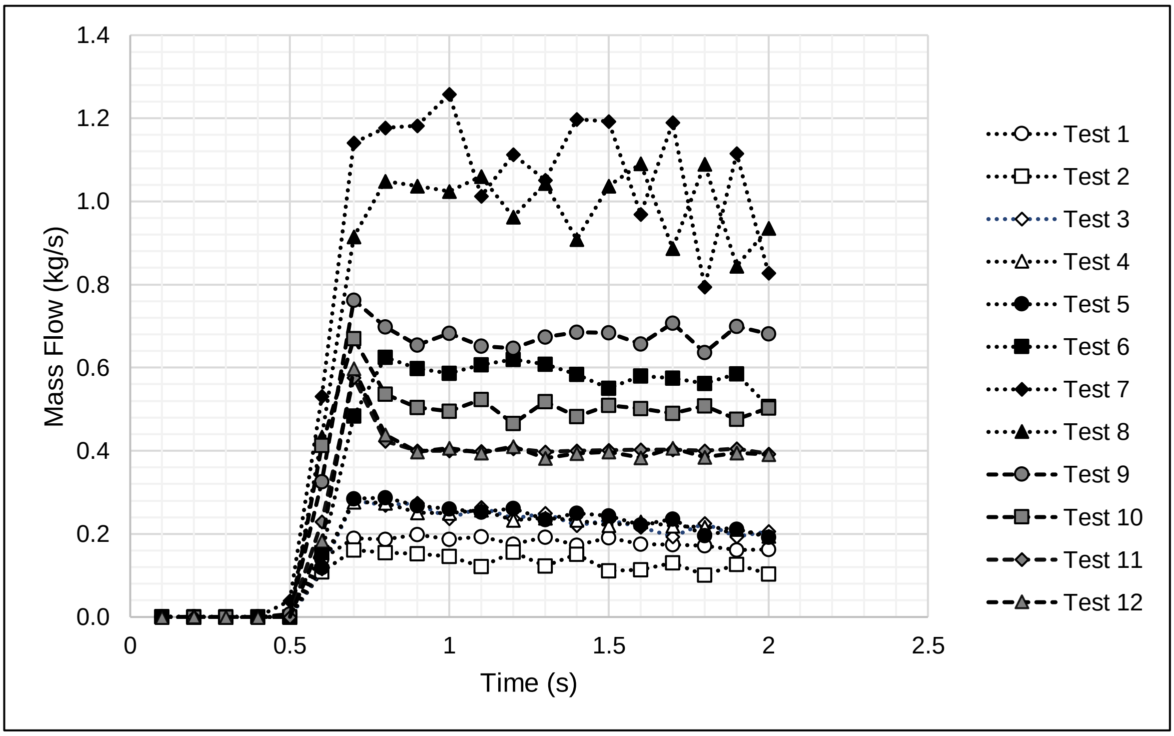

Figure 6.6 Expander head flow rig measured raw mass flow against time data for the 12 test points.

To calculate the approximate velocity through the valve, the equation for a truncated cone was utilised in combination with the valve lift geometry. Combined with the equation for the conservation of mass, the velocity in the valve seat can be calculated. The venturi incompressible flow method could not be utilised due to the choked from conditions at these test conditions, as the flow becomes compressible.

To calculate density the thermocouple measurement at position TC3, shown in Figure 6.4, was utilised. This not ideal as it does not represent the true temperature of the gas through the port, which will invariably be higher due to the Joule-Thomson effect as the air flow moves through the intake and valve area. It is therefore likely that the velocity calculated will be inaccurate. However, it still gives a useful approximation and response to the changes in pressure and valve area. The calculated velocity through the valve constriction is shown in Figure 6.7.

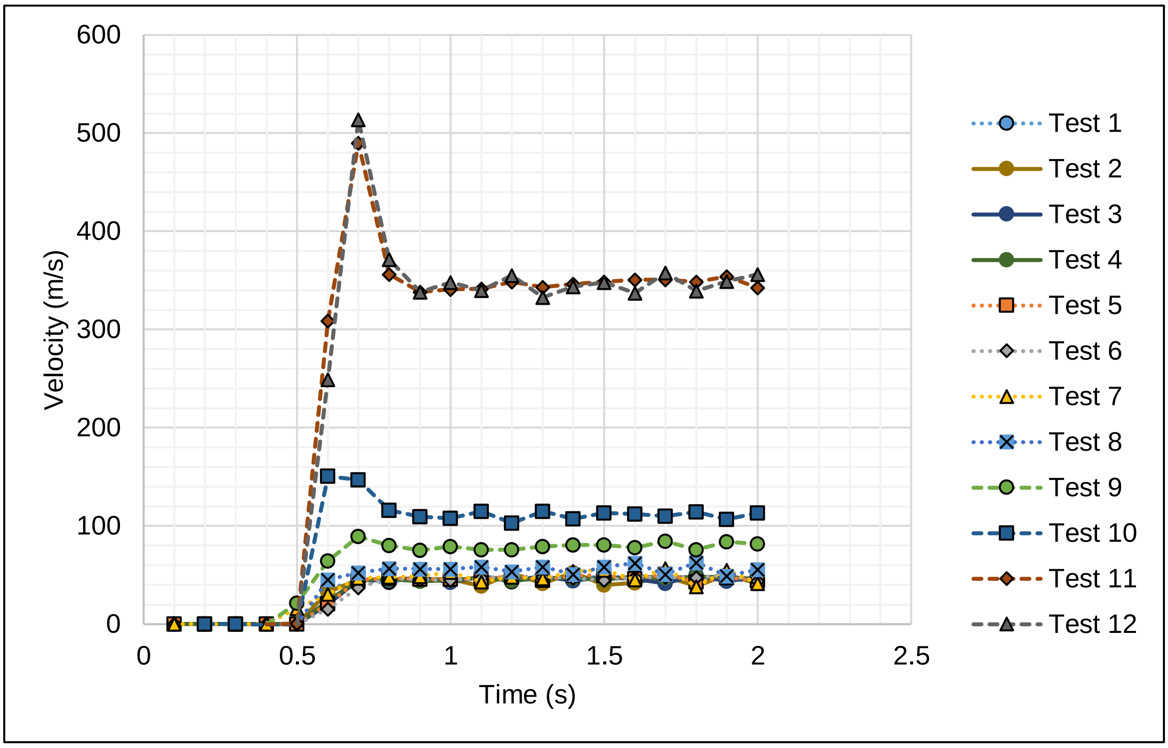

Figure 6.7 Calculated velocity through valve constriction using conservation of mass, uncorrected for valve lift extension.

At the higher-pressure test conditions, it was noted from the optical work that the valve stem was beginning to stretch by a large amount relative to the amount of lift that was set. This was most notable at the highest regulator pressure of 8.0MPa and the sub 1mm valve conditions. For this reason, the valve lift was corrected to account for stretch of the stem before the velocity is deduced through the conservation of mass equation. The velocity corrected for the extension of the valve under pressure is shown in Figure 6.8 and Figure 6.9.

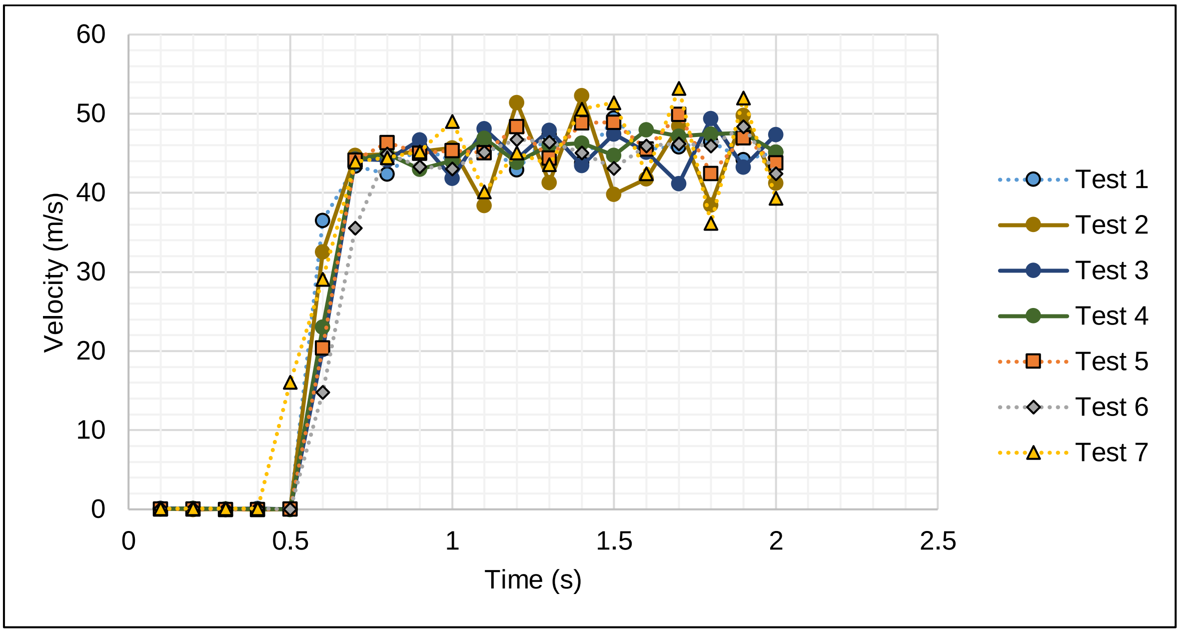

Figure 6.8 Calculated velocity through valve constriction using conservation of mass, corrected for valve lift extension for test points 1-7.

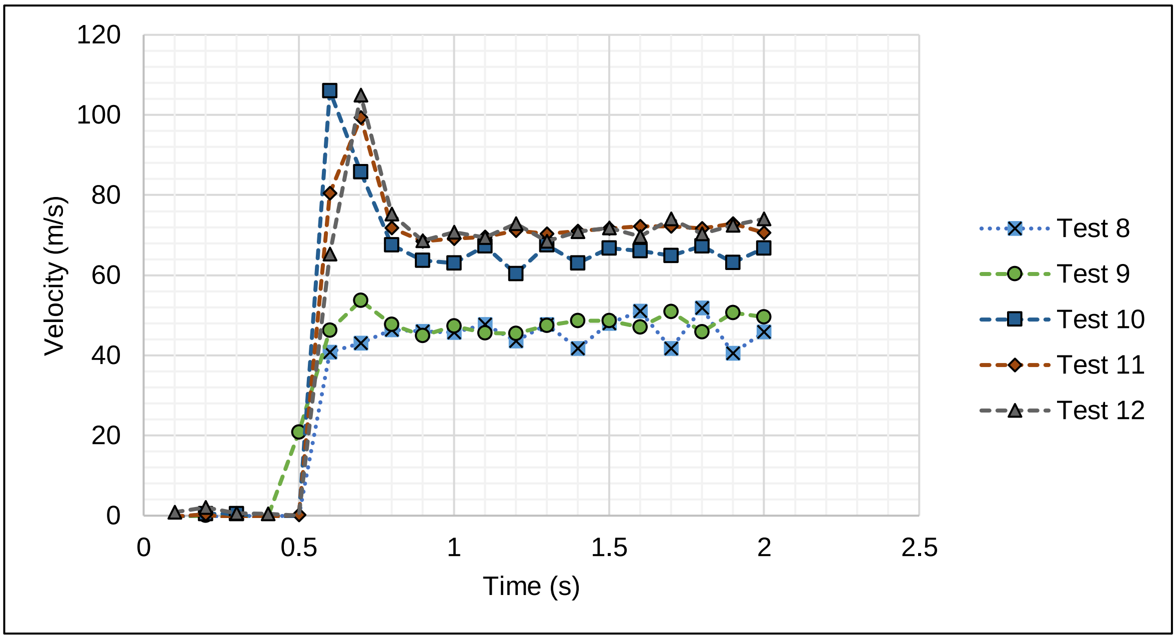

Figure 6.9 Calculated velocity through valve constriction using conservation of mass, corrected for valve lift extension for test points 8-12.

Within a margin of tolerance for noise, the cases with 1mm valve lift (Tests 1-7) displayed velocities of ~46ms^{-1}. As expected and shown in Figure 6.8 and Figure 6.9, at lower valve lifts the velocity through the valve constriction increased with the same upstream pressure and temperature conditions.

Figure 6.10 shows a Schlieren image of the air injection taken at 5.0MPa initial manifold pressure and 1mm valve lift, conditions representative of initial valve opening and a third of maximum valve lift in the SCCRE. The optical focus in this setup is the edge of the valve seat. The resulting images suggest shockwaves are formed in the cylinder, supporting past CFD work that the flow field is at least partially trans/supersonic and could be enhancing atomisation processes, and flow rig data demonstrating the flow to be choked [81], [173]. The image shows the flow field to be complex and potentially highly turbulent around and below the intake valve constriction. Two bow shocks in front of the valve seat and a separate recess around the valves are observed. Downstream of the valves into the valve 'curtain' Mach disks appear to form downstream of the bow shocks. Other poppet valve investigations have shown similar flow fields produced at elevated pressures and relatively low lift conditions [189]. Finding this flow field in a conventional ICE cylinder head utilising air or other working fluid is a unique condition to SCEs.

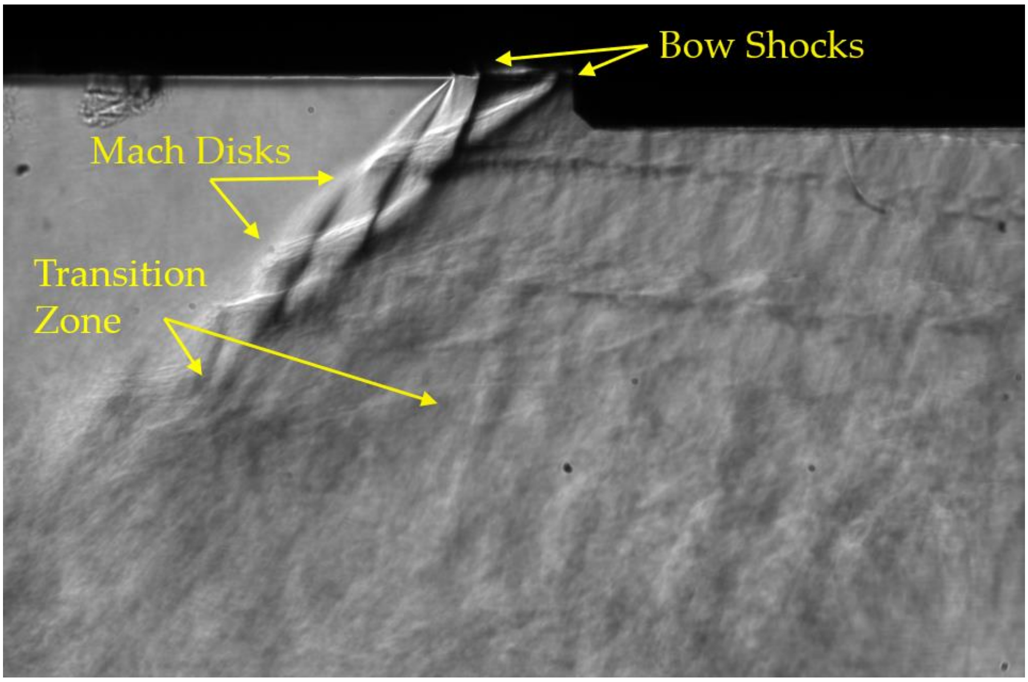

Figure 6.10 Schlieren of air jet 'curtain' created around poppet valve in first optical setup, at 5.0MPa and 1mm valve lift.

It is worth reminding that Mach disks are complex flow field structures made visible by abrupt changes in local density and pressure as the (typically supersonic) air passes through a series of standing shock waves and expansion fans. They typically appear when the static pressure of the air exiting a nozzle is less than the ambient pressure. The higher ambient pressure will then compress the flow, and if the resulting pressure increase in the air downstream is adiabatic, the reduction in velocity will also cause the static temperature to be increased. The pattern of disks would repeat indefinitely if the gases were ideal and frictionless. However, phenomena such as turbulent shear causes the wave pattern to fade with distance.

The focus of the image presented in Figure 6.11 is slightly offset of the centre line of the chamber and just below the valves. This area was chosen to enable examination of the interface of the shocks from each valve, as well as the transition zone beneath them. The initial manifold pressure and valve lift were set at 5.0MPa and 1mm valve lift, the same conditions as Figure 6.10. At these conditions, the structured flow diminishes approximately 5mm directly below the valves and the transition zone begins. However, the interface of the shocks created an almost completely vertical turbulent shock or possible Mach disks from the superimposed shocks.

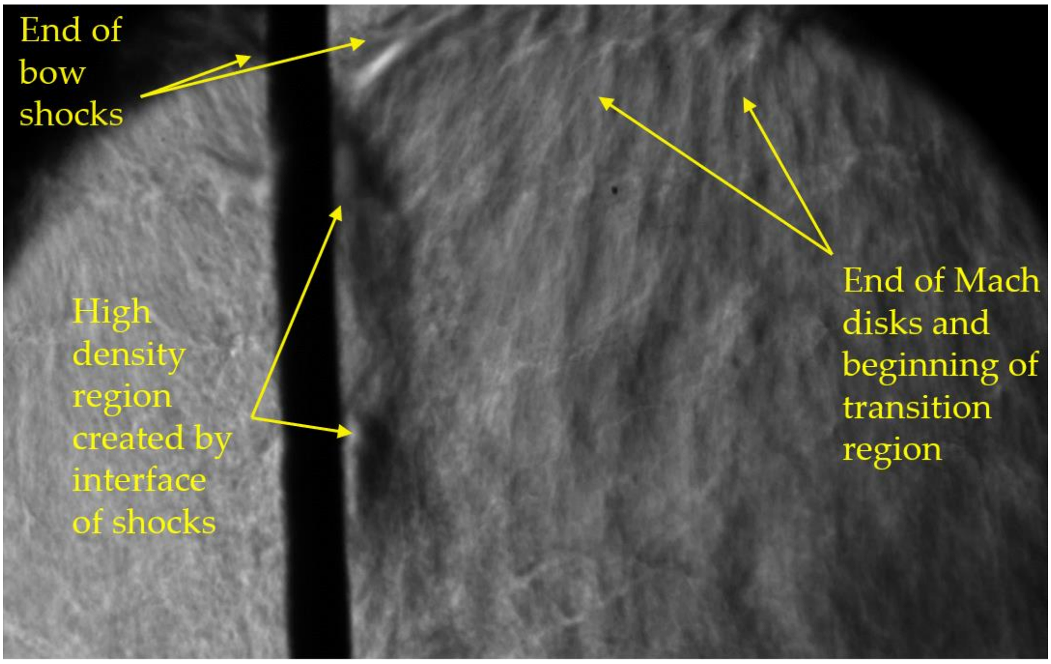

Figure 6.11 Schlieren of combining air jet 'curtains' below the poppet valves, slightly off centre of the centrally mounted thermocouple (TC2), in the second optical setup, at 5.0MPa and 1mm valve lift.

Although the Schlieren results cannot be used to quantitively assess velocity, directions of flow and between that of the current initial experiment and a previous CFD case can be compared. Firmansyah et al. produced Reynolds averaged Navier-Stokes (RANS) results in Figure 6.12 [81] which was annotated by the author to display the areas optically captured in Figure 6.10 and Figure 6.11. The CFD case ran at 2.5MPa but as velocity is choked through the constriction the velocity is unchanged, enabling the cases to be compared. While the manifold pressures are not the same and the exact low valve lift in the CFD case is unknown, there is a generally good agreement in terms of flow direction between the simulation case and the optical experiments.

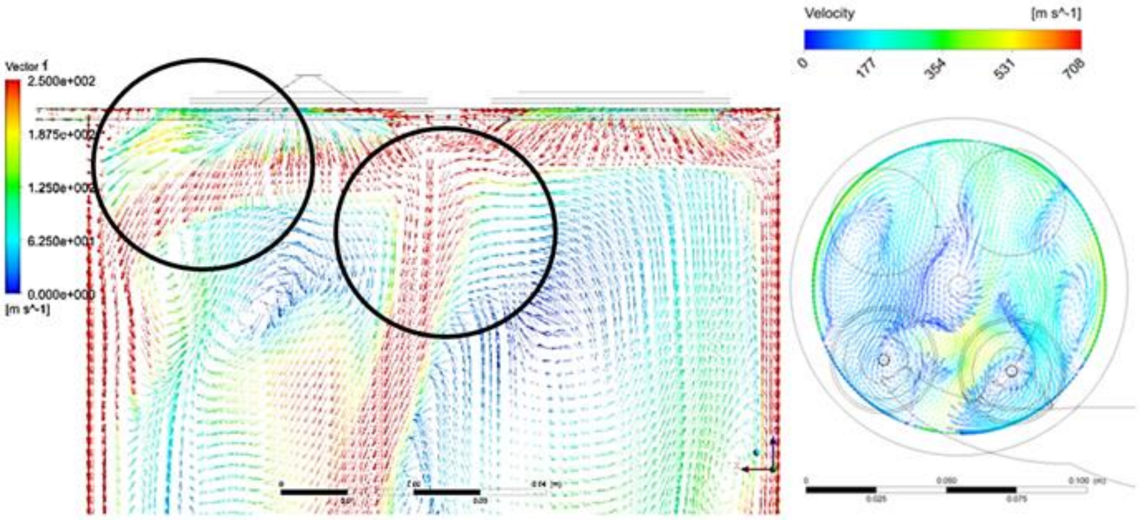

Figure 6.12 Annotated comparison of previous published RANS CFD work by Firmansyah et al. [34], with the two the areas of focus in the Schlieren optical setups, at 2.5MPa and low valve lift presented in Figure 6.10 and Figure 6.11.

6.5 Discussion

Several hypotheses were discussed for increased atomisation and fuel mixing in a RSCE or general SCE. It is clear from experimentation that the unique conditions from the high upstream pressure from the expander chamber can have an influence on the conditions and combustion. However, it is not clear for how long this takes place in the case of a closed volume, although the effects of the jets and shockwaves are likely to still be experienced after choked flow conditions have ended. It is clear that a conventional ICE filling and atomisation are not optimised for these conditions. There is the potential to use the high pressure air flow as the main source energy for of fuel atomisation, but the volumetric efficiency and other requirements of the expander must also be considered. A recommendation on potential combustion system pathways will be presented in this discussion.

Two main development pathways are considered by the author. 1) Conventional fuel injector is utilised with targeted air jets created by choked flow conditions for rapid mixing at IVO. 2) Separation of the air fuel mixing and cylinder filling, through a combined fuel and air injector, such as a pintle injector, with conventional poppet valves utilised and optimised for breathing and volumetric efficiency. Both of these pathways could produce on demand homogenous charge pressure ignition process. The process is roughly outlined below:

1. At IVO, air starts to be injected into chamber, this high momentum cold air jet begins mixing with hot residual exhaust gas from the previous cycle.
2. Fuel begins to be injected into air jet, relative low fuel injection pressure is required to keep droplets a relatively large size, allowing high amount of mixing due to catastrophic breakup of fuel droplets.
3. Fuel stops injection.
4. Air continues injection until pressure equalisation occurs between the upstream conditions of the valves and the expander chamber.
5. IVC occurs at the point of pressure equalisation or capitalises on ram air effect/ pressure pulsations to trap a maximum volume in the chamber.
6. Temperature equalises post pressure equalisation and causes multiple ignition points throughout the mixture.

This ignition and combustion process could in theory achieve on demand premix combustion with controlled autoignition. However, for control over a range of temperature, pressure, and load conditions, variable valve duration and/or lift would be required to respond and control the autoignition event of the fuel as the chamber heats up.

The Joule-Thomson effect must be considered for the fuel utilised, for air in the majority of conditions will present cooling. However, hydrogen fuel would induce heating and the propensity for autoignition from this heating would need to be considered and evaluated.

Chapter 7 Discussion, Conclusions, Implications & Future Direction

7.1 Summary Answers to & Discussion of Research Questions

In this chapter the answers to the questions laid out in Section 1.2 will be addressed and discussed in summary from the research.

1. Can an ICE achieve both high efficiency and ultra-low emission combustion?

It is possible for a reciprocating heat engine to be sustainable if it utilises a sustainable “green” chemical fuel and has a combustion system that produces low/zero toxic emissions. This will also require high efficiency to reduce wasted energy and lower the GHG emissions per joule or kWh used.

From the simple analysis presented in Chapter 3 it is theoretically possible for an ICE to achieve 61% efficiency while staying below the NO_x formation limit for a low toxic emissions ICE at source, i.e., in the combustion chamber with no aftertreatment. The bulk temperature of 2200K combined with good air fuel mixing should still provide enough heat for the combustion reaction to reach completion and not produce CO, soot, and other emissions from incomplete combustion.

2. Can conventional Otto or Diesel ICE cycles and combustion methods meet both ultra-low emissions and high efficiency targets?

While it is possible for conventional cycles to reach 61% efficiency, it is unlikely to achieve this in combination with low emissions, due to the coupling of high temperature and thermodynamic efficiency in conventional cycles. Toxic emissions can be reduced with low start of combustion temperatures and a premix style of combustion to reduce the formation of NO_x and low soot. Conventional ICEs are unable to decouple the issue of high peak temperatures and efficiency, as they rely on maximising the difference in temperature through high compression ratios, which inherently leads to higher NO_x.

There are currently limited novel cycles being research which are able to decouple the high temperature requirement, due to the difference in temperature leading to higher efficiency. A thermodynamic cycle in which the temperature and entropy difference can be maintained or increased for a lower maximum temperature is required. One novel thermodynamic cycle that has the potential to achieve this is the RSCE, due to the cooling of the working fluid in the compression stroke.

3. What does the ideal RSCE expander thermodynamic cycle look like?

The ideal parameters for the RSCE are not dissimilar to that of conventional ICE cycles. Combustion should occur ATDC but ideally as close to TDC as possible. Ideally combustion would occur as fast as possible. Unlike conventional cycles, it is beneficial for the expander efficiency for the IVP to be as short as possible and for the IVC to occur at or just after TDC. Ideally control of valve lift and duration would be required to maximise efficiency over a range of load, recuperator temperatures, and other conditions.

The thermodynamic cycle tends towards an architecture with large bore with large or many intake valves to maximise volumetric efficiency, as well as reducing IVP to as short as possible. Consideration of peak change in volume and how this effects the recompression work during the upstroke. Consideration of effect of valve timing on architecture, with a change in valve timing this can cause a change in optimum ER.

There needs to be consideration of the recuperator efficiency to understand whether decreasing ER in the RSCE expander would be beneficial to system efficiency. Past research suggests if the recuperator effectiveness is greater than ~70%, then decreasing ER would be beneficial to overall system efficiency. If the ER is decreased, the specific power of the engine can increase as volume at IVC dictates the amount of air in the chamber. There are potential further benefits of dropping ER in the expander for efficiency, making combustion more manageable and improving overall efficiency of the RSCE system. However, the effect on other losses must be considered and full system analysis would need to be performed.

There are issues with testing the RSCE and expander in typical engine testing approached. Constant air flow or constant pressure approaches each have pros and cons. Constant air flow is constant Rankine work the other is constant combustion work. Ideally constant work for the transient condition of the recuperator temperature is required to be understood and test appropriately on a complete RSCE system.

4. Does the RSCE expander respond to stimuli in line with conventional ICEs and combustion methods?

Broadly the RSCE expander responds in line with conventional ICEs. NO_x soot trade-off is still present, and there are expected responses from the studies in line with ICE combustion. However, there are lower emissions responses than that of conventional ICEs, with NO_x responses in particular suggest that there is possibly a higher amount of mixing occurring, at least in parts of the combustion chamber. Stable combustion was achieved over a wide range of conditions compared to previous research. However, soot responses at high intake pressures (4.0MPa) are high (~5 FSN), suggesting there is still plenty of improvement and development possible with the combustion system to increase mixing and provide higher loads (>0.9MPa GIMEP) and at higher speeds (>1,200 RPM) with low emissions response. The inlet conditions have a marked change on the inlet flow, atomisation, combustion, and fluid and thermal barriers typically formed in conventional ICEs.

5. What are the potential fundamental physical processes governing induction, and therefore combustion, processes in the RSCE expander that are different to conventional ICEs?

The high differential pressure across the intake valves has a profound effect on the flow field and breathing of the RSCE expander. Flow dynamics that are not typically attributed to closed volume combustors are created. This presents unique challenges and potential fuel atomisation gains for SCEs and the RSCE. High velocity and choked flow coupled with divergent valve geometry impedes the breathing of the expander and produces shockwave phenomena, at least during initial filling. There is the potential to use this phenomena as the main source of mixing, moving away from high pressure fuel led atomisation that has dominated diesel and recently gasoline engines over the last several decades.

This presents an opportunity for a rapid on demand premix style of combustion in a direct injection engine with a single fuel injector. Capitalising on this requires a ground up rethink of the combustion system. With a pintle injector, crossflow atomisation, or other approach required to maximise mixing.

6. Could the RSCE expander achieve ultra-high efficiency and low emission combustion?

The RSCE expander shows promise for achieving high efficiency and low emission combustion. With the expander alone proven to achieve a TE of 88.1% and BE of 48.3%. However, as discussed, there are issues with using these metrics without the effects of compression work account for. The metrics proposed for accounting for this show best case ETE of 50.6% and EFE of 35.6%. However, a low CE of 60-70% across all test points account for the large drop between ETE and EFE. If the combustion system is developed an optimised to 90+% CE, in line with conventional ICEs, it would be possible to achieve 50% expander efficiency, before the additional benefits of recuperation and quasi-isothermal compression are accounted for. Increasing volumetric efficiency through increased engine breathing and valve geometry is of interest to further maximise expander efficiency. As stated previously, a new combustion system designed from the ground up to capitalise on the unique conditions present in SCEs and RSCE will be required to maximise both CE and provide low emissions at high intake pressures.

7.2 Future work

Drawing from the experiments presented in this research, there are several thoughts and propositions for future work. It would be beneficial to repeat the experiments, especially in the cases where sensor error or reliability hampered a deep dive into high frequency cylinder pressure data. Particularly the pressure and temperature study, which are required to calibrate the engine for transient variations in recuperator temperature in operation.

The optical investigation on the cylinder head airflow rig can be increased in levels of complexity. Introducing a closed volume, potential for alternative optical views, fuel injection, and variable intake air temperature are all considerations that could be added before the stage of utilising a fully optical reciprocating expander to assess the RSCE expander. Utilising a full optical single cylinder engine would be the ideal scenario. However, the high amount of soot and potential high PRR would cause concern for length of optical views and life of windows respectively.

There are two main potential developmental paths forward for development of combustion system to maximise energy output from fuel and reduce emissions, as outlined previously. An optical research rig without combustion would be a good starting point for future work on this area. This will likely lead to novel fuel injector and/or intake valve designs for SCE and RSCEs.

Now that transferable understanding of the RSCE expander has started to be understood and can be compared to conventional ICEs, a move to green fuel experiments should be taken. There are further independent benefits to emissions, and potentially efficiency through fast burn rate, that can be had from these fuels. Specifically, soot can be reduced or eliminated completely through the purity and highly refined nature of a synthetic fuel compared to fossil fuel alternatives due to the nature of their production, or by using fuels that do not contain carbon, such as hydrogen.

A full system incorporating the compressor and expander is required to understand the real cost and benefit to these systems, rather than ideal theoretical calculation. However, a high amount of independence is still desirable for experimentation. For example, it would be beneficial to have an exhaust fed recuperator in addition to another source of heating to replicate and investigate responses to certain conditions and load. As the gas burner on the SCCRE was also limited, an exhaust fed recuperator in tandem with a gas fed recuperator system would allow for control and further experimentation at higher temperatures.

An investigation to an asymmetric injector would provide a relatively fast and relatively easy experiment to perform before combustion system redesign to gain some understanding of how the air fuel mixture is formed.

Another source of airflow measurement, such as a venturi, would be beneficial to capture true airflow. Rather than relying on calculations based on fuel balance and AFR.

There is potential development in temperature measurement of the intake air temperature entering the expander due to pulsed flow, as the k type thermocouple approach provides a time average. A high speed temperature measurement would be of interest for CFD study data inputs and comparison.

List of References

[1] M. W. Coney, C. Linnemann, K. Sugiura, and T. Goto, “First prototype of the high-efficiency isoengine,” *Power Eng.*, no. SEP., pp. 5–19, 2004.

[2] G. Dong, R. E. Morgan, and M. R. Heikal, “Thermodynamic analysis and system design of a novel split cycle engine concept,” *Energy*, vol. 102, pp. 576–585, May 2016, doi: 10.1016/j.energy.2016.02.102.

[3] R. E. Morgan, N. Jackson, A. Atkins, G. Dong, M. Heikal, and C. Lenartowicz, “The Recuperated Split Cycle - Experimental Combustion Data from a Single Cylinder Test Rig,” *SAE Int. J. Engines*, vol. 10, no. 5, pp. 2017-24–0169, Sep. 2017, doi: 10.4271/2017-24-0169.

[4] World Health Organisation, “Ambient (outdoor) air pollution,” 2021. https://www.who.int/news-room/fact-sheets/detail/ambient-(outdoor)-air-quality-and-health (accessed Dec. 21, 2021).

[5] K. Vohra, A. Vodonos, J. Schwartz, E. A. Marais, M. P. Sulprizio, and L. J. Mickley, “Global mortality from outdoor fine particle pollution generated by fossil fuel combustion: Results from GEOS-Chem,” *Environ. Res.*, vol. 195, no. February, p. 110754, 2021, doi: 10.1016/j.envres.2021.110754.

[6] Public Health England, “Review of interventions to improve outdoor air quality and public health,” *PHE Publ.*, p. 15, 2019, [Online]. Available: https://assets.publishing.service.gov.uk/government/uploads/system/uploads/attachment_data/file/937341/Principal_interventions_for_local_authorities-air_quality_public_health.pdf%0Ahttps://assets.publishing.service.gov.uk/government/uploads/system/uploads.

[7] R. N. Colvile, E. J. Hutchinson, J. S. Mindell, and R. F. Warren, “The transport sector as a source of air pollution,” *Atmos. Environ.*, vol. 35, no. 9, pp. 1537–1565, 2001, doi: 10.1016/S1352-2310(00)00551-3.

[8] EEA, “Understanding pollutant emissions from Europe’s cities.,” p. 16, 2013, doi: 10.2800/51246.

[9] Greater London Authority, “Air quality in London 2016-2020,” *London Environ.*

Strateg. Air Qual. Impact Eval., no. October, 2020.

[10] European Environment Agency, “National emissions reported to the Convention on Long-range Transboundary Air Pollution (LRTAP Convention).” 2019, [Online]. Available: https://www.eea.europa.eu/data-and-maps/daviz/contribution-of-the-transport-sector-6.

[11] K. Vanherle and E. Delhaye, “Road versus Short Sea Shipping: Comparing emissions and external costs,” 2010.

[12] Air Quality Consultants, “Covid-19 , Air Quality and Mobility Policies : Six European Cities,” 2021. [Online]. Available: https://www.transportenvironment.org/wp-content/uploads/2021/07/J4178 Covid-19 and Mobility Policies_v5_final March 2021_1.pdf.

[13] G. Fontaras, N.-G. Zacharof, and B. Ciuffo, “Fuel consumption and CO2 emissions from passenger cars in Europe – Laboratory versus real-world emissions,” *Prog. Energy Combust. Sci.*, vol. 60, pp. 97–131, May 2017, doi: 10.1016/j.pecs.2016.12.004.

[14] Transport & Environment, “Euro VI trucks still don’ t meet emission limits on the road,” 2021.

[15] ERTRAC CO2-Evaluation Group, “Report from ERTRAC CO2 Integrated Approach,” 2017. [Online]. Available: https://www.ertrac.org/uploads/images/3. CO2_Evaluation_Group_ ERTRAC2017.pdf.

[16] Transport & Environment, “Truck CO2: Europe’s chance to lead. Position paper on the review of the HDV CO2 standards,” 2022. [Online]. Available: https://www.transportenvironment.org/wp-content/uploads/2022/09/202209_HDV_CO2_position_paper_final-1.pdf.

[17] European Environment Agency, “Carbon dioxide emissions from Europe’s heavy-duty vehicles,” 2018. doi: 2800/246711.

[18] European Parliament and Council, “REGULATION (EU) 2019/1242 OF THE EUROPEAN PARLIAMENT AND OF THE COUNCIL of 20 June 2019 setting

CO 2 emission performance standards for new heavy-duty vehicles and amending Regulations (EC) No 595/2009 and (EU) 2018/956 of the European Parliament and of t," *Off. J. Eur. Union*, 2019, [Online]. Available: https://eur-lex.europa.eu/legal-content/EN/TXT/?uri=CELEX%3A32019R1242&qid=1665070521341.

[19] European Commission, "Proposal for a REGULATION OF THE EUROPEAN PARLIAMENT AND OF THE COUNCIL amending Regulation (EU) 2019/1242 as regards strengthening the CO_2 emission performance standards for new heavy-duty vehicles and integrating reporting obligations, and repealing Reg," 2023, [Online]. Available: https://eur-lex.europa.eu/legal-content/EN/TXT/?uri=CELEX:52023PC0088.

[20] World Health Organisation, *Evolution of WHO air quality guidelines: past, present and future*. 2017.

[21] World Commission On Environment and Development, "Report of the World Commission on Environment and Development: Our Common Future," Jan. 1987.

[22] European Commission, "Proposal for a REGULATION OF THE EUROPEAN PARLIAMENT AND OF THE COUNCIL on type-approval of motor vehicles and engines and of systems, components and separate technical units intended for such vehicles, with respect to their emissions and battery durabili," *Com(2022)*, vol. 0365, no. 715, 2022.

[23] The Transport Energy Network, "A collaborative approach to understanding decarbonised transport in 2050," 2020.

[24] T. Grigoratos, G. Martini, and G. Martini, *Non-exhaust traffic related emissions . Brake and tyre wear PM Literature review*. 2014.

[25] G. Domingues-Olavarría, F. J. Márquez-Fernández, P. Fyhr, A. Reinap, and M. Alaküla, "Electric roads: Analyzing the societal cost of electrifying all Danish road transport," *World Electr. Veh. J.*, vol. 9, no. 1, pp. 1–11, 2018, doi: 10.3390/wevj9010009.

[26] Advanced Propulsion Centre UK, “Automotive industry demand forecast Q4 2021 Update,” no. June, 2022, [Online]. Available: https://www.apcuk.co.uk/automotive-industry-demand-forecast-q4-2021-update/.

[27] G. Bartzas, P. E. Tsakiridis, and K. Komnitsas, “Nickel industry: Heavy metal(loid)s contamination - sources, environmental impacts and recent advances on waste valorization,” *Curr. Opin. Environ. Sci. Heal.*, vol. 21, p. 100253, 2021, doi: 10.1016/j.coesh.2021.100253.

[28] L. Mancini, N. A. Eslava, M. Traverso, and F. Mathieux, “Assessing impacts of responsible sourcing initiatives for cobalt: Insights from a case study,” *Resour. Policy*, vol. 71, no. October 2020, p. 102015, 2021, doi: 10.1016/j.resourpol.2021.102015.

[29] S. Dey, B. Tripathy, M. S. Kumar, and A. P. Das, “Ecotoxicological consequences of manganese mining pollutants and their biological remediation,” *Environ. Chem. Ecotoxicol.*, vol. 5, no. January, pp. 55–61, 2023, doi: 10.1016/j.enceco.2023.01.001.

[30] K. K. Rana, S. Natarajan, and S. Jilakara, “Potential of Hydrogen Fuelled IC Engine to Achieve the Future Performance and Emission Norms,” Jan. 2015, doi: 10.4271/2015-26-0050.

[31] M. A. Kromer and J. B. Heywood, “Electric Powertrains: Opportunities and Challenges in the U.S. Light-Duty Vehicle Fleet,” *Challenges*, no. May, p. 153, 2007, [Online]. Available: http://web.mit.edu/sloan-auto-lab/research/beforeh2/files/kromer_electric_powertrains.pdf.

[32] P. Atkins, E. Pike-Wilson, and R. E. Morgan, “Can Hydrogen Engines Support Decarbonisation in the Heavy Duty Sector?,” no. July, 2021.

[33] Automotive Council UK, “Thermal Propulsion Systems Roadmap,” 2017.

[34] O. Delgado and N. Lutsey, “The U.S. SuperTruck Program: Expediting the development of advanced heavy-duty vehicle efficiency technologies,” *Int. Counc. Clean Transp.*, no. June, 2014, [Online]. Available:

http://www.theicct.org/sites/default/files/publications/ICCT_SuperTruck-program_20140610.pdf.

[35] S. Siegemund *et al.*, “E-Fuels study. The potential of electricity-based fuels for low-emission transport in the EU,” *Dtsch. Energie-Agentur GmbH*, 2017.

[36] H. Kobayashi, A. Hayakawa, K. D. K. K. A. Somarathne, and E. C. Okafor, “Science and technology of ammonia combustion,” *Proc. Combust. Inst.*, vol. 37, no. 1, pp. 109–133, 2019, doi: 10.1016/j.proci.2018.09.029.

[37] W. Paper, “e-Methanol: A universal green fuel,” 2020.

[38] World Health Organisation, “Health Effects of Particulate Matter,” 2013.

[39] J. Daintith, *Oxford Dictionary of Chemistry*, Sixth. Oxford University Press, 2008.

[40] G. P. Smith *et al.*, “GRI-Mech 3.0.” [Online]. Available: http://www.me.berkeley.edu/gri_mech/.

[41] M. Frenklach, H. Wang, and M. J. Rabinowitz, “Optimization and analysis of large chemical kinetic mechanisms using the solution mapping method—combustion of methane,” *Prog. Energy Combust. Sci.*, vol. 18, no. 1, pp. 47–73, Jan. 1992, doi: 10.1016/0360-1285(92)90032-V.

[42] G. P. Smith *et al.*, “GRI-Mech 3.0 Performance.” http://combustion.berkeley.edu/gri-mech/version30/text30.html (accessed May 13, 2023).

[43] D. J. Seery and C. T. Bowman, “An experimental and analytical study of methane oxidation behind shock waves,” *Combust. Flame*, vol. 14, no. 1, pp. 37–47, Feb. 1970, doi: 10.1016/S0010-2180(70)80008-6.

[44] R. K. Cheng and A. K. Oppenheim, “Autoignition in methane hydrogen mixtures,” *Combust. Flame*, vol. 58, no. 2, pp. 125–139, Nov. 1984, doi: 10.1016/0010-2180(84)90088-9.

[45] M. Mehl and H. Curran, “Chemical kinetic modeling of component mixtures relevant to gasoline,” *Eur. Combust. Meet.*, no. April 2009, pp. 1–6, 2009,

[Online]. Available: http://www.researchgate.net/publication/228655950_Chemical_kinetic_modeling_of_component_mixtures_relevant_to_gasoline/file/e0b4951d5828117f73.pdf.

[46] H. Wang *et al.*, “A high-temperature chemical kinetic model of n-alkane (up to n-dodecane), cyclohexane, and methyl-, ethyl-, n-propyl and n-butyl-cyclohexane oxidation at high temperatures, JetSurF version 2.0.” 2010, [Online]. Available: http://web.stanford.edu/group/haiwanglab/JetSurF/JetSurF2.0/index.html.

[47] B. Sirjean *et al.*, “A high-temperature chemical kinetic model of n-alkane oxidation, JetSurF version 1.0,” 2009. https://web.stanford.edu/group/haiwanglab/JetSurF/JetSurF1.0/Performance/Ignition Delay/Zhukov.html (accessed May 14, 2023).

[48] V. P. Zhukov, V. A. Sechenov, and A. Y. Starikovskii, “Autoignition of n-decane at high pressure,” vol. 153, pp. 130–136, 2008, doi: https://doi.org/10.1016/j.combustflame.2007.09.006.

[49] D. C. Horning, D. F. Davidson, and R. K. Hanson, “Study of the High-Temperature Autoignition of n-Alkane/O/Ar Mixtures,” *J. Propuls. Power*, vol. 18, no. 2, pp. 363–371, 2002, doi: https://doi.org/10.2514/2.5942.

[50] C. K. Westbrook, W. J. Pitz, O. Herbinet, H. J. Curran, and E. J. Silke, “A comprehensive detailed chemical kinetic reaction mechanism for combustion of n-alkane hydrocarbons from n-octane to n-hexadecane,” *Combust. Flame*, vol. 156, no. 1, pp. 181–199, 2009, doi: https://doi.org/10.1016/j.combustflame.2008.07.014.

[51] U.S. Environmental Protection Agency, “Nitrogen oxides (NOx), why and how they are controlled,” 1999. [Online]. Available: https://www3.epa.gov/ttncatc1/dir1/fnoxdoc.pdf.

[52] G. Myhre *et al.*, “Anthropogenic and Natural Radiative Forcing,” *Clim. Chang. 2013 Phys. Sci. Basis. Contrib. Work. Gr. I to Fifth Assess. Rep. Intergov. Panel Clim. Chang.*, pp. 659–740, 2013, doi: 10.1017/

CBO9781107415324.018.

[53] L. J. Muzio, T. A. Montgomery, G. S. Samuelsen, J. C. Kramlich, R. K. Lyon, and A. Kokkinos, “Formation and measurement of N2O in combustion systems,” *Symp. Combust.*, vol. 23, no. 1, pp. 245–250, Jan. 1991, doi: 10.1016/S0082-0784(06)80266-3.

[54] M. Semakula and P. F. Inambao, “The Formation, Effects and Control of Oxides of Nitrogen in Diesel Engines,” *Int. J. Appl. Eng. Res.*, vol. 13, no. 6, pp. 3200–3209, 2018.

[55] B. S. Haynes and H. G. Wagner, “Soot formation,” *Prog. Energy Combust. Sci.*, vol. 7, no. 4, pp. 229–273, Jan. 1981, doi: 10.1016/0360-1285(81)90001-0.

[56] R. A. Dobbins, “Hydrocarbon nanoparticles formed in flames and diesel engines,” *Aerosol Sci. Technol.*, vol. 41, no. 5, pp. 485–496, 2007, doi: 10.1080/02786820701225820.

[57] World Health Organisation, “Human health effects of polycyclic aromatic hydrocarbons as ambient air pollutants,” 2021.

[58] J. A. S. Lighty, J. M. Veranth, and A. F. Sarofim, “Combustion aerosols: Factors governing their size and composition and implications to human health,” *J. Air Waste Manag. Assoc.*, vol. 50, no. 9, pp. 1565–1618, 2000, doi: 10.1080/10473289.2000.10464197.

[59] G. Singh, “Overview of the DOE Advanced Combustion Engine R&D,” 2012. [Online]. Available: http://www.eere.energy.gov/vehiclesandfuels/pdfs/merit_review_2012/adv_combustion/ace00a_singh_2012_o.pdf.

[60] The Royal Society, “Sustainable synthetic carbon based fuels for transport,” 2019. [Online]. Available: https://royalsociety.org/topics-policy/projects/low-carbon-energy-programme/sustainable-synthetic-carbon-based-fuels-for-transport/.

[61] J. Fu and S. Q. Turn, “Characteristics and stability of neat and blended

hydroprocessed renewable diesel," *Energy and Fuels*, vol. 28, no. 6, pp. 3899–3907, 2014, doi: 10.1021/ef500544p.

[62] J. T. Houghton, L. G. Meira Filho, B. A. Callander, N. Harris, A. Kattenberg, and K. Maskell, "Climate change 1995: The science of climate change," Cambridge University Press, 1996.

[63] R. A. Alvarez *et al.*, "Assessment of methane emissions from the U.S. oil and gas supply chain," Jun. 2018. doi: 10.1126/science.aar7204.

[64] P. Forster *et al.*, "Changes in Atmospheric Constituents and in Radiative Forcing," in *Climate Change 2007: The Physical Science Basis*, Cambridge University Press, Cambridge, United Kingdom and New York, NY, USA, 2007.

[65] G. P. McTaggart-Cowan, S. N. Rogak, S. R. Munshi, P. G. Hill, and W. K. Bushe, "The influence of fuel composition on a heavy-duty, natural-gas direct-injection engine," *Fuel*, vol. 89, no. 3, pp. 752–759, 2010, doi: 10.1016/j.fuel.2009.10.007.

[66] E. Distaso, R. Amirante, G. Calò, P. De Palma, and P. Tamburrano, "Evolution of soot particle number, mass and size distribution along the exhaust line of a heavy-duty engine fueled with compressed natural gas," *Energies*, vol. 13, no. 15, 2020, doi: 10.3390/en13153993.

[67] R. Amirante *et al.*, "Effects of natural gas composition on performance and regulated, greenhouse gas and particulate emissions in spark-ignition engines," *Energy Convers. Manag.*, vol. 143, no. x, pp. 338–347, 2017, doi: 10.1016/j.enconman.2017.04.016.

[68] M. Caron *et al.*, "Pressure dependence of the auto-ignition temperature of methane/air mixtures," *J. Hazard. Mater.*, 1999, doi: 10.1016/S0304-3894(99)00004-7.

[69] Hydrogen Council, "Path to hydrogen competitiveness: a cost perspective," no. January, p. 88, 2020, [Online]. Available: www.hydrogencouncil.com.

[70] European Commission, "A hydrogen strategy for a climate-neutral Europe," 2020.

[71] T. DiChristopher, “Hydrogen technology faces efficiency disadvantage in power storage race,” *S&P Global*, 2021. https://www.spglobal.com/marketintelligence/en/news-insights/latest-news-headlines/hydrogen-technology-faces-efficiency-disadvantage-in-power-storage-race-65162028 (accessed May 15, 2023).

[72] S. Verhelst, “Recent progress in the use of hydrogen as a fuel for internal combustion engines,” *Int. J. Hydrogen Energy*, vol. 39, no. 2, pp. 1071–1085, 2014, doi: 10.1016/j.ijhydene.2013.10.102.

[73] N. Ash and T. Scarbrough, “Sailing on solar: Could green ammonia decarbonise international shipping?,” Environmental Defense Fund, London, 2019.

[74] N. A. Hussein, A. Valera-Medina, and A. S. Alsaegh, “Ammonia- hydrogen combustion in a swirl burner with reduction of NO x emissions,” *Energy Procedia*, vol. 158, no. 2018, pp. 2305–2310, 2019, doi: 10.1016/j.egypro.2019.01.265.

[75] C. Lhuillier, P. Brequigny, F. Contino, and C. Rousselle, “Performance and Emissions of an Ammonia-Fueled SI Engine with Hydrogen Enrichment,” *SAE Tech. Pap.*, vol. 2019-Septe, no. September, 2019, doi: 10.4271/2019-24-0137.

[76] A. J. Reiter and S. C. Kong, “Combustion and emissions characteristics of compression-ignition engine using dual ammonia-diesel fuel,” *Fuel*, vol. 90, no. 1, pp. 87–97, 2011, doi: 10.1016/j.fuel.2010.07.055.

[77] M. C. Chiong *et al.*, “Advancements of combustion technologies in the ammonia-fuelled engines,” *Energy Convers. Manag.*, vol. 244, no. July, p. 114460, 2021, doi: 10.1016/j.enconman.2021.114460.

[78] P. Dimitriou and R. Javaid, “A review of ammonia as a compression ignition engine fuel,” *Int. J. Hydrogen Energy*, vol. 45, no. 11, pp. 7098–7118, 2020, doi: 10.1016/j.ijhydene.2019.12.209.

[79] C. Kurien and M. Mittal, “Review on the production and utilization of green

ammonia as an alternate fuel in dual-fuel compression ignition engines," *Energy Convers. Manag.*, vol. 251, no. August 2021, p. 114990, 2022, doi: 10.1016/j.enconman.2021.114990.

[80] I. Lucentini, X. Garcia, X. Vendrell, and J. Llorca, "Review of the Decomposition of Ammonia to Generate Hydrogen," *Ind. Eng. Chem. Res.*, vol. 60, no. 51, pp. 18560–18611, Dec. 2021, doi: 10.1021/acs.iecr.1c00843.

[81] Firmansyah, R. Morgan, M. R. Heikal, and A. R. A. Aziz, "Effect of pressure in crossover port to the in-cylinder flow of split-cycle engine," 2018, p. 080003, doi: 10.1063/1.5075602.

[82] J. E. Dec, "A conceptual model of DI diesel combustion based on laser-sheet imaging," *SAE Pap. 970873 SAE Trans.*, vol. 106, no. 3, pp. 1319–48, 1997, doi: 10.4271/970873.

[83] R. B. Poola, R. R. Sekar, and R. L. Cole, "VARIABLE OXYGEN/NITROGENENRICHED INTAKE AIR SYSTEM FOR INTERNAL COMBUSTON ENGINE APPLICATIONS," 5,649517, 1977.

[84] J. A. Blandino, G. N. Coleman, C. H. Dutart, and E. C. Fluga, "INTAKE AIR SEPARATION SYSTEM FOR AN INTERNAL COMBUSTION ENGINE," US 6,543,428 B1, 2003.

[85] F. D. F. Chuahy and S. L. Kokjohn, "High efficiency dual-fuel combustion through thermochemical recovery and diesel reforming," *Appl. Energy*, vol. 195, pp. 503–522, 2017, doi: 10.1016/j.apenergy.2017.03.078.

[86] J. Benajes, A. García, J. Monsalve-Serrano, and V. Boronat, "Achieving clean and efficient engine operation up to full load by combining optimized RCCI and dual-fuel diesel-gasoline combustion strategies," *Energy Convers. Manag.*, vol. 136, pp. 142–151, 2017, doi: 10.1016/j.enconman.2017.01.010.

[87] K. Poorghasemi, R. K. Saray, E. Ansari, B. K. Irdmousa, M. Shahbakhti, and J. D. Naber, "Effect of diesel injection strategies on natural gas/diesel RCCI combustion characteristics in a light duty diesel engine," *Appl. Energy*, vol. 199, pp. 430–446, 2017, doi: 10.1016/j.apenergy.2017.05.011.

[88] C. Kavuri, J. Paz, and S. L. Kokjohn, “A comparison of Reactivity Controlled Compression Ignition (RCCI) and Gasoline Compression Ignition (GCI) strategies at high load, low speed conditions,” *Energy Convers. Manag.*, vol. 127, pp. 324–341, 2016, doi: 10.1016/j.enconman.2016.09.026.

[89] R. D. Reitz and G. Duraisamy, “Review of high efficiency and clean reactivity controlled compression ignition (RCCI) combustion in internal combustion engines,” *Prog. Energy Combust. Sci.*, vol. 46, pp. 12–71, 2015, doi: 10.1016/j.pecs.2014.05.003.

[90] F. D.F. Chuahy and S. L. Kokjohn, “Effects of reformed fuel composition in ‘single’ fuel reactivity controlled compression ignition combustion,” *Appl. Energy*, vol. 208, 2017, doi: 10.1016/j.apenergy.2017.10.057.

[91] J. Benajes, A. García, J. Monsalve-Serrano, I. Balloul, and G. Pradel, “An assessment of the dual-mode reactivity controlled compression ignition/conventional diesel combustion capabilities in a EURO VI medium-duty diesel engine fueled with an intermediate ethanol-gasoline blend and biodiesel,” *Energy Convers. Manag.*, vol. 123, pp. 381–391, 2016, doi: 10.1016/j.enconman.2016.06.059.

[92] S. Curran, Z. Gao, and R. Wagner, “Reactivity Controlled Compression Ignition Drive Cycle Emissions and Fuel Economy Estimations Using Vehicle Systems Simulations with E30 and ULSD,” *SAE Int. J. Engines*, 2014, doi: 10.4271/2014-01-1324.

[93] J. Benajes, A. García, J. Monsalve-Serrano, and D. Villalta, “Exploring the limits of the reactivity controlled compression ignition combustion concept in a light-duty diesel engine and the influence of the direct-injected fuel properties,” *Energy Convers. Manag.*, vol. 157, pp. 277–287, 2018, doi: 10.1016/j.enconman.2017.12.028.

[94] M. P. B. Musculus, P. C. Miles, and L. M. Pickett, *Conceptual models for partially premixed low-temperature diesel combustion*, vol. 39, no. 2–3. Elsevier Ltd, 2013.

[95] B. Chehroudi, “Recent experimental efforts on high-pressure supercritical

injection for liquid rockets and their implications," *Int. J. Aerosp. Eng.*, 2012, doi: 10.1155/2012/121802.

[96] A. R. Karagozian, "Transverse jets and their control," *Prog. Energy Combust. Sci.*, vol. 36, no. 5, pp. 531–553, 2010, doi: 10.1016/j.pecs.2010.01.001.

[97] Z. Si, Y. Ashida, N. Shimasaki, K. Nishida, and Y. Ogata, "Effect of cross-flow on spray structure, droplet diameter and velocity of impinging spray," *Fuel*, vol. 234, no. July, pp. 592–603, 2018, doi: 10.1016/j.fuel.2018.07.061.

[98] R. Surya Prakash, A. Sinha, G. Tomar, and R. V. Ravikrishna, "Liquid jet in crossflow – Effect of liquid entry conditions," *Exp. Therm. Fluid Sci.*, vol. 93, no. January 2017, pp. 45–56, 2018, doi: 10.1016/j.expthermflusci.2017.12.012.

[99] D. A. Dickmann and F. K. Lu, "Shock/Boundary-Layer Interaction Effects on Transverse Jets in Crossflow over a Flat Plate," *J. Spacecr. Rockets*, vol. 46, no. 6, pp. 1132–1141, Nov. 2009, doi: 10.2514/1.39297.

[100] C. hai Liang, M. bo Sun, Y. Liu, and Y. xin Yang, "Shock wave structures in the wake of sonic transverse jet into a supersonic crossflow," *Acta Astronaut.*, vol. 148, no. February, pp. 12–21, 2018, doi: 10.1016/j.actaastro.2018.04.009.

[101] J. Manin, C. Crua, and L. M. Pickett, "Transcritical mixing of sprays for multi-component fuel mixtures," in *ILASS–Europe 2017: 28th Conference on Liquid Atomization and Spray Systems*, 2017, no. September.

[102] C. Crua, J. Manin, and L. M. Pickett, "On the transcritical mixing of fuels at diesel engine conditions," *Fuel*, vol. 208, pp. 535–548, 2017, doi: 10.1016/j.fuel.2017.06.091.

[103] M. J. Guzman, "Behavior of water on a hot plate. Graph shows heat transfer (flux) v. temperature (in degrees Celsius) above TS, the saturation temperature of water, 100 °C (212 °F)." .

[104] F. Gorelli, M. Santoro, T. Scopigno, M. Krisch, and G. Ruocco, "Liquidlike Behavior of Supercritical Fluids," *Phys. Rev. Lett.*, vol. 97, no. 24, p. 245702,

Dec. 2006, doi: 10.1103/PhysRevLett.97.245702.

[105] G. G. Simeoni *et al.*, “The Widom line as the crossover between liquid-like and gas-like behaviour in supercritical fluids,” *Nat. Phys.*, vol. 6, no. 7, pp. 503–507, Jun. 2010, doi: 10.1038/nphys1683.

[106] D. T. Banuti, “Crossing the Widom-line - Supercritical pseudo-boiling,” *J. Supercrit. Fluids*, vol. 98, pp. 12–16, 2015, doi: 10.1016/j.supflu.2014.12.019.

[107] J. Thomas, “Drive Cycle Powertrain Efficiencies and Trends Derived from EPA Vehicle Dynamometer Results,” *SAE Int. J. Passeng. Cars - Mech. Syst.*, vol. 7, no. 4, pp. 1374–1384, 2014, doi: 10.4271/2014-01-2562.

[108] VVT, “Vehicle energy efficiencies,” *IEA EGRD Work.*, 2013.

[109] R. Stone, *Introduction to the Internal Combustion Engine*. .

[110] S. Saxena and I. D. Bedoya, “Fundamental phenomena affecting low temperature combustion and HCCI engines, high load limits and strategies for extending these limits,” *Prog. Energy Combust. Sci.*, vol. 39, no. 5, pp. 457–488, Oct. 2013, doi: 10.1016/j.pecs.2013.05.002.

[111] S. M. Jerome and S. Sundararaj, “Experimental Study on the Effect of Thermal Barrier Coating on Cylinder Head of a Semi-Adiabatic Diesel Engine,” *SAE Tech. Pap.*, 2017, doi: 10.4271/2017-28-1978.Copyright.

[112] J. R. Serrano, F. J. Arnau, J. Martin, M. Hernandez, and B. Lombard, “Analysis of Engine Walls Thermal Insulation: Performance and Emissions,” Apr. 2015, doi: 10.4271/2015-01-1660.

[113] N. Uchida and H. Osada, “A New Piston Insulation Concept for Heavy-Duty Diesel Engines to Reduce Heat Loss from the Wall,” *SAE Int. J. Engines*, 2017, doi: 10.4271/2017-24-0161.

[114] M. F.Shabir, S. Authars, S. Ganesan, R. Karthik, and S. K. Madhan, “Low Heat Rejection Engines - Review,” May 2010, doi: 10.4271/2010-01-1510.

[115] H. Kosaka *et al.*, “Concept of ‘Temperature Swing Heat Insulation’ in Combustion Chamber Walls, and Appropriate Thermo-Physical Properties for

Heat Insulation Coat,” *SAE Int. J. Engines*, 2013, doi: 10.4271/2013-01-0274.

[116] A. Kawaguchi, H. Iguma, H. Yamashita, N. Takada, N. Nishikawa, and C. Yamashita, “Thermo-Swing Wall Insulation Technology; - A Novel Heat Loss Reduction Approach on Engine Combustion Chamber,” *SAE Tech. Pap.*, 2016, doi: 10.4271/2016-01-2333.Copyright.

[117] G. Zhang *et al.*, “Power and efficiency factors for comprehensive evaluation of thermoelectric generator materials,” *Int. J. Heat Mass Transf.*, vol. 93, pp. 1034–1037, 2016, doi: 10.1016/j.ijheatmasstransfer.2015.10.051.

[118] A. Massaguer *et al.*, “A method to assess the fuel economy of automotive thermoelectric generators,” *Appl. Energy*, vol. 222, pp. 42–58, 2018, doi: 10.1016/j.apenergy.2018.03.169.

[119] H. Aghaali and H. E. Ångström, “A review of turbocompounding as a waste heat recovery system for internal combustion engines,” *Renew. Sustain. Energy Rev.*, vol. 49, pp. 813–824, 2015, doi: 10.1016/j.rser.2015.04.144.

[120] A. S. Panesar, “An innovative Organic Rankine Cycle system for integrated cooling and heat recovery,” *Appl. Energy*, vol. 186, pp. 396–407, 2017, doi: 10.1016/j.apenergy.2016.03.011.

[121] R. Morgan, G. Dong, A. Panesar, and M. Heikal, “A comparative study between a Rankine cycle and a novel intra-cycle based waste heat recovery concepts applied to an internal combustion engine,” *Appl. Energy*, vol. 174, pp. 108–117, 2016, doi: 10.1016/j.apenergy.2016.04.026.

[122] J. Finneran, C. P. Garner, M. Bassett, and J. Hall, “A review of split-cycle engines,” *Loughbrgh. Univ. Institutional Repos.*, pp. 0–42, Aug. 2018, doi: 10.1177/1468087418789528.

[123] G. B. Brayton, “Improvement in Gas Engines,” US125166A, 1872.

[124] F. A. Taylor, “Catalog of the Mechanical Collections Of The Division Of Engineering,” *United States National Museum Bulletin 173*. United States Government Printing Office, 1939.

[125] D. Morrison, “Harry Ricardo – A Passion for Efficiency,” in *The Piston Engine Revolution: Papers from a Conference on the History of Reciprocating Internal Combustion Engines Held at the Museum of Science and Industry*, Newcomen Society, 2012, pp. 153–176.

[126] R. Meldolesi, G. Bailey, C. Lacy, I. Gilbert, J.-P. Pirault, and A. Perkins, “Scuderi Split Cycle Fast Acting Valvetrain: Architecture and Development,” *SAE Int. J. Engines*, vol. 4, no. 1, pp. 2011-01–0404, Apr. 2011, doi: 10.4271/2011-01-0404.

[127] J. Karuppaswamy, A. Bhat, and D. Gangadkar, “Estimation of Performance Characteristics of a Split Cycle Based SI Engine,” 2016, doi: 10.4271/2016-28-0090.

[128] T. Janhunen *et al.*, “ULTRA-LOW NOx HCCI-COMBUSTION IN THE Z ENGINE,” 2019.

[129] J. Tiainen, A. Saarinen, T. Grönlund, and M. Larmi, “Novel Two-Stroke Engine Concept, Feasibility Study,” *SAE Tech. Pap.*, 2003, doi: 10.4271/2003-01-3211.

[130] T. Grönlund and M. Larmi, “Valve train design for a new gas exchange process,” *SAE Tech. Pap.*, no. 724, 2004, doi: 10.4271/2004-01-0607.

[131] C. Ailloud, A. Keromnes, B. Delaporte, G. Schmitz, and L. Le Moyne, “Development and Validation of a Five Stroke Engine,” Sep. 2013, doi: 10.4271/2013-24-0095.

[132] T. Li, B. Wang, and B. Zheng, “A comparison between Miller and five-stroke cycles for enabling deeply downsized, highly boosted, spark-ignition engines with ultra expansion,” *Energy Convers. Manag.*, vol. 123, pp. 140–152, Sep. 2016, doi: 10.1016/j.enconman.2016.06.038.

[133] R. Babayev, M. Ben Houidi, A. Andersson, and B. Johansson, “Isobaric Combustion: A Potential Path to High Efficiency, in Combination with the Double Compression Expansion Engine (DCEE) Concept,” in *SAE Technical Papers*, Jan. 2019, vol. 2019-Janua, no. January, pp. 1–18, doi:

10.4271/2019-01-0085.

[134] N. Lam, M. Tuner, P. Tunestal, A. Andersson, S. Lundgren, and B. Johansson, “Double Compression Expansion Engine Concepts: A Path to High Efficiency,” *SAE Int. J. Engines*, vol. 8, no. 4, pp. 2015-01–1260, Apr. 2015, doi: 10.4271/2015-01-1260.

[135] N. Lam, “Double Compression-Expansion Engine Concepts: Experimental and simulation study of a split-cycle concept for improved brake efficiency,” Lund University, 2019.

[136] N. Lam, A. Andersson, and P. Tunestal, “Double Compression Expansion Engine Concepts: Efficiency Analysis over a Load Range,” *SAE Tech. Pap.*, vol. 2018-April, pp. 1–18, Apr. 2018, doi: 10.4271/2018-01-0886.

[137] N. Lam, P. Tunestal, and A. Andersson, “Simulation of System Brake Efficiency in a Double Compression-Expansion Engine-Concept (DCEE) Based on Experimental Combustion Data,” *SAE Tech. Pap. Ser.*, vol. 1, pp. 1–22, 2019, doi: 10.4271/2019-01-0073.

[138] E. Musu, R. Gentili, and R. D. Reitz, “Homogeneous Charge Progressive Combustion (HCPC): CFD Study of an Innovative Diesel HCCI Concept,” Apr. 2009, doi: 10.4271/2009-01-1344.

[139] E. Musu, R. Rossi, R. Gentili, and R. D. Reitz, “Clean Diesel Combustion by Means of the HCPC Concept,” *SAE Int. J. Engines*, vol. 3, no. 1, pp. 2010-01–1256, Apr. 2010, doi: 10.4271/2010-01-1256.

[140] E. Musu, R. Rossi, R. Gentili, and R. D. Reitz, “CFD study of HCPC turbocharged engine,” *SAE Tech. Pap.*, Oct. 2010, doi: 10.4271/2010-01-2107.

[141] E. Musu, R. Rossi, R. Gentili, and R. D. Reitz, “Heavy duty HCPC,” *SAE Tech. Pap.*, Aug. 2011, doi: 10.4271/2011-01-1824.

[142] R. Rossi, E. Musu, S. Frigo, R. Gentili, and R. D. Reitz, “Simultaneous reduction of soot and NOX emissions by means of the HCPC Concept: Complying with the heavy duty EURO 6 limits without aftertreatment system,”

in *SAE Technical Papers*, Sep. 2013, vol. 6, no. X, doi: 10.4271/2013-24-0093.

[143] M. W. Coney, A. M. Cross, C. Linnemann, R. E. Morgan, and B. Wilson, “Engineering aspects of a novel high efficiency reciprocating internal combustion engine,” *Proc. 2002 Int. Jt. Power Gener. Conf.*, pp. 935–943, 2002, doi: 10.1115/ijpgc2002-26047.

[144] M. W. Coney, P. Stephenson, A. Malmgren, C. Linnemann, and R. E. Morgan, “Development Of A Reciprocating Compressor Using Water Injection To Achieve Quasi- Isothermal Compression,” in *International Compressor Engineering Conference*, 2002, p. 10, [Online]. Available: http://docs.lib.purdue.edu/icec/1508.

[145] P. L. Stephenson, M. Coney, W. Hill, B. Park, and W. Sn, “Computer modelling of isothermal compression in the reciprocating compressor of a complete isoengine.”

[146] M. Coney, “A thermodynamic analysis of a novel high efficiency reciprocating internal combustion engine?the isoengine,” *Energy*, vol. 29, no. 12–15, pp. 2585–2600, Dec. 2004, doi: 10.1016/j.energy.2004.05.014.

[147] M. Coney, C. Linnemann, K. Sugiura, and T. Goto, “Isoengine Data Analysis and Future Design Options,” *Int. Counc. Combust. Engines*, no. January, 2004.

[148] Z. Chen and C. D. Copeland, “Inverted Brayton Cycle Employment for a Highly Downsized Turbocharged Gasoline Engine,” 2015, doi: 10.4271/2015-01-1973.

[149] N. Owen *et al.*, “A Practical Recuperated Split Cycle Engine for Low Emissions and High Efficiency,” in *SAE Technical Papers*, Sep. 2019, vol. 2019-Septe, no. September, doi: 10.4271/2019-24-0190.

[150] M. Jaya Vignesh *et al.*, “Use of cryogenic fluids for zero toxic emission hybrid engines,” in *Internal Combustion Engines and Powertrain Systems for Future Transport 2019: Proceedings of the International Conference on Internal*

Combustion Engines and Powertrain, (ICEPSFT 2019), 1st Editio., Taylor and Francis, 2020, pp. 117–130.

[151] J. M. Gopal, G. Tretola, R. Morgan, G. de Sercey, A. Atkins, and K. Vogiatzaki, “Understanding Sub and Supercritical Cryogenic Fluid Dynamics in Conditions Relevant to Novel Ultra Low Emission Engines,” *Energies*, vol. 13, no. 12, pp. 1–23, Jun. 2020, doi: 10.3390/en13123038.

[152] G. Dong, R. Morgan, and M. Heikal, “A novel split cycle internal combustion engine with integral waste heat recovery,” *Appl. Energy*, vol. 157, pp. 744–753, Nov. 2015, doi: 10.1016/j.apenergy.2015.02.024.

[153] Mercedes AMG HPP, “THE MOST POWERFUL F1 MERCEDES EVER!” https://www.mercedes-amg-hpp.com/the-most-powerful-f1-mercedes-ever/.

[154] Wärtsilä, “Five ways the Wärtsilä 46TS-DF helps you decarbonise now and in the future,” 2022. https://www.wartsila.com/insights/article/five-ways-the-wartsila-46ts-df-helps-you-decarbonise-now-and-in-the-future.

[155] F. Khalid *et al.*, “Towards zero emission engines through the adoption of combustion- lead engine design realised using a split cycle topology,” 2018.

[156] Luo, Z., Som, S., Sarathy, S. M., Plomer, M., Pitz, W. J., Longman, D. E., “Development and validation of an n-dodecane skeletal mechanism for spray combustion applications,” *Combust. Theory Model.*, vol. 18, pp. 187–203, 2014.

[157] J. Chen, Z. Yan, G. Lin, and B. Andresen, “On the Curzon-Ahlborn efficiency and its connection with the efficiencies of real heat engines,” *Energy Convers. Manag.*, vol. 42, pp. 173–181, 2001, doi: 10.1016/S0196-8904(00)00055-8.

[158] C. Wu, L. Chen, and J. Chen, *Recent Advances in Finite-time Thermodynamics*. Nova Science Publishers, 1999.

[159] S. K. Chen and P. F. Flynn, “Development of a Single Cylinder Compression Ignition Research Engine,” Feb. 1965, doi: https://doi.org/10.4271/650733.

[160] D. Sandoval and J. B. Heywood, “An Improved Friction Model for Spark-

Ignition Engines," Mar. 2003, doi: https://doi.org/10.4271/2003-01-0725.

[161] S. F. Rezeka and N. A. Henein, "A New Approach to Evaluate Instantaneous Friction and Its Components in Internal Combustion Engines," Feb. 1984, doi: https://doi.org/10.4271/840179.

[162] E. Pipitone, "A New Simple Friction Model for S. I. Engine," Jun. 2009, doi: 10.4271/2009-01-1984.

[163] J. B. Heywood, *Internal Combustion Engine Fundamentals*. McGraw-Hill Book Co, 1989.

[164] R. Morgan *et al.*, "The Ultra Low Emissions Potential of the Recuperated Split Cycle Combustion System," in *SAE Technical Paper Series*, Sep. 2019, vol. 1, doi: 10.4271/2019-24-0189.

[165] E. Olofsson *et al.*, "A high dilution stoichiometric combustion concept using a wide variable spark gap and in-cylinder air injection in order to meet future CO2 requirements and world wide emission regulations," *SAE Tech. Pap.*, vol. 2001, no. 724, Mar. 2001, doi: 10.4271/2001-01-0246.

[166] Y.-H. H. Seo, "Development of air-assisted injection system for MPI gasoline engine," *SAE Tech. Pap.*, no. 724, Feb. 1998, doi: 10.4271/981056.

[167] J. Sureshkumar, R. Elayaraja, J. M. Mallikarjuna, and G. Venkitachalam, "Transient Spray Characteristics of Air Assisted Fuel Injection," *SAE Tech. Pap.*, vol. 2015-April, no. April, Apr. 2015, doi: 10.4271/2015-01-0920.

[168] G. Cathcart and C. Zavier, "Fundamental Characteristics of an Air-Assisted Direct Injection Combustion System as Applied to 4-Stroke Automotive Gasoline Engines," in *SAE Technical Papers*, Mar. 2000, vol. 2000, no. 724, doi: 10.4271/2000-01-0256.

[169] M. S. Brogan, D. Swallow, R. J. Brisley, D. Worth, and K. Yang, "A new approach to meeting future european emissions standards with the orbital direct injection gasoline engine," *SAE Tech. Pap.*, no. 724, Oct. 2000, doi: 10.4271/2000-01-2913.

[170] C. Koci, R. Florea, S. Das, M. Walls, S. Simescu, and C. Roberts, “Air-assisted direct injection diesel investigations,” *SAE Tech. Pap.*, vol. 2, Apr. 2013, doi: 10.4271/2013-01-0907.

[171] G. Cathcart and J. Tubb, “Application of Air Assisted Direct Fuel Injection to Pressure Charged Gasoline Engines,” in *SAE Technical Papers*, Mar. 2002, vol. 2002, no. 724, doi: 10.4271/2002-01-0705.

[172] A. A. Boretti *et al.*, “Experimental and Numerical Study of an Air Assisted Fuel Injector for a D.I.S.I. Engine,” Apr. 2007, pp. 776–790, doi: 10.4271/2007-01-1415.

[173] F. Gerbino, R. Morgan, P. Atkins, and K. Vogiatzaki, “Assessment of modelling capability for numerical simulations for designing higher efficiency and lower emission systems,” 2019.

[174] T.-M. Jia, G.-X. Li, Y.-S. Yu, and Y.-J. Xu, “Effects of ultra-high injection pressure on penetration characteristics of diesel spray and a two-mode leading edge shock wave,” *Exp. Therm. Fluid Sci.*, vol. 79, pp. 126–133, Dec. 2016, doi: 10.1016/j.expthermflusci.2016.07.006.

[175] M. C. Kocsis, S. Joo, T. Briggs, and T. Alger, “Impact of Swirl Ratio on Combustion Performance of a Non-Pent Roof Combustion Chamber Engine,” Apr. 2015, doi: 10.4271/2015-01-0743.

[176] A. OY, “Z-HCCI combustion: A new type of combustion having low emissions and high BMEP,” 2008.

[177] M. Day, S. Tachibana, J. Bell, M. Lijewski, V. Beckner, and R. K. Cheng, “A combined computational and experimental characterization of lean premixed turbulent low swirl laboratory flames: I. Methane flames,” *Combust. Flame*, vol. 159, pp. 275–290, 2012, doi: 10.1016/j.combustflame.2011.06.016.

[178] M. Day, S. Tachibana, J. Bell, M. Lijewski, V. Beckner, and R. K. Cheng, “A combined computational and experimental characterization of lean premixed turbulent low swirl laboratory flames II. Hydrogen flames,” *Combust. Flame*, vol. 162, pp. 2148–2165, 2015, doi: 10.1016/j.combustflame.2015.01.013.

[179] M. Y. Leong, V. G. McDonell, and G. S. Samuelsen, *Mixing of an Airblast-Atomized Fuel spray injected into a crossflow of air*, no. November 2000. 2000.

[180] R. Ragucci, A. Bellofiore, and A. Cavaliere, “Breakup and breakdown of bent kerosene jets in gas turbine conditions,” *Proc. Combust. Inst.*, vol. 31 II, pp. 2231–2238, 2007, doi: 10.1016/j.proci.2006.07.204.

[181] R. Surya Prakash, H. Gadgil, and B. N. Raghunandan, “Breakup processes of pressure swirl spray in gaseous cross-flow,” *Int. J. Multiph. Flow*, vol. 66, pp. 79–91, 2014, doi: 10.1016/j.ijmultiphaseflow.2014.07.002.

[182] J. E. Seay and G. S. Samuelsen, “Atomization and Dispersion of a Liquid Jet Injected Into a Crossflow of Air,” *Stand*, p. 144, 1996.

[183] Z. Ren, B. Wang, G. Xiang, D. Zhao, and L. Zheng, “Supersonic spray combustion subject to scramjets: Progress and challenges,” *Prog. Aerosp. Sci.*, vol. 105, no. June 2018, pp. 40–59, Feb. 2019, doi: 10.1016/j.paerosci.2018.12.002.

[184] B. Chehroudi and D. Talley, “Interaction of acoustic waves with a cryogenic nitrogen jet at sub- and supercritical pressures,” in *40th AIAA Aerospace Sciences Meeting & Exhibit*, Jan. 2002, no. January, doi: 10.2514/6.2002-342.

[185] S. Kook and L. Pickett, “Effect of Ambient Temperature and Density on Diesel-Spray-Generated Shock Waves,” 2008, [Online]. Available: http://www.ilass.org/recent/conferencepapers/Paper W1-A-1.pdf.

[186] F. J. Salvador, J. De la Morena, H. Taghavifar, and A. Nemati, “Scaling spray penetration at supersonic conditions through shockwave analysis,” *Fuel*, vol. 260, no. October 2019, p. 116308, Jan. 2020, doi: 10.1016/j.fuel.2019.116308.

[187] M. Oschwald *et al.*, “Injection of fluids into supercritical environments,” *Combust. Sci. Technol.*, vol. 178, pp. 49–100, 2006, doi: 10.1080/00102200500292464.

[188] B. Chehroudi, “Physical Hypothesis for the Combustion Instability in

Cryogenic Liquid Rocket Engines,” *J. Propuls. Power*, vol. 26, no. 6, pp. 1153–1160, 2010, doi: 10.2514/1.38451.

[189] M. Lazzaro, F. Catapano, and P. Sementa, “Experimental Characterization of Methane Direct Injection from an Outward-Opening Poppet-Valve Injector,” *SAE Tech. Pap. Ser.*, vol. 1, no. September, pp. 1–10, 2019, doi: 10.4271/2019-24-0135.

[190] Ofgem, “Ofgem Electricity Wholesale Markets.” https://www.ofgem.gov.uk/energy-data-and-research/data-portal/wholesale-market-indicators (accessed May 30, 2023).

[191] ARGUS, “Green hydrogen: Recent trends and the need for a green energy carrier,” no. June, pp. 1–6, 2020, [Online]. Available: www.argusmedia.com.

Appendices

Appendix 1

Estimates used for vehicle cost per year calculations (including capital) for UK class 8 truck. Infrastructure costs are not considered. Cost estimates are wholesale with no tax or subsidy. Electricity costs are based on Ofgem wholesale electricity costs and predictions [190]. Green hydrogen costs utilise estimates and predictions from the EC H2 Strategy [70]. Green ammonia costs utilise estimates and predictions from white papers by Ricardo and Argus Media [73], [191]. DAC efuel costs utilise estimates and predictions by the Royal Society [60]. High and low capital costs are rough estimates by the author.

	2020		2040	
Fuel Cost	**High**	**Low**	**High**	**Low**
Diesel Price £/litre	£0.60	£0.30	£0.60	£0.30
Electricity Cost (£/ kWh)	£0.10	£0.02	£0.10	£0.02
Green Hydrogen Cost (£/kg)	£4.70	£2.15	£2.50	£0.50
Green Ammonia (£/kg)	£0.55	£0.50	£0.25	£0.20
eFuel DAC (£/kg)	£2.30	£1.20	£1.50	£0.80

Baseline Truck	**High**	**Low**	**High**	**Low**
MPG (UK)	7	8	7	8
Annual Mileage	75000	75000	75000	75000
Litres per UK Gallon	4.54609	4.54609	4.54609	4.54609
Annual Diesel Used, Litres	48708	42620	48708	42620
Baseline Diesel Efficiency	44%	44%	44%	44%
Annual energy consumption (MJ)	910842	796986	910842	796986
Annual diesel fuel Cost £	£29,225	£12,786	£29,225	£12,786
Class 8 tractor cost	£100,000	£80,000	£90,000	£70,000
Split Cycle Equivalent cost	£120,000	£100,000	£100,000	£80,000
Large Battery Truck Costs	£270,000	£220,000	£200,000	£120,000
Small Battery Tuck Cost	£160,000	£130,000	£110,000	£70,000
Fuel Cell Truck Costs	£300,000	£200,000	£250,000	£150,000
Class 8 baseline 10 year cost	£392,249	£207,859	£382,249	£197,859
Diesel Engine annual cost	£39,225	£20,786	£38,225	£19,786

Diesel Engine Green Fuels annual cost	**High**	**Low**	**High**	**Low**
Diesel Engine Green Hydrogen	£81,079	£32,453	£43,127	£7,547
Diesel Engine Green Ammonia	£61,212	£48,692	£27,824	£19,477
Diesel Engine eFuel DAC	£107,720	£49,176	£70,252	£32,784

Split Cycle Truck Based on Wet Thermopower	**High**	**Low**	**High**	**Low**
Useful Life (years)	10	12	10	12
Split Cycle Efficiency	50%	53%	53%	60%

Efficiency Improvement	14%	20%	20%	36%
Annual Diesel, Litres	42,863	35,382	40,437	31,254
SCE diesel annual cost	£25,718	£10,615	£24,262	£9,376
SCE Green hydrogen annual cost	£71,349	£26,942	£35,804	£5,535
SCE Green Ammonia annual cost	£53,867	£40,423	£23,099	£14,283
SCE eFuel DAC annual cost	£94,793	£40,826	£58,322	£24,042

Electric Truck - Large Battery	**High**	**Low**	**High**	**Low**
Useful Life (years)	5	6	6	7
Electric Drivetrain efficiency (%)	75%	85%	75%	85%
Electricity Consumption (MJ)	1214455	937631	1214455	937631
Electricity Consumption (kWh)	337254	260380	337254	260380
Big Battery annual electricity cost	£33,725	£6,249	£33,725	£6,249
Annual cost including capital	£87,725	£42,916	£67,059	£23,392

Electric Truck - Small Battery	**High**	**Low**	**High**	**Low**
Useful Life (years)	6	8	7	9
Annual energy consumption (MJ)	910842	796986	910842	796986
Electric Drivetrain efficiency (%)	80%	90%	80%	90%
Electricity Consumption (MJ)	1138552	885540	1138552	885540
Electricity Consumption (kWh)	316176	245915	316176	245915
Small Battery annual electricity cost	£31,618	£5,902	£31,618	£5,902
Annual cost including capital	£58,284	£22,152	£47,332	£13,680

Fuel Cell Truck	**High**	**Low**	**High**	**Low**
Useful Life (years)	8	10	8	10
Annual energy consumption (MJ)	910842	796986	910842	796986
Fuel Driveline efficiency (%)	50%	60%	50%	60%
Hydrogen Consumption (kg)	12829	9354	12829	9354
Annual Hydrogen fuel cost	£60,295	£20,112	£32,072	£4,677
Annual cost including capital	£97,795	£40,112	£63,322	£19,677